International Journal of Modern Physics A
Vol. 36, No. 30 (2021) 2130018 (155 pages)

DOI: 10.1142/S0217751X21300180

World Scientific
www.worldscientific.com



# The NUMEN Technical Design Report

Francesco Cappuzzello,[1,2,*] Clementina Agodi,[1] Luciano Calabretta,[1] Daniela Calvo,[3] Diana Carbone,[1] Manuela Cavallaro,[1] Maria Colonna,[1] Paolo Finocchiaro,[1] Felice Iazzi,[3,4] Roberto Linares,[5] José R. B. Oliveira,[6] Luciano Pandola,[1] Elena Santopinto,[7] Domenico Torresi,[1] Salvatore Tudisco,[1] Luis Acosta,[8] Carmen Altana,[1] Paulina Amador-Valenzuela,[9] Luis Humberto Avanzi,[10] Jessica Bellone,[1] Danilo Bonanno,[1] Ismail Boztosun,[11] Sandro Brasolin,[3] Giuseppe A. Brischetto,[1,2] Oscar Brunasso,[3] Salvatore Calabrese,[1] Luigi Campajola,[12,13] Vittoria Capirossi,[3,4] Efrain R. Chávez Lomelí,[8] Irene Ciraldo,[1,2] Vitor Ângelo Paulino de Aguiar,[6] Franck Delaunay,[1,2,14] Carlo Ferraresi,[3,15] Maria Fisichella,[1] Elisa Gandolfo,[12,13] Marcilei Aparecida Guazzelli,[10] Francesco La Via,[16] Daniel J. Marin Lambarri,[8] Horst Lenske,[17] Jesus Lubian,[5] Nilberto H. Medina,[6] Paolo Mereu,[3] Mauricio Moralles,[18] Annamaria Muoio,[1] Horia Petrascu,[19] Federico Pinna,[3,4] Diego Sartirana,[3] Onoufrios Sgouros,[1] Selçuk O. Solakci,[11] Vasilis Soukeras,[1,2] Alessandro Spatafora,[1,2] Antonio D. Russo[1] and Aydin Yildirim[11]

[1] *Istituto Nazionale di Fisica Nucleare, Laboratori Nazionali del Sud, I-95125 Catania, Italy*
[2] *Dipartimento di Fisica e Astronomia "Ettore Majorana", Università di Catania, I-95125 Catania, Italy*
[3] *INFN, Sezione di Torino, Torino, Italy*
[4] *DISAT, Politecnico di Torino, Torino, Italy*
[5] *Instituto de Física, Universidade Federal Fluminense, Niterói 24210-340, Brazil*
[6] *Instituto de Fisica, Universidade de São Paulo, São Paulo, Brazil*
[7] *INFN, Sezione di Genova, Genova, Italy*
[8] *Instituto de Física, Universidad Nacional Autónoma de México, Mexico City, Mexico*
[9] *Departamento de Aceleradores y Estudio de Materiales, Instituto Nacional de Investigaciones Nucleares, Apartado Postal 18-1027 C.P. 11801, Mexico*
[10] *Centro Universitário FEI, São Bernardo do Campo, Brazil*
[11] *Department of Physics, Akdeniz University, 07058 Antalya, Turkey*
[12] *INFN, Sezione di Napoli, Napoli, Italy*
[13] *Dipartimento di Fisica, Università di Napoli Federico II, Napoli, Italy*
[14] *Laboratoire de Physique Corpusculaire de Caen, Normandie Université, Ensicaen, Unicaen, CNRS/IN2P3, 14000 Caen, France*
[15] *DIMEAS, Politecnico di Torino, Torino, Italy*
[16] *CNR-IMM, Sezione di Catania, Catania, Italy*
[17] *Department of Physics, University of Giessen, Germany*
[18] *Instituto de Pesquisas Energéticas e Nucleares IPEN/CNEN, Brazil*
[19] *IFIN-HH, Bucharest, Romania*
[*] *cappuzzello@lns.infn.it*

Received 29 September 2021
Accepted 18 October 2021
Published 1 December 2021

[*]Corresponding author.

NUMEN proposes an innovative technique to access the nuclear matrix elements entering the expression of the lifetime of the double beta decay by cross-section measurements of heavy-ion induced Double Charge Exchange (DCE) reactions. Despite the fact that the two processes, namely neutrinoless double beta decay and DCE reactions, are triggered by the weak and strong interaction respectively, important analogies are suggested. The basic point is the coincidence of the initial and final state many-body wave functions in the two types of processes and the formal similarity of the transition operators. The main experimental tools for this project are the K800 Superconducting Cyclotron and MAGNEX spectrometer at the INFN-LNS laboratory. However, the tiny values of DCE cross-sections and the resolution requirements demand beam intensities much higher than those manageable with the present facility. The on-going upgrade of the INFN-LNS facilities promoted by the POTLNS[a] project in this perspective is intimately connected to the NUMEN project. This paper describes the solutions proposed as a result of the R&D activity performed during the recent years. The goal is to develop suitable technologies allowing for the measurements of DCE cross-section under extremely high beam intensities.

*Keywords*: Nuclear matrix elements for neutrinoless double beta decay; NUMEN project; nuclear reactions; heavy ions; high luminosity.

PACS numbers: 29.27.−a, 29.30.−h, 29.40.−n, 29.85.−c, 23.40.−s



## Contents



[a]PIR01_00005 — potenziamento dell'infrastruttura di ricerca Laboratori Nazionali del Sud per la produzione di fasci di ioni ad alta intensitá.

## 1. Introduction

The neutrinoless double beta decay ($0\nu\beta\beta$) is nowadays the most promising resource to establish the Majorana nature of neutrinos and potentially to shed light on the absolute neutrino mass and hierarchy. A critical aspect is that the associated Nuclear Matrix Elements (NMEs) must be known with good accuracy, even if the intrinsic many-body nature of the involved states of the parent and daughter nuclei makes this task particularly challenging. An updated comparison of the results of NME calculations, obtained within various nuclear structure frameworks,[1–5] indicates that significant differences are indeed found, which makes the present situation not satisfactory. In addition, some assumption common to different competing calculations, like the unavoidable truncation of the nuclear many-body wave function, could cause overall systematic uncertainties.

NUMEN[6–8] proposes to use Heavy-Ion Double Charge Exchange (HI-DCE) reactions as a tool to access quantitative information, relevant for $0\nu\beta\beta$ decay NME. These reactions are characterized by the transfer of two charge units, leaving the mass number unchanged, and can proceed by a sequential nucleon transfer mechanism or by exchange of two isovector mesons, in an uncorrelated or correlated fashion. Despite $0\nu\beta\beta$ decays and HI-DCE being mediated by different interactions, they present a number of similarities (see Subsec. 2.1). The key aspects are that initial and final nuclear states are the same and the transition operators in both

cases present a superposition of short-range isospin, spin–isospin and rank-2 tensor components with a relevant available momentum (100 MeV/$c$ or so). In addition, NUMEN aims at the exploration of all the relevant reaction channels promoted by the projectile/target interaction. They include elastic and inelastic scattering, single and double nucleon transfer reactions and single charge exchange (SCE) reactions.

NUMEN is conceived in a long-range time perspective, in the view of a comprehensive study of many candidate systems for $0\nu\beta\beta$ decay. Moreover, the project promotes and is strictly connected with a renewal of the INFN-LNS research infrastructure and with a specific R&D activity on detectors, materials and instrumentation. In the last years the project developed along the following three main directions: measuring DCE cross-sections for a few cases of interest; making a deep R&D investigation for the new detection technologies to be used for the future high luminosity beams; developing a fully microscopic and quantum theory for DCE reactions, specifically conceived to extract nuclear structure information from measured cross-sections.

The experimental campaigns have been conducted so far at INFN-LNS, using the K800 Superconducting Cyclotron to accelerate beams and the MAGNEX large acceptance magnetic spectrometer for the detection of the ejectiles.[9] MAGNEX is a large acceptance magnetic device made up of a large aperture vertically focusing quadrupole and a horizontally bending dipole magnet. It allows the identification of heavy ions with very good resolution in mass ($\Delta A/A \sim 1/160$), angle ($\Delta\theta \sim 0.2^\circ$) and energy ($\Delta E/E \sim 1/1000$), within a large solid angle ($\Omega \sim 50$ msr) and momentum range ($-14\% < \Delta p/p < +10\%$). High-resolution measurements for quasi-elastic processes, characterized by differential cross-sections falling down to tens of nb/sr, were already performed by this setup.[9–16] A crucial feature was the implementation of a technique of trajectory reconstruction, based on differential algebraic techniques, which allows solving the equation of motion of each detected particle to 10th order.[17] The experimental activity with accelerated beams proposed and presently in progress in NUMEN consists of two main classes of experiments, corresponding to the exploration of the two directions of isospin lowering $\tau^-\tau^-$ and rising $\tau^+\tau^+$, characteristic of $\beta^-\beta^-$ and $\beta^+\beta^+$ decays, respectively.[10,18] First experimental results obtained at the INFN-LNS laboratory for the $^{40}$Ca($^{18}$O, $^{18}$Ne)$^{40}$Ar reaction at 270 MeV gave an encouraging indication on the capability of the proposed technique to access relevant quantitative information[10] (see also Subsec. 2.4). Further measurements of the ($^{20}$Ne, $^{20}$O) reaction on $^{116}$Cd confirmed the experimental feasibility of accurate cross-section measurements in the region of interest.[19]

The results obtained by NUMEN so far indicate that suitable information from DCE reactions can be extracted.[10] However, the tiny values of such cross-sections (few nb) and the resolution requirements demand beam intensities much higher than those manageable with the present facility keeping the background of the

order of 1 nb. For a systematic exploration of all the cases of interest for $0\nu\beta\beta$ a much larger dataset of DCE data is necessary, including statistically significant data at different bombarding energies and with several isotopic targets. These considerations suggest that the DCE experiments should be performed with much higher beam energy and current, such as foreseen in the POTLNS project. Moreover, for a systematic study of the many hot cases of $\beta\beta$ decays, an upgraded MAGNEX setup, able to work with a two or three orders of magnitude higher current than the present, is necessary. As a consequence, the present limits of beam power (100 W) for the CS accelerator and acceptable rate for the MAGNEX focal plane detector (FPD) (few kHz) must be sensibly revised. This goal can be achieved by a substantial change in the technologies implemented in the beam extraction, in the detection of the ejectiles and in the target cooling. For the accelerator the change of the beam extraction technology from electrostatic deflector to a stripper foil is an adequate choice.[20] For the spectrometer the main foreseen upgrades are as follows:

- The construction of an FPD tracker based on micro-patterned gas detector. The requested characteristics of the tracker which will guarantee tracking performances compatible with the ray reconstruction technique implemented in MAGNEX are: horizontal position resolution 0.7 mm (FWHM), horizontal angle resolution 0.5° (FWHM), vertical position resolution 0.7 mm (FWHM), vertical angle resolution 0.7° (FWHM).[21]
- The construction of a wall of telescopes of SiC–CsI detectors for ion identification with radiation hardness of the order of $10^{11}$ ions/$(\mathrm{cm}^2 \cdot \mathrm{yr})$ assuming 120 days of full power irradiation per year; particle identification (PID) capability for identification of $Z \sim 10$ and $A \sim 20$ and time resolution better than 2–3 ns.[22,23]
- The introduction of an array of scintillators for measuring in coincidence the emitted $\gamma$-rays with energy resolution $< 3$–25% (FWHM) depending on the nucleus; time resolution $< 5$ ns (FWHM); observational limit $(\sigma_{\mathrm{DCE}}/\sigma_R) < 10^{-8}$ and radiation tolerance $> 10^{10}$ n/cm$^2$.
- The development of suitable front-end and read-out electronics, for a fast read-out of the detector signals, a high signal-to-noise ratio (SNR) and adequate hardness to radiation. The NUMEN data acquisition system (DAQ) must be tailored in order to fulfill the specific requirements of each subsystem, which are: a medium energy resolution, 1 ns time resolution and very high speed for the TRACKER; high-energy resolution, 1 ns time resolution and high speed for the PID; high-energy resolution, 1 ns time resolution and very high speed for the calorimeter. Moreover, other features that have been considered in the choice of the electronics are: uniform front-end and read-out hardware architecture; programmable signal handling algorithm, tailorable to each detector type; very good energy resolution, 16 bit conversion; very good timing, resolution better than 1 ns; pile-up detection and tagging; high data throughput.

- The implementation of a suitable architecture for data acquisition, storage and data handling. For that, the required performances are: handling and writing on disk of a TPC/IP formatted data stream, having rate between 10 and 100 MB/s; performing automatic data backup; implementing modular software for the online analysis, with a cross-platform support; one commercial 32-core server, dedicated to the first-level data processing in real-time (or quasi-real-time); developing simulation of the detector performance.
- The development of accurate detector response simulations.
- The enhancement of the maximum accepted magnetic rigidity, with minimal distortion of the measured magnetic field for the optical elements with a power supply upgrade to obtain 2.1–2.2 Tm, i.e. 70 MeV/u $^{18}Ne^{10+}$ and $\sim$ 42 MeV/u $^{20}O^{8+}$.[24,25]
- The design and installation of a beam dump to stop the high-power beams. The beam dump has to handle a power up to 10 kW and must have enough shielding to reduce significantly the background in the MAGNEX focal plane detector due to the neutron and gamma radiation produced by the interaction of the beam with the cooled target of the beam dump.

In addition, we are developing the technology for suitable nuclear targets to be used in the experiments. Here the challenge is to produce and cool isotopically enriched thin films able to resist to the high power dissipated by the interaction of the intense beams with the target.[26]

NUMEN is fostering the development of a specific theory program to allow an accurate extraction of nuclear structure information from the measured cross-sections. The heavy-ion induced SCE have been analyzed in detail in Refs. 27–29 in view of the connection to single beta decay NME. It was shown that the surface localization of the SCE, due the strong absorption of the target-projectile nucleus–nucleus potential, allows for a strong simplification of the reaction description, making the isovector meson exchange mechanism relevant at forward detection angles. The development of a second-order perturbation theory for DCE is being accomplished relying on the use of the Distorted Wave Born Approximation (DWBA) is focused on the development of microscopic models for DCE reactions, employing several approaches (QRPA, shell model, IBM) for inputs connected to nuclear structure quantities (see Ref. 5 and references therein). We are also investigating the best way to link the theoretical description of the $0\nu\beta\beta$ decay and DCE reactions.[29–31]

Some of the recently achieved scientific results from NUMEN have been summarized in Refs. 6 and 29. Instead, in this paper the focus is on the results from R&D, with a detailed description of the solutions proposed for the upgrade. The paper is organized as follows. In Sec. 2, an overview of the NUMEN project is given. Then, the extended description of the proposed solution for each item is presented from Secs. 3 to Sec. 11.

## 2. Overview of the NUMEN Project

### 2.1. *Heavy-ion induced double charge exchange reactions and $0\nu\beta\beta$ decays*

A DCE reaction is a process induced by a projectile $a$ on a target $A$, in which two neutrons (protons) of the target are converted in two protons (neutrons), $\Delta Z_A = \pm 2$, $\Delta N_A = \mp 2$, being the mass number unchanged, with opposite transition simultaneously occurring in the projectile, $\Delta Z_a = \mp 2$, $\Delta N_a = \pm 2$. In the isospin representation, DCE reactions probe the double isovector excitations generated, at four-body level, by $\tau_a^{\pm}\tau_a^{\pm}\tau_A^{\mp}\tau_A^{\mp}$ combination of the isospin rising and lowering operators acting on two nucleons in the projectile $a$ and the target $A$, respectively. Similarly to single charge exchange reactions, DCE probe nuclear response to the isospin degree of freedom. An important feature of DCE reactions induced by nuclear collisions is that no light projectiles can be practically used. The lightest projectiles allowed are tritons or $^3$He, and even in these cases the $(t, 3p)$ or the $(^3\mathrm{He}, 3n)$ reactions are very challenging from the experimental point of view and, to our knowledge, never explored. Also moving to heavier projectiles, the experiments become rather demanding. First pioneering explorations of the heavy-ion induced DCE reactions are the $(^{18}\mathrm{O}, ^{18}\mathrm{Ne})$, $(^{18}\mathrm{O}, ^{18}\mathrm{C})$ and $(^{14}\mathrm{C}, ^{14}\mathrm{O})$ reactions, which were performed at Berkeley, NSCL-MSU, IPN-Orsay, ANU-Pelletron, Los Alamos laboratories.[32–34] The main purpose was to determine the mass of neutron rich isotopes by reaction $Q$-value measurements. However, these experiments were not conclusive for deeper spectroscopic investigations, mainly due to the poor statistical significance of the few DCE observed events; hence, no other experiment was proposed. Also the theory, which was initiated to study the DCE reaction mechanism[35,36] soon followed the trend and the field was abandoned for a long time.

In recent years, major interest has raised for DCE studies, especially because of their possible connection to $0\nu\beta\beta$ decay. New reactions have been considered, such as the $(^8\mathrm{He}, ^8\mathrm{Be})$,[37] the $(^{11}\mathrm{B}, ^{11}\mathrm{Li})$ or the $(^{12}\mathrm{C}, ^{12}\mathrm{Be})$, explored at RIKEN and RCNP. The $(^8\mathrm{He}, ^8\mathrm{Be})$ was used to search for the tetra-neutron system by the $^4\mathrm{He}(^8\mathrm{He}, ^8\mathrm{Be})4n$.[37] The $(^{11}\mathrm{B}, ^{11}\mathrm{Li})$ and $(^{12}\mathrm{C}, ^{12}\mathrm{Be})$ were investigated with the main goal to find the Double Gamow–Teller (DGT) resonance and provide quantitative information about the DGT sum-rule.[38] Another new DCE reaction, the $(^{20}\mathrm{Ne}, ^{20}\mathrm{O})$ have been introduced at INFN-LNS Catania, with the aim to probe $\beta^-\beta^-$-like nuclear response. In addition to that, important results have been recently achieved by the renewed use of the $(^{18}\mathrm{O}, ^{18}\mathrm{Ne})$ reaction in upgraded experimental conditions.[10,39] In Ref. 10 the $^{40}\mathrm{Ca}(^{18}\mathrm{O}, ^{18}\mathrm{Ne})^{40}\mathrm{Ar}$ was studied at 15 MeV/u at the MAGNEX facility of INFN-LNS,[9] showing that high mass, angular and energy resolution, energy spectra and accurate absolute cross-sections are at reach, even at very forward angles, where the spectroscopic information is more directly accessible. The completely new and unique capability achieved in the Catania measurements to isolate the ground-state to ground-state transition in a DCE process has opened the perspective of studying the connection of DCE with $0\nu\beta\beta$ decay, raising the

question whether DCE can be used toward the experimental access to $0\nu\beta\beta$ decay NMEs.

Although the DCE and $0\nu\beta\beta$ decay processes are mediated by different interactions, there are several important similarities among them:

- Parent/daughter states of the $0\nu\beta\beta$ decay are the same as those of the target/residual nuclei in the DCE.
- Short-range Fermi, Gamow–Teller and rank-2 tensor components are present in both the transition operators, with relative weight depending on incident energy in DCE. Performing the DCE experiments at different bombarding energies is essential to gain sensitivity to the individual contribution of each component.
- A large linear momentum ($\approx 100$ MeV/$c$) is available in the virtual intermediate channel in both processes. This is a distinctive similarity since other processes such as single $\beta$ decay, $2\nu\beta\beta$ decay, light-ion induced SCE cannot probe this feature. An interesting development is the recently proposed $\mu$-capture experiments at RCNP.[40]
- The two processes are nonlocal and are characterized by two vertices localized in a pair of valence nucleons.
- Both processes take place in the same nuclear medium. In-medium effects are expected to be present in both cases, so DCE data could give a valuable constraint on the theoretical determination of quenching phenomena on $0\nu\beta\beta$.
- An off-shell propagation through virtual intermediate channels is present in the two cases.

A relevant feature of DCE, not present in $0\nu\beta\beta$ decay, is the contribution coming from multi-nucleon transfer reactions, representing a competitive route with respect to the direct exchange, leading to the same final states. The effects of multi-nucleon transfer start from the fourth order in the nucleon–nucleon potential since two protons (neutrons) should be stripped from the projectile and two neutrons (protons) picked-up from the target. In Ref. 10 it is shown that, under the experimental conditions set for the experiment at INFN-LNS, the contribution of multi-nucleon transfer is negligible (less than 1%). Similar results are being found in the preliminary analysis of the other explored cases. Consequently, the leading DCE reaction mechanism is connected to nucleon–nucleon isovector interaction, which acts between two neutrons in the projectile and two protons in the target for the ($^{18}$O, $^{18}$Ne) and between two protons in the projectiles and two neutrons in the target for the ($^{20}$Ne, $^{20}$O) reaction. A useful way to consider the DCE process is by means of the exchange of two charged $\pi$ or $\rho$ mesons between the involved nucleons. An interesting question is whether the two mesons are exchanged independently of each other in analogy to $2\nu\beta\beta$-decays or in a correlated way, as in the $0\nu\beta\beta$-decays. This last question is quite interesting for the connection of DCE reactions to $0\nu\beta\beta$-decays.[29] This aspect is also important from the point of view of nuclear reaction theory, since it could indicate a new way to access nucleon–nucleon short-range correlations, see Sec. 11.

### 2.2. *The NUMEN goals*

The NUMEN project proposes to access the nuclear matrix elements entering the expression of the life time of the $0\nu\beta\beta$ decay by measuring cross-sections of DCE reactions at different incident energies using the K800 Superconducting Cyclotron for the acceleration of the heavy-ion beams and of the MAGNEX large acceptance magnetic spectrometer for the detection of the ejectiles. The project, born in 2014, stems out as a natural evolution of the successful pioneering investigation of the $^{40}$Ca($^{18}$O, $^{18}$Ne)$^{40}$Ar DCE reaction performed at INFN-LNS.[10]

In order to determine the $0\nu\beta\beta$ decay NMEs we need to define how the DCE measured cross-sections and, in turn, DCE matrix elements are connected to $0\nu\beta\beta$ decay NMEs. This implies an accurate description of the reaction mechanism, factorized in a reaction part and a nuclear structure part, the latter separated in a projectile and target matrix elements. The development of a consistent microscopic description of the DCE reaction and the nuclear structure part is essential to explore this opportunity. The use of the quantum approach for the DWBA or Coupled Reaction Channel (CRC) cross-sections with form factors including transition densities from state-of-the-art nuclear structure approaches is a suitable framework in which this theory is developing. Experimentally, it is required to build up a systematic set of appropriate data, facing the relative experimental challenges connected with the low cross-sections, the high sensitivity needed to distinguish the DCE signal from the background and the requirement of high resolutions.

The measurement of the DCE absolute cross-sections that NUMEN wishes to provide will also have a major impact for tuning the nuclear structure theories of $0\nu\beta\beta$ decay NMEs. The NMEs for DCE and $0\nu\beta\beta$ decay probe the same initial and final wave functions by operators with similar structure. Consequently, the measured DCE absolute cross-sections allow to test the validity of the assumptions done for the unavoidable truncation of the many-body wave functions. The reaction part needs to be precisely controlled to this purpose, a result that NUMEN aims to pursue within a fully quantum scattering framework. Once the nuclear wave functions have been tested by DCE cross-sections, the same can be used for $0\nu\beta\beta$ decay NMEs. Promoting the development of these kinds of DCE constrained theories for the NME of the $0\nu\beta\beta$ decay is thus an important goal that NUMEN can achieve even with a reduced experimental dataset and without assuming cross-section factorization.

Finally, on the long term, NUMEN will provide relative NME information on the different candidate isotopes of interest for the $0\nu\beta\beta$ decay. The ratio of the measured cross-sections can give a model independent way to compare the sensitivity of different half-life experiments to the average neutrino mass. This result can be achieved even in presence of sizeable systematic errors in the measured cross-sections and in the extraction of DCE matrix elements, as they are largely reduced in the ratio. Performing these comparative analyses could have strong impact in the

future developments of the field, especially in a scenario were fundamental choices for the best isotope candidates for $0\nu\beta\beta$ decay need to be made.

### 2.3. *The phases of the NUMEN project*

The NUMEN project is conceived in a long-range time perspective, planning to perform a comprehensive study of many candidate systems for $0\nu\beta\beta$ decay. Moreover, this project promotes and is strictly connected with a renewal of the INFN-LNS (POTLNS project) research infrastructure and with a specific R&D activity on detectors, materials and instrumentation, as described in the following sections. Consequently, other research activities are likely to also benefit from such upgrades. NUMEN represents the main physics case of the on-going POTLNS project, supported by EU, and it is strongly synergic with the NURE project of ERC. The NUMEN project is divided into the following four phases.

**Phase 1: "The pilot experiment."** In 2013, the $^{40}$Ca($^{18}$O, $^{18}$Ne)$^{40}$Ar DCE reaction was measured at the INFN-LNS laboratory together with the competing processes: single charge exchange, two-proton transfer and two-neutron transfer.[10] This work showed for the first time high resolution and statistically significant experimental data on DCE reactions in a wide range of transferred momenta. The measured cross-section angular distribution is characterized by a clear oscillating pattern, described by an $L = 0$ Bessel function, indicating that a simple mechanism seems dominant in the DCE reaction. This is confirmed by the observed suppression of the multi-nucleon transfer routes. DCE matrix elements were extracted under the hypothesis of a two-step charge exchange process. Despite the approximations used in our model, which determine an uncertainty of $\pm 50\%$, the obtained results are compatible with the values known from the literature. This makes the ($^{18}$O, $^{18}$Ne) reaction very interesting to investigate the DCE response of the nuclei involved in $0\nu\beta\beta$ research.

**Phase 2: From the pilot experiment toward the "hot" cases.** The results of Phase 1 indicate that suitable information from DCE reactions can be extracted. However, with the present experimental setup, it is difficult to suitably extend the achievements of the pilot experiment to the "hot" cases, i.e. the nuclei candidate for $0\nu\beta\beta$ because:

- In the reaction studied in the pilot experiment, the $Q$-value was particularly favorable ($Q = -2.9$ MeV), while in the DCE reactions involving candidate isotopes of interest for $0\nu\beta\beta$ the $Q$-values are more negative. A sensible reduction of the cross-section is thus expected in these cases, especially at very forward angles.
- The isotopes of interest are heavier than $^{40}$Ca, consequently the nucleus–nucleus potential in the initial and final state are expected to be more absorptive with consequent further reduction of the cross-section for direct reactions as DCE.

– The DCE cross-section is expected to decrease at higher bombarding energies (at least in the energy range explored by NUMEN, i.e. 10 to 70 MeV/u) since both $\tau$ and $\sigma\tau$ components of the nucleon–nucleon effective potential show this trend.
– The ($^{18}$O, $^{18}$Ne) reaction, investigated in the pilot experiment, could be particularly advantageous, due to the presence of super-allowed transitions. However, this reaction is of $\beta^+\beta^+$ kind, while most of the research on $0\nu\beta\beta$ decay is on the $\beta^-\beta^-$ side. None of the reactions of $\beta^-\beta^-$ kind look like as favorable as the ($^{18}$O, $^{18}$Ne). NUMEN proposes the ($^{20}$Ne, $^{20}$O) reaction, which has smaller $B$(GT), so a reduction of the yield could be foreseen in these cases.
– In some cases, e.g. $^{136}$Xe or $^{130}$Xe, gas or implanted target will be necessary, which are normally much thinner than solid state films obtained by evaporation or rolling technique, with a consequent reduction of the yield.
– The achieved energy resolution (typically about half MeV) is not always enough to separate the ground from the excited states in the final nucleus. In these cases the coincident detection of gamma rays from the de-excitation of the populated states is necessary, but at the price of reducing the yield.

All these considerations suggest that the beam current for the DCE experiments must be increased. In particular, for a systematic study of the many "hot" cases of $\beta\beta$ decays, an upgraded setup, able to work with two or three orders of magnitude higher current than the present, is necessary. This goal can be achieved by a substantial change in the technologies used in the beam extraction and transport, in the target and in the detection of the ejectiles. These requirements have triggered the POTLNS project of upgrade of the INFN-LNS infrastructure for the production of high intensity ion beams.

During the NUMEN Phase 2, the R&D activity necessary for the above-mentioned upgrades has been carried out still preserving the access to the present facility. In the meanwhile, experiments for a selected set of systems have been performed. These runs require several weeks of data taking for each reaction, since thin targets (a few $10^{18}$ atoms/cm$^2$) are mandatory in order to achieve enough energy and angular resolution in the measured energy spectra and angular distributions. The attention is presently focused on a few favorable candidate cases for $\beta\beta$ decay, as discussed below, with the goal to achieve conclusive results for them. More details on the experimental activity with accelerated beams performed during NUMEN Phase 2 are given in Subsec. 2.4. In addition, during Phase 2 a deeper understanding of the main features which limit the experimental sensitivity, resolution and systematic errors is being pursued.

During this phase, the data reduction strategy is optimized and the link with the theoretical physics strengthened, especially in view of the construction of a "universal" framework, where $\beta\beta$-decay and DCE reactions are coherently analyzed.

The experimental activity of NUMEN Phase 2 and the analysis of the results is the main aspect of the NURE project[41] awarded in 2016 by the European Research

Council. The synergy between the two projects is an added value which significantly enhance the discovery potential already achieved in NUMEN Phase 2.

**Phase 3: The facility upgrade.** Once all the building blocks for the upgrade of the whole facility will be ready at the INFN-LNS, the NUMEN Phase 3, will proceed with the disassembling of the old setup and reassembling of the new will start. A duration of 24–30 months is estimated. During this period, the data analysis of the NUMEN Phase 2 experiments will continue. In addition, tests of the new detectors and selected experiments will be performed in other laboratories in order to provide still missing information in the explored reactions network. As an example, a research program to transfer the present MAGNEX focal plane detector to iThemba LABS (South Africa) has been proposed and approved. The goal is to perform their DCE studies in line with NUMEN Phase 2. The experiments are expected to be performed during NUMEN Phase 3.

**Phase 4: The experimental campaign with upgraded facility.** The NUMEN Phase 4 will consist of a series of experimental campaigns at high beam intensities (some $p\mu A$) and integrated charge of hundreds of mC up to C, for the experiments in which $\gamma$-coincidence measurements are required, spanning all the variety of $0\nu\beta\beta$ decay candidate isotopes of interest, like: $^{48}$Ca, $^{76}$Ge, $^{76}$Se, $^{82}$Se, $^{96}$Zr, $^{100}$Mo, $^{106}$Cd, $^{110}$Pd, $^{116}$Cd, $^{110}$Sn, $^{124}$Sn, $^{128}$Te, $^{130}$Te, $^{136}$Xe, $^{130}$Xe, $^{148}$Nd, $^{150}$Nd, $^{154}$Sm, $^{160}$Gd, $^{198}$Pt.

Based on the know-how gained during the experimental activity of Phases 2 and 3, the Phase 4 will be devoted to determine the absolute DCE cross-sections and their uncertainties. The use of upgraded theoretical analyses will give access to the challenging NMEs $0\nu\beta\beta$ decay, that is the ambitious goal of NUMEN.

The experiments will be performed at different incident energies in order to study the reaction mechanism and in particular to explore the dependence on energy of the different spin–isospin components of the nucleon–nucleon interaction and unfold the Fermi, GT and tensor components in the nuclear matrix elements.

A schematic description of the strategy for the experimental activity with accelerated beams in NUMEN Phase 4 is given in Subsec. 2.5.

### 2.4. *The experimental activity with beams in NUMEN Phase 2*

The experimental activity with accelerated beams proposed and presently in progress within NUMEN Phase 2 consists of two main classes of experiments, performed at INFN-LNS using the superconducting cyclotron and the MAGNEX magnetic spectrometer. A figure showing the MAGNEX spectrometer is shown in Fig. 1.

The two classes of experiments correspond to the exploration of the two directions of isospin lowering $\tau^-\tau^-$ and rising $\tau^+\tau^+$, characteristic of $\beta^-\beta^-$ and $\beta^+\beta^+$ decays, respectively. Since NMEs are time invariant quantities, they are common to a DCE and to its inverse, so the contextual measurements of $\beta^-\beta^-$ and $\beta^+\beta^+$ reactions represent a useful test bench of the procedure to extract NME from the measured DCE cross-section.

Fig. 1. The MAGNEX spectrometer.

In particular, the $\beta^+\beta^+$ direction in the target is investigated using an $^{18}O^{8+}$ beam and measuring the ($^{18}$O, $^{18}$Ne) DCE transitions, together with other reaction channels involving same beam and target. Similarly, the $\beta^-\beta^-$ direction is explored via the ($^{20}$Ne, $^{20}$O) reaction, using a $^{20}Ne^{10+}$ beam and detecting the reaction products of the DCE channel and of the other open channels characterized by same projectile and target. Exploratory investigations of the two classes of experiments have been already performed on selected targets, highlighting the strengths and the challenging aspects of the adopted technique and establishing the best working conditions.[10,18,42,43] The choice of the target isotopes is the result of a compromise between the interest of the scientific community to specific isotopes and related technical issues. In particular, the possibility to separate g.s. to g.s. transition in the DCE measured energy spectra and the availability of thin uniform target of isotopically enriched material was considered. Important experimental issues must be addressed to measure heavy-ion induced DCE reactions of both classes of experiments. The main challenges are related to the request to detect heavy ions with good isotopic separation and energy resolution in a wide angular range, including zero-degree, in order to distinguish transitions to individual states and explore a wide momentum transfer range. In addition, the rather tiny DCE cross-sections (down to few nb) demand for a remarkably high experimental sensitivity, which strongly depends on the rejection capability against unwanted events. These later may be generated by competing reaction processes, which are rather likely to occur in view of the small DCE cross-sections. For this reason, high-resolution particle identification is a prerequisite for the experiment. Spurious data associated to a wrong determination of detection parameters could casually be misinterpreted as good DCE data. Such background sources can be subtle and require stringent conditions for the experimental setup together with a very careful characterization of the detection response in order to get rid of and gain the necessary sensitivity for performing meaningful DCE investigations.[19]

**Experiments with $^{18}$O beam ($\beta^+\beta^+$ direction).** For the experiments of this class, the reaction channels of our interest are listed as follows:

– Elastic and inelastic scattering ($^{18}$O, $^{18}$O),
– DCE reaction ($^{18}$O, $^{18}$Ne),
– Charge exchange reaction ($^{18}$O, $^{18}$F),
– Two-proton pickup reaction ($^{18}$O, $^{20}$Ne),
– One-proton pickup reaction ($^{18}$O, $^{19}$F),
– Two-neutron stripping reaction ($^{18}$O, $^{16}$O),
– One-neutron stripping reaction ($^{18}$O, $^{17}$O).

One of the main challenges of such experiments is the measurement at very forward angles, including zero-degree. This is performed by placing the spectrometer with its optical axis at $+3^\circ$ with respect to the beam axis. Thanks to its large angular acceptance, a range $-2^\circ < \theta_{\rm lab} < +9^\circ$ is thus covered. The MAGNEX quadrupole and dipole magnetic fields are set in order that the incident beam, after passing through the magnets, reaches a region besides the FPD. For this class of experiments, in fact, the incident beam ($^{18}O^{8+}$) has higher magnetic rigidity ($B\rho$) than the ones of the ejectiles of interest (namely $^{18}$Ne, $^{18}$F, $^{20}$Ne, $^{19}$F, $^{16}$O, $^{17}$O with maximum charge state). In the setup of NUMEN Phase 2 the beam stops in a specifically designed Faraday cup, which measures the incident charge in each run, placed in the high-$B\rho$ region besides the FPD. A drawing of the MAGNEX spectrometer and an example of the typical $^{18}$O beam trajectory inside the spectrometer is shown in Fig. 2.

In NUMEN Phase 4, instead, due to radioprotection issues, the beam must get out from MAGNEX and be transported to a specially designed beam dump, as discussed in Sec. 3

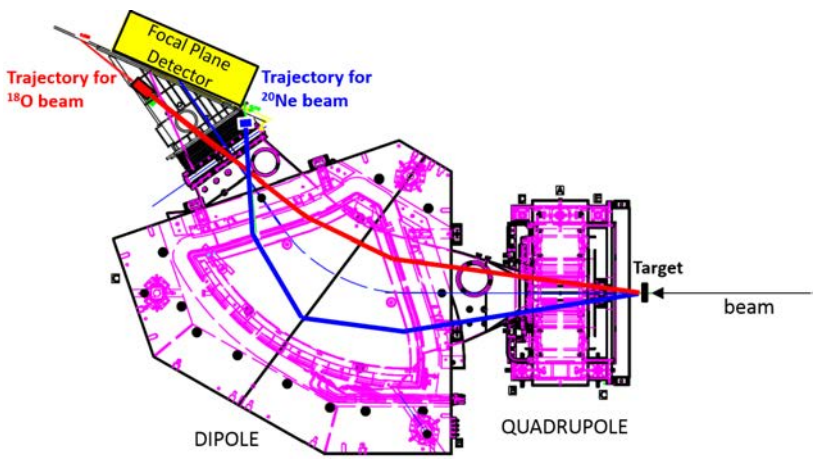


Fig. 2. Drawing of the MAGNEX spectrometer showing two typical trajectories of the $^{18}$O and $^{20}$Ne beams in the experimental conditions used for the DCE measurements.

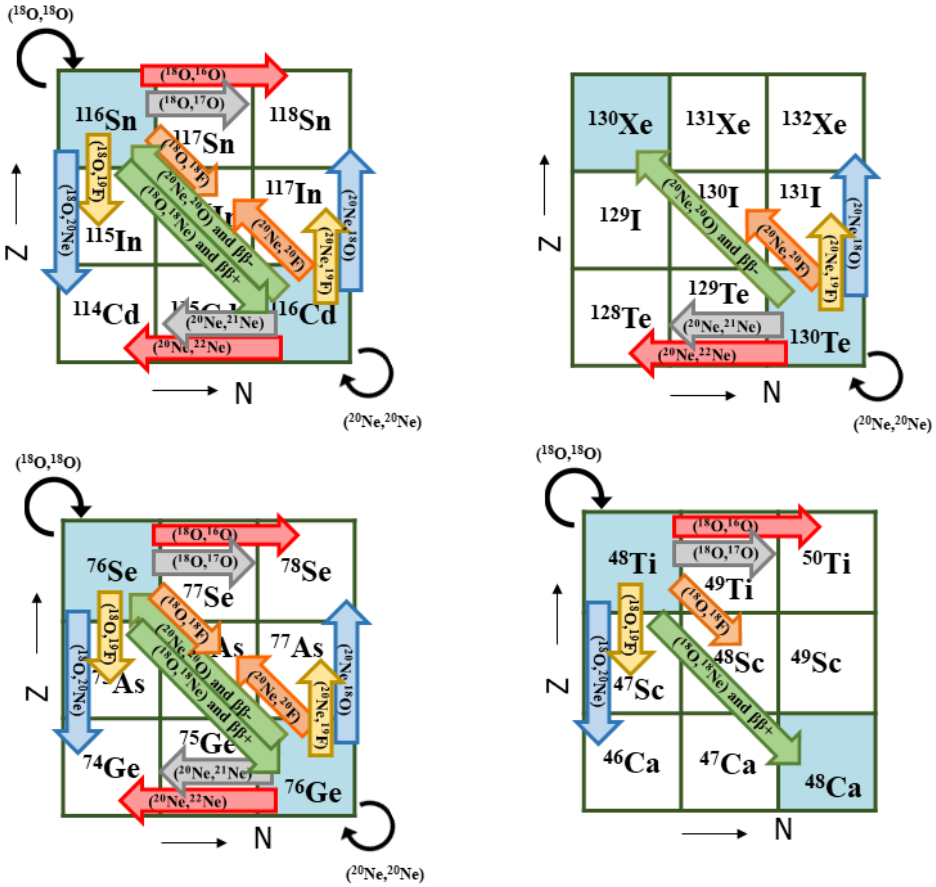


Fig. 3. Scheme of the reaction channels already studied within the NURE and NUMEN experiments.

$^{116}$Sn, $^{76}$Se and $^{48}$Ti are the targets already explored via ($^{18}$O, $^{18}$Ne) reaction at 15 AMeV in order to study the $^{116}$Sn $\rightarrow$ $^{116}$Cd, $^{76}$Se $\rightarrow$ $^{76}$Ge and $^{48}$Ti $\rightarrow$ $^{48}$Ca transitions, respectively, and the competing channels as shown in Fig. 3. The reduction and analysis of the collected data are presently in progress.

**Experiments with $^{20}$Ne beam ($\beta^-\beta^-$ direction).** In the class of experiments with $^{20}$Ne$^{10+}$ beams, the reaction channels we are interested are the following:

– Elastic and inelastic scattering ($^{20}$Ne, $^{20}$Ne),
– DCE reaction ($^{20}$Ne, $^{20}$O),
– Charge exchange reaction ($^{20}$Ne, $^{20}$F),
– Two-proton stripping reaction ($^{20}$Ne, $^{18}$O),
– One-proton stripping reaction ($^{20}$Ne, $^{19}$F),
– Two-neutron pickup reaction ($^{20}$Ne, $^{22}$Ne),
– One-neutron pickup reaction ($^{20}$Ne, $^{21}$Ne).

For these experiments, the incident beam ($^{20}Ne^{10+}$) has a lower magnetic rigidity with respect to the reaction ejectiles of interest. Thus, for a fixed magnetic field setting, the beam will be more bent than the ejectiles of interest. The spectrometer optical axis is typically placed at $-3°$, thus the covered angular range is $-8° < \theta_{lab} < +3°$. The quadrupole and dipole magnetic fields of MAGNEX are set in order that the $^{20}Ne^{10+}$ beam reaches the low-$B\rho$ region besides the FPD. Even in this case a major difference between the Phase 2 and Phase 4 is the position of the Faraday cup, which in Phase 4 will require the use of an external beam dump due to the foreseen intensities of the beams.

A peculiarity of these experiments concerns the treatment of the different charge states of the beam emerging out of the target. The beam components characterized by charge states lower than 10+, mainly $^{20}Ne^{9+}$ and $^{20}Ne^{8+}$, produced by the interaction of the beam with the electrons of the target material, have a magnetic rigidity which is similar to the ions of interest. Therefore, they enter in the FPD acceptance, causing a limitation in the rate tolerable by the detector. In order to stop these unwanted $^{20}Ne$ particles, two aluminum shields are mounted upstream the sensitive region of the focal plane detector. The shields act on a limited phase space region which stops the 9+ and 8+ beams and elastic scattering at very forward angles, but not the other reaction channels generated by these beams. It is known that the charge state distribution of a heavy-ion beam after crossing a material depends on the bombarding energy and on the chemical composition of the target. The targets relevant for NUMEN generate an unwanted charge distribution that can be conveniently changed, minimizing the amount of $^{20}Ne^{9+}$ and $^{20}Ne^{8+}$, by adding an appropriate second foil (post-stripper) downstream of the isotopic target. Recently a specific study of different materials to be used as post-stripper has been performed.[44] The main result is that carbon-based materials are very efficient to this purpose. In Phase 4, the use of pyrolytic graphite (HOPG) as a substrate for the evaporation of the isotopes will work not only for thermal dissipation, thanks to its high thermal conductivity as described in Sec. 9, but also as a post-stripper material.

The systems already experimentally explored using the ($^{20}Ne, ^{20}O$) reaction at 15 AMeV are the $^{116}Cd$ target (to study the $^{116}Cd \rightarrow {}^{116}Sn$ transition), the $^{130}Te$ (for the $^{130}Te \rightarrow {}^{130}Xe$) and the $^{76}Ge$ (for the $^{76}Ge \rightarrow {}^{76}Se$). The data reduction and analysis is in progress. A scheme of the transitions already studied in the experimental runs is shown in Fig. 3.

### 2.5. *Strategy for experiments in NUMEN Phase* 4

Here we will give a schematic description of the strategy for the experimental activity with accelerated beams in NUMEN Phase 4. It will be shown that a careful strategy is mandatory in order to avoid a fast and unsustainable saturation of the throughput and data storage volume.

**(1) DCE g.s. to g.s. studies in condition where MAGNEX separates the g.s. transition.** The maximum beam current at the target foreseen after the CS upgrade maintaining the beam performances in terms of emittance is about $10^{13}$ pps, depending on the bombarding energy and beam species. A first experimental mode for NUMEN runs in Phase 4 will be dedicated to the study of the Double Charge Exchange (DCE) ground state-to-ground state (g.s. to g.s.) transitions in condition where the ground state peak is well isolated by MAGNEX inclusive measurements. Most of these cases have been already explored at 15 MeV/u incident energy in Phase 2 even if with low statistics. The beam current for this mode will be the maximum one ($\sim 10^{13}$ pps). The MAGNEX FPD acceptance will be reduced to 10% exploring only the ground state region. No gamma array detector (G-NUMEN) will be used. The expected data throughput will be about 60 MB/sec, corresponding to $\sim 5$ TB/day.

If we consider that in Phase 2 we measured something like 30 events for the DCE g.s. transition in the case of $^{116}$Cd($^{20}$Ne, $^{20}$O)$^{116}$Sn$_{\text{g.s.}}$ experiment at 15 AMeV in about 20 days acquisition time ($\sim 1.5$ DCE g.s. counts/day), we can expect $10^4$ DCE g.s. events collected in 2 days in Phase 4, meaning that we can also build a statistically robust angular distribution.

**(2) Other than DCE g.s. to g.s. (common to all experimental campaigns).** During a NUMEN runs, other than measuring the DCE g.s. transition we also measure several other reaction channels (single charge exchange, multi-nucleon transfer, elastic and inelastic) and we get an extended energy spectrum of DCE up to large excitation energy. All of these "other than DCE g.s." data are important and are characterized by much larger cross-sections, so they do not need a full power beam. In NUMEN Phase 4 such "other than DCE g.s." data can be collected at $\sim 10^{11}$ pps. The MAGNEX FPD will work in full (100%) momentum acceptance. Coincidence with gamma array is typically not needed for these studies. The expected data throughput will be about 6 MB/sec, corresponding to $\sim 0.5$ TB/day.

In NUMEN Phase 2 we have collected data for these channels for a few days for each campaign at beam currents of about $6 \cdot 10^9$ pps for the $^{18}$O and $3 \cdot 10^9$ pps for the $^{20}$Ne induced ejectiles. In NUMEN Phase 4 at $10^{11}$ pps we will gain more than one order of magnitude in 2–3 days of data collection. In case we want to use G-NUMEN, we have to add about 5 TB/day, which is still affordable with standard solutions.

**(3) DCE g.s. to g.s. studies when MAGNEX does not separate the g.s. transition.** In many experimental conditions, the DCE g.s. to g.s. transition is not well isolated by using MAGNEX standalone and measurements of the $\gamma$ decay of the first excited states with the G-NUMEN array are needed. In these cases, the beam current should be limited to $\sim 10^{12}$ pps in order to limit the average reactions occurring at the target per beam bunch to about 1, thus keeping the best observational limit for DCE g.s. The $\gamma$ spectra will be gated in the energy region of interest. The MAGNEX FPD momentum acceptance will be reduced to

10% measuring only at the g.s. region. Under these conditions the data throughput would be ∼60 MB/s, corresponding to ∼5 TB/day.

The typical experiment duration will be of the order of 30 days, producing a data storage of ∼150 TB, which is affordable. About $10^3$ DCE g.s. coincidence events are expected after the proper analysis.

## 3. The Particle Accelerator for NUMEN: The Upgrade of the LNS Superconducting Cyclotron and the New Beam Lines

The LNS, CS, is a three-sector compact accelerator. Figure 3 (top left panel) shows a layout of the accelerator structure. Two pairs of superconducting coils generate a magnetic field at center variable between 2.2 and 4.8 T. Twenty trim coils, wound on each of the six sectors (120 in total), allow to achieve the isochronous magnetic field requested for the acceleration of all the ions, from molecular Hydrogen ($H_2^+$) up to Uranium, in a wide range of energies, between 10 and 80 AMeV.[45] Due to the CS compactness, the orbit separation at the outer turns is small about few mm. This limits the extraction efficiency, which is of 50–60%. Most of the accelerated beam is stopped by the septum of the first electrostatic deflector (ED), and, although it is water-cooled, serious thermal issues occur when the extracted power exceeds 100 W. The NUMEN experiment plans to use mainly beams of Carbon, Oxygen and Neon with intensity beyond $10^{13}$ pps. The required energies are in the range 15–70 AMeV, and the beam power in the range 1–10 kW, see Table 1. As a consequence, the extraction of 1–10 kW beams is not feasible using the EDs. Moreover, the existing extraction channel has small transversal size and no thermal shields to dissipate the beam power coming from beam halos. For these reasons, the CS will be upgraded with a new extraction channel designed just for extraction by stripping.[20,46–48] This technique requires that ions are accelerated with a charge state $(Z-5) < q < (Z-2)$ and after crossing a stripper foil, they become fully stripped ($q = z$). The use of a stripper foil, placed on the hill 2 of CS in the radius range from 865 mm to

Table 1. List of the ions to be extracted by stripping and expected power extracted.

| Ion | Energy [AMeV] | $I_{\text{source}}$ [e$\mu$A] | $I_{\text{accelerated}}$ [e$\mu$A] | $I_{\text{extracted}}$ [pps] | $P_{\text{extracted}}$ [Watt] |
|---|---|---|---|---|---|
| $^{12}C^{4+}$ | 45 | 400 | 60(4+) | $9.4 \times 10^{13}$ | 8100 |
| $^{12}C^{4+}$ | 60 | 400 | 60(4+) | $9.4 \times 10^{13}$ | 10800 |
| $^{18}O^{6+}$ | 19 | 400 | 60(6+) | $6.2 \times 10^{13}$ | 3420 |
| $^{18}O^{6+}$ | 29 | 400 | 60(6+) | $6.2 \times 10^{13}$ | 5220 |
| $^{18}O^{6+}$ | 45 | 400 | 60(6+) | $6.2 \times 10^{13}$ | 8100 |
| $^{18}O^{6+}$ | 60 | 400 | 60(6+) | $6.2 \times 10^{13}$ | 10800 |
| $^{18}O^{6+}$ | 66 | 360 | 54(6+) | $5.6 \times 10^{13}$ | 10700 |
| $^{20}Ne^{7+}$ | 28 | 400 | 60(7+) | $5.3 \times 10^{13}$ | 4800 |
| $^{20}Ne^{7+}$ | 60 | 400 | 60(7+) | $5.3 \times 10^{13}$ | 10280 |
| $^{40}Ar^{13+}$ | 60 | 370 | 56(13+) | $2.7 \times 10^{13}$ | 10338 |

895 mm and in the angular range of 24°, allows the beam trajectories to escape from the region of the cyclotron pole. In particular, all the ions of interest, with mass $\leq 40$ amu and energy $\geq 15$ AMeV, are fully stripped with efficiency higher than 99%.[49] Beam losses inside the cyclotron should stay below 100–200 W, which is a reasonable value as far as activation concerns. Table 1 summarizes the expected results for the beam power delivered at the exit of the cyclotron for some of the studied cases. Conservative values of the beam currents delivered by the ion source and accelerated by the cyclotron are also shown.

A careful study of beam dynamics is crucial for the extraction by stripping since the axial and radial envelopes have to be maintained as small as possible along the whole extraction path from the stripper to the exit of cyclotron, although the trajectories cross the hill boundaries with nonregular angles. It is important to minimize the number of correction elements to be used along the new extraction channel to reduced as much as possible the unwanted losses, in particular only to new magnetic channel will be installed along the new extraction channel, MCS1 and MCS2. The design of the extraction channel has been performed considering that each ion extraction trajectory is different from the others. After a detailed beam dynamics study[20,47,48] and with an appropriate positioning of the stripper foil system,[50] it is possible to transport all the beams listed in Table 1 cross the same exit point, as shown in Fig. 4(b).

The extraction by stripping is a multiturn extraction, i.e. ions with a different number of acceleration loops (and consequently energy) can be subjected to the stripping by the foil. It is thus mandatory to consider in the simulations the proper multiturn induced energy spread after the crossing of the stripping foil to evaluate correctly the radial beam size. According to Ref. 51 and as confirmed by our simulations, this energy spread is within ±0.3% for all the investigated ions and energies.

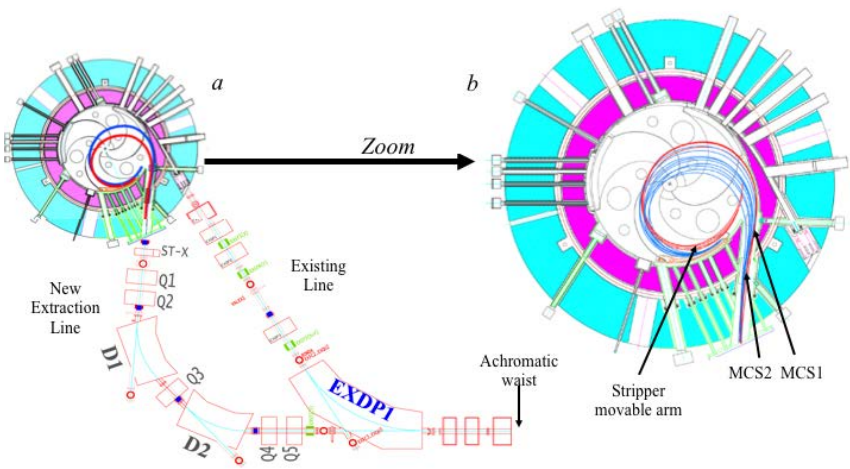


Fig. 4. Part (a) shows the new beam line to be used for extraction by stripping. Part (b) shows some trajectories studied along the extraction channel for different ions and energies.

Figure 4(a) shows the new extraction channel and its main elements, joining to the existing transport line at the magnet EXDP01. This line is designed to handle beams extracted by stripping with an energy spread up to ±0.3% and to compensate the chromaticity of the extraction path to produce an achromatic beam waist at the position shown in Fig. 4(a).[52]

The new beam transport line (setup) of the LNS is shown in Fig. 5. In particular, the high intensity has to be handled by the FRAgment Ion SEparator (FRAISE)

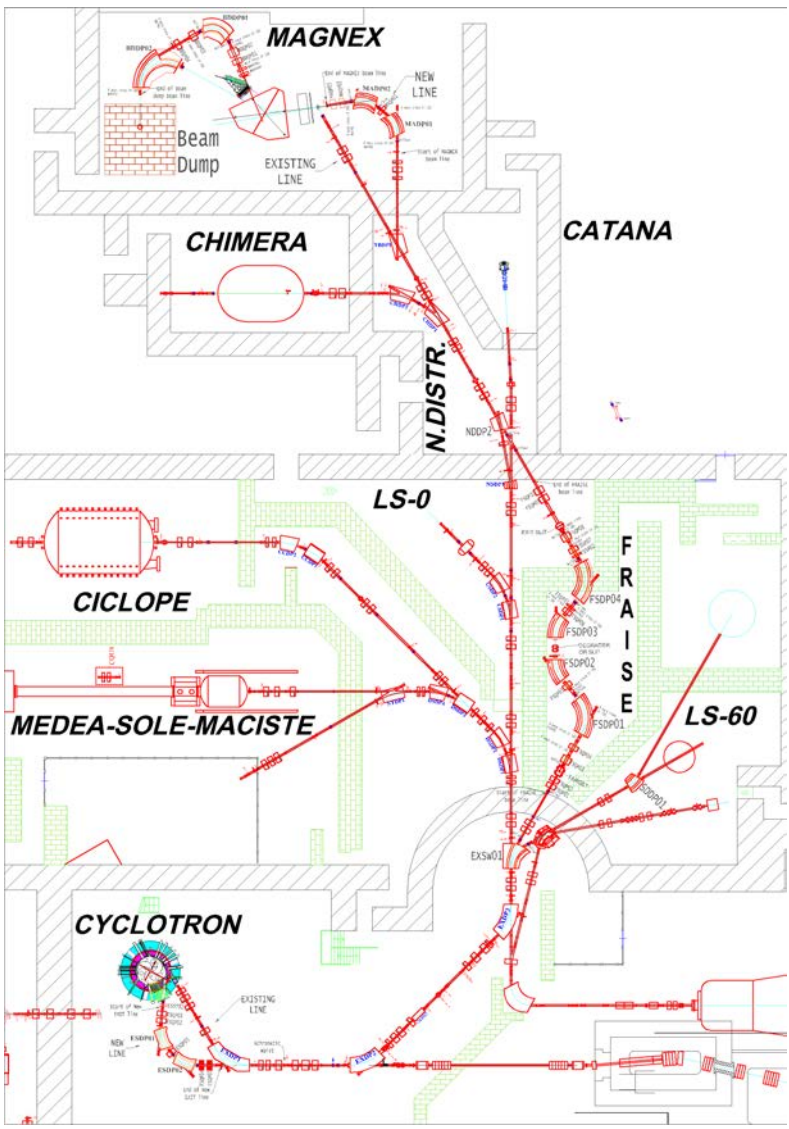


Fig. 5. New layout of the LNS. From the CS the beams reach MAGNEX area through the FRAISE line. The experimental MAGNEX area has to be modified to host a large beam dump.

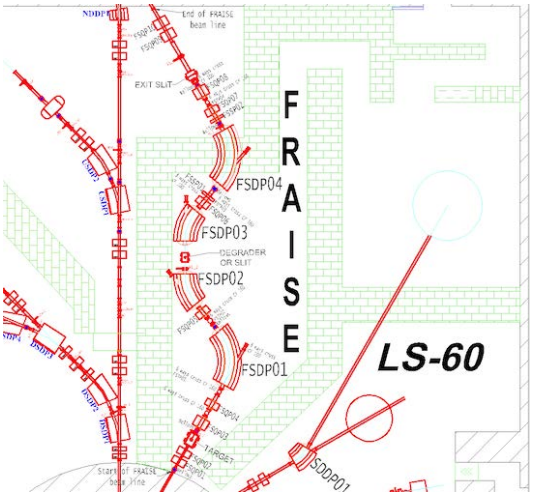


Fig. 6. Layout of the FRAISE beam line, that will be used to select the energy spread and the beam emittance size to match the NUMEN experiment request.

line[53] before the MAGNEX experimental hall, see Fig. 6. FRAISE is designed for the production and separation of radioactive ion beams. The beam strikes the production target where about 10–15% of power is dissipated while most of the beam is stopped in the vacuum chamber of the dipole FSDP01. The FRAISE hall is designed to dissipate primary beam power up to 3 kW. For this reason, the FRAISE hall is the proper place where to tailor the beam characteristics to match the request of NUMEN. To perform the NUMEN experiments, it is mandatory to have a beam spot on the target with radial size of 1 mm, radial divergence of 4 mrad and energy spread of 0.1% (all these values are referred to FWHM). These characteristics are quite far to be satisfied by the beam extracted from the cyclotron. For this reason we have to reshape the beam emittance, cutting far extending tails (haloes) in radial and axial planes, then, reducing the beam emittances. Also the beam energy beam can be reduced by an appropriate tuning of FRAISE. The radial size can be significantly reduced at the FRAISE target position dedicated to the production of radioactive beams. There, the beam can be strongly focused and the tails exceeding the size of 1 mm in horizontal and 1.6 mm in vertical can be intercepted by an appropriate cooled collimator. Further collimators will be installed just before the quadrupole FSQP03 and FSQP04 to define the horizontal and vertical divergence, respectively. To mitigate the heating of these collimators, their thickness is chosen to reduce the energy of the particles crossing them of only 10–20%. Indeed, the energy lost through the collimators allows the first dipole FSDP01 of the FRAISE line to bend these particles on the inner side of its vacuum chamber, which is designed to substain beam power dissipation up to 4 kW, see Fig. 5.

To reduce the intrinsic energy spread of the beams extracted by stripping from the expected value of 0.4% FWHM down to 0.1% FWHM, two options are under

investigation. The first option is to adopt a basic approach and is based on the use of the high dispersive properties of the FRAISE line at the symmetry plane (25 mm of radial dispersion for an energy spread of 1%) and to select the energy spread using collimators slits. Despite this solution being very efficient, it is limited from the total beam power we could stop inside the FRAISE room. According to the shielding properties of the FRAISE hall, the maximum beam power we could stop at the symmetry plane stay below 2 kW. This means that if the tail of the energy distribution of the beam extracted from the cyclotron exceed the 60% of the required value, we could deliver to the NUMEN experiment a maximum beam power of 1.5 kW.

The improvement of the overall efficiency from beam injection up to extraction, is crucial for the CS. The study of a new central region of the CS is ongoing at LNS aimed at maximizing the injection efficiency.[54] The use of phase slits installed inside the accelerator, just outside the central region, will be investigated to reduce the energy spread at the extraction. However, our simulations have demonstrated that the energy gain per turn contributes only partially to the beam energy spread at the extraction and the main contribution is due to the large emittance injected in the central region of the cyclotron.

More elegant solution is to use a well-shaped wedged degrader that, according our preliminary simulations, could reduce the energy spread below the request value of 0.1%. This second option is very appealing and we are evaluating and simulating the effect of the increase on the final size and divergence in the horizontal plane. We are also investigating where it could be convenient to intercept the trajectories that exceed the radial size and divergence taking into account that the second half of the FRAISE line is not so well shielded as the first half. Indeed, the best position where the NUMEN beam could be tailored is at the exit point of the FRAISE line, even if unfortunately at this position the beam power losses have to be limited to less than 100 W. The final adopted solution to minimize the beam losses and to respect the limits of beam power loss along the different areas of the beam transport line, will likely consist in a good combination of all these methods.

### 3.1. *Forseen modification in the CS*

The extraction by stripping of beams with power up to 10 kW needs an acceleration chamber with a larger vertical gap inside the cyclotron to minimize the beam losses and to provide a better vacuum conductance. In our project, the vertical gap in the pole region will be increased from 24 mm, the actual value, to 30 mm. This will be achieved by the replacement of the exiting liners with new ones with a smaller thickness. The results of the beam dynamics study show that it is mandatory to have a new extraction channel into the cryostat of the cyclotron with a different direction and larger clearance both in radial and vertical directions, with respect to the existing extraction channel. Then, the present cryostat has to be replaced with a new one.[53] The call for tenders for the construction and installation of

the new cryostat and the new superconductives coils was closed on the January 2019 and after the signature of the agreement of *Programma Operativo Nazionale* between the Italian *Ministero dell'Istruzione, dell'Universitá e della Ricerca* and the *Istituto Nazionale di Fisica Nucleare*, the order was signed (July 2019). Compared to the design of about 35 years ago, new technologies will be used to build the new superconducting coils guaranteeing the same performance using smaller coils with higher current density. This simplifies the design of the cryostat and reduces the consumption of cryogenic liquids like liquid Helium and liquid Nitrogen. The smaller size of the new coils also allows to increase the vertical gap in the extraction channels up to 60.5 mm versus the present value of 30.5 mm. The wider clearance makes it easier the insertion of the magnetic channels, which are additional iron elements, placed outside the pole radius, use to change locally the magnetic field and help the radial focusing and slightly steer the beam when necessary. According to our simulations, two magnetic channels are enough for all the foreseen ions to be extracted by stripping, even if position displacements are needed according to the specific ion and energy to be extracted. Moreover, two compensating iron bars have considered to be placed inside the cryostat to minimize field perturbations introduced by the magnetic channels. Also the position of the compensating bars changes according to the extracted beam, see Refs. 20 and 48.

Since the extraction by deflector will be maintained for the other ions of the CS operating diagram, the new penetrations and subsystems have been designed to avoid mechanical interferences with the existing ones. Figure 7 shows the present and the final shape of the so-called central ring of the CS yoke. The central ring of yoke has a height of $\pm 125$ mm above and below the median plane and its inner and outer radii are 1340 and 1903 mm, respectively. The beam leaves the cyclotron through the extraction holes. In Fig. 7 (right side) the optimized central ring profile is shown. The iron in the central ring has been redistributed considering the new

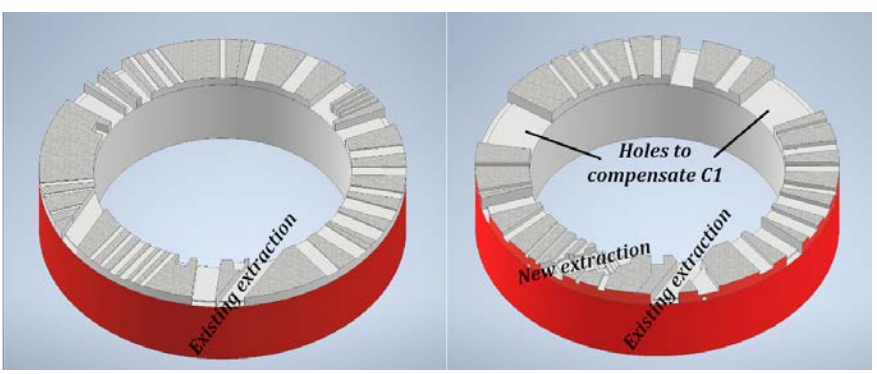


Fig. 7. Views of the changes in the central iron ring of the CS. The first one, on the left side, is a top view of the state-of-the-art of the CS. The existing extraction channel is labeled. On the right side, the results of the optimization's process are shown. The areas indicated by the solid lines show where the iron has been removed to eliminate unwanted field harmonic component C1.

penetrations necessary for the extraction by stripping and filling the unused holes. The straight lines indicate the extra iron removed from the central ring to correct the field perturbations introduced by the new nonsymmetrical penetrations. With this iron configuration, the first and second harmonics of the magnetic field as functions of the radius are under control along the whole acceleration path. In particular, the first harmonic stays below 5 Gauss and the second harmonic is even smaller.

### 3.2. *The new beam dump*

The beam dump has to handle a power up to 10 kW and must have enough shielding to reduce significantly the background in the MAGNEX focal plane detector due to the neutron and gamma radiation produced by the interaction of the beam with the cooled target of the beam dump. The beam dump is shielded by a concrete box with both lateral sides of 4.5 m and height of 4 m. The installation of this beam dump in the MAGNEX experimental room is a challenging task and many solutions were investigated before to choose the final one presented in Fig. 8. One of the main issues to select the position of the beam dump inside the MAGNEX area is related to the request of NUMEN experiment to detect particles that have magnetic rigidity lower or higher of the incident beam.

To match this requirement, the incident beam has to leave the MAGNEX spectrometer through two possible exit ways, one stay at the left side of the focal plane detector (MAGNEX rotated of $+3°$ with respect to the incident beam) and another on the right side (MAGNEX rotated of $-3°$ with respect to the incident beam), see

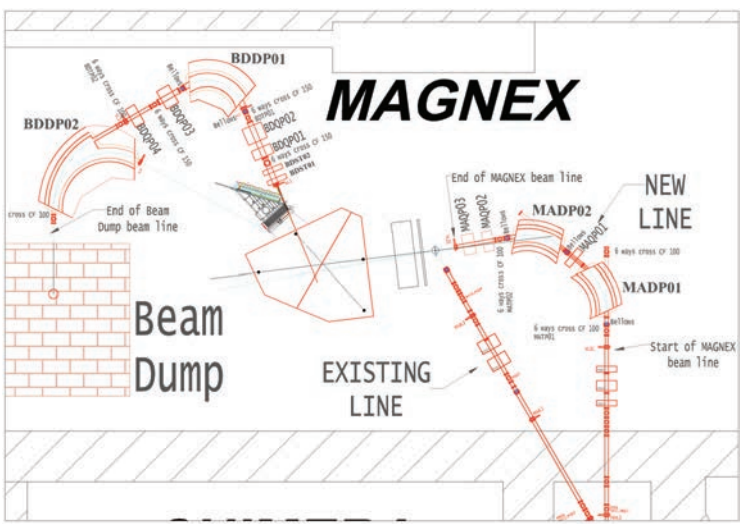


Fig. 8. Layout of the new MAGNEX experimental area. The wall on the left side will be moved of about 4.5 m to allow the installation of the large beam dump. The MAGNEX spectrometer will be rotated of 70° respect to its 0° position to allow the transport of the beam coming out from the spectrometer to be transported inside the beam dump. A new line is necessary to send the beam to the MAGNEX new position.

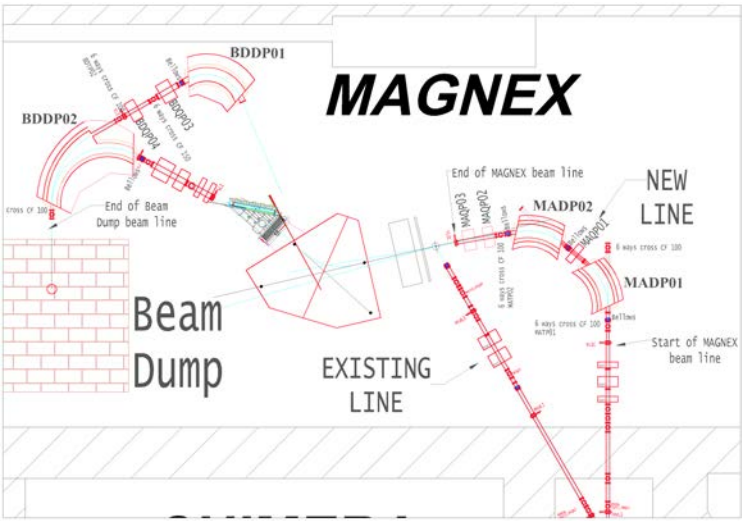


Fig. 9. Layout of the exit beam line on the right side of MAGNEX spectrometer.

Figs. 8 and 9. The left or the right exit is used when the ions to be detected have magnetic rigidity lower or higher of the incident beam, respectively.

To host this large beam dump, the MAGNEX hall needs to be enlarged of about 4 m on the west side and the spectrometer needs to be rotated of 70° with respect its original position. As a consequence, the installation of a new beam line at the entrance of the spectrometer is also needed, see Fig. 8.

### 3.3. *The new beam line*

A layout of the new beam line transporting the beam to the MAGNEX spectrometer is shown in Fig. 8. It consists of the existing quadrupole triplet also called TeBe line and of two new dipoles and three new quadrupoles to be installed. The two dipoles MADP01 and MADP02 are equal and have bending angle of 47.5°. The characteristics of the last two quadrupoles have been optimized to keep a distance of at least 700 mm between the end of the last quadrupole and the target, while the quadrupole between the two dipoles MADP01 and MADP02 is an existing one of the LNS.

The beam envelope along the beam transport line from the FRAISE exit to the NUMEN target is shown in Fig. 10. The top view of new beam line inside the MAGNEX experimental area is shown in Fig. 11. According to the request of the experiment, the beam spot on the target has the following size $x = 1$ mm and $y = 2.5$ mm @FWHM. Also the divergences stay below the values of 8.5 mrad and 15 mrad @FWHM in the horizontal and vertical directions, respectively. As discussed before to achieve this goal, the geometrical emittances of the beam needs to be properly shaped and the energy spread needs to be reduced to the request value of 0.1% @FWHM.

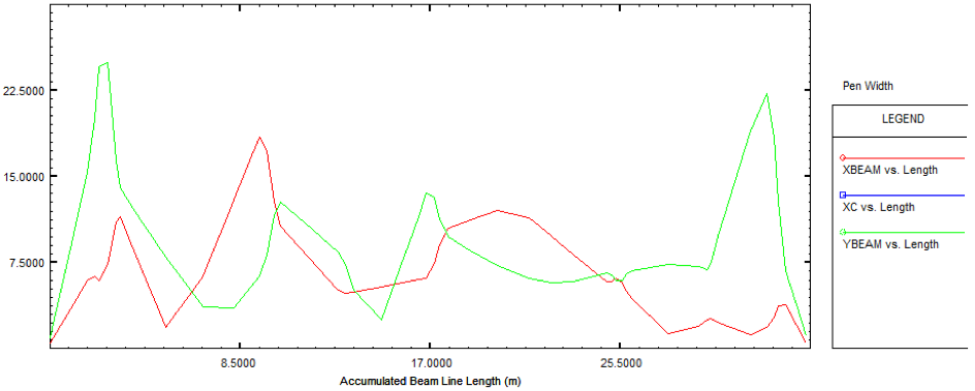


Fig. 10. Beam envelope (mm) as a function of the transport beam line length (m) from the end of the FRAISE line to the NUMEN target.

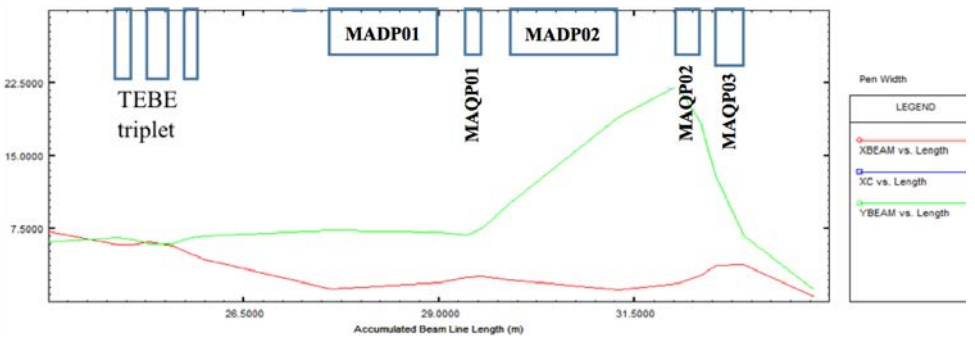


Fig. 11. Beam envelope (mm) as a function of the transport beam line length (m) inside the MAGNEX area.

Table 2. Characteristics of the magnetic quadrupoles of the new beam line.

| Quadrupole | Effective length | Diameter | Maximum field | Gradient |
|---|---|---|---|---|
| MAQP01 | 200 mm | 70 mm | 0.7 T | 20.0 T/m |
| MAQP02 | 300 mm | 80 mm | 0.57 T | 14.3 T/m |
| MAQP03 | 350 mm | 70 mm | 0.67 T | 19.2 T/m |

The mechanical and magnetic characteristics of the quadrupoles and dipoles of the new beam line are presented in Tables 2 and 3. The vacuum chamber of the quadrupoles and of the dipoles is up to 43% larger than the maximum size of the beam envelope. In the new beam line, the diameter of the vacuum chamber of the three quadrupoles of the new beam line is at least 90% larger than the maximum beam envelope, and also the vertical gap of the three dipoles is at least 84% larger than the maximum beam sizes across each element. Indeed, the quadrupole magnets have a pole diameter of at 70 mm, except the MAQP01 that has a pole diameter

Table 3. Characteristics of the magnetic dipoles for the new beam line in MAGNEX area.

| Dipole | Bending angle | Radius [m] | Inner gap of vacuum chamber | Maximum field | In/out face angle | Uniformity $\Delta B/B$ $3 \times 10^{-4}$ |
|---|---|---|---|---|---|---|
| MADP01, MADP02 | 47.5° | 1.6 | 66 mm | 1.7 T | 23.8°/23.8° | in ±25 mm |

of 80 mm. Similarly, the vacuum gap of the two dipoles is 66 mm. This constraint was imposed in order to minimize the risk of beam losses through these elements and consequently minimize the background in MAGNEX focal plane detector.

### 3.4. *The two beam transport lines from MAGNEX to the beam dump*

A key point for the NUMEN experiment is to transport the beam up to the beam dump after the beam strikes the target and passes through the MAGNEX spectrometer. Moreover, MAGNEX will be rotated of +3° or −3° versus the direction of the incident beam so as to allow the detection of the reaction products with magnetic rigidity lower or higher of the incident beam, see Figs. 8 and 9. To minimize the cost of the two beam lines from MAGNEX to the beam dump, the first part of these two lines was designed to have the same magnetic elements with the same characteristics. Moreover, in order to leave enough room around the detector of MAGNEX, we decided to plug the first part of the exit line to the left or to the right exit side (+3° or −3°), according to the experiment request. This means that it will be necessary to move this beam line section from the left side to the right side of the new MAGNEX exit using a dedicated automatic system. The beam line is about 3 m long, consisting of two steerer magnets and of two big quadrupoles and it will be installed on a single support, that allow to move the whole line. All the other devices of the two exit beam lines do not need to be moved (see Subsec. 8.3.1).

The first part of the two exit lines consists of two equal steerer magnets BDST1 and BDST2, with an effective length of 142 mm, able to deflect the beam at maximum magnetic rigidity at 2.55 T · m by about ±5°. These two steerer magnets could be the same as the steerer ESST01 of the new extraction line. The distance between the BDST1 and BDST2 is about 300 mm and this configuration compensates a misalignment of about 38 mm when these steerers deflect the beam of +5° and −5°. This chicane is necessary because the beams coming out from the MAGNEX spectrometer could change their position and direction of about ±9 mm, and ±8 mrad, respectively. These results were achieved by the simulations of the four beams shown in Table 4 and assuming the MAGNEX spectrometer is rotate of +3° or −3° with respect to the direction of the incident beam.

In Table 5, the positions of the four reference beams at the exit of MAGNEX are listed. The coordinates and the divergences are evaluated in the reference system centered in the middle plane of the exit valve of the MAGNEX dipole. In Table 6

Table 4. Characteristic of the four simulated beams for the transport line design.

| MAGNEX position | Ion | Br[T · m] |
|---|---|---|
| −3° | $^{20}$Ne, 15 AMeV, $q = 10+$ | 1.1 |
| −3° | $^{20}$Ne, 34 AMeV, $q = 10+$ | 1.7 |
| +3° | $^{18}$O, 15 AMeV, $q = 8+$ | 1.3 |
| +3° | $^{18}$O, 60 AMeV, $q = 8+$ | 2.6 |

Table 5. Characteristics of the four simulated beams centroid at the MAGNEX exit points related to MAGNEX reference beam frame.

| Ion | $X$ [mm] | $X'$ [mrad] | $Y$ [mm] | $Y'$ [mrad] |
|---|---|---|---|---|
| $^{20}$Ne, 15 AMeV, $q = 10+$ | −240.4 | −328.4 | 0.2 | 0.1 |
| $^{20}$Ne, 34 AMeV, $q = 10+$ | −256.5 | −335.9 | 0.0 | 0.0 |
| $^{18}$O, 15 AMeV, $q = 8+$ | 72.8 | 227.0 | 0.0 | 0.0 |
| $^{18}$O, 60 AMeV, $q = 8+$ | 89.5 | 235.6 | 0.1 | 0.0 |

Table 6. Optical and geometrical features of the four simulated beam at the MAGNEX exit points. $X$ is the dispersive direction.

| Direction | Ion | Energy AMEV | Emittance | $\alpha$ | $\beta$ | Size [mm] | Divergence [mrad] | Correlation |
|---|---|---|---|---|---|---|---|---|
| $X$ | $^{20}$Ne | 15 | 86.4 | 0.8 | 0.2 | 4.2 | 26.7 | −0.7 |
| $X$ | $^{20}$Ne | 34 | 69.3 | 0.3 | 0.2 | 3.6 | 20.4 | −0.3 |
| $X$ | $^{18}$O | 15 | 36.0 | 11.2 | 22.3 | 28.3 | 14.3 | −1.0 |
| $X$ | $^{18}$O | 60 | 29.1 | 7.4 | 15.1 | 21.0 | 10.3 | −1.0 |
| $Y$ | $^{20}$Ne | 15 | 26.5 | −6.7 | 18.2 | 22.0 | 8.1 | 0.1 |
| $Y$ | $^{20}$Ne | 34 | 22.2 | −6.9 | 19.8 | 20.9 | 7.4 | 0.1 |
| $Y$ | $^{18}$O | 15 | 25.5 | −5.4 | 15.7 | 20.0 | 7.1 | 0.1 |
| $Y$ | $^{18}$O | 60 | 21.4 | −5.2 | 14.4 | 17.6 | 6.5 | 0.1 |

the horizontal (dispersive) and vertical emittances and the geometrical properties of the beam at the exit of the MAGNEX spectrometer are given. The beam envelope along these two lines and for the four ions simulated are shown in Figs. 12–15.

The characteristics of the magnetic quadrupoles and dipoles are presented in Tables 7 and 8.

Table 7. Characteristics of the magnetic quadrupoles of the two exit lines of MAGNEX.

| Quadrupole | Effective length | Diameter | Maximum field | Gradient |
|---|---|---|---|---|
| BDQP01, BDQP04 | 300 mm | 150 mm | 0.66 T | 8.82 T/m |
| BDQP02, BDQP03 | 500 mm | 200 mm | 0.66 T | 6.61 T/m |

Table 8. Characteristics of the magnetic dipoles of the two exit lines of MAGNEX.

| Dipole | Bending angle | Radius [m] | Inner gap of vacuum chamber | In/out face angle | Magnetic field min/max [T] |
|---|---|---|---|---|---|
| BDDP01 | 97° | 1.075 | 60 mm | 26.5°/26.5° | 1.04/1.58 |
| BDDP02 | 60° | 2.350 | 60 mm | 0°/0° | 0.48/0.73 |
| BDDP02 | 117° | 1.650 | 60 mm | 0°/0° | 0.76/1.55 |

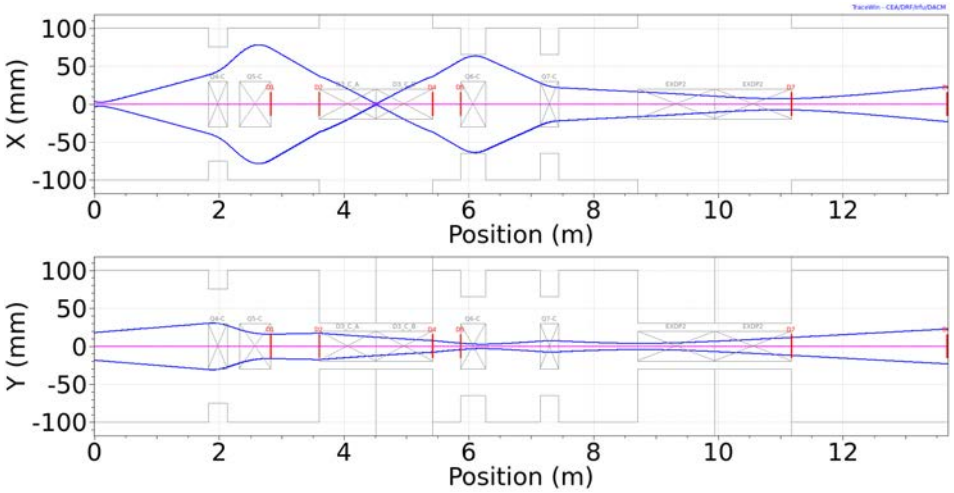


Fig. 12. Beam envelope for the ion $^{20}$Ne at 15 AMeV exit from the right side (−3°) of MAGNEX.

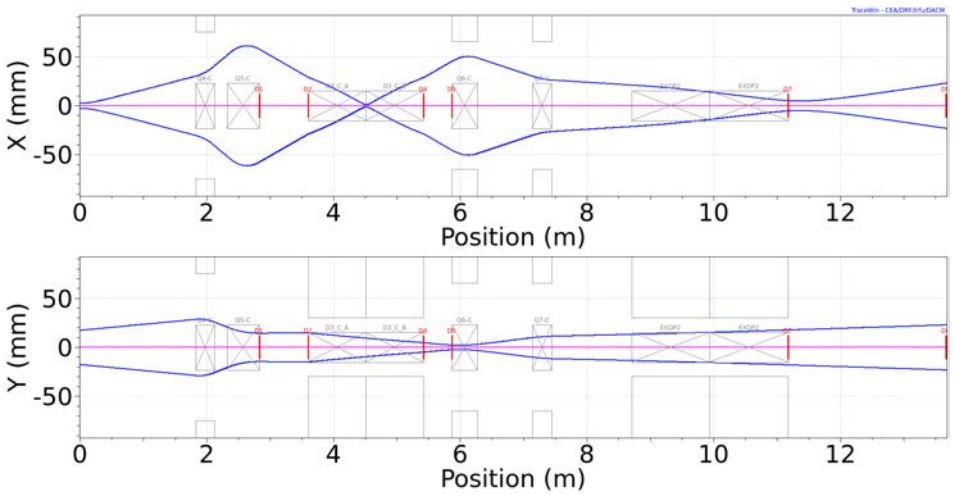


Fig. 13. Beam envelope for the ion $^{20}$Ne at 34 AMeV exit from the right side (−3°) of MAGNEX.

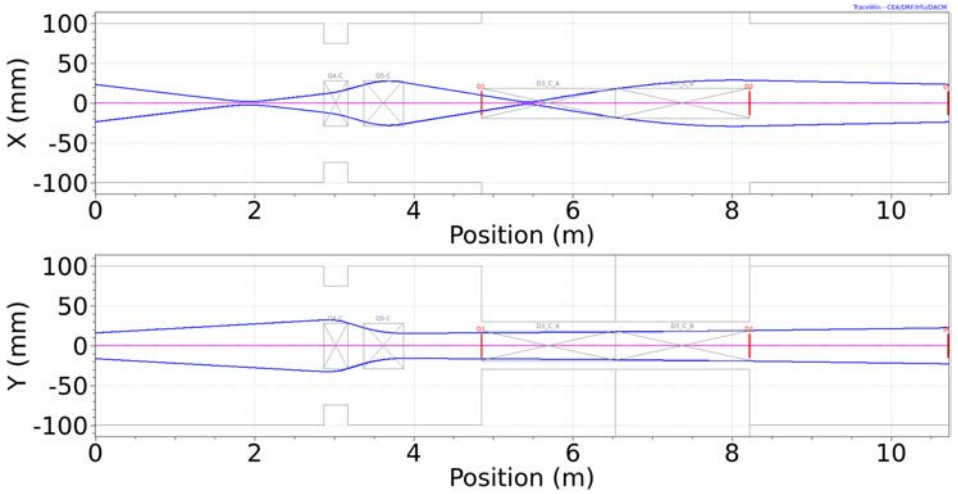


Fig. 14. Beam envelope for the ion $^{18}$O at 15 AMeV exit from the left side (+3°) of MAGNEX.

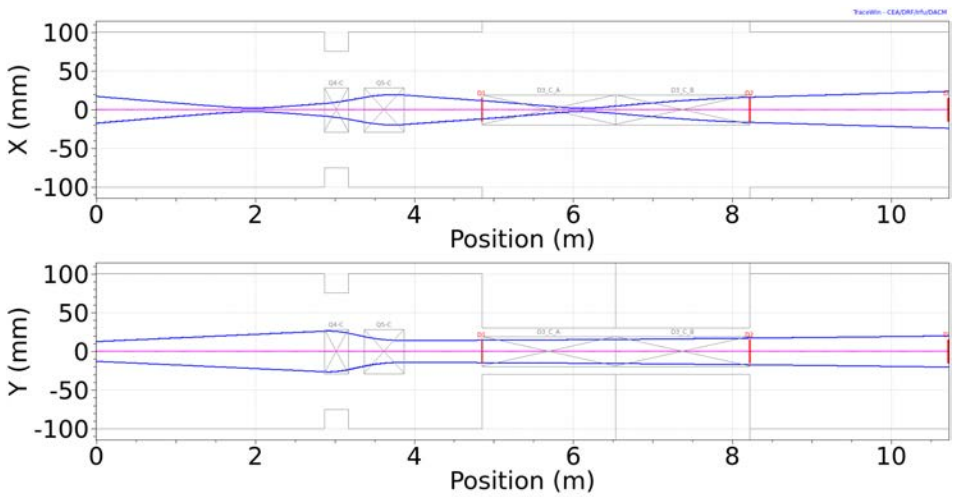


Fig. 15. Beam envelope for the ion $^{18}$O at 60 AMeV exit from the left side (+3°) of MAGNEX.

## 4. The FPD Gas Tracker

### 4.1. *Introduction*

A new 3D gas tracker for the MAGNEX focal plane detector, designed to work with the upgraded facility is under development within the NUMEN Phase 2 project. It is expected to be installed during the Phase 3 and will be operative during Phase 4. The present FPD gas tracker,[55] based on six drift chambers and on the use of long multiplication wires, is intrinsically limited to a few kHz rate, mainly due to the slow drift of positive ions from the multiplication wires to the Frisch grid.

The new FPD tracker must satisfy two main demands. First it must provide a high resolution of the phase space parameters at the focal plane ($X_{\rm foc}$, $Y_{\rm foc}$, $\theta_{\rm foc}$, $\phi_{\rm foc}$). This requirement is fundamental for the precise and accurate particle ray reconstruction, needed for the determination of the momentum vector at the target position.[17] Since the particle identification technique adopted for the MAGNEX data and described in detail in Ref. 56 requires also the use of the horizontal position measured at the focal plane $X_{\rm foc}$ or the use of the reconstructed momentum, also the identification quality is affected by the resolution of the mentioned parameters.

The second request is that it must be very fast since it should be able to bear a rate of the order of 40 kHz/cm expected after the accelerator upgrade.

The structure of the new tracker consists of three main stages:

- a drift region, that is the active volume of the detector, crossed by the ejectiles of interest;
- an electron multiplication stage, based on Micro-Pattern Gas Detectors (MPGDs);
- a segmented read-out electrode.

The operation principles of the gas tracker are the following: the incident charged particles exiting the MAGNEX dipole cross a thin Mylar window (thicknesses between 1.5 and 6 $\mu$m, depending on the specific case) and leave a track of ionized atoms and primary electrons in the low-pressure gas (typically from 10 to 100 mbar) between the cathode and the electron multiplication element. Under a uniform electric field, whose actual value depends on the voltage and gas pressure, the electrons drift with constant velocity. Thus, the drift time of electrons and consequently the vertical position and angles are measured. Reaching the multiplication element, electrons are accelerated in the strong electric field in correspondence of the MPGD multiplication elements. The resulting electron jets are then directed towards the segmented read-out electrode, where the horizontal position and angles are measured. From these information the full track of the ion can be reconstructed (i.e. impact point and angle of incidence at the focal plane).

The new tracker will cover a total volume of $1158 \times 206 \times 183$ mm$^3$ and it will have an active volume of $1122 \times 185 \times 108$ mm$^3$. A design of the full tracker is shown in Fig. 16. Moreover it is designed to be modular. In other words, it will be made of eight separate modules joined together. One of these modules has been used as prototype for testing purposes and will be described in detail in the following section.

### 4.2. *The prototype*

In order to develop and test the most performing and reliable solutions, a prototype consisting in a single module of reduced size of $100 \times 185 \times 108$ mm$^3$ has been built. This prototype has the same structure as the final FPD but is smaller just in the dispersive direction. The compact size of the prototype makes possible to perform tests in a smaller chamber.

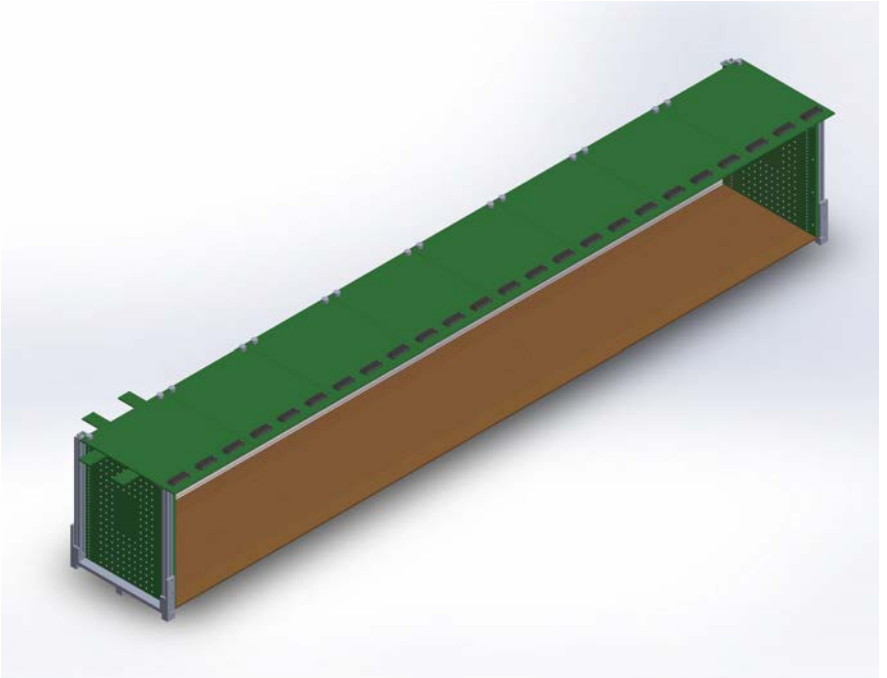

Fig. 16. Rendering of the full tracker that will be installed in FPD chamber.

The applied voltages, the gas pressure, the gas flowing system, the multiplication technology, the read-out and front-end electronics are among the main features tested with the small size prototype.

Even if the use of a gas quencher like pure isobutane is an excellent choice for operations with heavy ions at low pressure, the use of different gas mixture could be aim of further investigation.

#### 4.2.1. *The drift region*

The drift region extend for 18 cm, it is delimited by the cathode and the multiplication stage, is designed to set a uniform electric field of about 50 V/cm. Electrostatic simulations based on the Poisson Superfish code[57] have been performed in order to model and design the prototype field cage in the drift region. The code calculates the static electric field in the detector geometry by generating a triangular mesh and solving the field equations by a procedure of successive over relaxations for each mesh point. An example of an output plot is shown in Fig. 17. The cathode is modeled as a conductive element at −2000 V. Two series of shaping wires made of conductive material at increasing voltages from −2000 V to −1000 V are introduced to eliminate edge effect and make the field fairly uniform also at the border of the drift region, as displayed by the almost parallel equipotential lines.

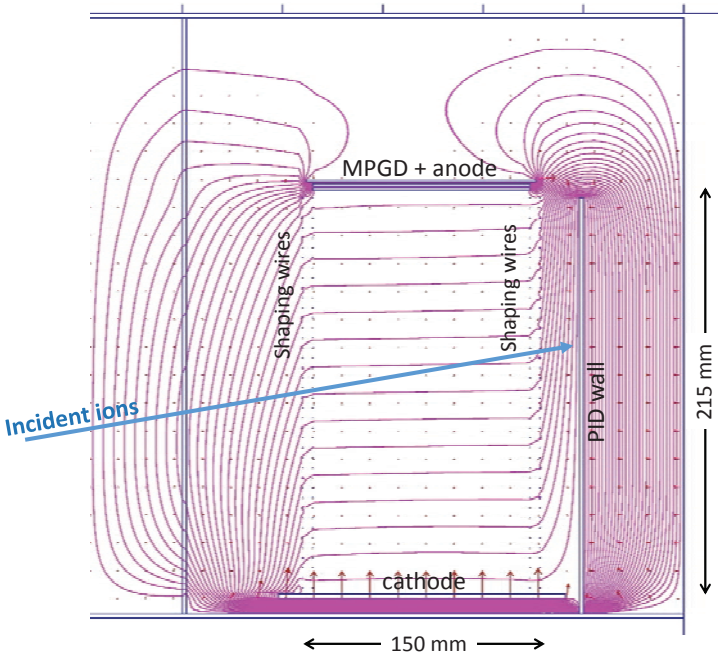


Fig. 17. Electric field calculation performed by mean of Poisson superfish code.

A much stronger electric field is simulated in the electron multiplication region (MPGD + anode) with the aim of exclusively study the field uniformity within the field cage. The presence of the PID-wall elements at high voltage and very close to the drift region could influence the field in the drift region. This effect has been taken into account introducing a conductive element with a voltage of −2000 V. Based on the results of the simulations, the field cage delimiting the drift region for the prototype has been built. The uniformity of the electric field in the drift region is obtained by using a field cage made of a printed circuit in the lateral walls and a double raw of gold-plated tungsten wires 50 $\mu$m thick, arranged at step of 5 mm, connecting the two lateral walls. This geometry reduces the interference of external potentials as those generated by the high-voltage-supplied PID detectors or by the Mylar entrance window at ground or at a floating potential.

Thanks to the use of 35 wires connected between them with 2.5 MΩ resistors the field cage provides a smooth distribution of the voltage and a safe value of the current (about 20 $\mu$A) flowing in the voltage divider. Figure 18 shows a 3D design prototype field cage and a picture.

The drift region is filled with gas at low pressure (10–100 mbar) that can be easily changed for different experimental conditions. The gas filling the drift region should have a high drift velocity in order to guarantee a fast collection of the charge, and should manifest a saturation of the drift velocity with the electrical field applied. For the operational value of $E/p$ of the drift region the lateral spread

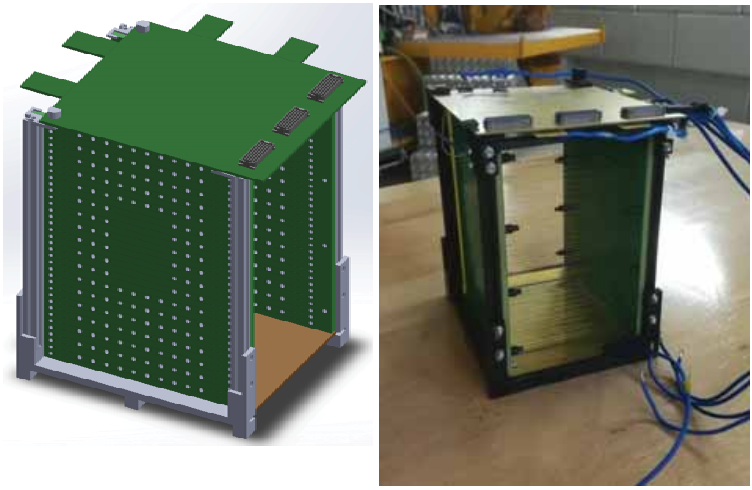

Fig. 18. The prototype field cage.

of the avalanche is about 130 $\mu$m/cm that correspond, for central trajectories, to a spread of 1.3 mm on the THGEM plane.

#### 4.2.2. *The electron multiplication region*

In the present FPD, the multiplication stage is based on wires. This choice is not appropriate for the new FPD, since this should be designed to work with very high rate. The present wire technology is intrinsically slow and generates a high ion backflow (IBF) that can alter locally and temporarily the uniformity of the field in the multiplication and drift region. For these reasons a Micro Pattern Gas Detector (MPGD) have been chosen for the multiplication stage.[58] Among the MPGD, the most suitable are the THGEM foils.[59,60] They are characterized by a narrow amplification gap ranging between 970 and 1370 $\mu$m, depending on the specific kind of THGEM, that should be compared to several millimeters for wire-based structures. The short drift path for ions overcomes the space charge effects present in wire chambers, where the slowly drifting ions may remain in the gas volume for milliseconds affecting the electric field.

The THGEM can guarantee an intrinsic rate capability higher than $10^6$ Hz/mm$^2$ (much higher than the expected rate for NUMEN), a very high spatial resolution (submillimeter accuracy) and timing in the 10 ns range (see Ref. 61 and references therein). The THGEM have already been used at low gas pressure to detect not minimum ionizing particles[21,62,63] thus making their use very appealing for NUMEN. In particular, a multiple THGEM (M-THGEM) technology has been tested for the tracker prototype. The M-THGEM consists of a densely perforated assembly of multiple insulating substrate sheets (e.g. FR-4, Rogers, ceramic), sandwiched between thin metallic-electrode layers, see Fig. 19.

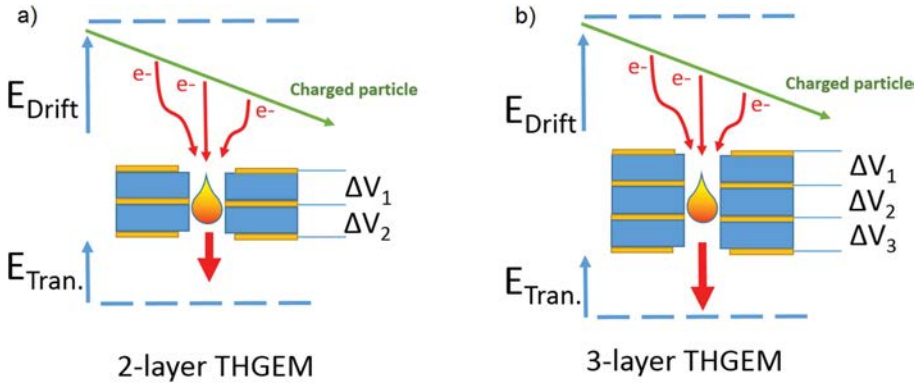


Fig. 19. Schematic drawing of (a) a 2-layer and (b) a 3-layer M-THGEM detector from Ref. 21.

Table 9. Geometrical characteristic of the tested THGEM.

| Type | Substrate material | No. layers | Finish board thickness | Hole diameter | RIM size | Hole spacing |
|---|---|---|---|---|---|---|
| A | Rogers 4350 | 2 | $0.7 \pm 0.1$ mm | $0.300 \pm 0.05$ mm | 0.1 mm | 0.75 |
| B | Rogers 4350 | 3 | $0.97 \pm 0.1$ mm | $0.300 \pm 0.05$ mm | 0.1 mm | 0.75 |
| C | Ceramic SD103K | 2 | $0.93 \pm 0.1$ mm | $0.300 \pm 0.05$ mm | 0.1 mm | 0.75 |
| D | Ceramic SD103K | 3 | $1.37 \pm 0.1$ mm | $0.300 \pm 0.05$ mm | 0.1 mm | 0.75 |
| E | PCB | 3 | 1.28 mm | 0.280 mm | 0.2 mm | 0.75 |

The electron avalance processes occur along the successive multiplication stages within the M-THGEM holes, under the action of strong electric fields resulting from the application of suitable potential differences between the electrodes. The intrinsically robust confinement of the avalanche volume within the M-THGEM holes provides an efficient reduction of the photon-induced secondary effects, resulting in a high-gain capabilities over a broad pressure range, including low-pressure operation. The operational principle and main properties under different irradiation conditions have been presented in Ref. 21. Five different geometries of M-THGEM foils have been produced for the tests of the prototype. Four of them have been designed at CERN and produced by Shenzhen HeLeeX Analytical Instrument Co. Ltd., using two different technologies for the insulating substrate: Rogers 4350 and ceramic SD103K, and a different number of layers (2-layer THGEM and 3-layer THGEM). Another type of 3-layer THGEM has been produced by Zener SRL, following the drawings developed at INFN-Catania by the NUMEN collaboration. In the latter model, the holes are arranged in five equidistant rows designed to be aligned to the trenches of the segmented read-out board. The geometrical characteristics of each series of M-THGEM are listed in Table 9, all the THGEMs have an area of $108 \times 108$ mm$^2$. Some of the above-mentioned M-THGEM foils are shown in Fig. 20.

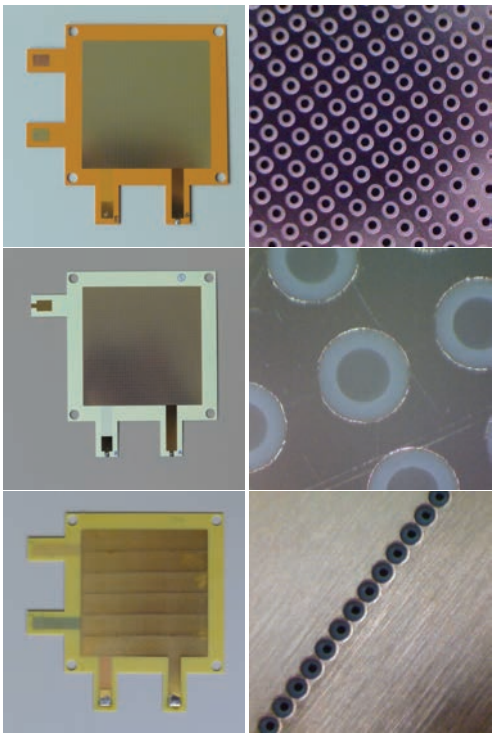

Fig. 20. Pictures of the different M-THGEM foils tested with the FPD prototype.

#### 4.2.3. *The segmented read-out board*

The read-out system is based on preamplifier and digitizers provided by CAEN, in Subsec. 7.1 it is described in detail. The signal from each strip is sent to a standard preamplifier, placed out of the chamber that houses the detector, and then it is sent to a digitizer. This gives as an output a time stamp with a resolution lower than ns and a value proportional to the electrons collected by the strip. Therefore the $x$-positions can be calculated applying a center of gravity calculation of the charge distribution. The $y$-positions instead will be obtained from the measurements of the arrival time of the charges into the strips.

### 4.3. *The test bench station*

A test bench station (TeBe) for the R&D activity of the gas tracker and of the other detectors for NUMEN has been developed in the MAGNEX hall. Two pictures and a schematic drawing of TeBe are shown in Fig. 21.

Both Tandem and Superconducting Cyclotron ion beams can be delivered in the TeBe station. The beam hits a target placed in the scattering chamber where there is room enough to place also small ancillary detectors. A Faraday cup is also present and is used to measure the beam intensity. The ions scattered by the target

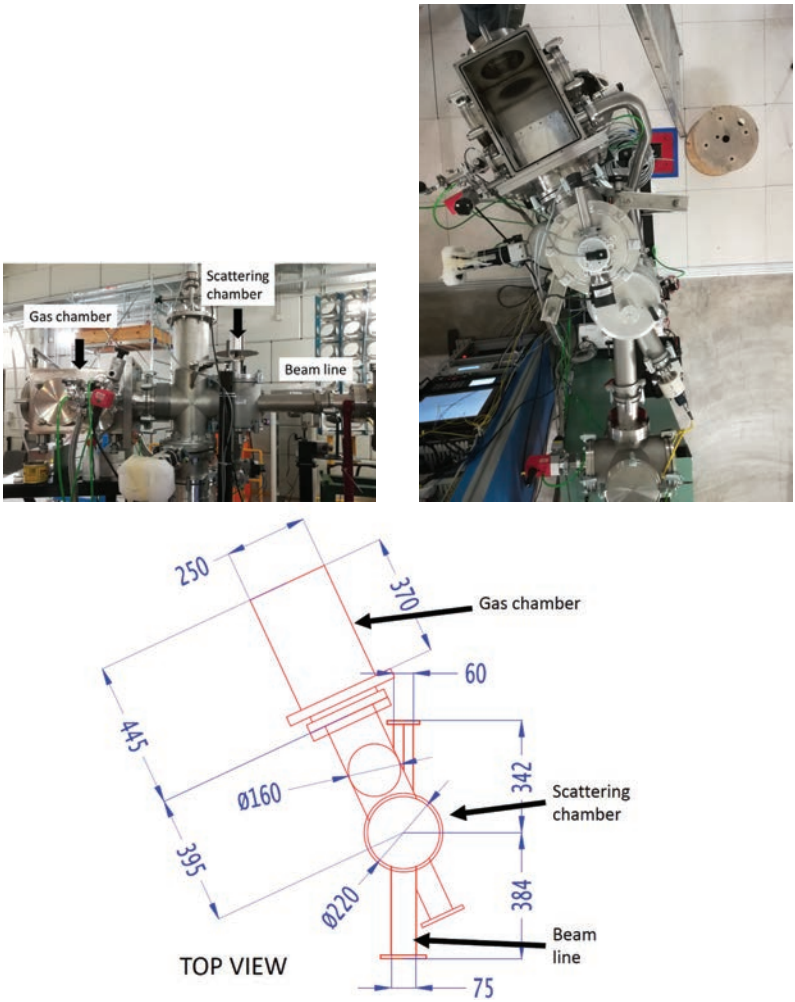


Fig. 21. Pictures of the TeBe line.

enter the gas chamber through a thin removable Mylar window (whose thickness can vary from 1.5 to 6 $\mu$m depending on the specific requirement) that separates the high-vacuum region from the gas-filled region where the tracker is placed. Between the Mylar window and the gas detector there is a gas dead layer whose thickness can range from 2 cm up to 10 cm.

Even if the TeBe beam line was specifically designed to test the tracker prototype, thanks to its flexibility, it is a multipurpose station that can be used to test several other detectors.

It is useful to underline that the gas flowing system and the slow control system (SCS) developed, tested and debugged in the TeBe station for the tracker prototype will be used for the final FPD in the NUMEN Phase 4. Only the mechanical support

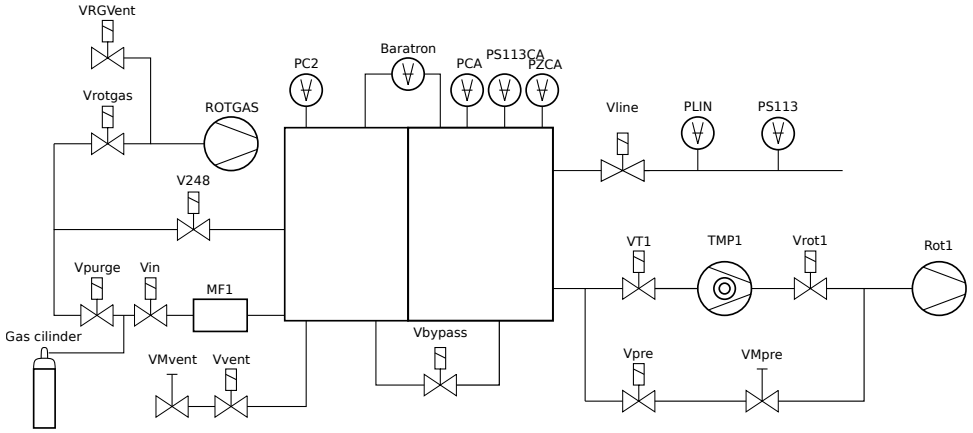


Fig. 22. Schematic diagram of the vacuum system for TeBe.

of the Mylar window and some vacuum tools to adapt the existing TeBe mechanics to the MAGNEX FPD one is required in Phase 4.

4.3.1. *The gas flowing system and the slow control system*

The gas continuously flows into the chamber in order to remove impurities or avoid contamination from air leakages. A schematic diagram of the TeBe vacuum/gas system is shown in Fig. 22, it is made of several elements that are listed as follows:

- a bistable bypass valve (Vbypass),
- an MKS flow control valve (V248),
- two rotative pumps (Rot1, ROTGAS),
- a turbo pump (TMP1),
- a mass flow controller (MF1),
- two full range (Pirani–Penning) pressure gauges (PCA, PC2),
- a piezoelectric pressure gauges (PZCA),
- a Baratron pressure gauge (Baratron),
- an MKS Type 250E controller,
- an MKS Type 647 controller,
- nine electrovalves.

An additional electrovalve (Vline) separates the TeBe experimental station by the beam line connected to the accelerator.

If not supplied by voltage (e.g. in case of black-out) all the valves close except the bypass valve, which must stay in the same state (O/C) as it is, to avoid to break the window.

The MF1 is a compact general purpose mass flow controller (MFC) with an all-metal sensor.

The MKS Type 248 Control Valve is a modified solenoid valve that, when supplied with a controlling current, is able to modulate the gas flow. When used with an MKS controller and appropriate flow sensor, the V248 valve modulates gas flow such that pressure or flow is maintained accurately and with precision to the set value.

The MKS Type 647 is a multichannel controller which provides both pressure and flow control. Multipurpose controller supplies power, provides gas flow readouts and simultaneously displays all channels with pressure.

The MKS Type 250E Pressure/Flow Controller controls any one of a variety of flow valves to accurately maintain a set pressure or flow. The 250 controller can provide a $\pm 15$ VDC output and accepts inputs from a variety of pressure transducers and mass flow meters.

The SCS for the TeBe line is used to setup, control and monitor the vacuum/gas system which is not time-critical, and can be run at a low priority. The heart of the SCS is an embedded CompactRIO controller (NI cRIO-9038 manufactured by National Instruments) that has been chosen for its modularity and reliability. It is based on a FPGA (Xilinx Kintex-7), and a 1.33 GHz Intel Atom dual-core processor, on which runs a Linux Real-Time OS. The controller can host up to eight modules for the control and monitoring of the devices and sensors.

The modules presently installed in the CompactRIO are: NI 9425 used to read the valves status and some pressure probe; NI 9476 used to open and close electrovalves and rotative pumps; NI 9205 and NI 9269 used to control and read the status of the beam collimators; NI 9870 and NI 9871 used to control and monitor the devices supporting RS232 or RS422/RS485 connection, i.e. the turbo-molecular pump, the MKS647 controller and the TPG256.

The SCS works in two modes: a full-manual mode and an automatic mode. In the first the user has the full control of all the electrically controlled elements and it is free to command them except for the line valve that can be opened only if on both side of the line valve there is an high vacuum (better than $10^{-5}$) or if there is atmospheric pressure (defined as a pressure higher than 980 mbar). The second mode is an automatic mode.

Three possible states are defined for the system: atmospheric pressure, high vacuum, flowing gas. The user can decide to move the system from one state to one of the others. All the main operations are automatically performed by the system (opening or closing of valves, turning on pumps etc.) while for those operations that cannot be controlled by the system (mechanical operation like opening of the gas cylinder) the user is guided by panel messages. Several cross checks are performed by the system to avoid misoperations of the user. The diagram in Fig. 23 schematically shows the possible transitions among the three different states defined in the SCS. At any moment the system can be switched to manual mode to permit the user to perform operations not allowed in the automatic mode. Figure 24 shows the visual interface of the slow control system of TeBe.

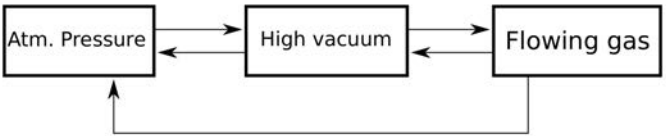


Fig. 23. Schematic diagram of the allowed transition between the three state of TeBe defined in the SCS.

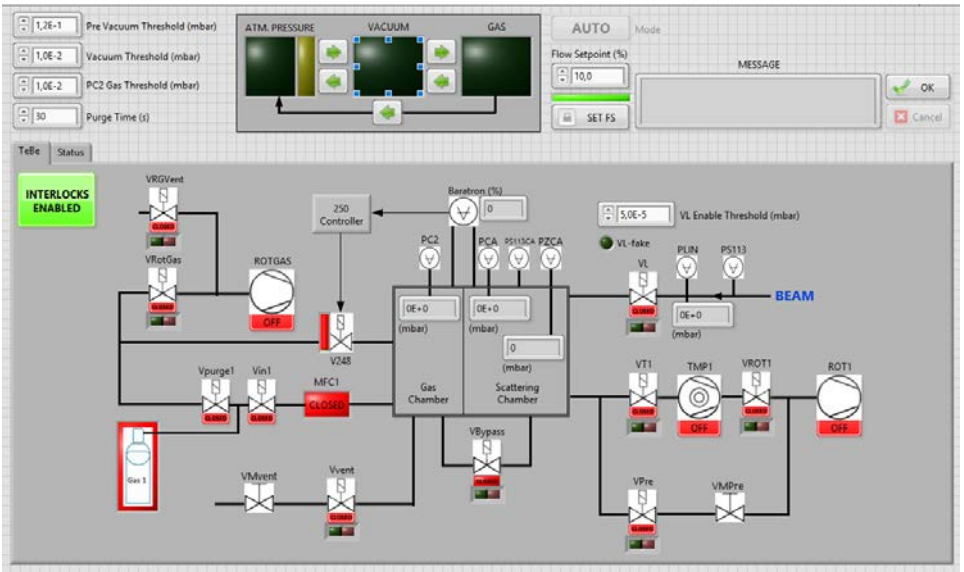


Fig. 24. Visual interface of the slow control system implemented in TeBe.

### 4.4. *Tests*

All the tests described in the following, have been performed at Laboratori Nazionali del Sud. Those involving the use of radioactive $\alpha$-sources or ion beams have been performed on the TeBe station placed in the MAGNEX experimental hall.

#### 4.4.1. *THGEM quality test*

Tests of the different M-THGEM have been performed at INFN-LNS and INFN-Catania with the aim to check their manufacturing quality. A first visual inspection was performed by using a digital microscope with magnification ranging from 10 times to 200 times. A general uniformity of the external metalized surfaces has been observed. In few cases, some defects in the manufacturing or some specks of dust are visible. Some examples are shown in Fig. 25.

For a deeper investigation, a Keithley electrometer model 6517A has been used as a voltage source at +1000 V. The voltage source is configured to be internally

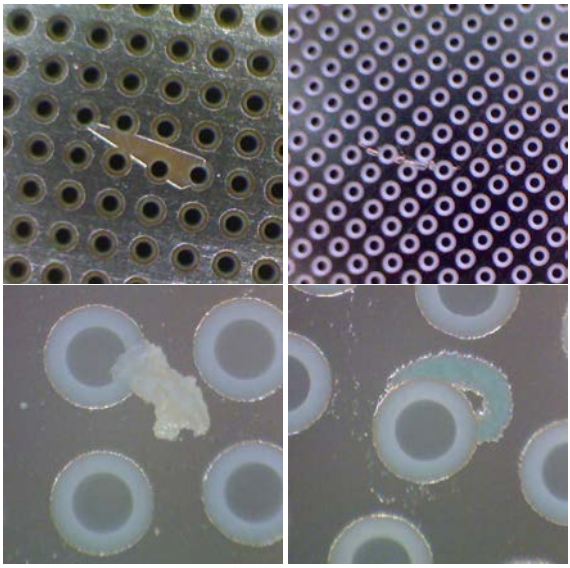

Fig. 25. Example of some defect on the THGEM.

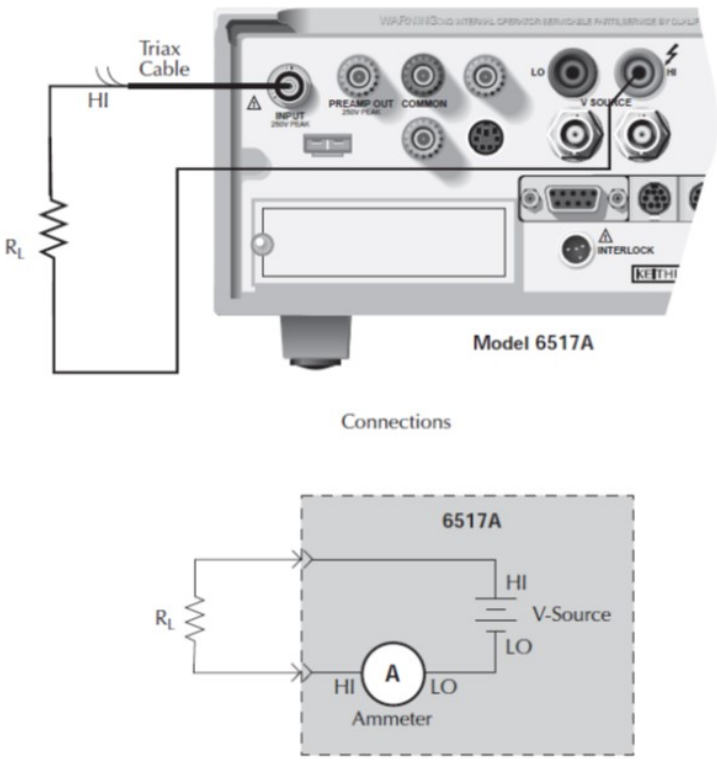


Fig. 26. Connection scheme of the test with the Keithley electrometer.

connected to the ammeter to measure current using the connection scheme shown in Fig. 26. With this setup it is possible to measure small currents below 1 nA. For such precision measurements low noise cables, proper shielding and guarding techniques have been used. Among all the M-THGEM foils tested with this setup, those with a measured current larger than 1 nA have been discarded and excluded by the subsequent characterization and tests.

4.4.2. *Experimental setup in the TeBe station*

The FPD prototype has been tested in the detector chamber of the TeBe station built at UNAM. The bias schemes used for the detector tests are illustrated in Figs. 27 and 28. In all the tests of measurement of currents, the bias scheme of Fig. 27, where the anode is biased with a small voltage (15 V) in order to be able to read the current, has been used. In the tests with electronics, the used bias scheme is shown in Fig. 28, where the anode is connected to electronics and therefore to the ground.

A 16-channel high-voltage power supply (CAEN SY5527 mainframe with A1515 board[64]) specifically designed for powering multiple GEM detectors has been used. The main features that make this power supply system a reliable solution for our

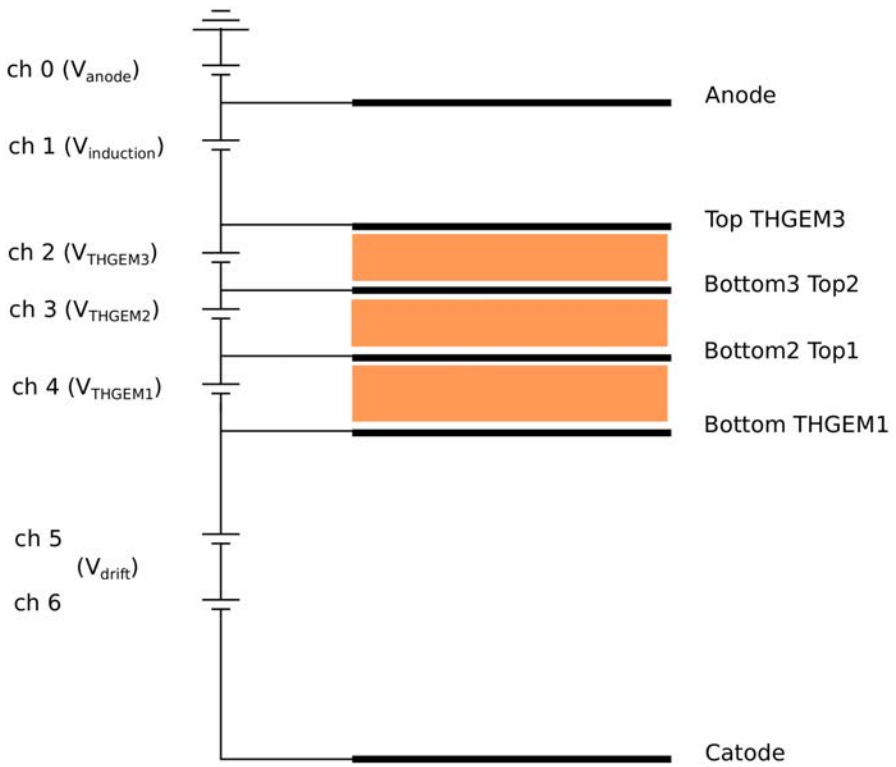


Fig. 27. Bias scheme of the tracker prototype for the anodic current measurements.

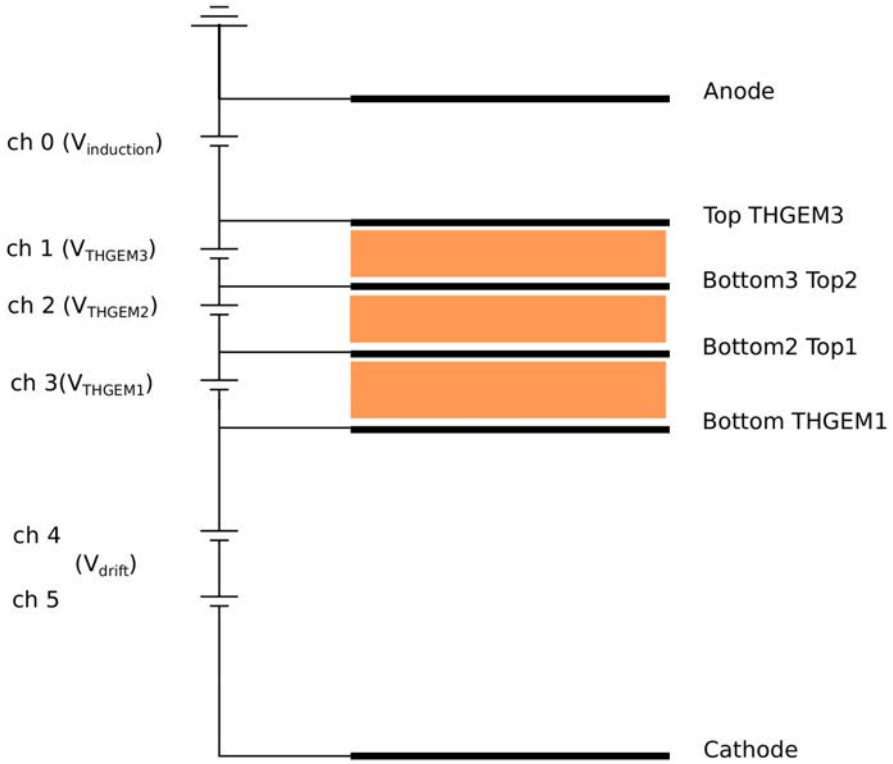


Fig. 28. Bias scheme of the tracker prototype for the measurements with electronics.

purposes are the following: (i) the channels have floating return, independent one from another, insulated up to 5 kV; (ii) the maximum output range for each channel is 1 kV and it is possible to monitor the current with 100 pA sensitivity in the 0–100 $\mu$A range and with 1 nA sensitivity for larger values; (iii) the board is provided with a current protection that can turn off all the channels if overcurrent occurs and (iv) the voltage ramp time can be modified for each channel down to 1 V/s.

During all the tests the detector chamber was filled with 99.95%-pure isobutane ($C_4H_{10}$) at pressures ranging from 10 to 100 mbar. The gas was continuously flowing at a rate of 145 sccm (standard cubic centimeter per minute).

### 4.4.3. *Discharge tolerance*

A preliminary test has been performed on the drift chamber to ensure the capability to keep high voltage necessary to the operation of the drift chamber. The whole system has been tested in each constituent part from the flange connectors to the cage. Every channel has been tested at the most critical situation from the discharge point of view, i.e. up to 1500 V and at a pressure of isobutane of 20 mbar. All the components and the whole assembly are compliant with high-voltage application.

#### 4.4.4. *Measurements of the current*

A measurement of the currents flowing in all the electrical segments of the prototype has been performed. These measurements allow to estimate the ion backflow and the gain of the THGEM as well as the charge diffusion losses (the electrons and positive ions that flows in elements other than anode and cathode).

The tests have been performed on triple THGEM types B and D of Table 9, because these types of THGEM guarantee an electron/ion current high enough to be measured by the power supply. The tests have been repeated on more than one THGEM per type giving similar results.

The software controlling the power supply CAEN SY5527LC (GECO 2020) generates log files of the currents of the different channels recording the changes in the current values with a time clock of 1 sec. Once the system is biased the current measurements is carried out after about half an hour, in order to make the system stable.

An $^{241}$Am $\alpha$-source with an activity of 55 kBq is placed inside the gas chamber and a shutter is located just in front the active area of the prototype allows to "turn on and off" the $\alpha$-source. In this way it is possible to compare the current flowing into different channels when the $\alpha$-source is *turned on* and when is *turned off*. From the differences of the two conditions it is possible to extract the effective current induced by the charged particle crossing the detector and subtracting the dark current. Figure 29 shows an example of the measured current for each channel. The effect on the current read when the shutter is open and closed is well visible.

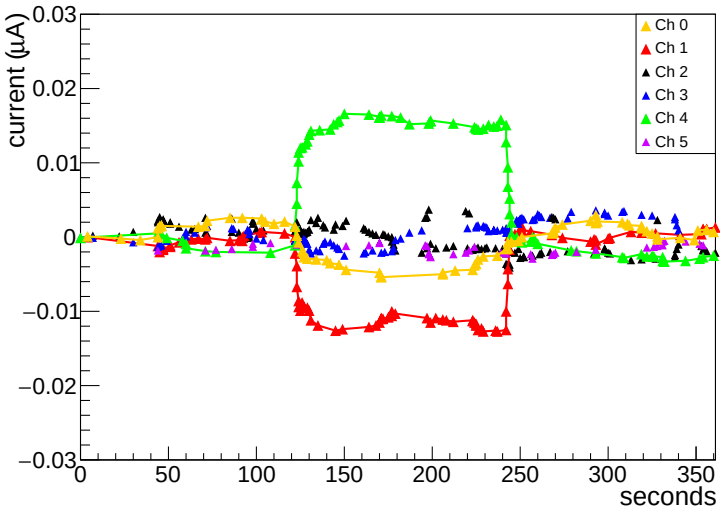


Fig. 29. Example of a log current file. The effects on the read current when the shutter in front of the $\alpha$-source is open (around second 120) and closed (around second 240) are clear. See Fig. 30 for a description of the different measured currents. Channels ch2 and ch3 refer to the intermediate electrode of the THGEM, for them currents different from zero have never been measured.

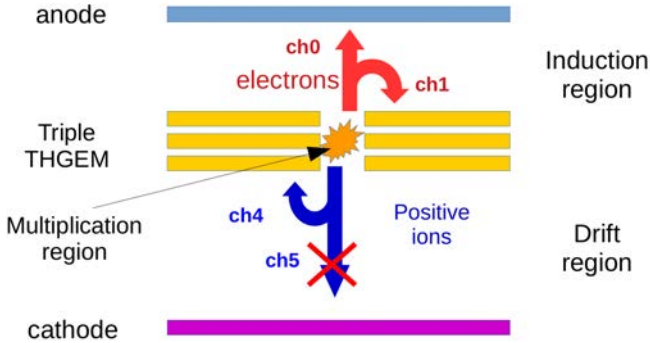


Fig. 30. Scheme of the currents (and relative channel of the power supply) measured in the tests. The channels ch2 and ch3 are not shown for the sake of clarity they correspond to the intermediate electrodes of the THGEM.

Knowing the number of $\alpha$-particle entering the active region of the detector per second and their energy losses in the gas, it is possible to estimate the THGEM multiplication factor. In the same way it is possible to measure the ion backflow and the diffusion losses in the top and in the bottom of the THGEM. A schematic drawing of all the mentioned currents is illustrated in Fig. 30. The electrons generated by the $\alpha$-particle in the drift region migrate through the multiple THGEM where multiplication occurs. The electrons produced in this region drift partially through the anode (generating a current $I_0$) and partially through the top of the multiple THGEM stack ($I_1$), while the positive ions produced in the multiplication region moves on the opposite side and can reach either the bottom of the multiple THGEM stack ($I_4$) or the cathode ($I_5$). In all the measurements performed we were able to measure $I_4$, while the current $I_5$ was below the measurements sensitivity. Therefore we conclude that all the positive charge produced in the multiplication region was collected by the bottom of the THGEM stack to a level better than 5%.

All the mentioned currents have been measured varying four parameters: gas pressure, voltage applied to the induction region ($V_{\mathrm{ind}}$), voltage applied to the drift region ($V_{\mathrm{drift}}$), voltage applied to the multiple THGEM ($V_{\mathrm{THGEM}}$) (each THGEM was biased with the same voltage).

**Anodic current versus induction voltage.** A first study investigated the behavior of the anodic current ($I_0$) as a function of the induction voltage ($V_{\mathrm{ind}}$). The measurements of the anodic currents require that the anode is not connected directly to ground in order to read the electron current flowing in. The used scheme is shown in Fig. 28.

Figure 31 shows the ratio between the anodic current ($I_0$) and the positive current flowing in the lower surface of the first THGEM ($I_4$). At high value of the voltage in the induction region, this ratio saturates, reaching 100%. This means that, when the electric field is intense enough, the electron current on the anode ($I_0$) is equal to the current $I_4$ that is the total positive current produced. Therefore

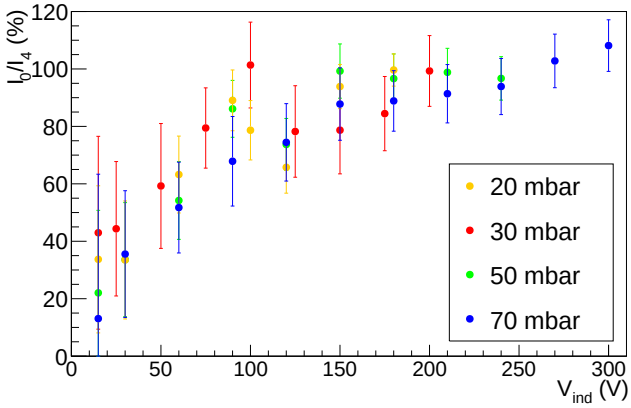


Fig. 31. Ratio between the anodic current ($I_0$) and the current on the top of the last THGEM ($I_4$) as a function of the induction voltage ($V_{\rm ind}$) for different pressures of the isobutane filling the drift chamber.

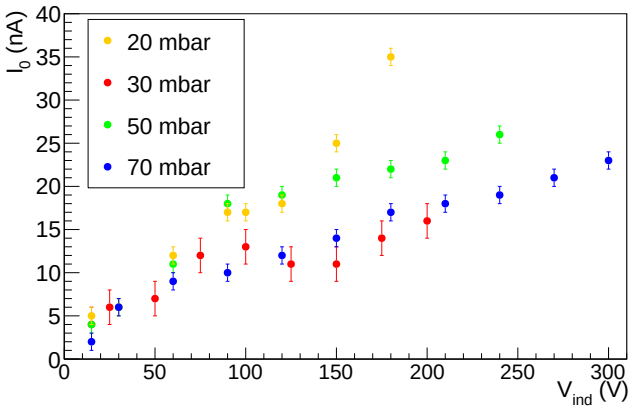


Fig. 32. Anodic current ($I_0$) versus induction voltage ($V_{\rm ind}$) for different pressures of the isobutane filling the drift chamber. For each pressure a different value of the THGEM voltage has been used.

all the electrons produced in the multiplication region are collected by the anode and a not measurable amount of electrons are collected by the upper surface of the last THGEM ($I_1$).

In Fig. 32 the current read in the anode ($I_0$) is shown as a function of the voltage of the induction region ($V_{\rm ind}$) for different values of the gas pressure. For each pressure the voltage applied to the THGEM was different, that is the reduced electric field $E/p$ was different for each pressure. Anyway, even if the curve refers to different values of $E/p$. It is important to underline that the curves do not saturate. This means that even if all the electrons are collected by the anode, the total number of electrons collected, after a small plateau in the region around 100 V, continues to increase. This is a clear evidence of the fact that after a given value of the electric

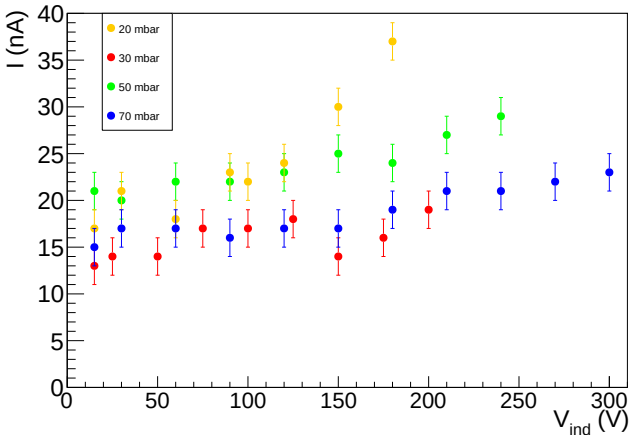


Fig. 33. Sum of the current in channels 0 and 1 of the high voltage CAEN power supply versus voltage in the induction region.

field in the induction region the multiplication region starts to expand out of the THGEM holes producing more and more electrons.

This phenomenon is confirmed looking at Fig. 33 where the sum of the currents in channels 0 and 1 are shown versus the voltage applied to the induction region. The sum of current in channels 0 and 1 (anode + induction region) corresponds to the total amount of electrons produced in the multiplication region. The fact that there is a region where the sum is constant and a region where the current increases is a clue that above a voltage value some additional multiplication occurs.

A long run has been performed in order to test the stability of the system and the stability of the THGEM gain. In more than 13 hours just two short sparks occurred and there is no evidence of variation trend in the current measured in the different elements (see Fig. 34).

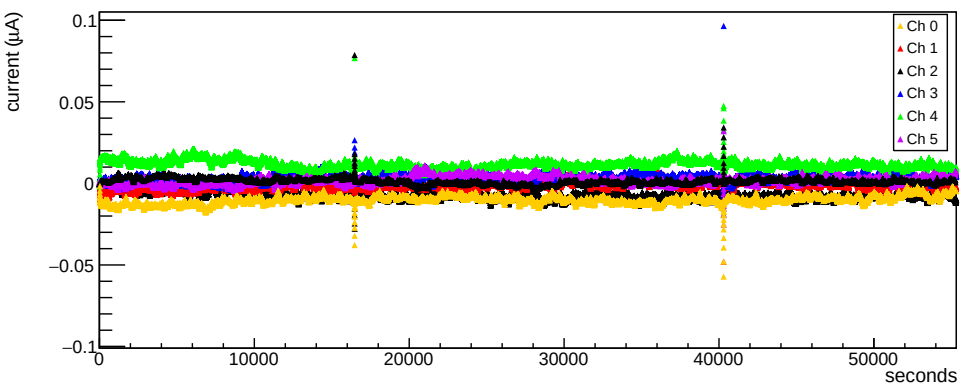


Fig. 34. Stability test.

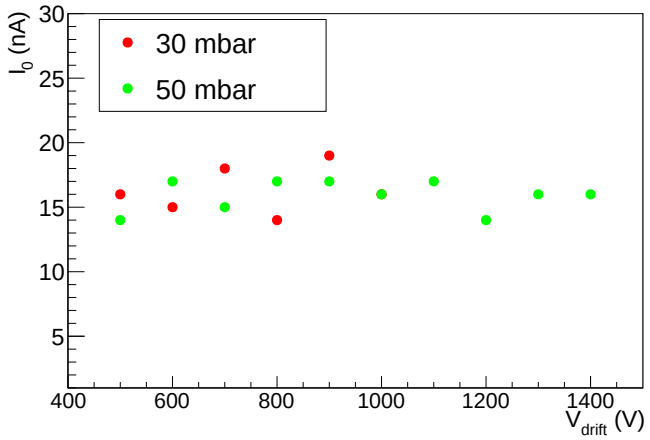


Fig. 35. Anodic current as a function of the voltage applied to the drift region.

The effect of the voltage applied to the drift region ($V_{\text{drift}}$) on the current measured in the anode has also been studied. As it is shown in Fig. 35, no significative effect has been observed in the investigated voltage range. This means that the electric field in the drift region is already enough to drive the electron in the THGEM without a significant attenuation.

**Anodic current versus THGEM voltage.** In order to calculate the multiplication factor we have to consider the energy loss of $\alpha$-particles in the detector active area, the average energy required to create an electron-ion pair and the rate of charged particles entering the detector. Once all these are correctly taken into account we can calculate the multiplication factor of the THGEM measuring the anodic current. Figure 36 shows that the anodic current clearly increases with the

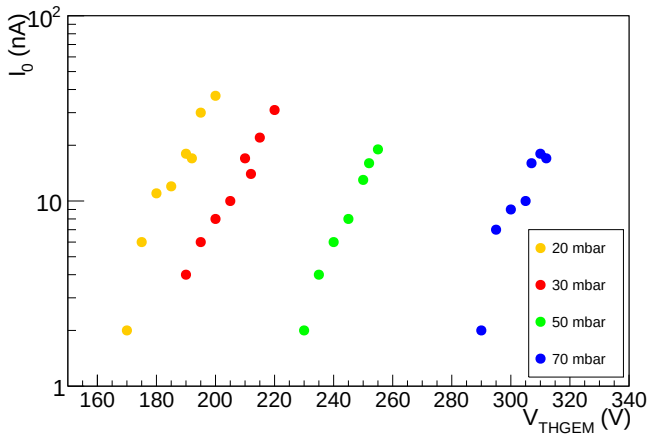


Fig. 36. Anodic current versus voltage applied to THGEM ($V_{\text{THGEM}}$) at different pressures of the isobutane.

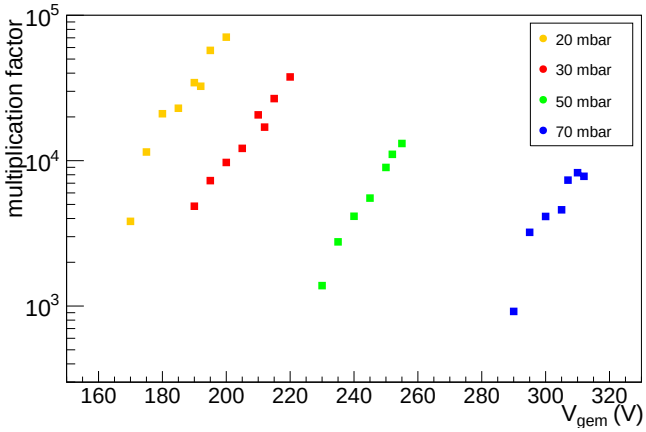


Fig. 37. Multiplication factor versus ($V_{\mathrm{THGEM}}$) at different pressures of the isobutane.

voltage applied to the THGEM, this trend is maintained for different gas pressures, the extracted multiplication factor is shown in Fig. 37 where gains up to $6 \cdot 10^4$ can be reached.

One should notice that since the precision of the current measured by the power supply is quite low ($\sim 2$ nA) large THGEM multiplication factors (gain) are required in order to make the current observable by the instrument.

In order to better characterize the gain factor of the detector tests with a higher precision picoammeter can be performed.

**Ion backflow.** The ion backflow (IBF) is defined as the ratio between the current, generated by positive charge, read on the cathode and the sum of the current generated by the electrons produced in the multiplication region. Having Fig. 30 as a reference, the IBF could be described by the following formula:

$$\mathrm{IBF} = \frac{\mathrm{ch5}}{\mathrm{ch0} + \mathrm{ch1}} .$$

The IBF has been studied as a function of the $V_{\mathrm{THGEM}}$ and $V_{\mathrm{drift}}$ for different value of isobutane pressure. In Fig. 38 the IBF as a function of the voltage applied to the THGEM is shown. The main features of the curves are that the lower value of the IBF is obtained for higher value of $V_{\mathrm{THGEM}}$. In Fig. 39 the IBF as a function of the voltage applied to the drift region is shown. In this case, the IBF shows an increasing monotonic behavior with the $V_{\mathrm{drift}}$.

### 4.4.5. *Test with electronics*

A test has been performed using the electronics described in Subsec. 7.1. The electronics used for the test is made of an A1429 a 64-channel preamplifier and a V2740, a 64-channel, 125 MS/s, 16-bit Waveform Digitizer. For the test a single digitizer module and a single preamplifier was used, therefore just 64 strips over a total of

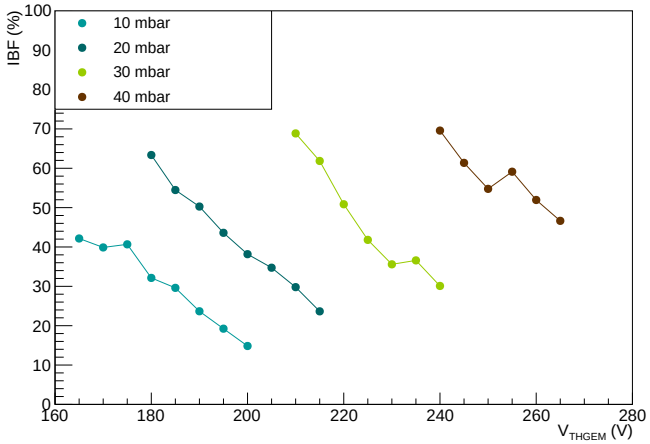


Fig. 38. The ion backflow versus the voltage applied to the THGEM for different pressure of the isobutane.

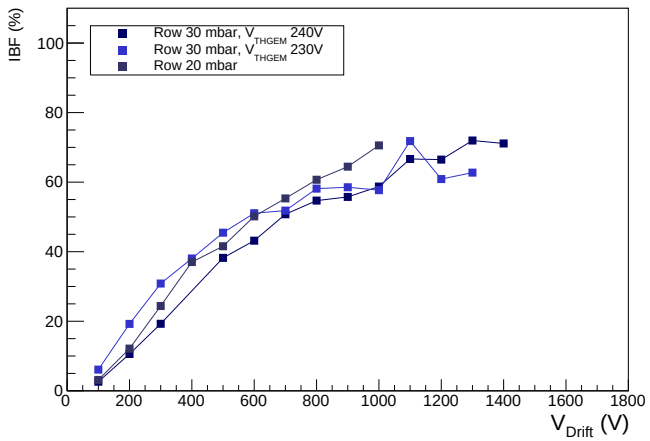


Fig. 39. The ion backflow versus the voltage applied to the drift region for different pressure of the isobutane.

192 were connected to the electronics. The scheme of the electronics is very simple: the signal from the segmented anode are sent to the A1429 preamplifier through an passive adapter, the output of the preamplifier is directly sent to the V2740 digitizer.

The hardware of the V2740 requires a Digital Pulse Processing (DPP) firmware typically Pulse Height Analysis (PHA), i.e. a trapezoidal filter for the determination of the pulse height and a corresponding software. Anyway, since the firmware is under development the present test has been performed reading the signals in "scope" mode, that is acquiring the full shape of each of the 64 channels by mean of a common trigger (the *OR* of all the channels). Therefore all the 64 channels

are acquired at the same time and on each channel a trapezoidal filter is applied to obtain the pulse height, by using a read-out software. It is important to underline the filter applied with the software is exactly the same filter that the firmware under development will apply.

The tracker prototype has been biased as in the previous test by using the power supply CAEN SY5527. The values of the voltages used in this test was $V_{\rm ind} = 50$ V, $V_{\rm THGEM} = 190$ V, $V_{\rm drift} = 600$ V. An $^{241}$Am alpha source has been placed in front of the active volume of the tracker, and a remotely controlled shutter was placed in such a way that if closed it stops the $\alpha$ entering the active area of the detector.

The quality of the signal that the alpha particles generates in the single strip is very good. The algorithm that generates the triangle (timing and trigger) and the trapezoid is working properly and the signal is shaped in the correct way as shown in Fig. 40. In the top panel the full shape of the digitized signal coming

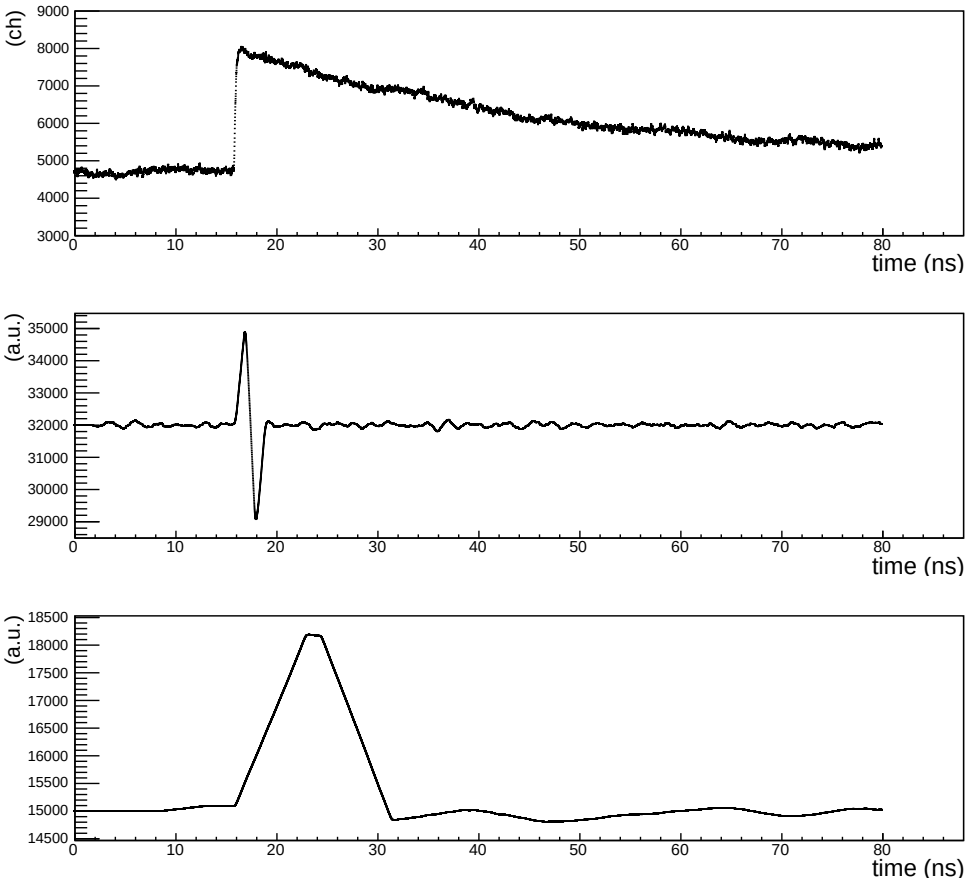


Fig. 40. Example of a signal in a strip induced by an alpha source. From top to bottom: the full shape of the digitized signal coming out from the preamplifier, the triangle filter and the trapezoid filter (see text for more details).

out from the preamplifier is shown. In the middle panel the triangle filter used for timing and trigger is shown. In the bottom panel the trapezoid filter used to generate the amplitude of the signal is shown. Once it was demonstrated that the PHA algorithm is working properly with the signals of the segmented anode of the tracker, we proceed with the determination of the tracks generated by the $\alpha$-particles coming from the source.

Before describing the tracking capability of the prototype, it is worth to shortly remind the basic working principles of the tracker. When a charged particle crosses the tracker it ionizes the gas, the electrons drift under the effect of the electric field present in the drift region and reaches the THGEM. The THGEM has five rows of holes 18 mm spaced, each raw defines a $z$ coordinate. Just the electrons produced in correspondence of this rows are multiplied by the THGEM and can generate a signal in the segmented anode. An ideal track with an angle $\theta$ on the plane $x$–$z$ generates signals on five strips, that is the strips that correspond to the crossing of the five THGEM rows with the ion track. The $x$ coordinate is defined by the corresponding hit strip. In the real case not just a single strip is hit but, due to the broadening of the electron clouds a group of adjacent strips is hit. The electrons generated by the incident charged ion have a different arrival time on the anode due to the vertical position where they are produced. Therefore from the time measurement of the strip signals, it is possible to determine the $y$ coordinate. In this way we are able to have a full 3D track.

In Figs. 41–43 a typical track generated by an $\alpha$-particle of 5.486 MeV is shown. Due to the fact that just a portion of the anode was connected to the electronics, the tracker prototype was able to reconstruct just tracks with a small angle $\theta$

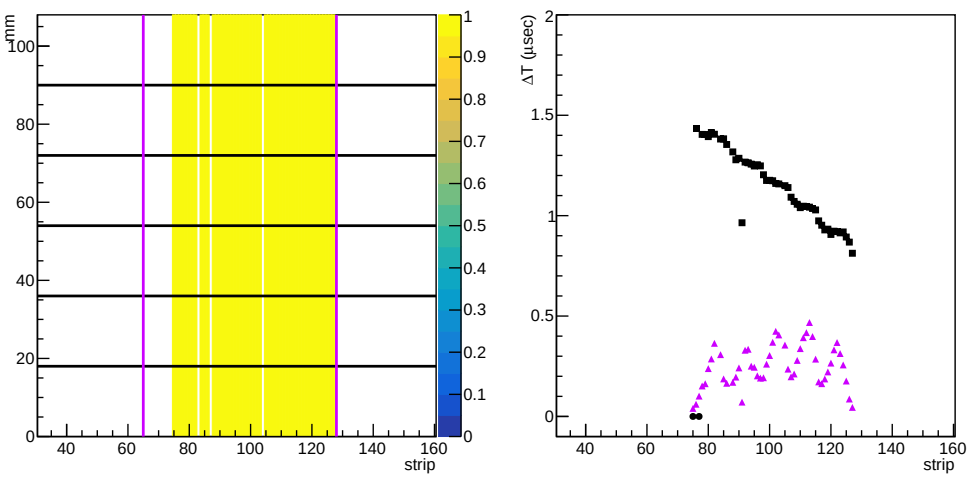


Fig. 41. (Color online) On the left are shown the strip hit in the event. On the right the corresponding values of time (black squares) and energy in arbitrary units (violet triangles) for each hit strip. The timescale offset is arbitrary.

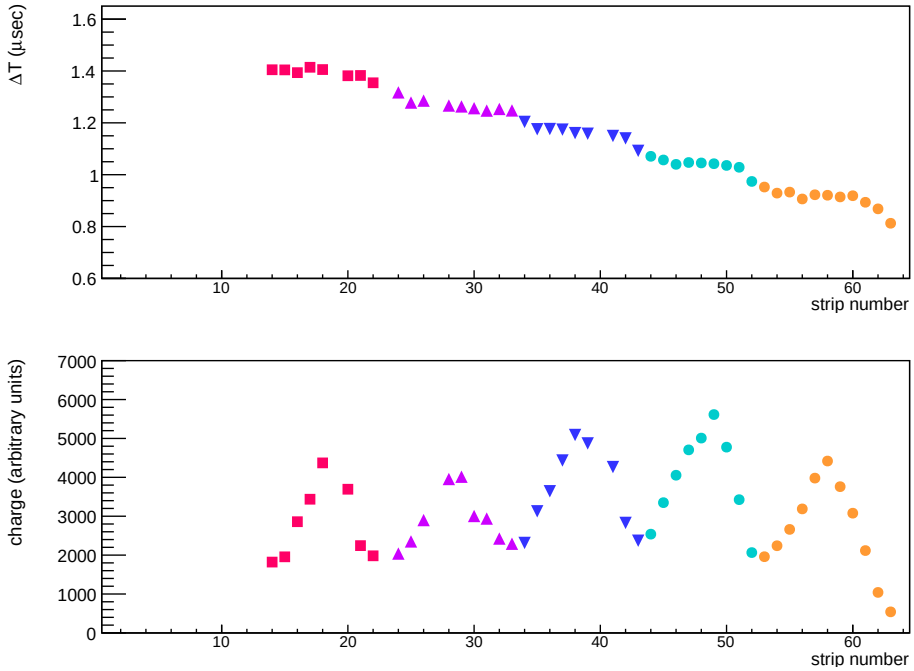


Fig. 42. (Color online) Time ($\mu$s) and energy (a.u.) for the five different rows of holes in the THGEM.

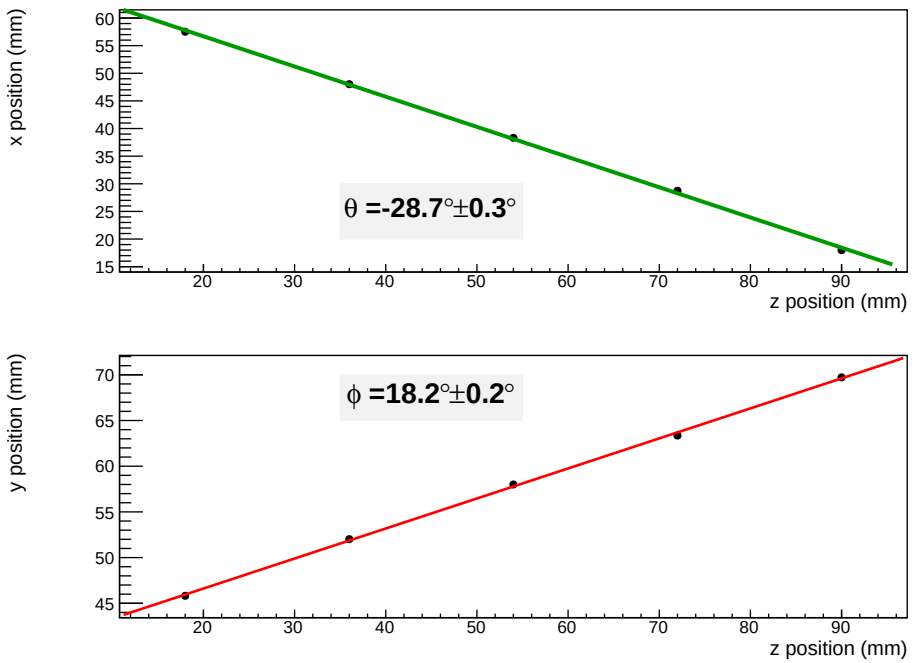


Fig. 43. Fit applied to extract the vertical and horizontal angle of the track.

(maximum angle 24°). In Fig. 41 the hit map of the anode, for this event all the strip from 75 to 128 where hit (yellow region of the anode). In Fig. 42 (top) the difference in the measured time $\Delta T$ with respect to the first strip is shown for each strip, the different colors corresponds to a different row (i.e. to a well-defined $z_i$ position). Whilst at the bottom panel of the same figure the charge induced in each strip is plotted. Each group has a well-defined bell shape. For each group of strip corresponding to a row the average time (directly correlated with $y_i$), the centroid of the energy distribution (i.e. $x_i$) and the corresponding $z_i$ value are obtained.

In order to determine the $y_i$ coordinate, the $\Delta$T has been converted in mm, knowing the drift velocity of electrons in the gas or alternatively using a geometrical calibration procedure.

Once the $x_i$, $y_i$ and $z_i$ coordinates for the five points have been extracted, it is possible to extract the angles $\theta$ and $\phi$ by fitting $x_i$ versus $z_i$ and $y_i$ versus $z_i$, respectively. Finally in Fig. 43 the fit of $\theta'$ and $\phi$ with their corresponding errors is shown. The values and errors obtained with the above described procedure for this track are: $\theta = 28.7 \pm 0.3°$ and $\phi = 18.2 \pm 0.2°$. The reconstruction accuracy in both horizontal and vertical directions is quite good and satisfies the NUMEN requests.

Tests with beam have also been performed but using a different electronics based on VMM3 chip. The use of VMM-based electronics was motivated by the fact that the CAEN electronics was still not ready at the time the on beam test were performed. The test was successful and the prototype was able to reconstruct the beam ion trajectory.

Concluding, the test with CAEN electronics was very successful. The signals extracted from segmented anode are well formed by the PHA algorithm, therefore it is possible to determine the time of each strip and the amplitude of the signal. The track generated from $\alpha$-particles is easily extracted as shown above.

## 5. The Particle Identification System

### 5.1. *Introduction*

The technology chosen for the new gas tracker of the MAGNEX spectrometer is not conceived to provide accurate information on ion energy loss, reducing the overall particle identification capabilities of the setup. Consequently, PID must be demanded to a dedicated wall of telescope detectors downstream the tracker. The most relevant aspects to be considered in the design of a suitable detection system for NUMEN, matching the fundamental requirement to identify ions unambiguously in the region of O, F and Ne atomic species are related to

(1) The radiation hardness, since the expected overall heavy-ion fluency will be of the order of $10^{11}$ ions/(cm$^2 \cdot$yr) assuming 120 days of full power irradiation per year.

(2) The energy resolution $\Delta E/E$, which must be better than $\sim 2\%$, in order to maintain the present performances in terms of atomic number and mass identification ($\Delta Z/Z \sim 1/48$ and $\Delta A/A \sim 1/160$)[65] or at least to allow an unambiguous identification of the ejectiles of interest for NUMEN, characterized by an atomic number $Z \sim 10$ and mass number $A \sim 20$. The energy resolution should also be good enough to guarantee the same sensitivity in the cross-section measurements, which is limited by the spurious events inside the identification graphical cuts.
(3) The time resolution, such to guarantee an accurate time-of-flight (TOF) measurement of the ejectiles from the target to the focal plane and the drift time of primary electrons in the gas tracker. The TOF measurement with resolution better than 2–3 ns[12] is necessary to effectively suppress the background in the coincident events between MAGNEX and the $\gamma$-ray calorimeter (see Sec. 6). The drift time is also used to reconstruct the vertical track of the ejectiles, for which a time resolution better than 5 ns would be acceptable.[66]
(4) The degree of segmentation; in order to keep the double-hit event probability below 3% in the whole FPD, modules of $1.5 \times 1.5$ cm$^2$ area are proposed.
(5) The geometrical efficiency, which should be high enough to obtain accurate measurement of the absolute cross-section and to reduce the background coming from events with partial charge collections, which could reduce the overall sensitivity of NUMEN to rare DCE events.
(6) The detectors thickness, which must be chosen in order to stop the ejectiles of interest in a wide dynamical range of incident energies (15–60 MeV/u).
(7) The scalability, which should guarantee that a large number of detectors can be easily built, assembled and managed at reasonable price, also in terms of time required for the calibration procedures.
(8) The coupling with the FPD tracker, which requires that the PID wall should work in a low-pressure gas environment (typically $C_4H_{10}$ at 10–50 mbar), where the presence of high voltages is to be considered.

Several nuclear physics experiments[67–69] have adopted the telescope solution to study and identify reaction products. This consists of at least two detectors assembled such that the particles of interest cross the first and stop into the second. The correlation between the energy loss signal in the thin detector ($\Delta E$ stage) and the residual energy ($E_r$) deposited in the stopping one is connected to the atomic number $Z$ of the detected ion through the Bethe–Bloch formula.[70] Due to the good energy resolution and linearity, thin Si detectors are typically used as $\Delta E$ stage, followed by a thick Si or scintillator detector (CsI, NaI, etc.) or even a gas detector. This configuration easily provides a good $Z$ identification, acceptable energy resolution and a high stopping efficiency. Nevertheless, all these solutions are limited by the radiation hardness of silicon. Telescopes based on thin Silicon Carbide (SiC) detectors and inorganic scintillators (CsI) were chosen and tested as the final solution for particle identification.

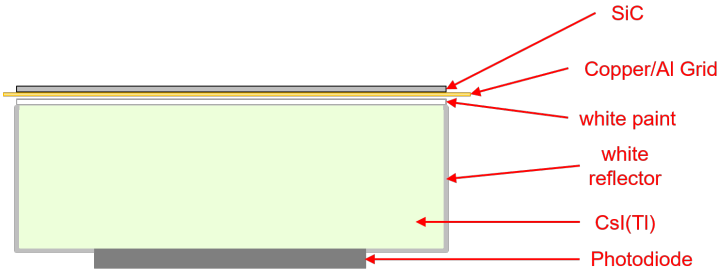


Fig. 44. Sketch of the single telescope cell.

### 5.2. *The particle identification detector*

The PID, with a required capability of withstanding a counting rate of as high as ten kHz/cm$^2$, is an array of 720 tiny identical $\Delta E - E$ telescopes covering the focal plane of the MAGNEX spectrometer. Each detector cell covers an active area of 1.5 cm $\times$ 1.5 cm, with a 0.4 mm dead space between cells. The $\Delta E$ layer is constituted by a thin SiC detector, whereas the $E_r$ layer, where all the particles are stopped, is a CsI(Tl) inorganic scintillator coupled to a photodiode of 1 cm $\times$ 1 cm (Fig. 44). The single detector cell must be capable to handle such a rate and to withstand the corresponding radiation damage, also considering that the impinging particles will be heavy ions (as a reference one can consider $^{16}$O between 20 and 70 MeV/amu). A simple estimate of the energy loss in the telescope, taking into account the layers of materials in between, is listed in Table 10 and plotted in Figs. 45 and 46 for the two reference cases.

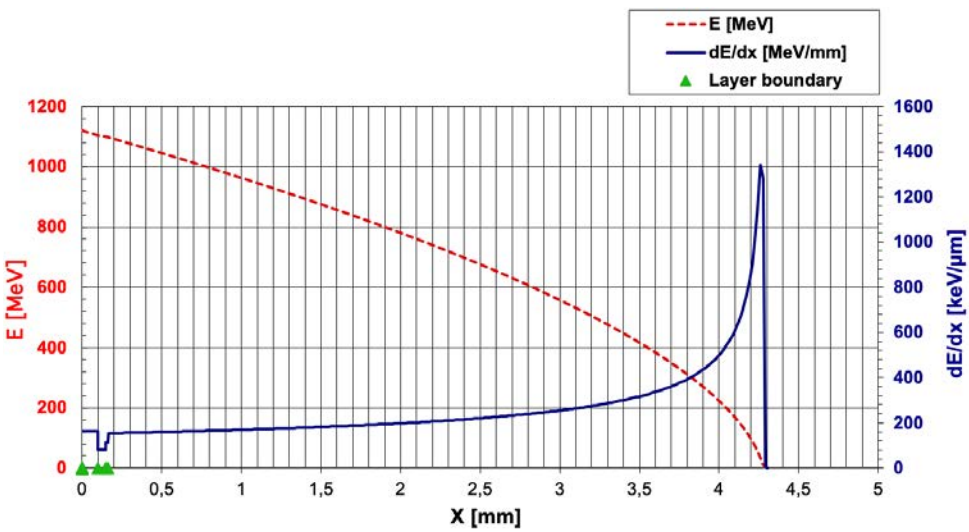


Fig. 45. Energy loss profile in the telescope for $^{16}$O at 70 MeV/amu.

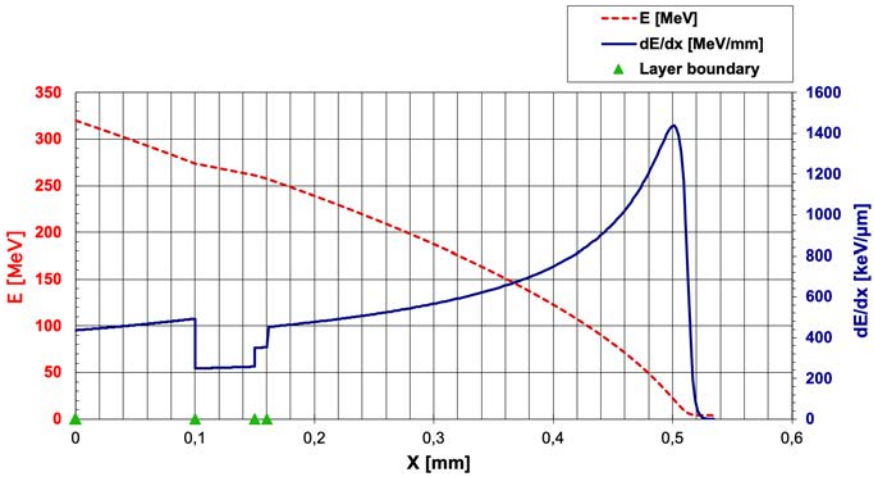


Fig. 46. Energy loss profile in the telescope for $^{16}$O at 20 MeV/amu.

Table 10. Energy loss and range in the telescope cell for two reference cases.

| $^{16}$O | 70 MeV/amu | 20 MeV/amu |
|---|---|---|
| Incident energy [MeV] | 1120 | 320 |
| Energy loss in SiC [MeV] | 16.3 | 46.4 |
| Energy loss in paint [MeV] | 1.1 | 3.4 |
| Energy loss in CsI [MeV] | 1102.6 | 270.2 |
| Range in CsI [mm] | 4.1 | 0.4 |

Table 11. Maximum useful energy, corresponding to a range slightly less than 5 mm in the CsI(Tl) crystal, for three typical ion species.

| Ion species | Max energy [MeV/amu] | Max energy [MeV] |
|---|---|---|
| $^{12}$C | 65 | 780 |
| $^{14}$N | 70 | 980 |
| $^{16}$O | 75 | 1200 |

The maximum useful energy for three typical ion species, corresponding to a range in the crystal slightly below its 5 mm thickness, is listed in Table 11. The minimum energy allowing to reach the CsI(Tl) crystal after crossing the front layers is $\geq$ 10 MeV/amu.

In order to keep a reasonable modularity, and to comply with the modularity of the electronics, it was decided to arrange the elementary cells into towers, each one consisting of 20 telescopes (Fig. 47). The full width of the MAGNEX focal

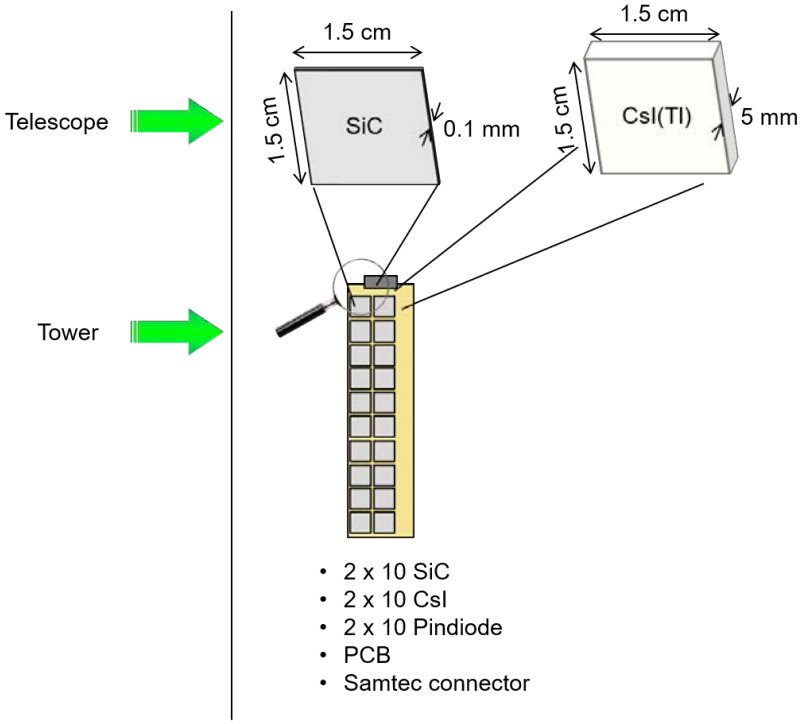


Fig. 47. Arrangement of a tower of 20 elementary telescope cells.

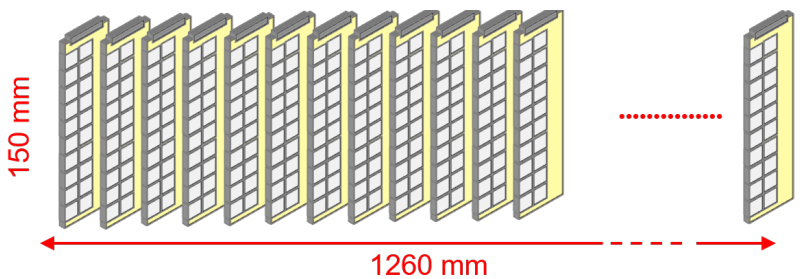


Fig. 48. Sketch of the arrangement of the towers covering the MAGNEX focal plane.

plane ($\approx$1000 mm) corresponds to $\approx$1260 mm projected on the PID wall and will be covered by 36 towers rotated by about 35° with respect to the vertical axis (Fig. 48). The expected counting rate profile along the vertical direction is such that the majority of the particle flux will impinge around $y = 0$ cm, quickly decreasing while going to $y = \pm 11$ cm. This means that a higher damage, if any, is to be expected on the central telescopes of each tower.

Table 12. 4H-SiC and Si main properties.

| Properties | 4H-SiC | Si |
|---|---|---|
| $E_{\text{gap}}$ [eV] | 3.23 | 1.12 |
| $E_{\text{breakdown}}$ [V/cm] | $3–4 \times 10^6$ | $3 \times 10^5$ |
| $\mu_e$ [$\text{cm}^2/\text{V} \cdot \text{s}$] | 800 | 1450 |
| $\mu_h$ [$\text{cm}^2/\text{V} \cdot \text{s}$] | 115 | 450 |
| $V_{\text{saturation}}$ [cm/s] | $2 \times 10^7$ | $0.8 \times 10^6$ |
| $Z$ | 14/6 | 14 |
| $\epsilon_r$ | 9.7 | 11.9 |
| $E - h$ energy [eV] | 7.6–8.4 | 3.6 |
| Density [$\text{g/cm}^3$] | 3.22 | 2.33 |
| Displacement $E$ [eV] | 30–40 | 13–15 |
| Thermal conductivity [$\text{W/cm} \cdot \text{K}$] | 4.9 | 1.5 |

### 5.3. *Silicon carbide $\Delta E$ detector*

Among the "robust" radiation-hard materials, the SiC has recently received special attentions also thanks to technological improvements within the SiCILIA project.[22] SiC is a compound semiconductor with a wide bandgap. The 4H polytype is considered the most appropriate for particle detector applications, characterized by an energy bandgap of 3.23 eV. It is thermally stable up to about 2000°C, even in oxidizing and aggressive environments. Some of the main physical properties of SiC are compared to those of Silicon (Si) at room temperature in Table 12.[71]

The first requirement for the new PID wall is the radiation hardness, i.e. the inertness of the detectors to high doses of particle irradiation. This is strictly related to the damage of the lattice created by traversing particles. SiC, due to its wide gap and strength of its chemical bonds, is a very valid alternative to Si for the production of radiation hard detectors. The usual design of a solid-state detector includes a diode structure operating under reverse bias, where a space charge region is formed. Ionizing particles produce ionization in a semiconductor when they are slowed down or absorbed. Thus, electron-hole pairs are formed and are then separated by the electric field and collected at the electrodes, yielding a current pulse in the detection circuit.

The current generated is directly correlated with the deposited energy. A detector should have a low concentration of impurities and defects, as they cause a decrease in the current pulse amplitude due to recombination of electron-hole pairs and scattering of charge carriers. Moreover, a low concentration of dopant impurities extends the thickness of the space charge region, i.e. the detection active region. The wide bandgap of SiC (3.28 eV) is useful, as it reduces significantly the rate of thermal noise. On the other hand, it also represents a disadvantage: a particle with a certain energy, ideally converting all its energy for the generation of electron-hole pairs, generates about three times more charge carriers in Si (bandgap 1.12 eV) than in SiC. Detectors based on SiC, therefore, have lower pulse amplitudes. However, the heavy ions to be detected in NUMEN generate a large number of primary

charge carriers, whose statistical fluctuations are not an issue. Furthermore, SiC-based detectors still have a high SNR at temperatures which are unattainable for Si-based devices, which instead need external cooling to keep the intrinsic carrier level sufficiently low.[72]

Traversing particles not only ionize the lattice but also interact with the atomic bodies via the electromagnetic and strong forces. The result is that atoms are displaced and create interstitials, vacancies and more complex structures. In addition, diffusing Si atoms or vacancies often form combinations with impurity atoms, like oxygen, phosphorus or carbon. All these lattice displacements or defects dislocation populate new levels changing the initial semiconductor properties. The resulting macroscopic changes are: (i) enhancement of the leakage current; (ii) change of the depletion voltage, mainly due to the creation of additional acceptor levels; (iii) decrease of the charge collection efficiency, due to new defects acting as traps for the generated carriers.

Radiation hardness of SiC devices irradiated with heavy ions stopping in small SiC detectors ($2 \times 2$ mm$^2$, 30 $\mu$m thick) was investigated in Ref. 73. The results proved that the detectors are able to accept fluencies as large as $10^{14}$ heavy ions/cm$^2$, thus matching with main requirements of NUMEN in terms of radiation hardness.

For time resolution, SiC detectors can profit from the high saturation velocities of the charge carriers ($2 \cdot 10^7$ cm/s) in the semiconductor — two times higher than in silicon — and to the possibility to effectively operate the devices at or close to the carrier velocity saturation condition. This is because the breakdown field in SiC is 3 MV/cm, ten times higher than in Si or GaAs: the junctions on SiC can hence reach extremely high internal electric field in the depleted region. Electric field as high as $10^5$ V/cm has been reached without suffering junction breakdown or significantly increasing the reverse current.[74] A timing resolution of hundreds of ps has been measured for SiC pixel detector.[75]

The thickness of SiC must be chosen in order to permit the detection of the ejectiles in the wide dynamical range of incident energies, i.e. 10 to 35 MeV/u for the ($^{20}$Ne, $^{20}$O) DCE reactions and 10 to 60 MeV/u for the ($^{18}$O, $^{18}$Ne) DCE reactions. An appropriate thickness for the $\Delta E$ stage is $\approx 100$ $\mu$m, which correspond to an energy loss $\Delta E \approx 25$ MeV for $^{20}$O at 40 MeV/u and $\Delta E \approx 180$ MeV for $^{18}$Ne at 10 MeV/u.

The detector is based on deposition of epitaxial layers. In the past few years steep improvements in the density of defects of the substrates and of the epitaxial layers have been achieved, with a consequent large reduction of micropipes and stacking faults. As a consequence, a new opportunity of constructing bipolar devices ($p/n$ junctions, transistors, ...), that greatly benefit by the reduction of this kind of defects is open. It is now possible to build detectors characterized by lower leakage current and a better SNR.

Prototypes have been constructed and tested in terms of resolution, timing and radiation hardness and the results are discussed in the following subsections.

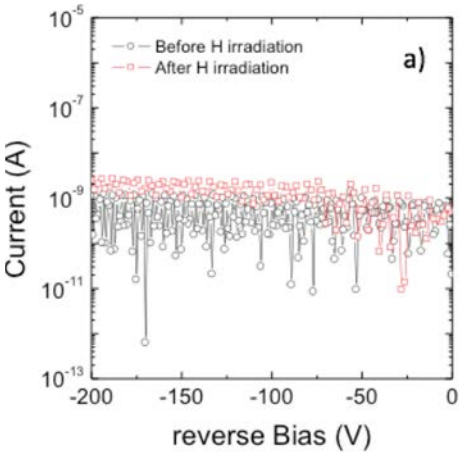


Fig. 49. Reverse current-voltage characteristic of $p-n$ junction detector before and after 60 MeV proton irradiation at a dose of 2 kGy.

#### 5.3.1. *Radiation hardness*

In order to study the radiation hardness performances of the SiC detectors, different tests were done. In the first one, the device was irradiated by 60 MeV $H^+$ at a maximum dose of 2 kGy and the reverse characteristics measured before and after the irradiation are shown in Fig. 49. They do not change significantly after irradiation and the leakage current measured up to $-200$ V remains low ($10^{-9}$–$10^{-10}$ A).[76]

The performances of the device against the implantation of an heavy-ion were investigated by a second irradiation test, performed with a Tandem beam of $^{16}O$ at 25 MeV. The response of a $p-n$ junction 10 $\mu$m thick SiC detector and a 300 $\mu$m silicon detector were compared in terms of resolution and Charge Collection Efficiency (CCE) for increasing values of the ion fluency. The results are shown in Fig. 50 in which the CCE is reported. The silicon detector starts to be deteriorated at $10^9$ particles/cm$^2$ and it is permanently broken starting from $10^{10}$ particles/cm$^2$. The CCE of the SiC device is reduced to $\sim$20% at a fluency of $10^{13}$ particles/cm$^2$, but it is restored up to $\sim$45% after $\sim$24 h at rest.

Regarding the resolution, a value of 0.3 MeV FWHM is obtained before the irradiation, it deteriorates to $\sim$0.7 MeV at $10^{13}$ particles/cm$^2$, but after the rest period it is completely restored.[77]

### 5.4. *The cesium iodide E detector*

#### 5.4.1. *Performance tests*

The $E_r$ detector is a 5 mm thick CsI(Tl) scintillator with active area 1.5 cm$\times$1.5 cm. When hit by radiation it produces scintillation light with a spectrum centered around 540 nm and a decay time constant $\approx$3 $\mu$s. The scintillation light read-out is

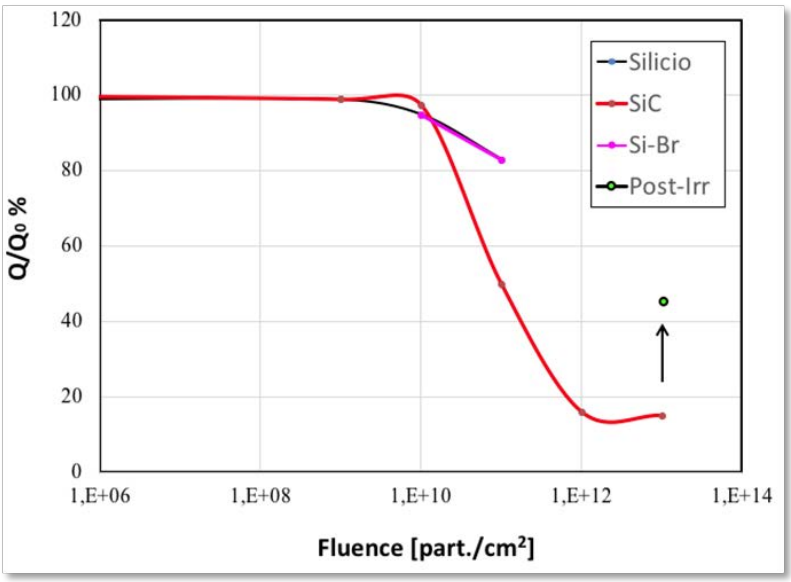


Fig. 50. (Color online) Charge collection efficiency as a function of the fluency of $^{16}$O ions at 25 MeV for 300 $\mu$m silicon detector (black line) and 10 $\mu$m SiC detector (red line). The range of the silicon break (magenta line) and the response of the SiC device after $\sim$24 h at rest (green dot) are also indicated.

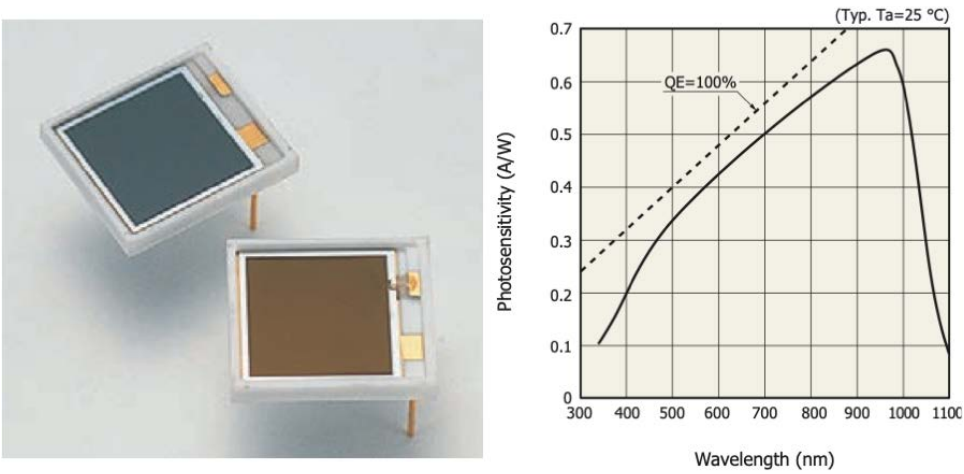


Fig. 51. The S3590 PIN photodiode from Hamamatsu.

performed by means of a PIN photodiode of 1 cm $\times$ 1 cm active area (Hamamatsu S3590-08, Fig. 51 (left)). The main characteristics of this photodetector are listed in Fig. 52, its spectral response is shown in Fig. 51 (right); the quantum efficiency at 540 nm, i.e. at the maximum of the CsI(Tl) emission spectrum, is 90%.

| Type No. | Spectral response range λ (nm) | Peak sensitivity wavelength λp (nm) | Photo sensitivity S λ=λp (A/W) | LSO 420 nm (A/W) | BGO 480 nm (A/W) | CsI(Tl) 540 nm (A/W) | Short circuit current Isc 100 lx (μA) | Dark current ID VR=70 V Typ. (nA) | Dark current ID VR=70 V Max. (nA) | Temp. coefficient of ID TCID VR=70 V (times/°C) | Cut-off Frequency fc VR=70 V (MHz) | Terminal capacitance Ct f=1MHz VR=70 V (pF) | NEP VR=70 V (W/Hz$^{1/2}$) |
|---|---|---|---|---|---|---|---|---|---|---|---|---|---|
| S3590-08 | 340 to 1100 | 960 | 0.66 | 0.20 | 0.30 | 0.36 | 100 | 2 | 6 | 1.12 | 40 | 40 | $3.8 \times 10^{-14}$ |
| S3590-09 | | | | 0.22 | 0.33 | 0.41 | 90 | | | | | | |
| S3590-18 | | | 0.65 | 0.28 | 0.34 | 0.38 | 100 | 4 | 10 | | | | $7.6 \times 10^{-14}$ |
| S3590-19 | | | 0.58 | 0.33 | 0.37 | 0.4 | 86 | | | | | | |

Fig. 52. Electrical and optical characteristics (Typ. $T_a = 25°C$, unless otherwise noted).

A PIN photodiode was coupled with a single CsI(Tl) crystal and exposed to a $^{22}$Na $\beta^+$ radioactive source, which produces gamma rays ($E_\gamma = 511$ keV) due to positron annihilation. The S3590 photodiode, biased at 70 V, was connected to an Ortec 142A preamplifier with a gain $G = 45$ mV/MeV. This value refers to a silicon detector hit by charged particles, where 1 MeV corresponds to $n_e$/MeV $\approx 276243$ electron-hole pairs. The nominal light yield of the scintillator for gamma rays is LY $\approx 50{,}000$ photons/MeV, and assuming a realistic light collection efficiency $\varepsilon_{\text{coll}} \approx 80\%$, given the quantum efficiency QE $\approx 90\%$ of the photodiode, the output signal $S$ is

$$S = \text{LY} \cdot E_\gamma \cdot \varepsilon_{\text{coll}} \cdot \text{QE} \cdot \frac{G}{n_{e/\text{MeV}}} \approx 50{,}000 \cdot 0.511 \cdot 0.8 \cdot 0.9 \cdot \frac{45}{276243} \approx 3 \text{ mV}\,, \quad (1)$$

that is exactly what was found, as shown in Fig. 53. It was not possible to detect the signals corresponding to the second peak of the source at $E_\gamma = 1275$ keV, since

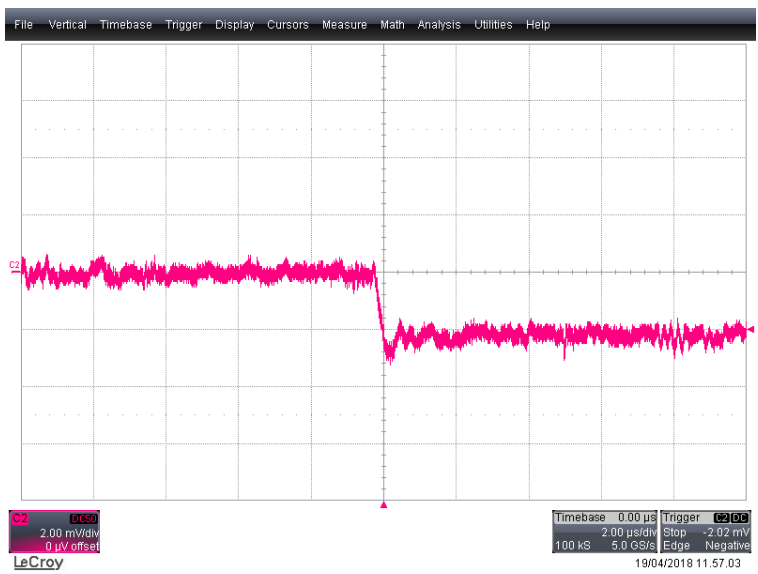


Fig. 53. Sample signal produced by a 511 keV gamma ray in the CsI(Tl) crystal coupled to an S3590 PIN photodiode and an Ortec 142A preamplifier.

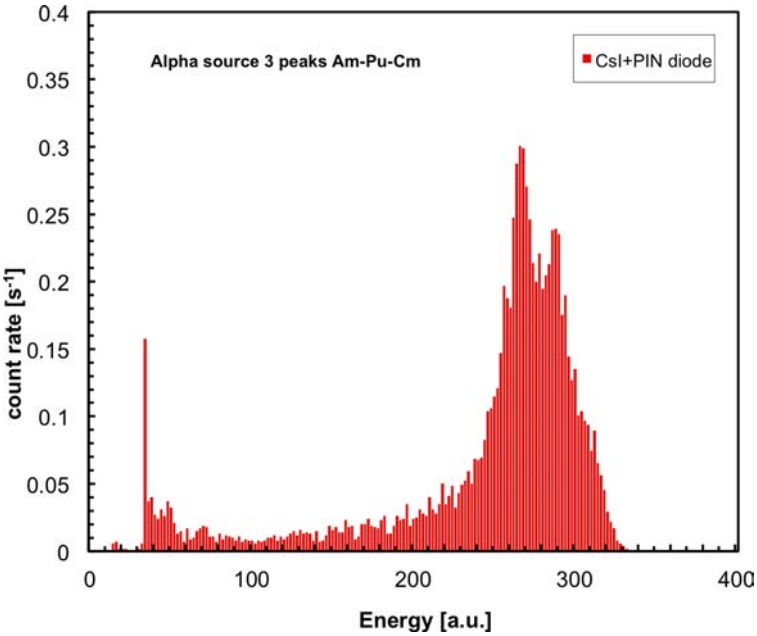


Fig. 54. Energy spectrum acquired with a three-peak Am–Pu–Cm alpha source using the CsI(Tl) + PIN photodiode detector assembly.

the detector is very thin and the full energy efficiency is very low, so the output is not visible at the oscilloscope for that energy. A further test was done with an Am–Pu–Cm alpha particle source. Since the entrance face of the tested crystal was covered with a reflector, a small hole was made in it to allow for the alpha particles to reach the scintillator. The detector was placed under vacuum in front of the source. The preamplifier output signal amplitude was $\approx 13 \div 15$ mV, in line with the expectation (we remark that the light yield of CsI(Tl) for alpha particles is about 30,000 photons/MeV). It was connected to an Ortec 572 amplifier, whose output was sent to a multichannel analyzer. The resulting spectrum, even though the input signals were tiny, has a reasonably good quality, as can be seen in Fig. 54 where two of three expected peaks are clearly distinguished and the third, not resolved, shows up as a bump at higher energy.

The suitability of such a scintillator for the particle identification task in NUMEN requires an energy resolution around 2% for the ion species at the energies of interest. A simple extrapolation, starting from the known features of the detection elements and from the results of the performed tests, shows that such a resolution (or even better) is feasible. Nonetheless, a test under realistic conditions was performed with a beam of $^{18}$O at 15.5 MeV/amu on a Selenium target, in order to prove that the proposed configuration could fulfill its duty. A small telescope was assembled, with a 100 $\mu$m silicon detector placed in front of CsI(Tl) crystal, installed inside the MAGNEX scattering chamber and positioned at 15° with respect

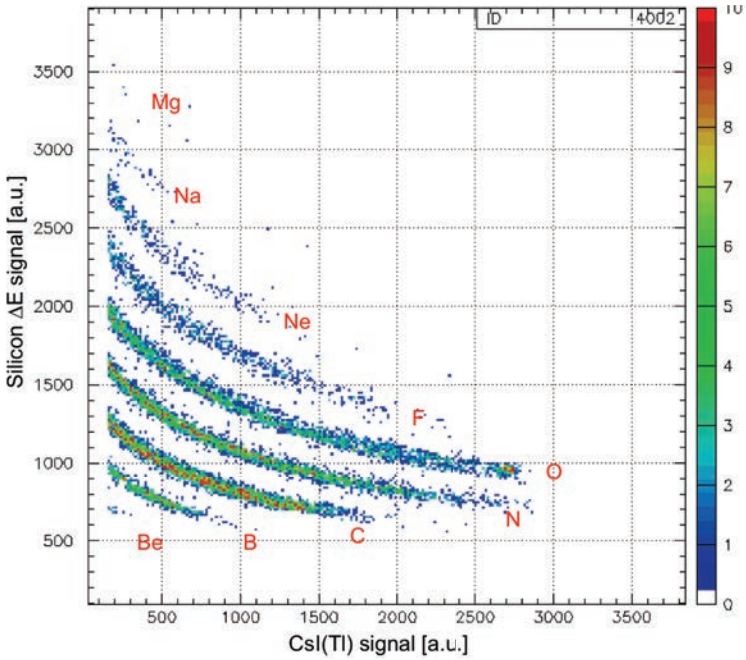


Fig. 55. $\Delta E$ versus $E$ plot obtained with a single element telescope (silicon + CsI(Tl)) (see the text).

to the beam and 20 cm from the target. The resulting plot (Fig. 55) shows an excellent atomic number resolution $\Delta Z/Z \approx 0.16$ in between nine adjacent species detected.

### 5.4.2. *Radiation hardness*

The radiation hardness of the CsI(Tl) crystal was tested under realistic conditions by means of direct irradiation with a heavy-ion beam. A crystal, shown in Fig. 56 (left), was installed in the TeBe test chamber at 0° with respect to the beam line. On the same assembly, just below the crystal, a scintillating alumina with a small hole was installed that was remotely visible by means of a CCD camera (Fig. 56 (right)). This way it was possible to check the alignment and the focusing of the beam, that was later reduced to the desired intensity by means of suitable slits and pepper-pots placed at the exit of the accelerator injector. A histogram of the output amplitude spectrum was produced by reducing the beam intensity to $\approx 10^4$ particles per second (pps) before the irradiation. Then the crystal was irradiated with $7.5 \times 10^{11}$ ions ($^{14}$N at 62.5 MeV/amu), and finally the same histogram was produced after reducing the beam intensity to $\approx 10^4$ pps. No amplitude drift nor resolution loss were observed, thus implying that the central part of the PID, which is subject to the highest particle rate, should be operational at least for about 7 years experiments assuming 120 beam days per year.

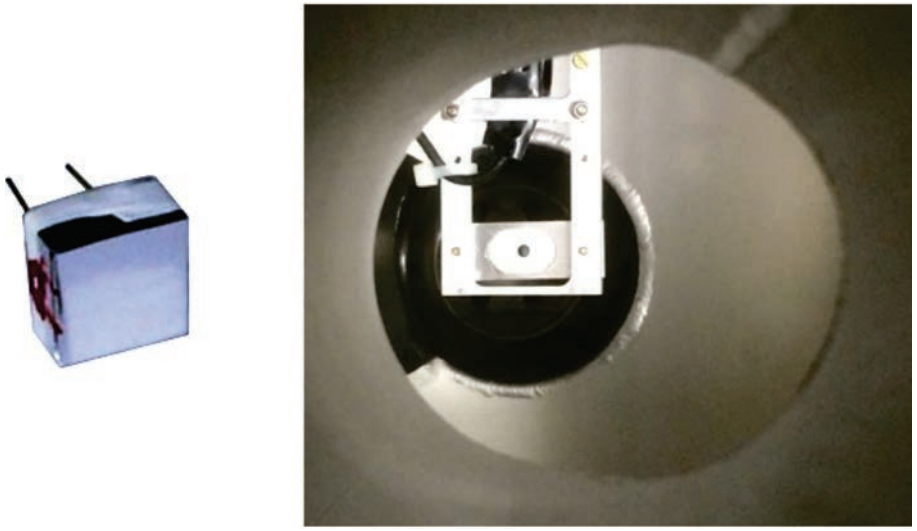

Fig. 56. Left: the CsI(Tl) crystal used for the radiation hardness test. Right: the mechanical support hosting the crystal and an alumina beam monitor to check the beam alignment and focusing.

### 5.5. *Particle identification tests*

A study of the response of some $\Delta E - E$ telescopes composed by SiC and CsI(Tl) detectors in various configurations to fragments produced in nuclear interactions is presented in Ref. 78. Two identification methods were used and their performance discussed: the $\Delta E - E$ technique and the Pulse Shape Analysis technique (for identification of nuclear fragments stopped in a single SiC layer). Identification capabilities similar to those obtained with the best available silicon detectors have been found for the SiC detector prototypes. In particular, the test reported in Ref. 78 was performed using beams of $^{40}$Ca and $^{48}$Ca at 40 AMeV impinging on a thin $^{12}$C target. Among the different telescope configurations, they tested a two-stage SiC–CsI(Tl) telescope in which the SiC is 100 $\mu$m thick with an active area of $1 \times 1$ cm$^2$, very similar to the one that will be used in NUMEN. The $\Delta E - E$ correlation plots reported in Ref. 78 demonstrated the capability of the SiC–CsI telescope to clearly identify the charge of the ions up to $Z \approx 20$. This result confirms the suitability of such telescope for the NUMEN experiments, in which the ejectiles of interest are typically in the region of atomic number $4 \leq Z \leq 12$.

However, the identification capabilities in terms of mass have also to be tested (mass range for NUMEN $10 \leq A \leq 25$). To test the feasibility of the telescope, also for the mass identification, a specific setup in which the telescope is coupled with the magnetic field of the MAGNEX spectrometer is necessary. Indeed, the mass identification technique used in MAGNEX exploits the properties of the Lorentz force, as it was introduced in Ref. 65. When dealing with a large acceptance device as MAGNEX, the best resolution in the identification technique is achieved performing

a precise reconstruction of the ions kinetic energy, as demonstrated in Ref. 65. However, when a high mass resolution is not necessary, as in the experimental conditions of the NUMEN reactions, which involve oxygen, fluorine and neon ions, the identification procedure is successfully performed using the correlation between the horizontal position at the focal plane ($X_{\rm foc}$) and the residual energy measured by a stop detector ($E_{\rm resid}$). The relationship between the two measured quantities ($X_{\rm foc}$ and $E_{\rm resid}$) is approximately quadratic with a factor depending on the ratio $m/q$

$$X_{\rm foc} \propto \frac{\sqrt{m}}{q}\sqrt{E_{\rm resid}}\,. \tag{2}$$

Therefore, in a $X_{\rm foc}$ versus $E_{\rm resid}$ plot the ions are distributed on different *loci* according to the ratio $\frac{\sqrt{m}}{q}$.

A feasibility test was performed with a $^{20}$Ne CS beam at 20 AMeV impinging on a $^{12}$C thin target. The MAGNEX spectrometer was placed with the optical axis at 10° with respect to the beam direction. A SiC–CsI(Tl) telescope was placed at the focal plane of MAGNEX, replacing one of the silicon detectors currently in use (thickness 1000 $\mu$m, area $5 \times 7$ cm$^2$). In order to compare the results of the new detector with the actual one, some silicon detectors were mounted next to the telescope.

The SiC–CsI telescope was composed by

- a SiC detector, 10 $\mu$m epitaxy thickness +100 $\mu$m substrate, area $1 \times 1$ cm$^2$ reverse mounted, biased at −50 V;
- a CsI(Tl) crystal, 5 mm thickness, area $1 \times 1$ cm$^2$, read-out by means of
- an Hamamatsu S3590-08 photodiode, area $1 \times 1$ cm$^2$, biased at −70 V.

The signal of the MAGNEX silicon detectors was sent to standard preamplifiers with 5 mV/MeV gain, placed inside the FPD chamber, then to charge amplifiers with 500 ns shaping time and peak sensing VME ADCs. The signals from the SiC and the photodiode were sent to the same kind of preamplifiers with 45 mV/MeV gain placed outside the FPD chamber and then to the same kind of amplifiers and ADCs. The trigger of the acquisition was done with a logical *OR* between the silicon and the CsI signals.

Typical results obtained with the MAGNEX FPD in the actual conditions are shown in Figs. 57 and 58. In particular, the $\Delta E - E$ correlation plot is obtained from the energy loss ($\Delta E_{\rm tot}$ in Fig. 57 (upper panel) in the gas section of the FPD, taken from the proportional wires, whereas the residual energy is measured from a silicon detector ($E_{\rm resid}$ in Fig. 57 (upper panel)). After a linearization of the $\Delta E - E$ plot and a calibration in charge it is possible to obtain the histogram shown in Fig. 57, from which a resolution of $\Delta Z/Z \sim 2.6\%$ FWHM is obtained. The correlation plot shown in Fig. 58 (upper panel) is obtained looking at the horizontal position measurement $X_{\rm foc}$ and the $E_{\rm resid}$ measurement, after a graphical selection of the oxygen ions in Fig. 57 (upper panel). These two quantities are related as indicated from Eq. (2), thus it is possible to distinguish different oxygen isotopes

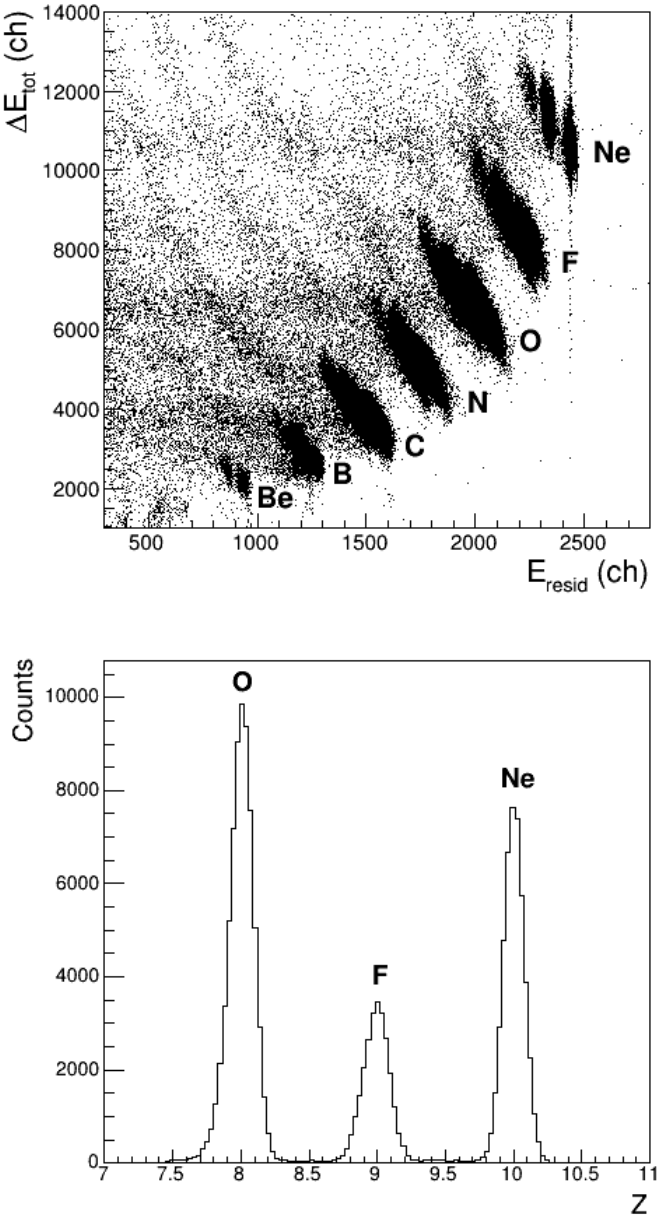


Fig. 57. Upper panel: $\Delta E_{\rm tot} - E_{\rm resid}$ correlation for a single silicon detector measured in the $^{20}$Ne+$^{12}$C reaction at 400 MeV. Lower panel: Nuclear charge histogram obtained after calibration from a linearization of the $\Delta E - E$ correlation of the upper panel in the region of interest.

in the plot of Fig. 58 (upper panel). From a linearization and a mass calibration we obtain the histogram shown in Fig. 58 (lower panel), from which a mass resolution $\Delta A/A \sim 0.9\%$ is obtained.

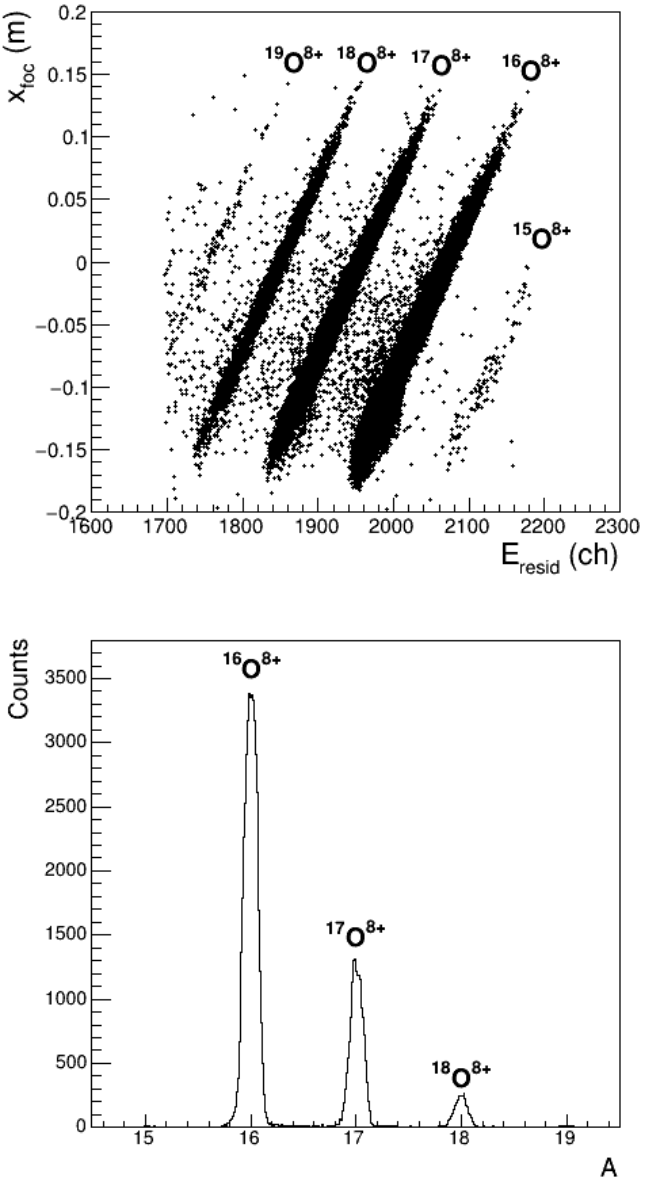


Fig. 58. Upper panel: $X_{\rm foc} - E_{\rm resid}$ correlation for the same silicon detector of Fig. 57 with a selection on the oxygen region. Lower panel: Mass spectrum obtained after calibration and linearization of the plot in the upper panel.

The same plots were obtained from the SiC–CsI telescope and the results are shown in Figs. 59 and 60. In this case the $\Delta E$ is taken from the SiC detector, whereas the $E_{\rm resid}$ one from the CsI stop detector. Using a similar linearization and calibration procedure we obtained the charge and mass spectra shown in

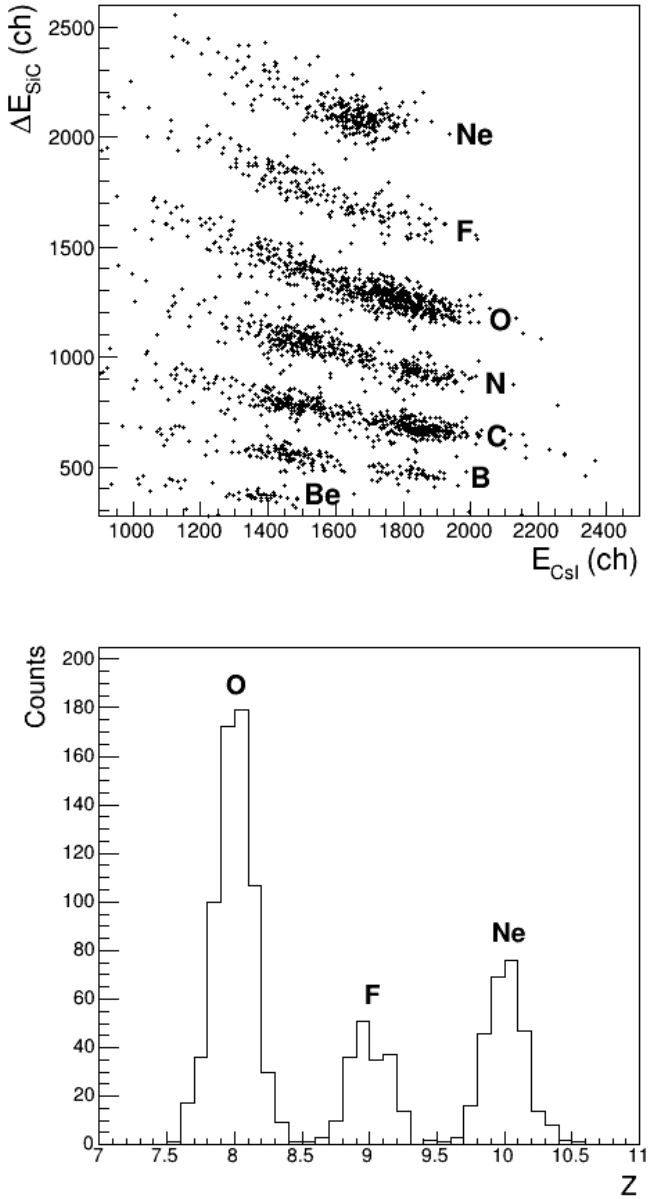


Fig. 59. Upper panel: $\Delta E - E$ correlation from the SiC–CsI telescope measured in the $^{20}$Ne+$^{12}$C reaction at 400 MeV. Lower panel: Nuclear charge histogram obtained after calibration from a linearization of the $\Delta E - E$ correlation of the upper panel in the region of interest.

Figs. 59 (lower panel) and 60 (lower panel), from which the obtained resolutions are $\Delta Z/Z \sim 4.1\%$ and $\Delta A/A \sim 2.1\%$. The worse values obtained using the SiC–CsI telescope with respect to the actual MAGNEX PID are not surprising, since it is well known that the resolution of the CsI is worse than the one of silicon detectors,

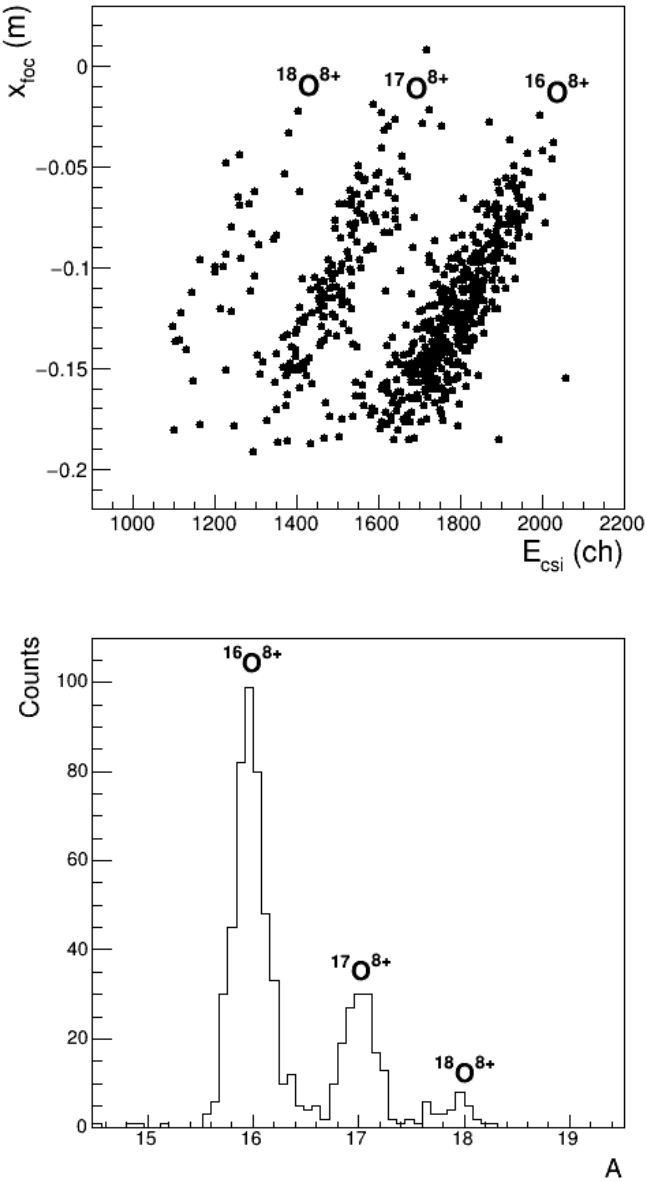


Fig. 60. Upper panel: $X_{\rm foc} - E$ correlation from the SiC–CsI telescope with a selection on the oxygen region in the plot of Fig. 59. Lower panel: Mass spectrum obtained after calibration and linearization of the plot in the upper panel.

but it is important to note that the obtained values are good enough to clearly identify the ions of interest both in charge and mass. Moreover it should be considered that the charge resolution could be improved using the 100 $\mu$m SiC detector in which the energy loss will be sensibly higher.

## 6. G-NUMEN, the Gamma Array

### 6.1. *Introduction*

In the last years, within the framework of NUMEN Phase 2, a feasibility study of a calorimeter for gamma rays to be detected in coincidence with the DCE ejectiles has also been performed. Differently from the other R&D activities described in the other sections of this paper, this study has been based on analytical models, simulations and experimental tests limited to at-home available equipment, without a dedicated financial budget. The essential part of the project for a calorimeter for NUMEN (G-NUMEN) is based on challenging experimental conditions dominated by a very high rate of signals coming from the projectile target interactions over which distinguish very few good DCE events in the region of interest. Radiation damage issues are also relevant in these conditions. Thus a key aspect of this study is based on accurate simulations of the foreseen harsh experimental conditions, which severely limit the choice of available technologies. We will show in this section that the use of an array of about 100 $LaBr_3$(Ce) 1500 $cm^3$ scintillators will make it possible to disentangle within a tolerable accuracy the transition to ground from that to excited states in DCE reaction channel. The implementation of G-NUMEN will allow to significantly improve the overall NUMEN discovery potential.

### 6.2. *Statement of the problem*

#### 6.2.1. *Introduction*

The nuclear transitions to be studied in the NUMEN project involve deformed and nondeformed nuclei which will be populated by means of the DCE or competing reactions. For nondeformed target nuclei and at low reaction energies, the energy resolution of MAGNEX with beams provided by the CS (about 0.2%) is sufficient to discriminate between the ground state $\left(I^{\pi} = 0^{+}\right)$ and first excited states $\left(I^{\pi} = 2^{+}\right)$ of both projectile-like and target-like species. However, for nuclei of interest in moderately and strongly deformed mass regions, such as $^{110}$Pd, $^{150}$Nd and $^{160}$Gd, and in all cases at high reaction energies, the energy spectra at the focal plane alone cannot resolve between states of the reaction products. In such cases a gamma detector array has been considered as an ancillary device to the magnetic spectrometer providing the necessary discrimination between nearby energy states.

Due to the high beam intensities to be used in the DCE experiments, the target region will become a very strong source of radiation, including gamma rays, fast neutrons, electrons, light and heavy ions. The charged particles as well as the low energy X-rays can be absorbed by a sufficient amount of solid material between the target and the array. Inorganic scintillators are normally quite tolerant to gamma and fast neutron radiation and are chosen to be the best candidates for the detector gamma-ray energy sensitive materials. Some inorganic scintillators, such as $LaBr_3$(Ce), $CeBr_3$, LYSO(Ce) and GAGG(Ce) were considered as possible candidates to be employed in the gamma array.

#### 6.2.2. *Energy resolution and photopeak efficiency*

Typical energy resolutions from 3–30%, depending on the gamma-ray energy and inorganic scintillator material, are sufficient to discriminate between low-lying gamma transitions of interest even in the worst cases of strongly deformed nuclei, such as $^{160}$Gd, with the first excited state at an energy of 75.3 keV and second excited state at 248.5 keV above the ground state. A high photopeak efficiency is desirable, however, which can be achieved with the highest density and effective atomic number materials.

#### 6.2.3. *High count rates versus low signal cross-section*

The gamma emission rates expected for the typical NUMEN Phase 4 experiments can reach the order of magnitude of GHz. In addition to that, a comparable amount of neutron production is expected, which could also leave signals in the gamma detectors. This means that the individual detector element solid angular coverage has to be kept small in order to avoid count rate levels leading to significant pulse pile-up probabilities. The DCE cross-sections, in contrast to that, are extremely rare, and therefore, a large array efficiency is required, with a high granularity. It is expected that photopeak efficiencies of about 20%, at least for the relatively low energies, adequate granularity and reasonable cost can only be achieved with the use of hundreds of scintillator crystals with widths in the 2–4 cm range.

#### 6.2.4. *Random coincidence background*

At the expected high reaction rates ($10^7$–$10^8$ Hz), possibly reaching or exceeding 1 nuclear reaction per cyclotron beam bunch, the main source of background will come from random coincidences of signals from reactions other than the DCE of interest. A timing resolution capable of clearly separating the events generated in subsequent cyclotron beam bunches (20–50 ns, corresponding to 60–15 MeV/A beam energies, respectively) is therefore mandatory. A gamma-particle coincidence time resolution of a few ns is therefore sufficient for this purpose and should be easily achieved with inorganic scintillators. With a typical beam bunch time width of 1–2 ns, however, it is technically hopeless to accomplish the discrimination of events generated by a pair of reactions occurring with beam particles from the same bunch, due to MAGNEX time resolution limitations originated in the projectile-like fragment (PLF) trajectory time variations. Based on Poisson statistics, it is possible to evaluate the uncertainty of the cross-section measurement originated by this type of background.

#### 6.2.5. *Statistical observational limits*

**Definition of observational limit.** The "observational limit" is a concept that evaluates the power of a gamma spectrometer. It is the lowest fraction of the signal

cross-section, relative to the total reaction cross-section, which can be measured by the spectrometer in a given experiment:

*Observational limit*:

$$\alpha_{\rm lim} = \frac{\sigma_{\rm min}}{\sigma_R} \,. \tag{3}$$

By being *measured*, it is meant that the cross-section of the reaction of interest (e.g. the DCE cross-section to the $0^+$ g.s.) has been obtained in the experiment with a minimum acceptable relative uncertainty, $u_{\rm rel}$. For example, if an uncertainty of $u_{\rm rel} = 10\%$ is required and there is no background, the spectrometer should be able to collect at least 100 signal counts in the course of the experiment. In this case, the relevant parameter of the spectrometer is its signal counting efficiency. In practice, however, there are background counts present together with the signal, and the power of the spectrometer in reducing this background becomes also an important concern in order to achieve the required precision of the measurement. The actual observational limit depends not only on the characteristics of the spectrometer itself, but also in the specific reaction to be measured, time duration and other characteristics of the experiment to be performed.

In the following paragraphs we will develop the theory to determine the observational limit in two different analysis modes: the "clean" mode, in which the data analysis is made with a condition in gamma sum energy and fold of the event, and the "dirty" mode, in which these conditions are not imposed.

**The "clean" mode.** At not too high beam energies, a typical nuclear reaction event has a moderate or high neutron and gamma multiplicity and total energy, while the DCE produces no neutrons, has low gamma multiplicity, and low total energy. Then, it should be possible to infer, from the coincidence data of a high efficiency calorimeter with the DCE PLF, analyzed by MAGNEX, that, an "other than DCE" reaction has occurred within the same beam bunch together with the DCE (by gating on multiplicity and total energy). If these events are discarded we will end up with only "clean" events, at the expense of rejecting some DCE gamma decay events. If we assume that the array has a total efficiency $\varepsilon_\gamma$ (for the decay from the excited state, e.g. the TLF $2^+$ state, formed with minimum DCE cross-section $\sigma_2$), the probability of detecting the "clean" DCE events is equal to the probability of detection $\varepsilon_\gamma$ times the probability that no other reaction has occurred, which, from Poisson statistics, is $e^{-\bar{k}}$ (where $\bar{k} = \frac{L\sigma_R}{f_c}$ is the average number of reactions per cyclotron beam bunch with frequency $f_c$, and total luminosity $L$). In general, the number of reactions of a given kind, during an experiment with time duration $T$, is related to the cross-section by: $N = L\sigma T$, where $L$ is the luminosity. Therefore, the observational limit for the first DCE excited state can be written as: $\alpha_2 = \frac{\sigma_2}{\sigma_R} = \frac{N_2}{N_R}$. Neglecting background, the square of the required relative uncertainty $u^2$ in a gamma peak is the inverse of the number of counts. For the first excited state transition from DCE: $u_2^2 = \frac{1}{A_2}$, where $A_2 = N_2\varepsilon_\gamma e^{-\bar{k}}$ is the peak area, $\varepsilon_\gamma$ is the gamma-ray detection probability (or efficiency for the

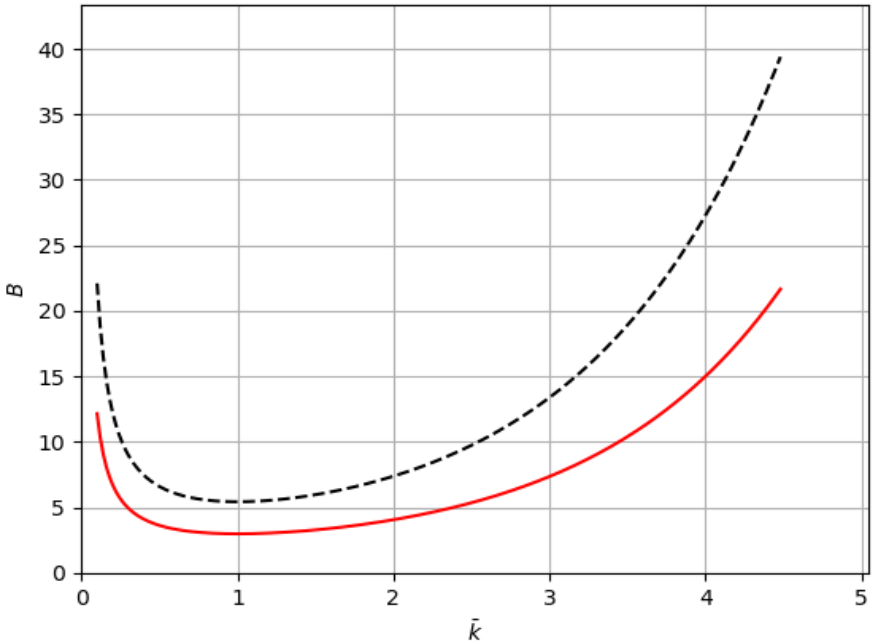


Fig. 61. Reduced observational limits in the "clean" mode as a function of $\bar{k}$ (solid: g.s., dashed: first excited state).

$2^+ \rightarrow 0^+$ transition), in a clean event (no nuclear reaction other than DCE, which occurs with probability $e^{-\bar{k}}$). From these relations one gets the observational limit: $\alpha_2 = \frac{N_2}{N_R} = \frac{e^{\bar{k}}}{u^2 \varepsilon_\gamma f_c \bar{k} T}$. Factoring out the $u^2 f_c T$ parameter combination (which is independent of the spectrometer characteristics), one can define a "reduced" observational limit function $B_2(\bar{k}) = \frac{e^{\bar{k}}}{\bar{k}\varepsilon_\gamma}$, which is related to spectrometer parameters. The efficiency $\varepsilon_\gamma$ is, however, assumed to be sufficiently large to identify the occurrence of a non-DCE reaction by total energy and/or multiplicity with nearly 100% probability (for small arrays this is not an appropriate assumption). Similarly, one can define a reduced observational limit (ROL) for the ground state (minimum) DCE cross-section $\sigma_0$, which with some algebra, can be shown to be: $B_0 \equiv \frac{\sigma_0}{\sigma_R} = [\varepsilon_\gamma + f(1-\varepsilon_\gamma)]B_2(\bar{k})$, where the new parameter $f = \frac{\sigma_2}{\sigma_0}$ is the ratio of the two DCE cross-sections. Figure 61 shows the reduced observational limits for the $2^+$ (dotted line) and $0^+$ (g.s. — continuous line) states for $f = 0.1$, $\varepsilon_\gamma = 0.5$ as a function of $\bar{k}$ (note that for $f = 1$ or $\varepsilon_\gamma = 1$ both limits are identical).

As it can be seen, the absolute observational limit of the spectrometer occurs at exactly $\bar{k} = 1$ in both cases. There is no improvement going beyond this beam intensity. This is because, although the population rate of each state increases linearly with $\bar{k}$, the probability of data contamination increases exponentially.

For reference, a reduced observational limit of 5 corresponds to $\alpha_{\rm Lim} \approx 10^{-11}$ for a one-week experiment ($T = 6 \times 10^5$), with a 20% uncertainty ($u = 0.2$) requirement

in the measurement, and with cyclotron beam bunch frequency $f_c = 20$ MHz. This, in turn, for a typical total reaction cross-section of $\sigma_R = 3b$, corresponds to a sensitivity to cross-sections as low as 30 Pb.

In this simplified model the main assumptions which can be checked with simulations are the following:

(1) There is 100% probability of identifying a non-DCE reaction contamination within the same bunch (in practice this should be less, but not small) in the PLF-gamma coincidence event. The simulations, that will be described in the following sections, allow to evaluate this probability to be 95.7% for the $^{20}$Ne + $^{116}$Cd system at 15 AMeV by gating on gamma-fold less than 3 and total energy less than 2 MeV. Nevertheless, the efficiency for the collection of the 463 keV transition from the second $0^+$ state populated by DCE gets reduced to 30% of what it would be without conditions.
(2) The "internal" background of the DCE gamma spectrum, coming mostly from Compton events, is negligible. This is corroborated by the simulation results presented in Subsec. 6.4.5. Other sources of background (BG) are also negligible, in the coincidence event, such as natural background and radioactivity build up inside the experimental hall due to unshielded radioactive fragment decay, or neutron-induced reactions in surrounding material, randomly detected within the few ns coincidence time window.
(3) The energy resolution of the gamma spectrometer is sufficient to clearly separate neighboring DCE excited states. As long as this can be accomplished, the value of the energy resolution is irrelevant to the measurement. If the Compton background is not negligible (assumption (2) not valid), though, some background will be present under the photopeak. The resolution of the detector in this case becomes relevant as the amount of background will increase with the peak width. However, as long as this background continues to be small, which happens with high photopeak efficiency detectors, the contribution to the total uncertainty continues to be dominated by the overall statistics, and the energy resolution of the detectors are only mildly relevant.

The relaxation of any of these conditions, of course, worsens the sensitivity of the measurement. The practical situation could be quite far from this ideal case, the purpose of which is to illustrate the origin of the major limitations in this type of experiment.

**The "dirty" mode.** In the "clean" mode, some DCE data is lost due to the presence of a non-DCE reaction within the same coincidence time window. Part of these events could be accepted, namely those which do not contribute with signals within the interest gamma transition energy window. We can, then, discard only these events which do not have such signals, increasing the DCE counting statistics. This is the "dirty" mode, since the accepted events are not composed from DCE reaction signals only.

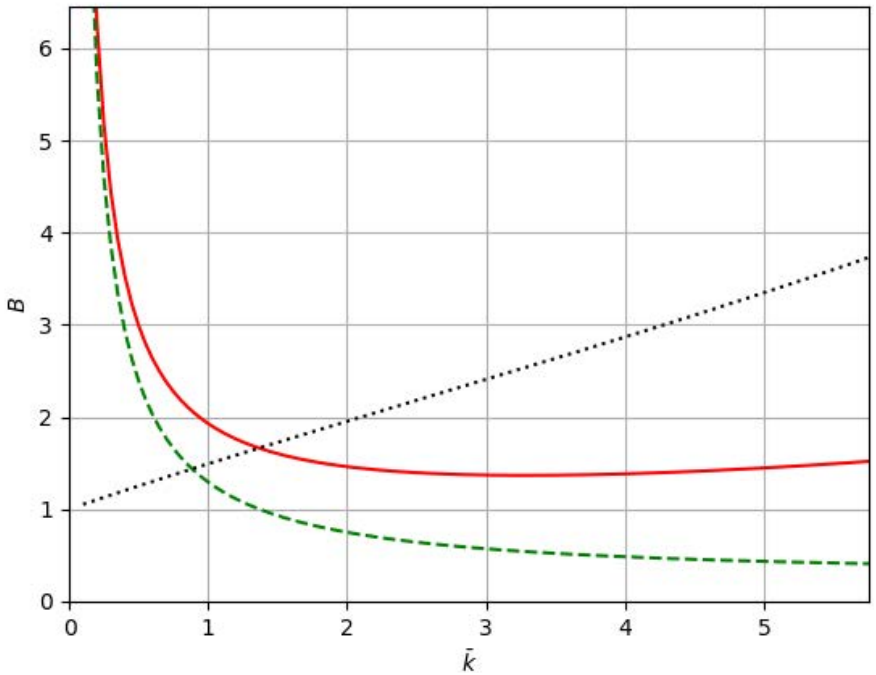


Fig. 62. Reduced observational limits in the "dirty" mode as a function of $\bar{k}$ for the g.s. Solid: LYSO(Ce) typical energy resolution; dashed: $LaBr_3$(Ce) typical energy resolution; dotted: ratio between the two.

In order to determine the observational limit in this mode, one has to evaluate the probability that a background signal within the energy window of the transition of interest is randomly generated. This could happen either because there are other nuclear reactions that produce gamma rays around this energy window, or that Compton scattering from higher energy gamma rays produces this signal. An additional parameter $p_{\rm BG}(E_\gamma)$ can be introduced in this more general model: the probability density of a signal with energy $E_\gamma$ (per unit energy interval), which, together with the gamma energy resolution $\Delta E_\gamma$, now play a relevant role. An analytical expression can be found for the reduced observational limits in this new model (with the additional assumption that $p_{\rm BG}(E_\gamma)\Delta E_\gamma$ is not close to 1), and the results can be appreciated in Fig. 62. The results for $B_0$ (the g.s. ROL) are shown for two different detector energy resolutions ($\Delta E_\gamma = 24$ keV — continuous line, and $\Delta E_\gamma = 6$ keV — dashed line). The following parameters: $f = 0.1$, $\varepsilon_\gamma = 0.5$, $p_{\rm BG}(E_\gamma) = 0.015$/keV have been assumed. The dotted line is the improvement ratio between the different energy resolutions.

One can see that in this case the beam intensity can be increased beyond the limit of $\bar{k} = 1$ with improvement of observational limit. However, it remains of the same order of magnitude, except for the best resolution case and at very high beam currents, which become prohibitive due to other effects which have been neglected,

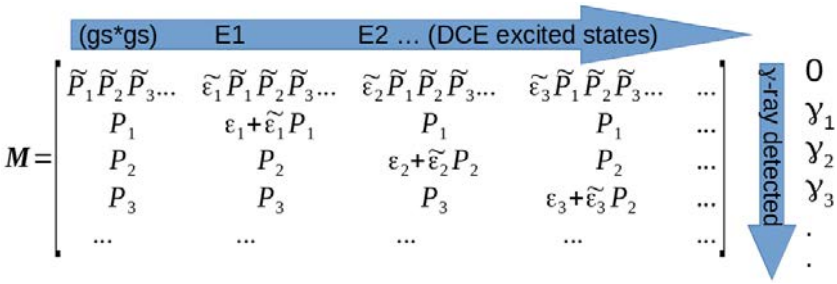


Fig. 63. Matrix which relates the experimental data to actual production of DCE states.

such as pile-up of signal pulses. If one remains in the $\bar{k} \approx 1$ region, these effects are still rather small. The improvement in observational limit, corresponding to the factor of 4 in energy resolution, is only a factor of 2, indicating that comparatively low resolution detectors remain competitive.

In the real cases more than one transition from excited DCE states from the PLF and TLF could be present, and the energy resolution of the PLF are affected by Doppler broadening. The relation of the experimentally extracted peak areas in PLF-$\gamma$ coincidence spectra $(A_0, A_1, A_2, \ldots)$, were $A_0$ is for anticoincidence with all DCE gamma rays, and $A_i$ is for coincidence with a specific gamma transition of state $i$, can be expressed in a matrix form:

$$\boldsymbol{A} = \boldsymbol{M}\boldsymbol{N}\,, \tag{4}$$

where the matrix $\boldsymbol{M}$ is related to the total photopeak efficiency $\varepsilon_i$, and $P_i$, the probability of one or more false counts in the gamma energy gate due to the background accidental coincidence with other than DCE reaction within the same beam bunch. The actual number of DCE states populated in the reaction is given by $\boldsymbol{N}$. A typical form of the $\boldsymbol{M}$ matrix is presented in Fig. 63. The tilde mark represents the complement ($\tilde{\varepsilon} = 1 - \varepsilon$ and $\tilde{P} = 1 - P$). In order to obtain the cross-sections and respective statistical uncertainties this matrix formula is inverted. This relation is useful to obtain also the predicted relative uncertainties from the simulated parameters of efficiency and background of a specific array and reaction.

### 6.3. *General design choices*

#### 6.3.1. *Choice of scintillator crystal*

**Characteristics of selected scintillator types.** The choice of the inorganic scintillator crystal material is of paramount importance for the performance of the gamma array. Several possibilities have been considered among which the most appropriate presently available in the market are LYSO(Ce), $LaBr_3$(Ce) and $CeBr_3$. LYSO(Ce) has the advantage of not being hygroscopic, and having the highest density ($\rho = 7.1$ g/cm$^2$) and effective atomic number ($Z \approx 65$), which translates, typically, in twice the photopeak efficiency (for the same crystal volume) around the

1 MeV range in comparison to the other two: $LaBr_3(Ce)$ ($\rho = 5.1$ g/cm$^2$, $Z \approx 46$), $CeBr_3(\rho = 5.2$ g/cm$^2$, $Z \approx 47$). However, the gamma-ray energy resolution of LYSO(Ce) is a factor of 3–4 worse than the other two, (which are comparable among themselves), $LaBr_3(Ce)$ being the best in this respect. LYSO(Ce) has also the disadvantage of having an intense intrinsic radioactivity (280 Bq per cubic cm), but which can be tolerated in time coincidence measurements. The scintillation decay time of these materials is in the range from 15–50 ns, $LaBr_3(Ce)$ being near the lowest extreme and LYSO(Ce) near the highest, all of which, however, very satisfactory for the present application which requires timing resolutions below a few ns.

High radiation tolerance to gamma rays and neutrons is also a requirement which is met by these types of materials. Other types of scintillators such as GAGG(Ce), which has interesting properties in some other respects, are too sensitive to neutrons due to its Gadolinium component. Semiconductors are, of course, ruled out due to crystal lattice structure radiation damage among other effects. As we shall see, energy resolution is important at the very high rates, where the random background, and not the production statistics, raises the observational limit of the spectrometer. For this and also foreseeing possible other types of applications rather than measurement of DCE cross-sections, $LaBr_3(Ce)$ was chosen as the scintillator crystal material for the array.

### 6.3.2. *Array granularity*

Detector size is a compromise between several factors: full energy absorption within the crystal volume, which requires larger crystals, pile-up loss at high count rates and Doppler broadening of projectile-like fragment gamma transitions, both of which improve with smaller detector entrance solid angles, and, ultimately, cost (which requires limited total crystal volume). Detailed response simulations of the system will be reported in the following section which will allow for a well-founded choice of the crystal dimensions. The practical compromise is the use of 38 mm diameter $LaBr_3(Ce)$ crystals with 5 cm length.

### 6.3.3. *Total solid angle coverage*

DCE reactions states are populated with very low reaction cross-sections. Their values are of course unknown, but a typical cross-section of a few nb can expected, based on preliminary measurements and theoretical estimates, and even below this value in some cases. The gamma-ray efficiency has, therefore, to be as large as possible, requiring maximum possible solid angle coverage. The gamma array, however, has its available space limited by the scattering chamber requirements, and only about 20% of the total solid angle is actually available for placement of the scintillation detectors.

## 6.4. *GEANT4 simulations*

### 6.4.1. *Introduction*

A special simulation procedure has been developed for the type of experiment foreseen in the advanced phase of the NUMEN project. First, the reaction, defined by the entrance channel and its various most probable exit channels are simulated with the GEANT4 Hadrontherapy model.[79–81] An imaginary detector spherical surface of $\sim 10$ cm diameter around the target is included, collecting all the information of each particle which traverses it (the "PhaseSpace"). The information of particles remaining in the target and backing are also preserved to allow for further evaluation of the activation. The second step is the simulation of the gamma array response to the PhaseSpace particles. In this step, the information of the interactions with each detector is registered. The final step is the simulation of the response of the array to the gamma transition decay from the excited states of the DCE reaction (GEANT4 radioisotope option), from the TLF and the PLF. The PLF requires the inclusion of the motion of the source, with its estimated flight velocity, which causes the Doppler shift effect and Doppler broadening of the spectral lines due to the finite opening of the detectors.

After these steps, the response of the gamma array from steps 2 and 3 is combined with statistical weights based on the Poisson probability distribution of the occurrence a number of other reactions in the same beam bunch, depending on the beam intensity. The PhaseSpace step 1 can be reutilized for the simulation of different detector and array geometries, as well as the scattering chamber thickness and other intervening objects such as the target frame, which cause absorption and scattering of gamma rays and neutrons, and also secondary radiation produced by other particles. The imaginary detector surface can be arbitrarily shrunk according to the needs of the subsequent simulation.

### 6.4.2. *Detector response*

Figure 64 presents the simulation of the energy spectrum of a $LaBr_3$(Ce) scintillator in response to gamma rays from a calibration source. The simulation includes the intrinsic radiation of the detector, and shows good agreement with experiment.

Figure 65 presents the simulated intrinsic photopeak efficiency $\varepsilon_{\rm ph}$ and peak-to-total ($P_T$) values as a function of energy for a $LaBr_3$(Ce) detector of 38 mm diameter and 50 mm length. Figure 66 shows schematically the relative intrinsic energy resolution used in the simulations for this type of detector. It is a parametrization based on values of the literature.[82]

### 6.4.3. *Typical particle production and spectra*

Figure 67 shows typical particle ($\gamma$ and $n$) production multiplicity spectra and Fig. 68 the energy and time spectra of the $^{20}$Ne+$^{116}$Cd reaction at 230 MeV, assuming a 1.4 mg/cm$^2$ target thickness, both without and with a 1.0 micron carbon

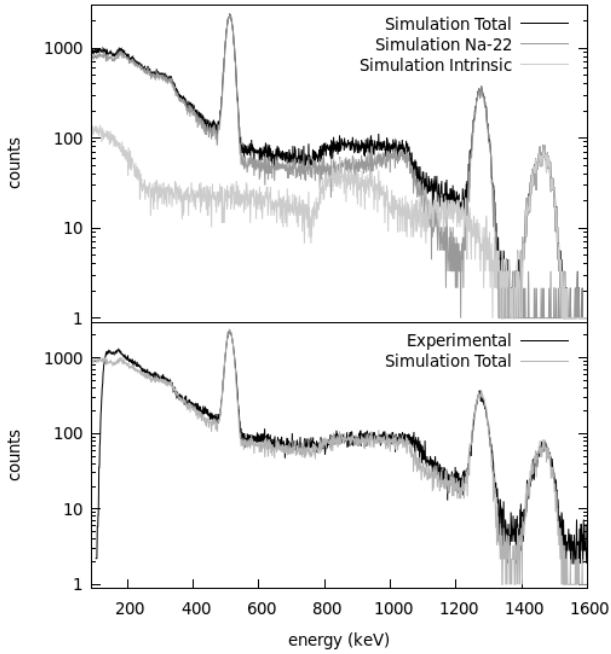


Fig. 64. GEANT4 simulation of total energy deposition in comparison to data from a $^{22}$Na calibration gamma source measured with a 38 mm diameter by 38 mm length $LaBr_3(Ce)$ crystal with PMT read-out. The top panel shows the total and the separate components from the calibration source and from the intrinsic detector radiation from the $^{138}$La isotope as obtained from the simulation, and the bottom panel the comparison to the experimental data.

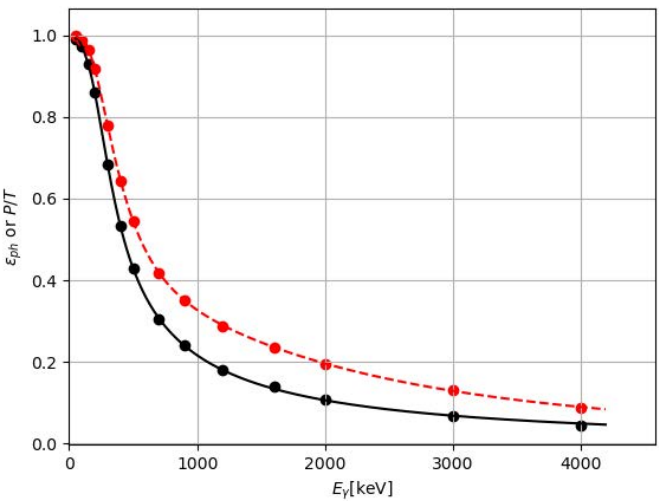


Fig. 65. (Color online) Simulated intrinsic photopeak efficiency (black dots) and peak/total ratio (red dots) for $LaBr_3(Ce)$ detector with a crystal size of 38 mm diameter and 50 mm length as a function of the gamma ray energy in keV. A parametrized empirical formula is adjusted to the data points.

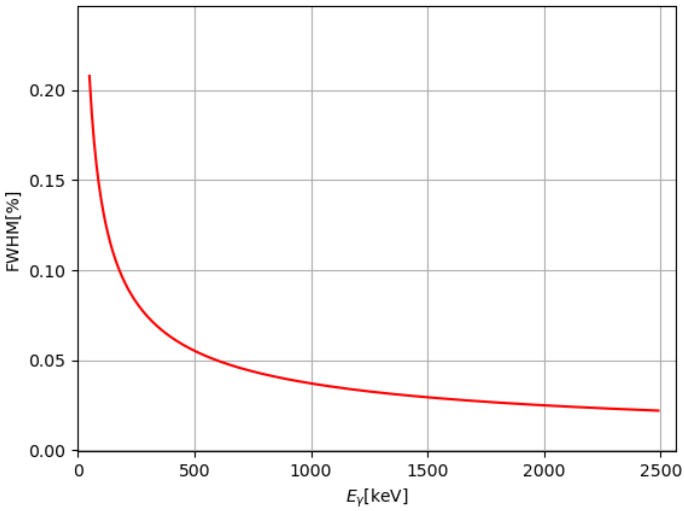


Fig. 66. Relative energy resolution FWHM (in %) as a function of the gamma ray energy (based on Ref. 82) assumed for $LaBr_3(Ce)$ simulations.

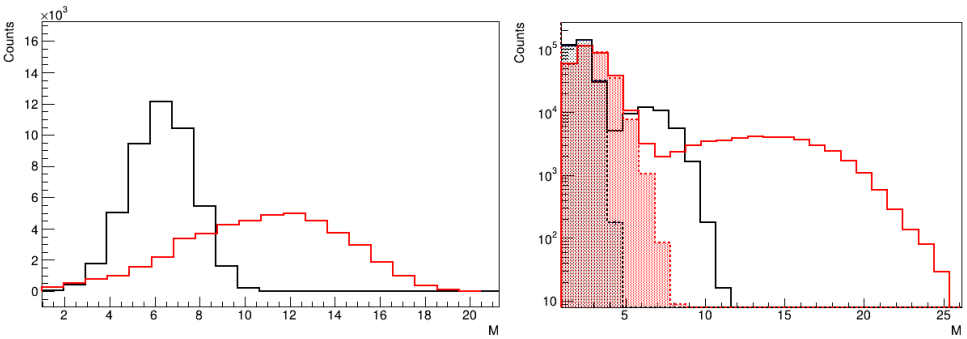


Fig. 67. (Color online) Simulated gamma (red) and neutron (black) emission multiplicity spectra from the $^{20}Ne + ^{116}Cd$ reaction at 230 MeV. Left: $^{116}Cd$ target only, right: $^{116}Cd$ target + carbon backing, shaded: backing only. Number of primaries: $2 \times 10^9$.

backing foil, necessary for target cooling at high beam currents. These results were obtained from the PhaseSpace step using $2 \times 10^9$ primaries. In the multiplicity spectra it can be seen that the reaction with the Cd target produces high gamma multiplicity events, with a peak around $M = 12$, and neutron events with moderately high multiplicity with a maximum probability at $M = 6$. When the C backing is introduced, a clearly separate distribution with lower multiplicity (around 3 for gammas and 2 for neutrons) is superposed to the original spectrum from the target. In the planned experiments a lower thickness of C backing (by a factor of $\approx 5$) and also lower thickness of target (by a factor of $\approx$ 2–3) are envisaged. The thicker values used in the simulation serve to speed up the computing time.

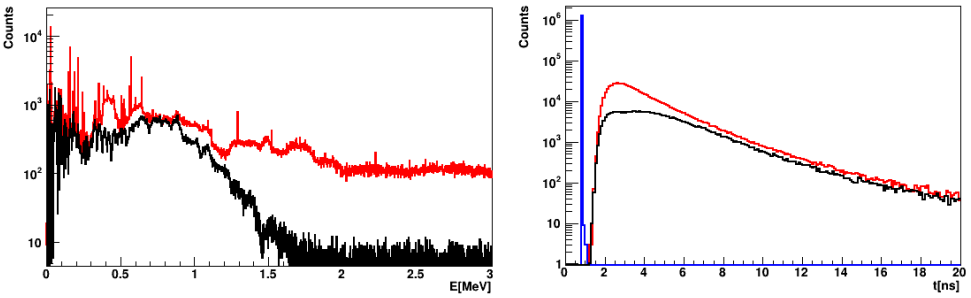


Fig. 68. (Color online) Typical spectra of left: emitted gamma-ray energy, right: neutron and gamma (blue) times from the $^{20}$Ne+$^{116}$Cd reaction. Black: $^{116}$Cd target only, red: $^{116}$Cd target + carbon backing.

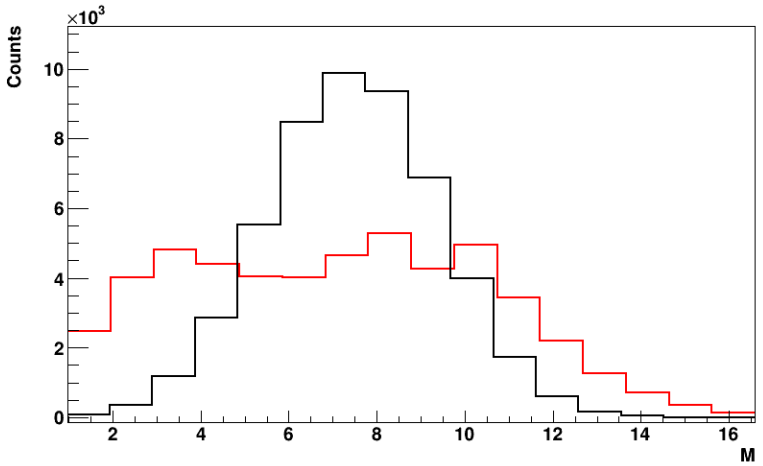


Fig. 69. (Color online) Gamma (red) and neutron (black) multiplicities for the $^{20}$Ne + $^{116}$Cd reaction (target only) at 600 MeV.

Figure 69 presents the gamma and neutron multiplicities for the same reaction but at 600 MeV beam energy. It can be seen that the gamma multiplicity has a broader shape with a reduced average, but still presenting significant high multiplicity events around 10 units. Neutron multiplicity is only slightly increased.

### 6.4.4. *Array response*

**Simulation setup.** Figure 70 (left) presents the geometry of the array used in the simulations. It consists of a set of 139 $LaBr_3$(Ce) detectors arranged in regular rings over an aluminum dome of 10 mm thickness, and the target with its Copper cooling frame with the dimensions of the actual design. For the relatively high-energy gamma rays involved in the present simulations, the absorption on aluminum has a relatively minor effect on the detection efficiency (see Fig. 71). In the actual

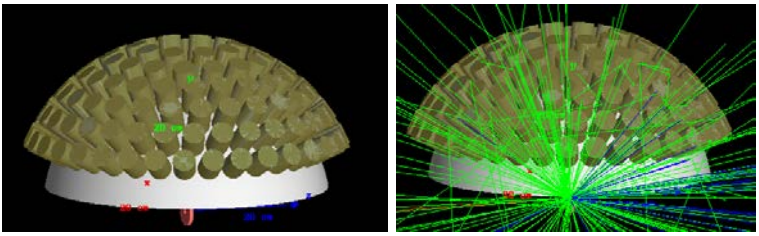

Fig. 70. The gamma detector array configuration geometry used for the GEANT4 simulations. Left: A set of 139 detector crystals wrapped in a thin Al casing, oriented to the center of the target outside a 10 mm Al spherical dome corresponding to the upper part of the MAGNEX scattering chamber (with 240 mm radius). The target frame is made of copper with the approximate dimensions to be used for the cooling of the target. Right: The tracking of the particles generated by 10 events of the $^{20}\mathrm{Ne} + {}^{116}\mathrm{Cd}$ reaction at 230 MeV (without carbon backing) is shown.

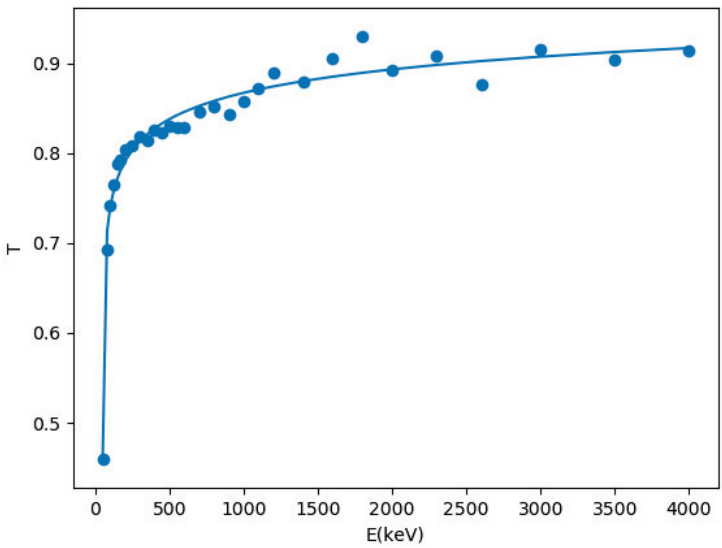


Fig. 71. Simulated transparency factor $\left(T = 1 - \frac{\varepsilon_{ph}}{P_T}\right)$ of a 10 mm aluminum thickness in front of the scintillator crystal (data points) as a function of gamma-ray energy (keV). The solid line is an empirical parametrized fit to the data. The gamma absorption in this thickness of aluminum is approximately the same as that of 2 mm of stainless steel.

mechanical design, the thickness of Al in front of the detectors could be reduced. The scattering in the Al dome, however, could be representative of other material which will be present in the final mechanical mount of the array. Figure 70 (right) shows the tracking of the particles emitted from 10 events.

**General fold and energy spectra.** Figure 72 presents the number of hits of different detectors (fold) distribution according to the simulation. Again it can be seen that the carbon backing introduces an additional distribution of lower fold events.

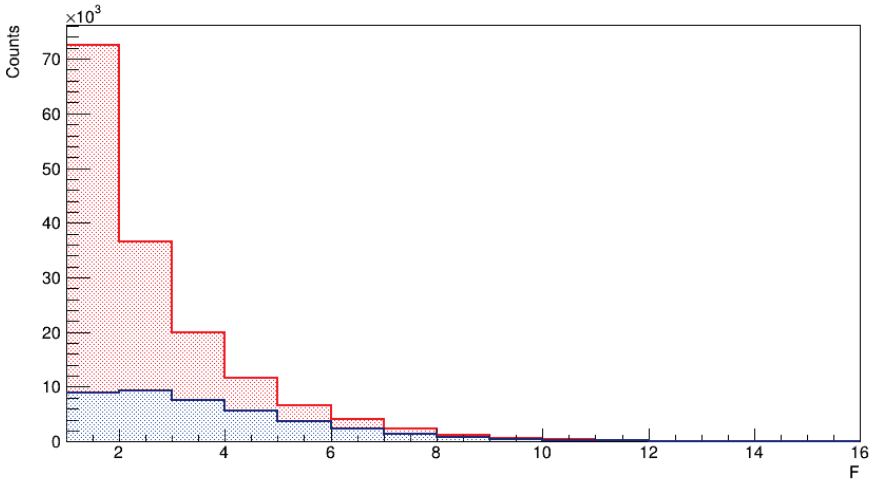


Fig. 72. (Color online) Simulated fold distributions (number of hit detectors) for the simulated array (139 $LaBr_3$(Ce) detectors total) with (red) and without (blue) the target backing for the $^{20}Ne + {}^{116}Cd$ reaction at 230 MeV (same number of primaries: $2 \times 10^9$).

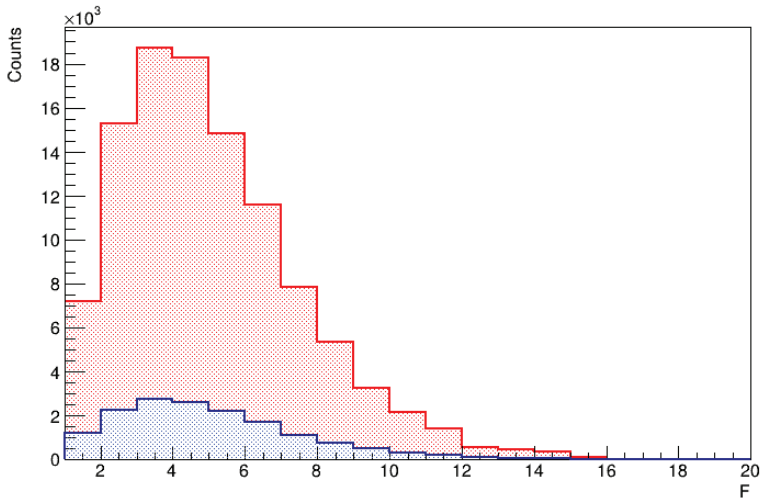


Fig. 73. (Color online) Spectra of the number of hits of the simulated array of detectors, discriminated by particle type. Blue: neutrons; red: gammas. Target only, $2 \times 10^9$ primaries.

Figure 73 presents the fold distributions discriminated by particle type for the target only simulation (no backing), while Fig. 74 shows the particle discriminated energy spectra.

Figure 75 presents the energy spectra detected by the simulated array in the two situations (with and without backing). Individual lines can be barely seen, except for the 511 keV positron annihilation line. In this simulation the finite resolution

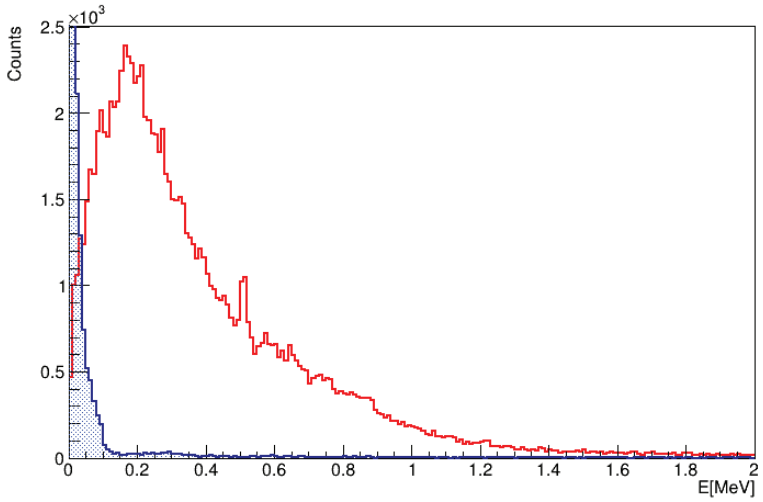


Fig. 74. (Color online) Energy spectra (MeV) discriminated by particle type (expansion at low energy). Blue: neutrons; red: gammas. Target only, $2 \times 10^9$ primaries.

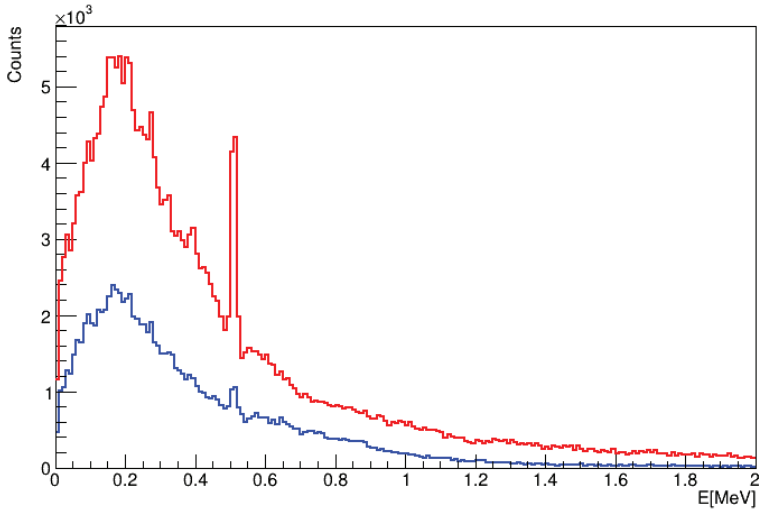


Fig. 75. (Color online) Simulated energy spectra (total projection, in MeV) of the array of 139 $LaBr_3(Ce)$ detectors with (red) and without (blue) the target backing for the $^{20}Ne+^{116}Cd$ reaction at 230 MeV (same number of primaries: $2 \times 10^9$).

of the detector was not introduced. It can be seen that the C backing contributes significantly with gamma rays of higher energy (above 1.5 MeV) in comparison to the target only spectrum.

Table 13 shows the expected approximate rates for a typical beam intensity of $1 \times 10^{12}$ beam particles/s, extracted from the $^{20}Ne + {}^{116}Cd$ reaction at 230 MeV, which is representative of this type of experiment.

Table 13. Expected rates for the $^{20}Ne + ^{116}Cd$ reaction at 230 MeV (only target).

| Target thickness | 1.4 mg/cm$^2$ |
|---|---|
| Reaction rate (2.6 b) | $R_R = 18$ MHz |
| Cyclotron frequency | $f_c = 20$ MHz |
| Reactions/beam bunch | $\bar{k} = 0.92$ |
| Gamma emission | $R_\gamma = 240$ MHz |
| Neutron emission | $R_n = 140$ MHz |
| Count-rate/detector | $R_{\rm det} = 400$ kHz |

**Efficiency loss due to pile-up effects.** The probability of occurrence of a second hit in the same detector from a high multiplicity event is not negligible. In general, this second hit adds significant energy to the previous signal and the information of the original gamma-ray energy is lost. The probability that no additional gamma ray hits the detector if $\bar{k}$ reactions occur on average in the same bunch is approximately given by

$$P_{\rm nop}(\bar{k}) = (1 - \varepsilon_{\rm tot})^{M_{\rm eff}\bar{k}}\,, \tag{5}$$

where $M_{\rm eff}$ is an effective multiplicity which, in principle, should be close to the average multiplicity of the reaction, and $\varepsilon_{\rm tot}$ is the total efficiency of the detector. Figure 76 presents the result of simulations of this quantity, which acts as an

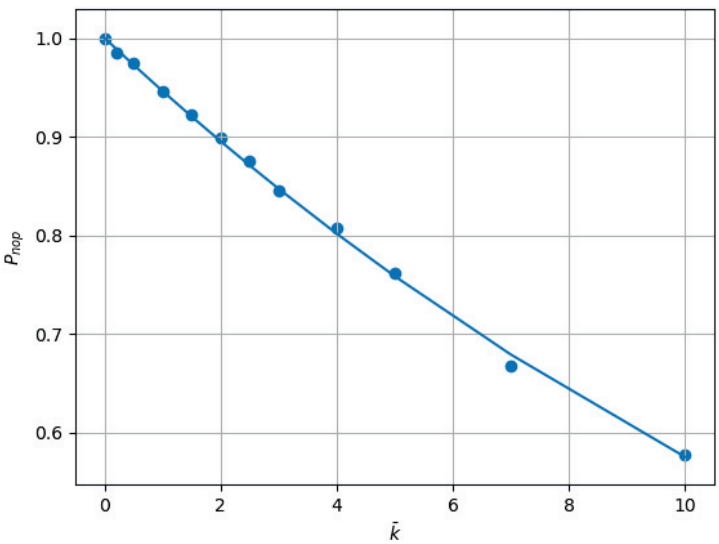


Fig. 76. Efficiency reduction factor due to pile-up (within the time window of 1 bunch only) as a function of $\bar{k}$ from a preliminary simulation of a different $LaBr_3(Ce)$ array with 126 detectors (distributed more or less evenly over the surface of a sphere) of geometric efficiency $\varepsilon_{\rm geo} = \frac{\Delta\Omega}{4\pi} = 0.004$ each, in response to radiation of the $^{20}Ne + ^{116}Cd$ reaction at 230 MeV with no C backing (closed circles). The curve is adjusted to the data yielding an effective multiplicity parameter of 13.8 (continuous line).

efficiency reduction factor of the detector photopeak efficiency. An adjusted effective multiplicity of $M_{\rm eff} = 13.8$ with Eq. (5) adequately describes the data up to the highest value simulated $\bar{k} = 10$ (using $\varepsilon_{\rm tot}$ equal to the geometric efficiency $\varepsilon_{\rm geo}$). This $M_{\rm eff} = 13.8$ value is close to the peak or average value of the gamma multiplicity $M_\gamma$ presented in Fig. 67. The interpretation of the parameters of Eq. (5) are not so important, as long as it reasonably describes the simulation data point in the region of interest. Instead, the simulation is more reliable since it includes all effects, such as Compton scattering between detectors and neutron signal events.

The simulations were repeated with the configuration of the array of Fig. 70, which has smaller geometric efficiency per detector, yielding similar results in terms of $M_{\rm eff}$. When the C backing is included in the simulation, one would expect that the efficiency reduction factor (the no-pile-up probability) would be given by

$$P_{\rm nopb}(\bar{k}) = (1-\varepsilon_{\rm tot})^{M_b \bar{k} r_{bt}} P_{\rm nop}(\bar{k}) = (1-\varepsilon_{\rm tot})^{(M_b r_{bt} + M_{\rm eff})\bar{k}}, \qquad (6)$$

where $r_{bt}$ is a new parameter representing the relative probability of occurrence of a reaction in the backing to that of the target $\left(r_{bt} = \frac{n_b \sigma_b}{n_t \sigma_t}\right)$, and $M_b$ is the C backing reaction effective gamma multiplicity. Note that in this approach $\bar{k}$ continues to be regarded as the average number of reactions per bunch *with the target* (therefore directly related to the DCE production) not including reactions with the C backing, which adds to the total average number of reactions per bunch: $k_{\rm tot} = \bar{k}(1 + r_{bt})$. The simulated result, however, is better adjusted with $M_b = 6$ (significantly higher than the value around 3, expected from Fig. 67). This perhaps can be explained by the much higher energy gamma transitions present in the backed target spectrum (Fig. 68), which are likely to produce more scattering and pair creation events. Again, the interpretation is not so important as long as the description of the functional dependence is reasonable.

So far we have considered the pile-up probability of signals originated in the very same beam bunch. Around the integration time of the detector pulse necessary for adequate gamma energy resolution (typically 200 ns), various other beam bunches can hit the target (with a typical period of 50 ns), producing additional reactions. This multiplies the exponent of Eq. (6) by an effective number of bunches $N$, corresponding to the integration time plus a couple of beam periods before the bunch, whose possible pulse tails can significantly degrade the energy evaluation of the gamma ray of interest. This effect is illustrated in Fig. 77 by the dot-dashed curve. Figure 77 presents also the effective yield, given by the product of the no-pile-up probability with $\bar{k}$. This shows that pile-up can be a severe limitation of the yield of the experiment at high beam currents, from around $\bar{k} = 2$.

Figure 78 shows an expansion of the spectrum around the 1.294 keV peak. It is possible to notice a small reduction in peak area as a result of the $P_{\rm nop}$ factor. The increase of background under the peak is also apparent. This effect is explored in the following subsection.

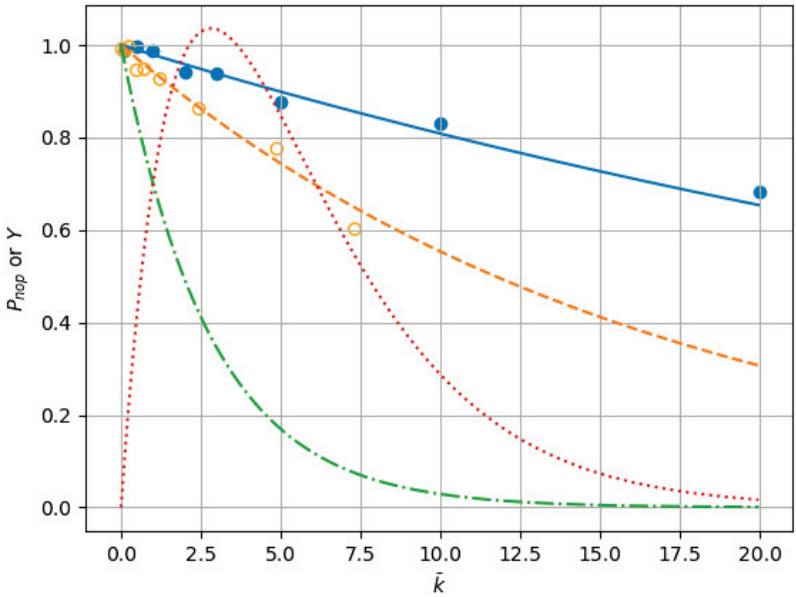


Fig. 77. Efficiency reduction factor due to pile-up as a function of $\bar{k}$ ($P_{\rm nop}(\bar{k})$) from simulation of a $LaBr_3(Ce)$ array of Fig. 70 with 139 detectors with geometric efficiency $\varepsilon_{\rm geo} = \frac{\Delta\Omega}{4\pi} = 0.00154$ each, in response to radiation of the $^{20}Ne + ^{116}Cd$ reaction at 230 MeV with no C backing (closed circles). The continuous line curve is calculated with an effective multiplicity parameter of 13.8 (same as in Fig. 76). The simulations with the inclusion of the 1 micron C backing are represented with the open circles. The dashed curve is for an effective backing gamma multiplicity of $M_b = 6$. The dot-dashed curve considers a number of bunches $N = 6$, related to the charge integration time of the signal. The dotted curve represents the effective yield $Y = \bar{k}P_{\rm nop}(\bar{k})$.

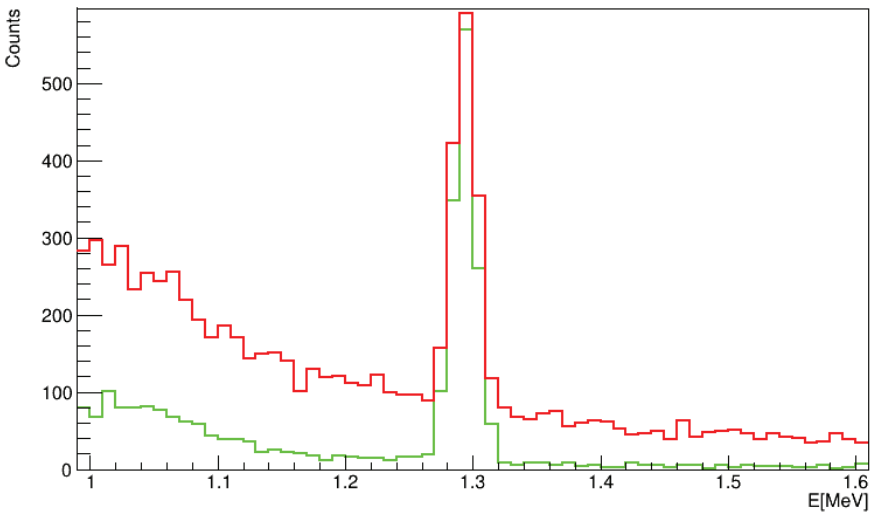


Fig. 78. (Color online) Expansion of the simulated $LaBr_3(Ce)$ spectra around the 1.294 MeV line (from TLF $2^+$ state) at two different values of $\bar{k}$ for the $^{20}Ne + ^{116}Cd$ reaction at 230 MeV with no C backing (green: $\bar{k} = 0.1$; red: $\bar{k} = 1.0$).

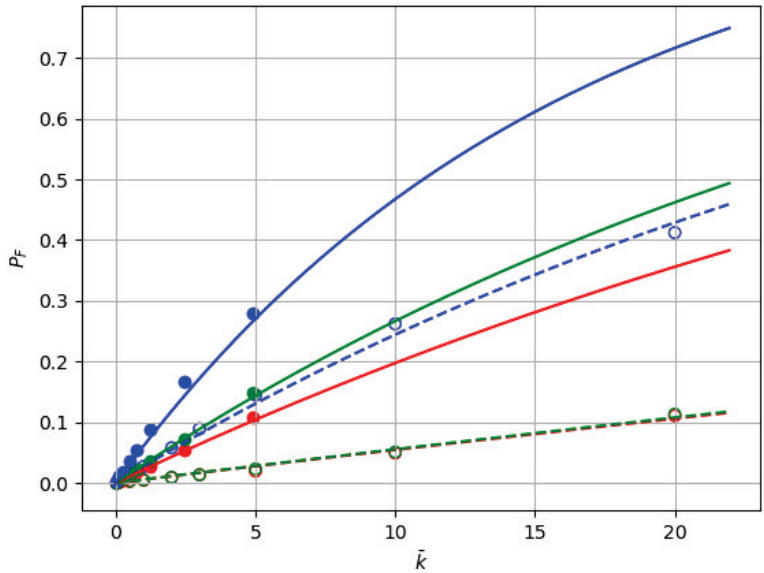


Fig. 79. (Color online) Simulated probability of background generation of at least one signal in the gamma gate on the transitions associated with the DCE states (green: PLF $2^+$, red: TLF $2^+$, blue: TLF $0^+(2)$) for the proposed array. $^{20}$Ne + $^{116}$Cd reaction at 230 MeV. Dashed curves/open symbols: without target backing. Solid curves/closed symbols: with target backing. The curves are from Eq. (7) with the fitted parameters listed in Table 14.

**Background probability parameter estimates.** As illustrated in Fig. 78, the background grows with the beam intensity. Systematic simulations can show this effect in graphical form (Fig. 79). Based on Poisson statistics, the probability of background generation of at least one signal in the gamma gate on the transitions associated with the DCE states $P_F$ (the $P_i$ parameters appearing in the $\boldsymbol{M}$ matrix of Eq. (4)) can be approximated by

$$P_F(\bar{k}) = 1 - e^{-b\bar{k}}\,, \tag{7}$$

where $b$ is a parameter depending on the energy of the transition of interest and on the detector energy resolution, including, eventually, the Doppler broadening. This parameter can be obtained from the fits to the simulation data. It can also be experimentally obtained with good precision for each of the transition energies of interest to the DCE measurement, as well as the efficiencies necessary to construct the $\mathbf{M}$ matrix.

Table 14. Background parameter values of the proposed array for the $^{20}$Ne + $^{116}$Cd reaction at 230 MeV.

| $E_\gamma$ (MeV) | State | Parameter | Value (target) | Value (target + backing) |
|---|---|---|---|---|
| 1.294 | TLF $2^+$ | $b_1$ | 0.0056 | 0.022 |
| 1.674 | PLF $2^+$ | $b_2$ | 0.0057 | 0.031 |
| 0.463 | TLF $0^+(2)$ | $b_3$ | 0.028 | 0.063 |

Table 14 presents the values obtained for the $b$ parameters in the present simulation evaluation.

### 6.4.5. *Expected performance*

**Typical gamma-ray energy coincidence spectra.** Figure 80 presents sample spectra simulated for the $^{20}\mathrm{Ne} + ^{116}\mathrm{Cd}$ reaction at 300 MeV for an array consisting

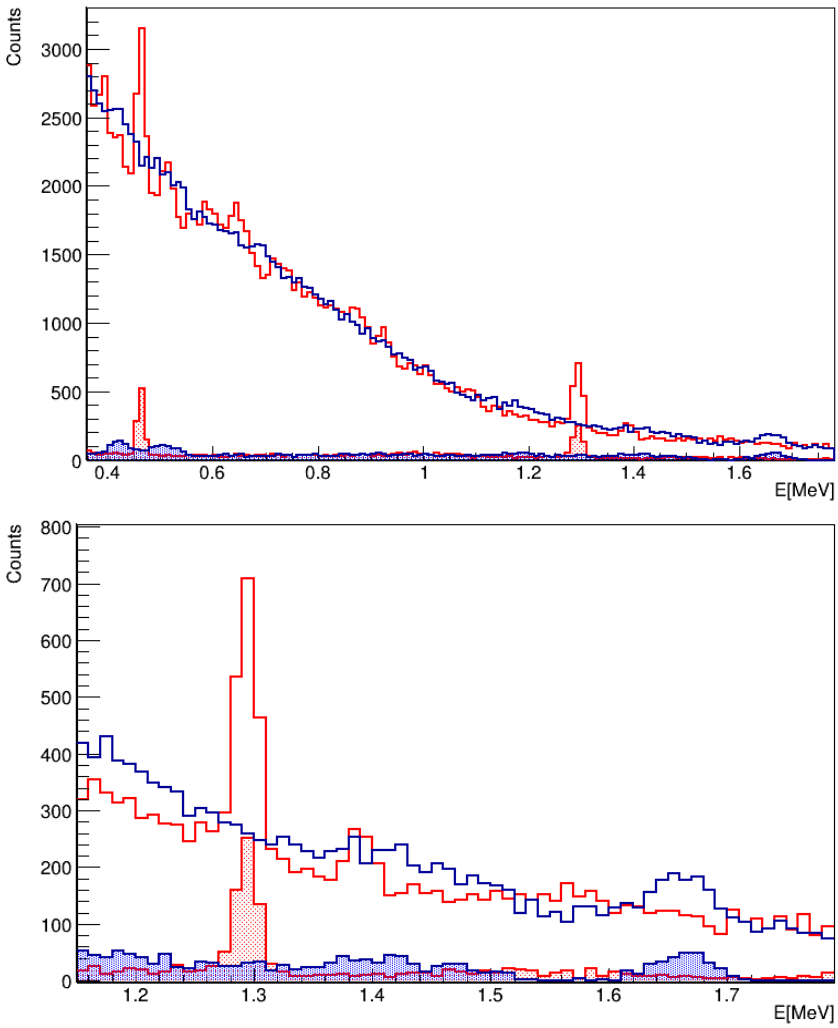


Fig. 80. (Color online) Simulated coincidence spectra (gated by PLF detection, but with no discrimination in energy between g.s. and first excited states) for the $^{20}\mathrm{Ne} + ^{116}\mathrm{Cd}$ reaction at 300 MeV at $\bar{k} = 1.0$. Red lines: without Doppler correction; blue lines: with Doppler correction assuming the speed of the PLF (recoil energy of $E \approx 295$ MeV). The shaded spectra are simulated in the absence of background from the other nuclear reactions (as if at $\bar{k} \approx 0$ in a very long experiment). Right: expansion around the first excited state transitions of TLF (1.29 MeV) and PLF (1.69 MeV).

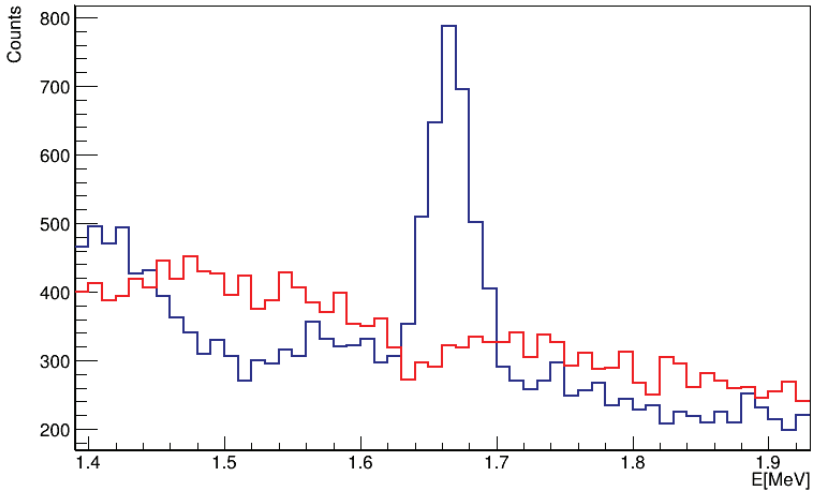


Fig. 81. (Color online) Expansion of the region around the 1.694 keV line (PLF) with (blue) and without (red) Doppler correction, at $\bar{k} = 1.0$ for the $^{20}$Ne + $^{116}$Cd reaction at 230 MeV with C backing (recoil energy of $E \approx 225$ MeV).

of the 0.004 geometric efficiency detectors mentioned in Fig. 76. It is assumed that the spectra is in coincidence with the PLF (both the PLF and the gamma rays were originating in the same beam bunch), but no discrimination between the DCE low-lying states (g.s.×g.s., $2^+$ PLF, $2^+$ TLF and $0^+(2)$ TLF, all simulated with the same cross-section) was performed. The transitions are clearly separated in the spectrum, the 0.463 MeV line indicating the presence of the $0^+(2)$ TLF, the 1.294 MeV line that of the $2^+$ TLF, and the 1.674 MeV one (after Doppler correction), the presence of the $2^+$ PLF. As shown in the expansion around the last two, the background contributes with statistical fluctuations to the evaluation of the cross-section. This is formally taken into account with the matrix equation of Eq. (3).

Figure 81 presents the result of the simulation of the array of Fig. 70 for the 1.674 MeV peak. A Gaussian fit to the Doppler corrected spectrum yields a FWHM resolution of 3.73%, while the expected value of the $LaBr_3$(Ce) detector for this energy (Fig. 66), is 1.47%, illustrating the Doppler broadening effect, particularly important at near 90° detection angles. This result is better than for the larger width detectors of Fig. 80.

**Typical FPD particle spectra in coincidence/anti-coincidence.** Figure 82 presents a typical MAGNEX focal plane detector (FPD) spectrum of the PLF ($^{20}$O selected) of the DCE reaction in coincidence with the 1.294 MeV ($2^+$ TLF) gamma-ray gate. Since the photopeak efficiency of the array is much less than 100%, the anti-coincidence spectrum contains a large amount of the 1.294 MeV excitation energy peak. Conversely, since there are background counts under the peak of 1.294 MeV in the gamma-ray gate, the g.s. × g.s. (both PLF and TLF in the ground state) peak, as well as other excitation not physically correlated with

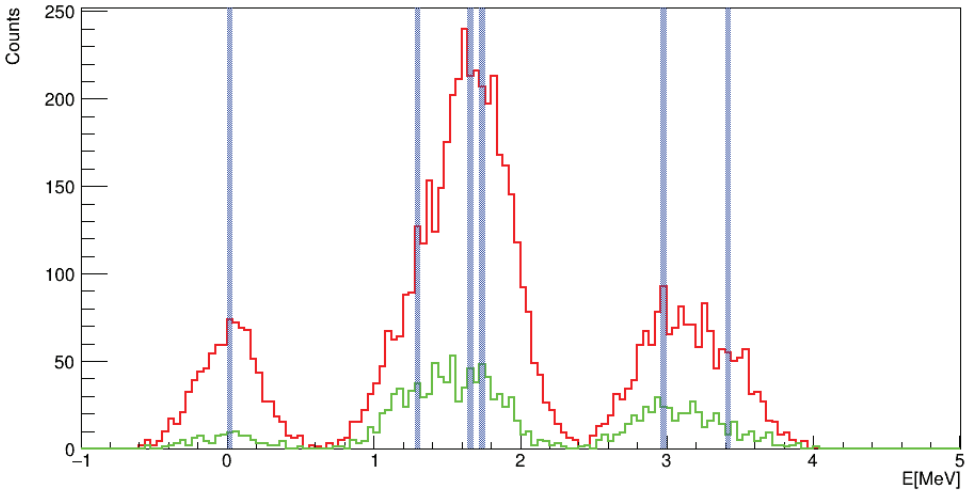


Fig. 82. (Color online) FPD spectra in coincidence (green) and anti-coincidence (red) with the TLF $2^+ \rightarrow 0^+$ transition, assuming a 500 keV energy resolution (FWHM). The blue vertical strips indicate the locations of the exact excitation energies of the DCE exit channel.

this gamma transition (other excitation from the PLF, TLF, and combinations of both), appear in the coincidence spectrum. Nevertheless, the extracted areas in coincidence with each gamma transition between the DCE reaction channel states constitute the area column matrix $\boldsymbol{A}$ of Eq. (4) (the experimental input). Knowing the efficiencies and background probabilities for each transition which constitute the $\boldsymbol{M}$ matrix, the number of DCE events of each state can be evaluated together with their relative statistical uncertainties (and therefore, the DCE cross-sections). In the 500 keV resolution case, depicted in Fig. 82, a selection can be made in the central peak, for example, restricting the number of dimensions of the matrix, and, of course, improving the quality of the results. At high beam energies, however, the FPD energy resolution may not be sufficient for a clear separation between the peaks within this energy region. In such high beam energy cases, as well as when the separation of the DCE g.s. and first excited states is small (deformed mass regions), the selections in FPD energy spectra are ineffective to improve significantly the quality of the results, except for the exclusion of much higher excitation energies populated in the reaction, which is taken for granted up to now.

**Achievable uncertainty in the DCE cross-section measurement.** Figure 83 presents the final relative uncertainties of the DCE cross-section states after 1 month of measurement of the $^{20}$Ne+$^{116}$Cd reaction at 230 MeV with a 1.4 mg/cm$^2$ target. It is assumed that the FPD detectors have selected the energy region including from the ground to the first three excited states (therefore not including the combined excitation of the PLF and TLF shown in Fig. 82). For a measurement without backing, all the states could be measured with a relative uncertainty below 10%, with $\bar{k}$ around 1–2. When the HOPG (C) backing (10 microns) is introduced, which

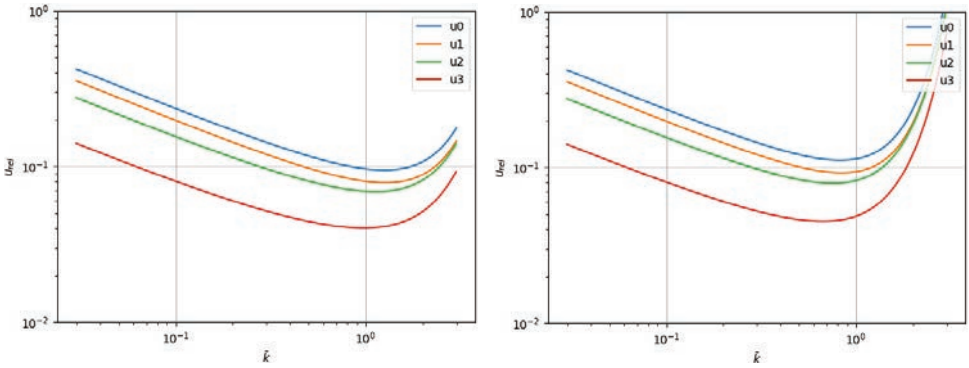


Fig. 83. Final relative uncertainties in the DCE cross-sections as a function of $\bar{k}$ with the proposed spectrometer after 4 weeks of data collection (left: without backing, right: with backing), assuming 1 nb for each of the 4 states: u0: g.s. × g.s., u1: $2^+$ TLF, u2: $2^+$ PLF, u3: $0^+(2)$ TLF.

is necessary particularly for the cooling of the lowest melting point target materials such as Cd or Sn, the uncertainty of the g.s.×g.s. state reaches a minimum somewhat above 10%, near $\bar{k} = 1$. It is foreseen that the thickness of the Highly Oriented Pyrolytic Graphite (HOPG) foil can be reduced to 2 microns. However, the typical targets used are also significantly thinner than 1.4 mg/cm$^2$ (by 2–3 times, which could be compensated by an increase of beam current to reach the same $\bar{k}$), so, the actual limit would be intermediate between the values of the two graphs of Fig. 83.

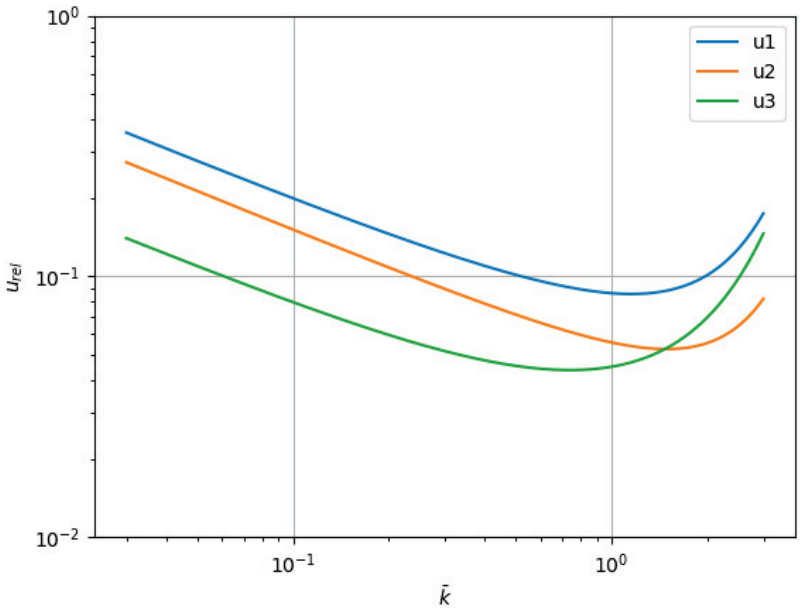


Fig. 84. Same as Fig. 83 (left: without backing), but excluding the g.s. × g.s. FPD peak (gate on middle peak of Fig. 82).

At low beam energies (about 500 keV resolution) it is possible to separate the g.s.×g.s. peak from the other 3, which can then be measured with help of the gamma array with improved precision (Fig. 84). This is important because the cross-section to the $2^+$ states could help to disentangle the contributions from the Fermi, Gamow–Teller and higher rank operators involved in the DCE reaction.



### 6.5. *Simulation validations*

#### 6.5.1. *EDEN data*

During the experiment NUMEN8, when the $^{18}O + ^{76}Se$ reaction at 275 MeV was measured, a 30 min test was performed with use of the liquid scintillator detectors of the EDEN array.[83] These detectors are also sensitive to gamma rays, which can be selected by 2D gating on Fast : Slow components of the electronic pulse. The results were published in Ref. 81. It was concluded that the simulations somewhat overestimate (by about 25%), but correctly reproduce the order of magnitude of the gamma-ray rates in correlation with the cyclotron beam RF reference, as well as the shape of the energy spectrum (above the experimental energy thresholds of the various detectors, around 0.2 MeV).

Another similar test was performed but with a $LaBr_3(Ce)$ detector and for the $^{20}Ne$ beam at 15 AMeV on $^{116}Cd$ or $^{nat}C$ (HOPG) target reactions. Preliminary results confirm that the simulations, done with various nuclear reaction models available in GEANT4, reproduce the gamma spectrum shape and total area within a factor of 2. The results, particularly good for the $^{nat}C$ case, should be sent for publication shortly.

### 6.6. *Mechanical design*

The gamma array space is limited by the other equipment around the scattering chamber, such as vacuum pumps, beam entrance sliding seal, quadrupole entrance, robotic arm entrance for target replacement etc. and the target-cooling system. Only about 20% of the total solid angle is actually available for placement of the gamma-ray detectors.

The $LaBr_3(Ce)$ detectors with 38 mm diameter and 50 mm length are arranged mainly in six conical rings as presented in (Fig. 110). Their axes will be directed toward the target with polar angles between 45° and 65° relative to the beam axis. This profits from the expected angular correlation of the gamma rays from DCE reactions with the PLF detected near 0° in the MAGNEX PID wall, peaked at 45° and $180 - 45°$ as in a electric quadrupole $L = 2$, $M = 0$ antenna. The total number of detectors in the array is 110, somewhat smaller than the number used in the simulations (139). However, the angular correlation effect approximately compensates for the reduced number of detectors resulting in the same effective detection efficiency for the DCE cases. In the detailed development of the project, this number of detectors might be slightly modified.

### 6.7. *Electronics design*

In order to be consistent with the general architecture of the electronic system for NUMEN, it was concluded that the best solution is to use $LaBr_3(Ce)$ scintillators coupled to standard photomultiplier tubes (PMTs) read-out, which allows also for the best energy and timing resolutions. The signal can then be directly sent to digitizers, and processed in the same manner as the pre-amplified signals from other detector arrays of the NUMEN system.

The gamma-ray data should be taken in coincidence with the FPD of the MAGNEX spectrometer. The time of each gamma-ray signal should be measured with relation to the cyclotron RF signal to ensure best resolution.

The FPD signal, with timing also referred to the cyclotron RF signal, if present, validates the gamma array signal processing enabling its conversion. If not present, the gamma signal conversion is aborted to reduce storage space. In order to avoid excessive rates in the data collection, the region of interest of the focal plane position, where the ground and first excited states of the DCE reaction channels appear, can be physically limited by introducing movable blockers. The precise positioning of these blockers can be adjusted in a low beam intensity run at the beginning of the experiment. After that, with the blockers in place, the beam intensity can be raised to planned final rate for the subsequent experimental runs. Besides limiting the dead time and the data acquisition rate load, this procedure is useful to reduce the radiation damage to the other sensors of the FPD which are not directly involved in the DCE reaction selection of the specific experiment. It is expected that, with this approach, the data rate is kept below about 1 MHz, which is manageable by the electronic system.

In order to measure the $P_F$ background parameters of the various transitions of interest, a sampling of the gamma data of nonphysically correlated beam bunches (those before and after the coincidence bunch correlated with the FPD detection time) will be collected.

## 7. Front-End and Data Acquisition

### 7.1. *Introduction*

The primary task of the NUMEN front-end and data acquisition system is to cope with the huge analog data rate coming from the detector subsystems. Then data have to be converted to digital and finally transferred to a storage system via large bandwidth channels.

Due to the intrinsic nature of the MAGNEX magnetic spectrometer the tracking algorithm is quite complex and consequently slow. Indeed it requires to sample the signals from many strips and to recognize those which belong to a track, performing weighted averages of signals from neighboring wires and matching them to signals from telescopes in the PID detector system. Processing and triggering the 90k events/s/strip expected maximum rate in real time, would require a too

challenging effort. Therefore only typical noise suppression by means of thresholds on individual signals is realistically foreseen.

Concerning the particle identification wall, the maximum expected event rate is just below 15k events/s/telescope in the median horizontal line of telescopes, being the average rate 5k events/s/telescope. In this case one can think of performing a noise reduction by means of thresholds and elementary $\Delta E - E$ coincidences.

The gamma CALORIMETER will face a huge incoming event rate whose handling will presumably be possible only during dedicated runs with a reduced beam current.

The basic DAQ requirements for the three subsystems can be summarized as follows:

- TRACKER: medium energy resolution, 1 ns time resolution, very high speed.
- PID: high-energy resolution, 1 ns time resolution, high speed.
- CALORIMETER: high-energy resolution, 1 ns time resolution, very high speed.

The originally proposed solution based on the VMM3 ASIC was discarded in favor of a better suited solution based on commercial products. This would be quite beneficial from the point of view of the maintenance and repair, hardware/firmware updates, backward compatibility in case of new developments and products. Obviously, the question was whether a feasible commercial solution existed, and it sounded reasonable to try opting for a digitizer approach with underlying FPGA firmware/hardware. Such an approach would be powerful and flexible, as it is open to tuning and rearrangements that in case of more traditional electronics would require hardware replacements. However, within a digitizer framework the idea of recording the waveforms is not suitable at all, due to the large number of channels and to the continuous mode of operation of the accelerator (in other facilities, with 1–2 s long duty cycles and smaller number of detectors, there is time between beam bursts to store the acquired waveforms).

Therefore several possible solutions were investigated, all making use of multichannel modules produced, or being finalized, by CAEN. The tests were done in collaboration with CAEN, and at first the idea was to make use of different modules for different kinds of detectors, in order to reduce the overall cost by choosing for each subsystem a module family better tailored to its features. The front-end readout system (FERS) module (64 channels), currently being developed, was tested as a candidate for the tracker along with digitizers operating at 62.5, 100, 500 MHz sampling rates. The same digitizers were tested as candidates for the PID wall and for the calorimeter, showing that a 100 MHz digitizer can satisfy the signal requirements of all the four detector types (i.e. tracker, SiC, CsI, LaBr), even though the PID could in principle be served by a 62.5 MHz digitizer. However, mixing different types of modules would require a considerable complication of the read-out architecture. Moreover, CAEN is currently finalizing a new high-performance 64-channel digitizer with 125 MHz sampling rate (VX2740),[84] which has also been chosen by the Darkside experiment.[85] Such a module, shown in Fig. 85 and whose operational

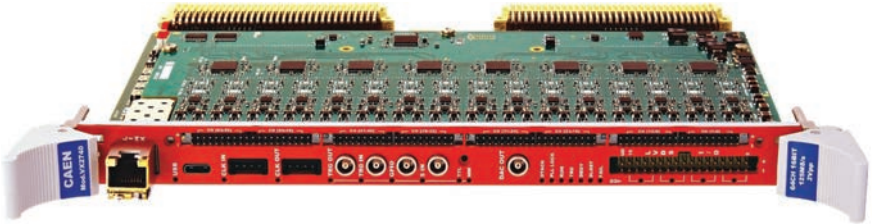

Fig. 85. The newly developed CAEN VX2740 digitizer module.

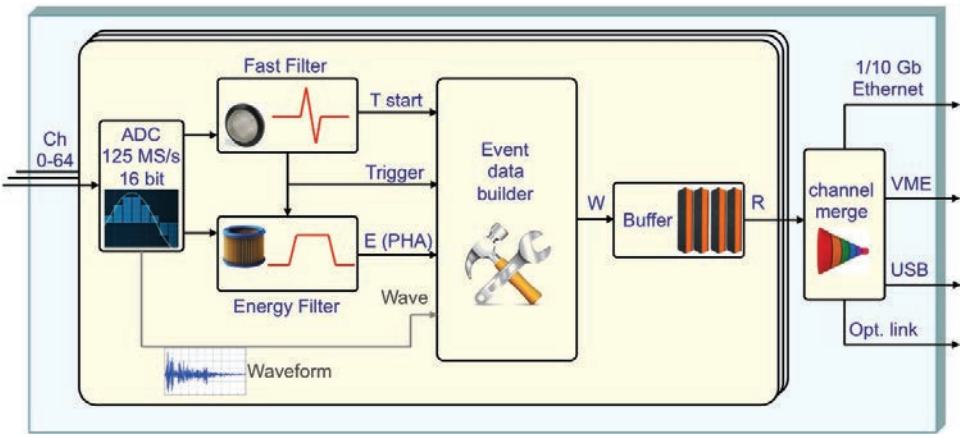


Fig. 86. Block scheme of the VX2740 digitizer operational features.

features block scheme is depicted in Fig. 86, would provide several advantages:

- uniform front-end and read-out hardware architecture;
- reduction and simplification of the spares;
- programmable signal handling algorithm, tailorable to each detector type;
- very good energy resolution, 16 bit conversion;
- very good timing capabilities, in 8 ps steps;
- pile-up detection and tagging;
- high data throughput;
- cost reduction due to purchasing only one model, with the additional benefit of being the same as in another important INFN experiment.

The VX2740 digitizer development is still being finalized: the hardware is ready whereas the firmware for the FPGA is still being tuned in order to accommodate also some special requests from the Darkside experiment. The new generation FPGA has quite a higher number of gates with respect to previous digitizers, thus allocating more hardware-emulating algorithms and a quad-core processor hosting a real-time Linux operating system.

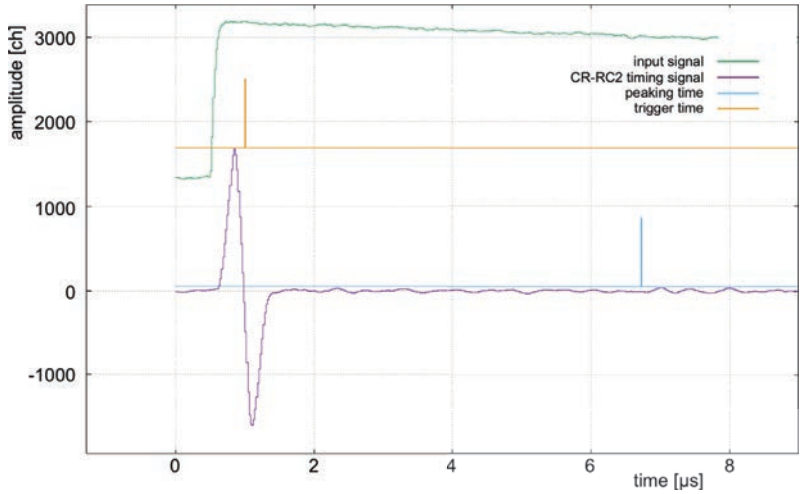


Fig. 87. Test signal from the A1442 preamplifier, corresponding to 1 MeV in silicon, sent to the digitizer. Shown are the bipolar signals, obtained with a suitable numerical transform and the corresponding (zero crossing) triggering time, the peaking time when the pulse height measurement is done. The numerical analysis is done in real time by the on-board FPGA.

### 7.2. *Tests of digitizers with TRACKER-like and PID-like signals*

Unfortunately at the time of this test there was no VX2740 prototype available, therefore the test was performed with another digitizer of an older generation, the V1782,[86] with slightly worse features: lower sampling rate (100 MS/s), smaller number of input channels (8), lower performance FPGA. The PHA algorithm of the VX2740 is the same as in the V1782, whereas the timing algorithm has been improved in order to perform a high precision interpolation of the zero-crossing, making possible a time resolution of the order of few tenths of ps. The test setup included a signal generator, a CAEN A1442[87] preamplifier, a V1782 digitizer. The signal sent to the test input of the preamplifier was tuned in order to correspond to a 1 MeV equivalent in a silicon detector.

Figure 87 illustrates the operation of the Fast filter and Trigger parts of the PHA algorithm (upper sections of Fig. 2). The output from the preamplifier, corresponding to 1 MeV in silicon ($\approx 0.5$ MeV in SiC and $\approx 30$ MeV for $^{16}$O ions in CsI) is sent to the digitizer and is shown as acquired in waveform mode. A suitable recursive numerical transform implementing a CR-RC2 filter produces a bipolar signal. The corresponding zero-crossing time is highlighted and used as triggering time. Figure 88 illustrates the operation of the Energy part of the PHA algorithm (lower section of Fig. 86). Another suitable recursive numerical transform on the digitized input signal produces a trapezoidal shape, whose flat-top height is proportional to the input signal amplitude, i.e. the energy. The peaking time indicates where on the flat top the pulse height measurement is done. All of the above numerical analysis is done in real time by the on-board FPGA, not introducing additional dead time

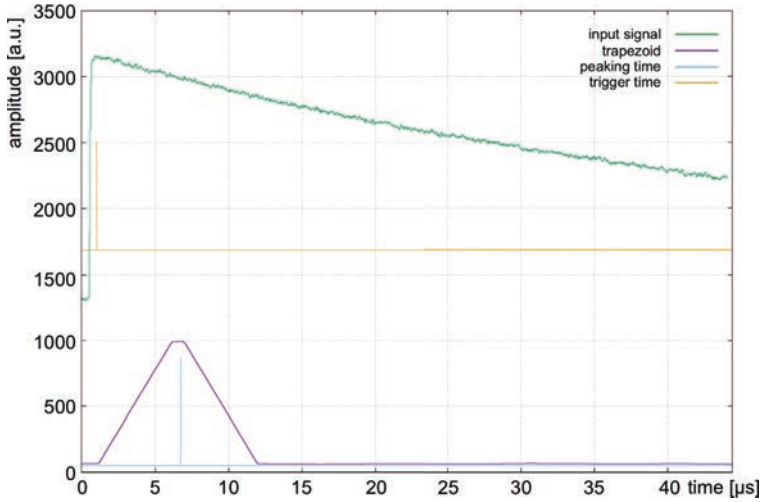


Fig. 88. The same test signal from Fig. 87, with the corresponding trapezoid obtained by means of a suitable transform performed in real time by the on-board FPGA.

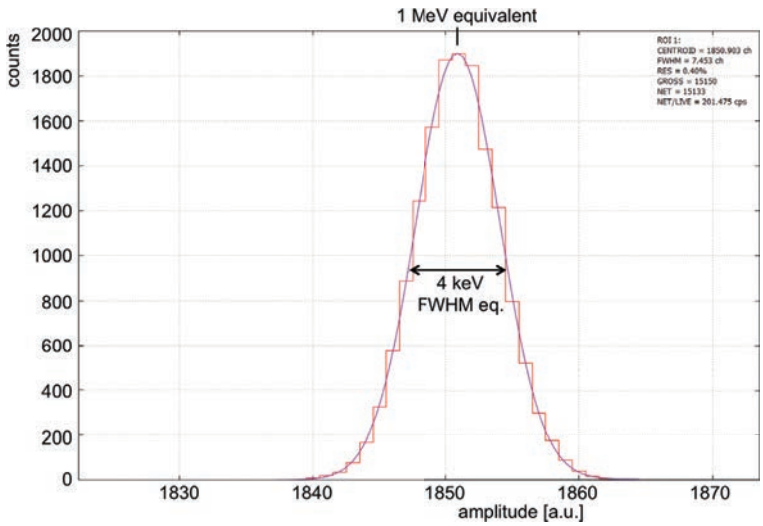


Fig. 89. Energy resolution measured in the same configuration of Figs. 3 and 4 with 1 MeV equivalent test signals from the A1442 preamplifier and the V1782 (100 MS/s) digitizer in Pulse Height Analysis (PHA) mode.

and therefore resolving or tagging the signal pile-up depending on the relative delay between two consecutive signals.

Figure 89 shows the amplitude spectrum obtained under these test conditions. The 4 keV silicon equivalent FWHM resolution indicates the additional noise contribution to be expected from this electronic setup in a measurement with a real detector as input. The same test was done with a DT5730 digitizer (500 MS/s,

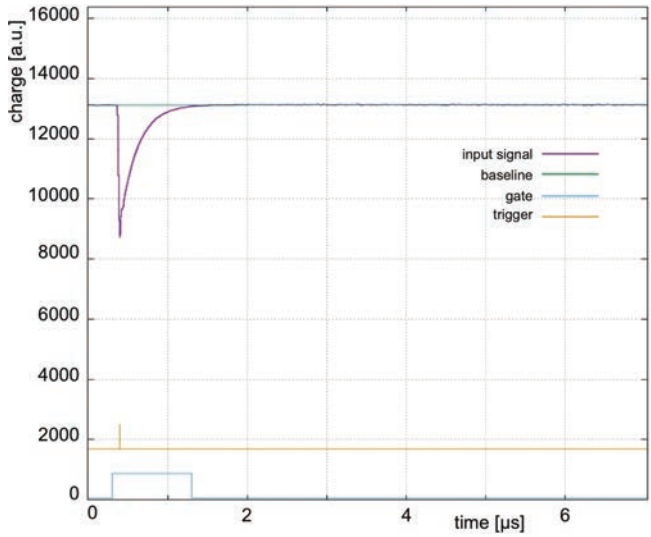


Fig. 90. Test signal from the A1442 preamplifier, corresponding to 1 MeV in silicon sent to a differentiating stage with time constant ≈100 ns and then to the QDC digitizer.

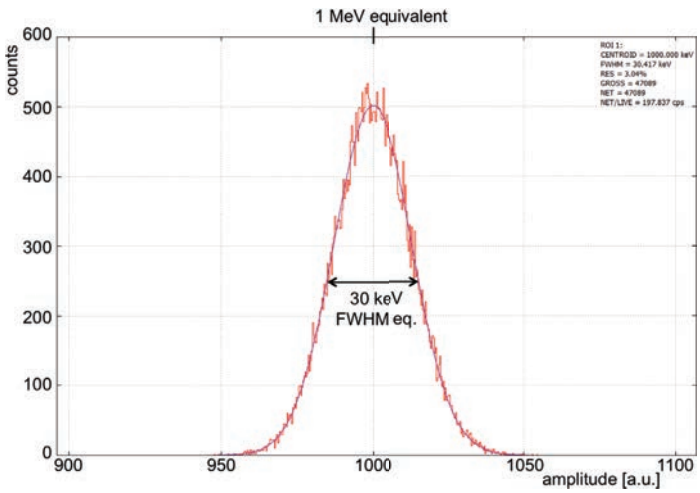


Fig. 91. Energy resolution measured with 1 MeV equivalent test signals from the A1442 preamplifier using the DT5730 digitizer (500 MS/s, 14 bit) in QDC mode. The integration gate was optimized at 1 $\mu$s.

14 bit[88]) running the QDC charge integration algorithm. The preamplifier output was sent to a differentiating stage with time constant ≈100 ns in order to match the digitizer input specifications, and the integration gate was optimized at 1 $\mu$s (Fig. 90). The resulting amplitude spectrum, shown in Fig. 91, has a worse 30 keV silicon equivalent FWHM resolution, thus clearly indicating the better quality of PHA with respect to QDC.

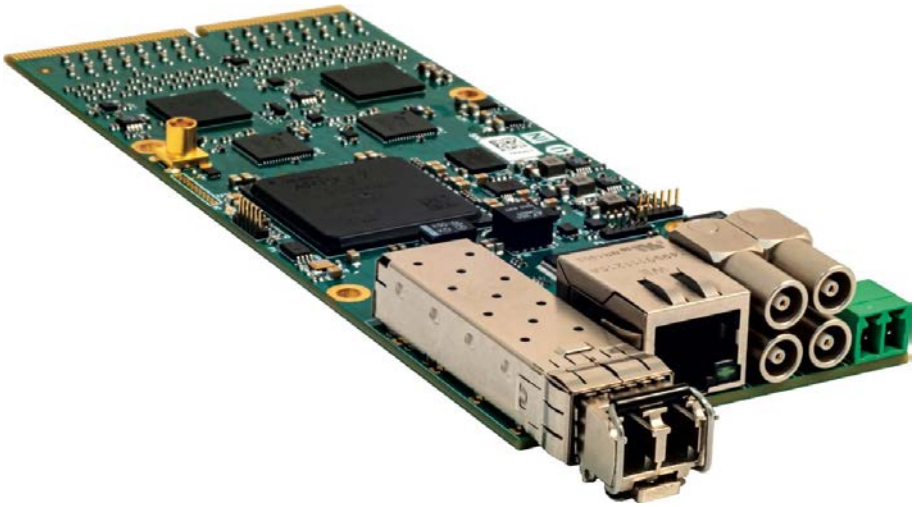

Fig. 92. The FERS module board.

### 7.3. *Test of FERS with TRACKER-like signals*

A recently developed module named FERS[89] (Fig. 92), based on two CITIROC-1A chips, was tested in order to assess its possible use with the TRACKER subsystem. It features 64 fast analog input channels with amplifier and shaper, can sustain up to 20 Mcps/channel and was originally thought for read-out of Silicon Photomultiplier (SiPM) arrays. As digitized output one can choose the integrated charge or the time-over-threshold (ToT). Unfortunately the gain range available on the chip is not high enough for the TRACKER requirements, and the signals needed an additional preamplification stage before entering the module. The output is nonlinear, even though linearizable, but unfortunately the final dynamic range resulted too narrow to be useful for NUMEN's purposes. Therefore, also in light of the additional complexity arising from the supplementary preamplifiers required, this solution was discarded.

### 7.4. *Test of a digitizer with CALORIMETER-like signals*

In order to assess the feasibility of a digitizer solution for the gamma CALORIMETER read-out two scintillators, coupled to photomultipliers, were placed face to face with a $^{22}$Na $\beta^+$ source in between producing two back-to-back gamma rays of 511 keV energy and a single one of 1274 keV (Fig. 93). The scintillators were a $1.5'' \times 2''$ $CeBr_3$ and a $2'' \times 2''$ $LaBr_3$. Figures 94 and 95 show oscilloscope snapshots of the respective signals. As mentioned before the test was performed with the V1782 digitizer which has worse performance than the planned VX2740. Nonetheless the test results were much better than expected, as will be shown in the following. The signals from the photomultiplier tubes were directly fed into two digitizer

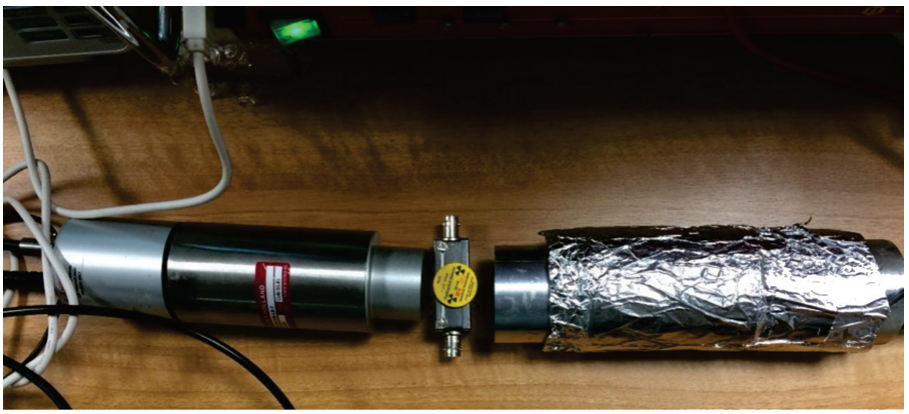

Fig. 93. The setup employed for energy and time resolution of the gamma CALORIMETER by using a V1782 digitizer (100 MS/s). Two scintillators, coupled to photomultipliers, were placed face to face with a $^{22}$Na $\beta^+$ source in between producing two back-to-back gamma rays of 511 keV energy and a single one of 1274 keV. On the left a CeBr scintillator, on the right a $LaBr_3$ scintillator.

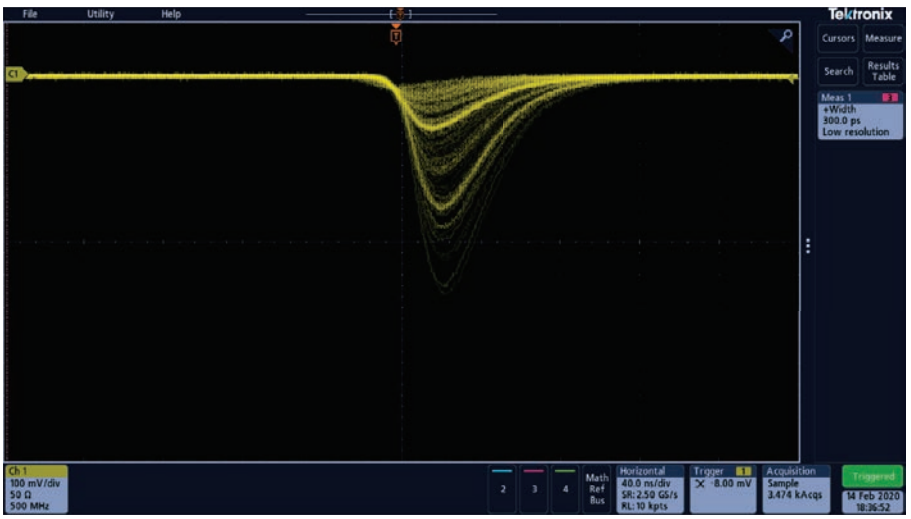


Fig. 94. Snapshot of the signals from the $LaBr_3$ detector. The 511 and 1274 keV signals are well defined. The overall duration of the signals is about 120 ns.

channels and the PHA analysis parameters were tuned accordingly but not strictly optimized, in order to test the system behavior under realistic, not perfectly tuned, conditions. Figure 96 shows the result of the PHA algorithm on a typical LaBr signal with a nicely flat-top trapezoid, and Fig. 97 the corresponding amplitude spectrum. The measured FWHM resolution at 511 keV was 4.5% ($CeBr_3$) and 3.4% ($LaBr_3$), roughly scalable to 4% and 3% at the 662 keV of the $^{137}$Cs peak. At variance with the VX2740 the V1782 digitizer cannot perform any on-board timing interpolation,

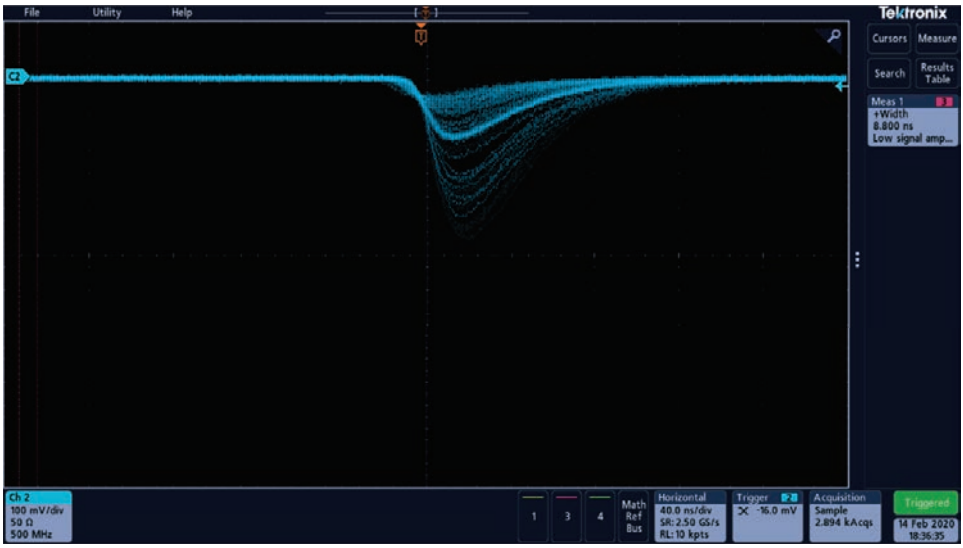


Fig. 95. Snapshot of the signals from the $CeBr_3$ detector. The 511 keV signals are well defined, even though with a very slightly worse resolution; the 1274 keV signals are not clearly evident. The overall duration of the signals is about 130 ns.

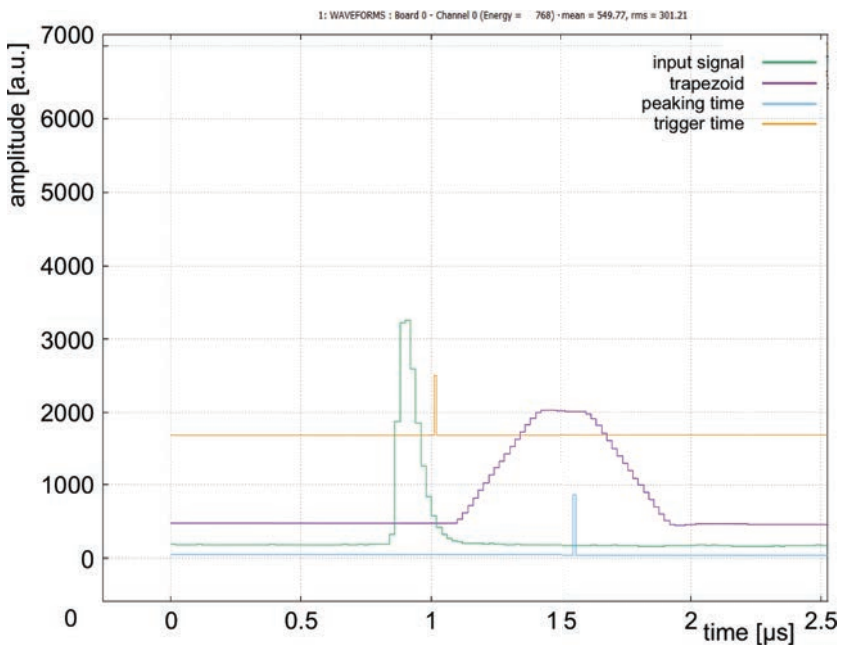


Fig. 96. A sample signal from the $LaBr_3$ detector, exactly as expected from the gamma CALORIMETER, acquired and handled by a V1782 digitizer (100 MS/s). The corresponding trapezoid obtained by means of a suitable transform performed in real time by the on-board FPGA is shown along with the indication of the trigger time and the peaking time.

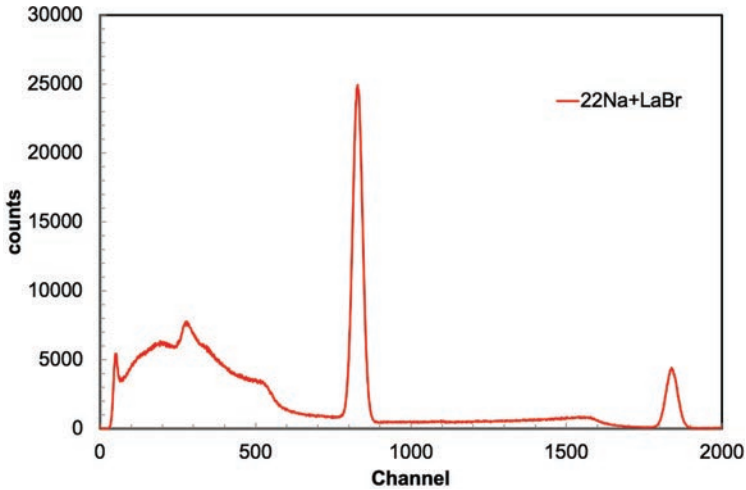


Fig. 97. Amplitude spectrum obtained with the LaBr scintillator and a $^{22}$Na source, under the conditions of Fig. 96.

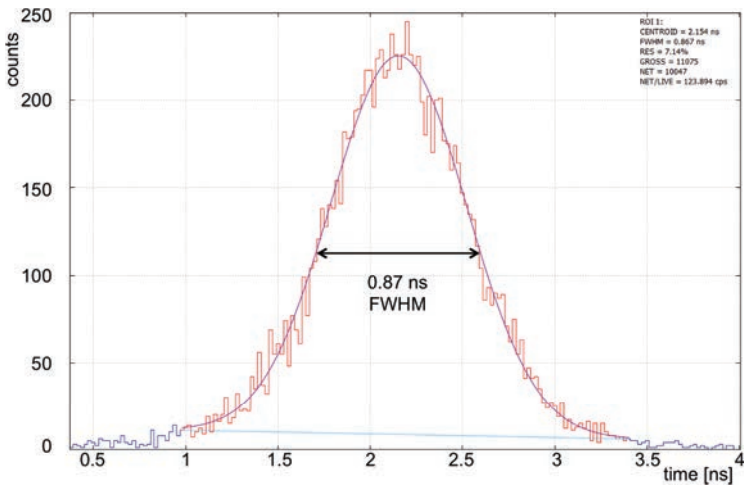


Fig. 98. Coincidence time spectrum between the CeBr and LaBr scintillators hit by back-to-back 511 keV gamma rays emitted by a $^{22}$Na source. The FWHM resolution is well below 1 ns.

due to FPGA limitations, therefore a number of waveforms were acquired and the interpolation between two points around the zero-crossing was performed offline. The coincidence time spectrum between the two scintillators was built and plotted in Fig. 98, showing an FWHM resolution of 0.87 ns. The same test was done by replacing the V1782 digitizer with a high performance DT5730 (500 MS/s, 14 bit), employing the PHA firmware and the on-board time interpolation, and obtaining the same result.

### 7.5. *Radiation hardness*

These new generation digitizers, as can be seen from bibliographical references, are used by NASA for the space missions and are immune to Neutron Single-Event Upset in case of thermal neutrons.[90–93] For LET Single-Event Latchup (SEL), instead, there is a threshold of $\approx 125$ MeV·cm$^2$/mg (i.e. 30 MeV in 1 $\mu$m silicon)[92,93] and they are also expected to be immune to SEL. This will be checked with some tests and, just in case, attenuated with polyethylene screens (1 cm of polyethylene is sufficient to take neutrons of 50–60 MeV below 10 MeV).

### 7.6. *Summary and conclusions*

In light of the results and of the consequent considerations a few alternative possible strategies have been deemed technically feasible, with different complexity and performance. In the end a strategy was chosen that optimizes the performance while at the same time simplifying the general architecture. This means choosing the most recent development, i.e. the VX2740 digitizer, for all the subdetector types. In a small-scale system one could save money by tailoring the detector front-end with the minimum performance that matches the requirements. In a case like NUMEN it comes out that diversifying the DAQ electronics with respect to each detector subsystem would result in a stronger effort in terms of complexity, money and manpower, both for the development and for the operational phases. Moreover, the chosen digitizer would allow to stay in the same production pipeline as the Darkside experiment, thus further reducing cost and supply time. A summary of the detector requirements with the corresponding input data rate and possible front-end and DAQ electronics is reported in Table 2. The most convenient candidates, both in terms of performance, complexity, handling, spare parts, maintenance and overall cost, are highlighted.

The use of a single module for all the subsystems simplifies enormously the hardware global time synchronization, mandatory to have a unique time stamp for the offline event reconstruction. Indeed the data volume is so large that there is no possibility to make use of a single data stream, therefore several independent high speed data read-out streams will flow separately. The output data structure of a hit channel is listed in Table 15. A special event will be generated every 100 ms with the function of global time synchronizer, to prevent possible misalignments of the separate read-out data streams.

Table 15. The 9-byte data format for each hit channel in the digitizer module.

| Byte 1 Byte 2 | Byte 3 Byte 4 Byte 5 | Byte 6 Byte 7 | Byte 8 Byte 9 |
|---|---|---|---|
| Module/Channel ID | Coarse time stamp (0–134 ms) | Fine time (8 ps step) | Energy |
| 16 bit | 24 bit | 10 bit | 16 bit |

The overall data output rate depends on the NUMEN running mode. Two modes are foreseen: inclusive and exclusive. The inclusive mode, for shorter periods at high beam current (nominal $10^{13}$ pps), does not consider coincident CALORIMETER data whose rate would be prohibitive. The expected read-out data rate in such a case is $\approx$610 MB/s, i.e. $\approx$00 MB/s from the TRACKER, $\approx$54 MB/s from PID-$\Delta E$ and 54 MB/s from PID-E.

The exclusive mode, in coincidence with the gamma CALORIMETER, is only feasible with lower beam current (nominal $\approx 10^{12}$ pps), and in such a case the expected read-out data rate is $\approx$571 MB/s, i.e. $\approx$510 MB/s from the CALORIMETER and $\approx$61 MB/s from the other subsystems. The possible selection of regions of interest by an appropriate gating of the signal amplitudes at the input of the VX2740 can significantly filter out unwanted signals from G-NUMEN. In a typical DCE experiment the gamma rays of interest have well-known energies, thus allowing the definition of narrow regions of interest within the spectrum and a consequent reduction of a factor of 10 and even more in the data collected by the calorimeter. In addition, a careful masking of the FPD by the insertion of thick metallic screens upstream the entrance window of the detector, can strongly suppress the count rate of the tracker, the PID-$\Delta E$ and PID-E when the focus is on transition to DCE ground state in both inclusive and exclusive modes. As a consequence the overall data throughput can be realistically maintained below 100 MB/s even in the challenging exclusive mode.

The VX2740 module features a front panel 10 Gbit Ethernet interface, which supports a very high data rate. By suitably choosing a dedicated Ethernet configuration/interconnection the total data flow can be reasonably split into a few lower bandwidth logically coherent streams.

## 8. Integration of Mechanical Devices

The new components for NUMEN have to be mechanically and electrically integrated with the old existing ones. At the same time, new components present complexities that require specific integration studies for each of them, some have already been described partially or completely in other sections as result of dedicated R&D activities.

The present spectrometer MAGNEX includes a platform (Fig. 99) on which all elements of the apparatus are placed.

The platform is a key component because it allows a continuous rotation, by using a dedicated circular rail, in a range between $-20°$ and $+90°$ of the spectrometer around the object point located at the target axis. The rail features 40 mm in height and 150 mm wide, the external radius being 5900 mm and the internal one 5750 mm. The scattering chamber, (with exclusion of the target holder system), the quadrupole, dipole and FPD are bound to the platform and then they can be positioned in-built with the structure at a specific angle as requested by the benchmark channel under study.

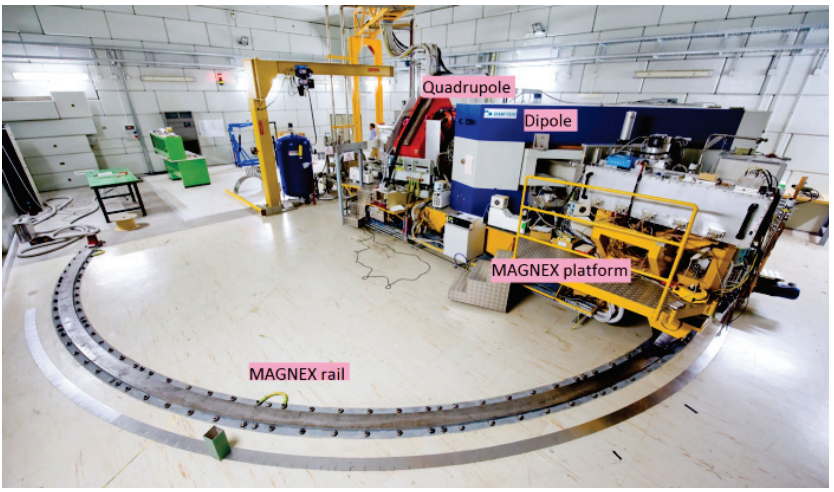


Fig. 99. Present MAGNEX spectrometer. The rail on which the platform can rotate is visible foreground. The quadrupole and dipole on the platform are indicated.

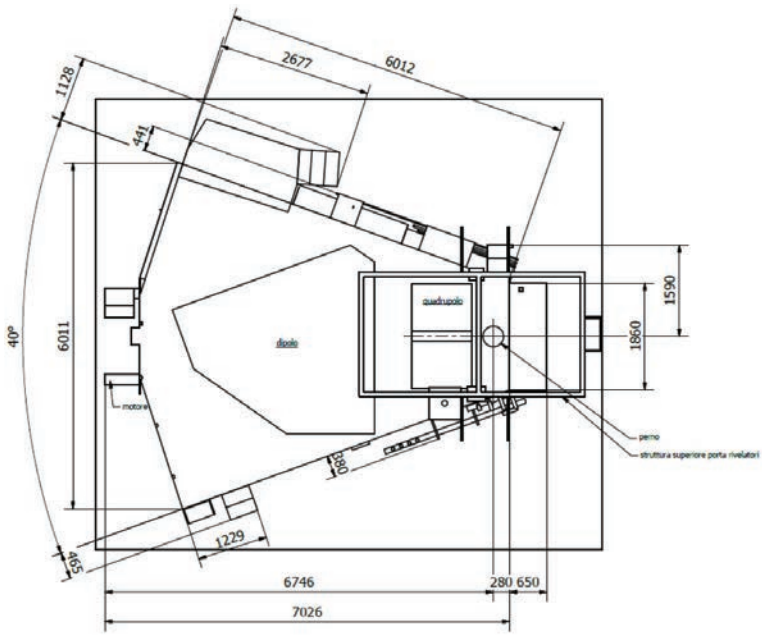


Fig. 100. Top view of the platform of MAGNEX. The measurements are listed on the drawing.

This rail and the platform will be reused for NUMEN, even if an in-depth maintenance is mandatory for the movement system during the refurbishment phase of the spectrometer. The overall dimensions of the platform are shown in the top view of Fig. 100.

The existing quadrupole and dipole are re-used even if they will be upgraded for what concerns the power supply and the cooling system of the coils according to a new cooling framework of the laboratory. A new scattering chamber and target, as well as the detectors of the FPD have been designed to be compliant with the new physics requirements. The installation of new detectors for $\gamma$-rays is planned close to the target, too. In addition to the existing setup, a beam dump will be installed in the MAGNEX hall. In the following subsections new parts that have not been discussed in other sections will be presented offering the results of the integration study and design:

- *The scattering chamber*,
- *The vacuum chamber*,
- *The beam dump part.*

### 8.1. *The scattering chamber*

The scattering chamber, designed for the NUMEN experiment, is a challenging part to be studied[94] because it has to fulfill new constraints in addition to the typical specifications already present in the old one.

The internal volume of the chamber has to be kept at a residual pressure ranging in the interval of $10^{-5} \div 10^{-6}$ mbar using suitable pumping system.

The chamber has a sphere-like shape and it is appropriately placed on the MAGNEX platform. It must rotate around its vertical axis which corresponds to the axis, passing through the spectrometer object point and to the target axis.

As it was already described, the target holder has been designed to contains a target made of the isotope under study, a raw substrate, an empty frame and an alumina target for the beam diagnostic and alignment.

Since the target with the isotope needs to be cooled, during the measurement, a cooling system has to be integrated taking into account that a linear vertical motion of the target is requested.

In order to set the MAGNEX accepted solid angle window, four independent slits are requested equipped with two blades each able to move independently in opposite directions to define the free opening to the passage of the ions.

Specifically for the ray reconstruction purposes, a pepper-pot able to select only selected groups of ion tracks is requested downstream the target.

Due to radioprotection rules it is not possible to measure the beam current at full power within the scattering chamber, this measurement being performed inside the beam dump by a suitable Faraday cup (F1). Nevertheless a Faraday cup (F2) for a power lower than 10 W is foreseen. Therefore a suitable mechanism to place F2 in and out along the beam line and downstream the target has to be studied too.

The high intensity of the ion beam together the foreseen range of the energy per nucleon poses a not negligible problem of radiation dose inside the chamber.

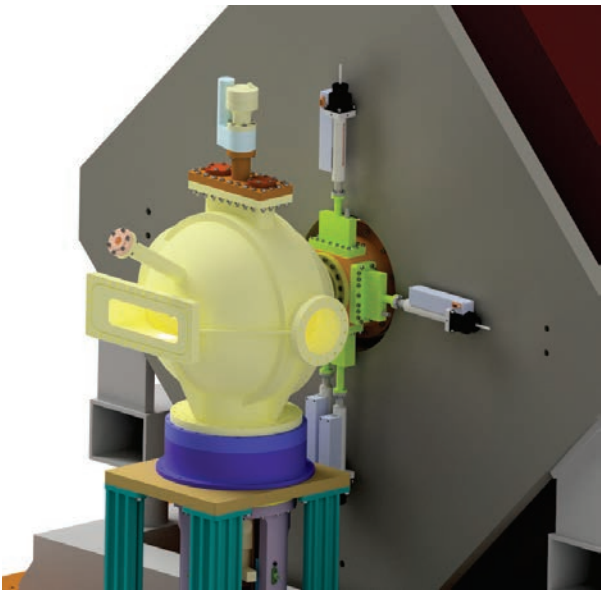

Fig. 101. View of the scattering chamber.

The activation of materials is not excluded and therefore it becomes important to solve the problem of replacing the target following its breakage or deterioration or in any other case it is needed.

An automated system capable of replacing the target must be designed and prepared to act in place of an operator's intervention.

The chamber is made of stainless steel, 3 mm thick towards the gamma detector, in the remaining parts ribs aid the mechanical stability. Its radius is 230 mm.

A turbomolecular pump limits the residual pressure below $10^{-5}$ mbar.

Figure 101 shows the chamber, further details and parts will be motivated and illustrated in the following subsections.

### 8.1.1. *Sliding window*

The incident beam will be transported to the MAGNEX experimental hall using two different lines, the High Intensity (HI) beam line and the Low Intensity (LI) beam line. A 70° angle rotation of the platform around its axis allows to align the optical axis of the apparatus along the two beam lines, respectively bringing it in configuration HI or configuration LI. Since the scattering chamber is in-built with the platform, each configuration requires its connection to the relative beam line.

The physics cases planned to be studied in the configuration HI ask for two angular positions of the apparatus with respect its optical axis, +3° and −3°. In the LI configuration, the requested rotation angle ranges between −6° and +25° with respect to the optical axis of the apparatus. Figure 102 shows a schematic

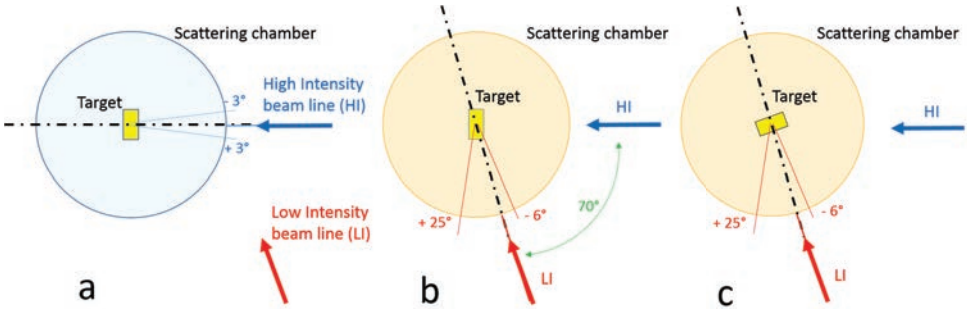


Fig. 102. Scheme of the two configuration of NUMEN: High Intensity (a) and Low Intensity (c). The (b) scheme represents the intermediate situation where the target system is not yet rotate for the LI mode. The dotted line represents the optical axis of the whole apparatus.

representation of the two possible configurations for the scattering chamber and the rotation angle range.

Since the target system is integral with the hall floor, it cannot rotate, then the target has to be independently rotated on the top of the cold finger, following the rotation angle existing between the HI and LI configurations, to be again perpendicular to the beam line.

The scattering chamber is connected to the HI beam line with a bellows. In the case of the connection with the LI beam line, a system is built that allows the sliding along the wall of the chamber while keeping the vacuum seal.

### 8.1.2. *Target-cooling system*

The target-cooling system includes the cryo-refrigerator and the target clamped by a copper frame on the top of its cold finger.[94]

In Fig. 103 a simplified section of target holder on the cryo-cooler is presented.

The vertical movement of the cryo-refrigerator is obtained by means of a vertical movement actuator placed beneath and guided by a cylinder; a bellow guarantees the requested stroke. The maximum axial load of the actuator is of 700 N and its vertical stroke is of 100 mm with a repetition accuracy of $\pm 0.05$ mm and a reversing backlash less than 0.1 mm. The integration of end switches and mechanical stops are foreseen. A series of flanges, fixed on the chamber base and integrally fixed to the guide cylinder allow the relative motion between the chamber and the target. These flanges house vacuum seals. In Fig. 104 a rendering of the target-cooling system is presented.

The disassembly of the cryo-refrigerator is obtained by dismounting the upper flange and by decoupling the cryo-refrigerator from the actuator and the helium pipes. In fact, pipes connect the cryo-refrigerator (a single stage cryo-cooler can be used with a suitable adapter towards the target support) to its compressor that has to be placed some meters far from the target system together a chiller based on water.

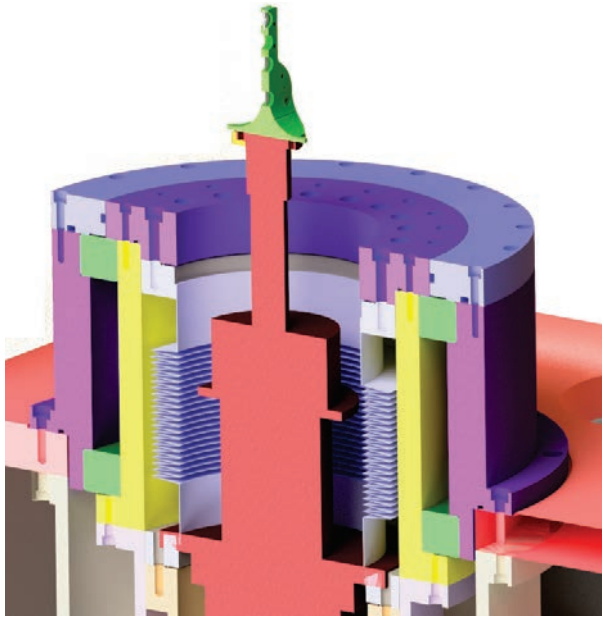

Fig. 103. Simplified section of the target holder on the top of the cold head of the cryo-cooler.

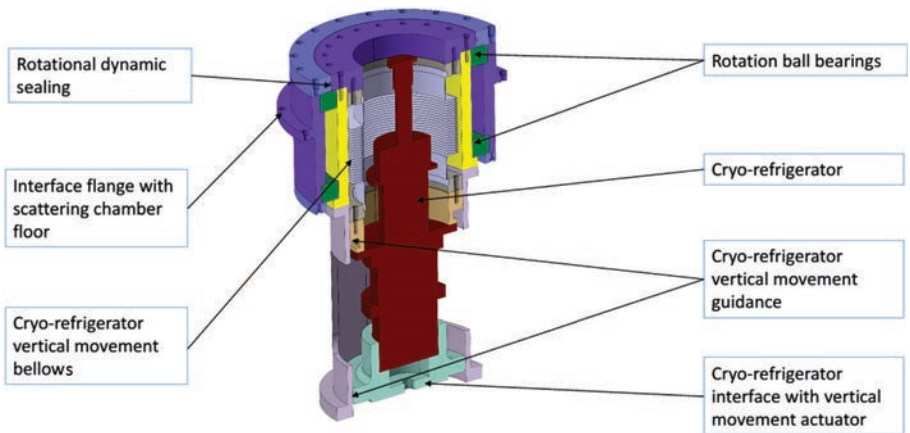


Fig. 104. Details of the parts around the cryo-refrigerator.

The choice of the type of seals and the material that has to be used is a challenging step in the design of the chamber because the expected radiation level at the maximum power of the ion beam may have an impact on that. EPDM o-rings and PEEK material show a acceptable tolerance (by Compilation of Radiation Damage Test Data, CERN) to radiation for their use in NUMEN.

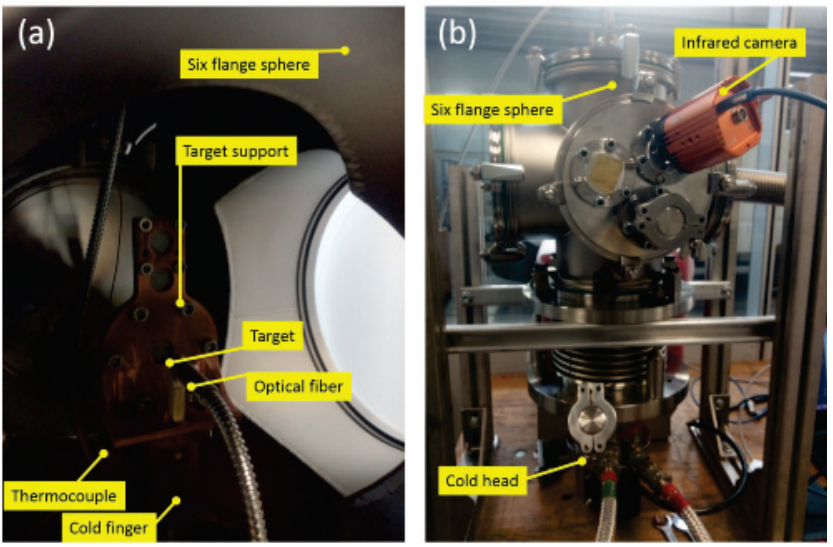


Fig. 105. The setup of a reduced scale scattering chamber that implements the target-cooling system: (a) internal view and (b) outside view.

### 8.1.3. *Prototype of the target-cooling system*

To study the target-cooling system, a first prototype of a reduced scale scattering chamber has been built using a preexisting cryo-refrigerator, based on a cold head COOLPOWER 5/100. It has to be noticed that its refrigerating capacity does not cover the complete range requested by NUMEN (less than 20 W), nevertheless the concept of the proposed cooling system can be validated.

The cold head was connected to a vacuum system composed of a six flange sphere and on the top of its cold finger a prototype of the target support was screwed. The heating source was a infrared diode-laser and its light was transmitted up to the target using a suitable optical fiber. A Si-diode measures the temperature below the upper plate of the cold finger. An infrared camera was arranged outside a germanium window to take pictures of the target surface allowing the evolution study of the system under irradiation and heating. Figure 105 shows the inside and outside the reduced scale scattering chamber.

Using the infrared diode a Te target made of an 800 nm layer of tellurium evaporated on a graphite substrate 10 $\mu$m thin was tested.

Two tests were performed at two different optical powers. Using the same experimental setup described above, the fiber end was placed in front of the target about 1 cm away.

Two optical power values were tested inside the target, 16.5 W and 19.6 W. Figure 106 shows the temperature trends measured on the cold finger and in the center of the target during the two tests that had the purpose of verifying the refrigeration capacity of the cryo-cooler and then a stable behavior of the two measured

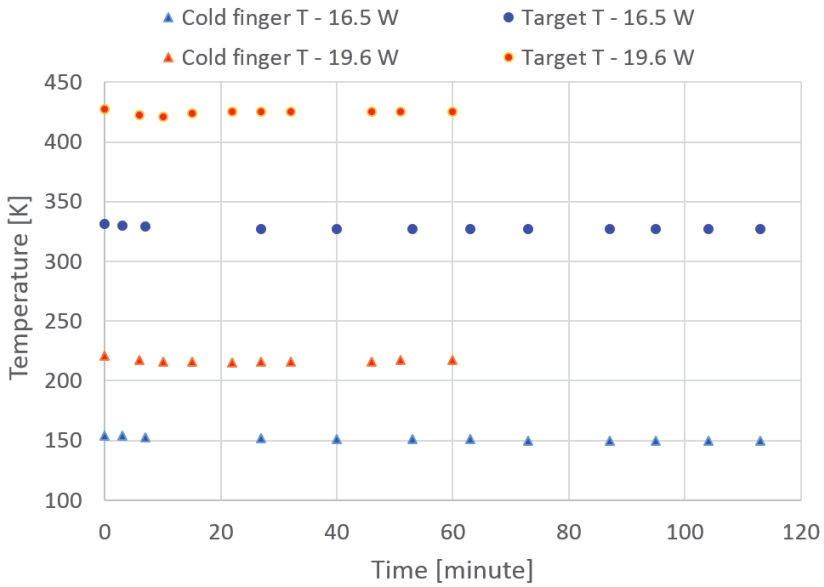


Fig. 106. (Color online) Temperatures of the cold finger (triangles) and of Te target (circles) at two different optical powers provided by a infrared laser diode: 16.5 W (blue) and 19.6 W (orange).

temperatures. By observing the stable values of temperatures the produced heating inside the target is completely removed from the cooler, even if the measured temperatures of the cold finger are lower than the expected ones, less than 10%, with respect the calibration curve of the cryo-refrigerator. The explanation could be found in a reflection on the surface of the target and/or also in the fact that the temperature of the cold finger is measured a few cm away from the top of its upper plate.

### 8.1.4. *Slit system, pepper-pot and Faraday cup*

To control the acceptance of the reaction products towards the FPD, a slit system is requested.

The interaction products are expected to be emitted in a cone of about $\pm 7.5°$ in the vertical direction and about $\pm 6.5°$ in the horizontal direction.

The slit system features four blades, each of them can be moved independently by a dedicated motor on a individual level along the beam axis.

The most suitable material for blades is tantalum (less than 2 mm thick) which limits neutron production from light-ion interaction and guarantees high temperature tolerance. Alternatively molybdenum could be used.

In Fig. 107 the drawing of the system is presented, blades with their rails.

It was estimated that the maximum power that has to be dissipated in each blade is less than 1 W. Therefore a simple cooling can be obtained via a metallic contact.

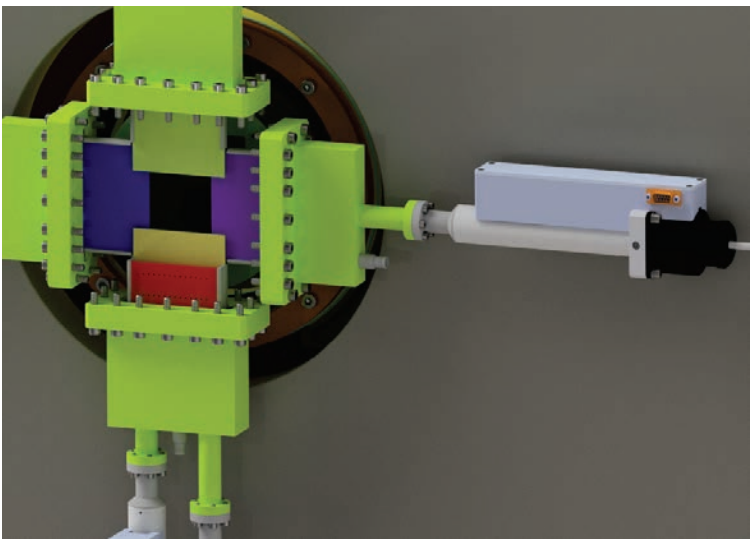

Fig. 107. (Color online) Drawing of the slit system. The pepper-pot is in red color.

A pepper-pot is operated with a dedicated linear drive and on demand it can be moved to intercept the ion beam for trajectory calibration purposes. It is positioned upstream the lower blade of the slit system.

The Faraday cup inside the scattering chamber measures the DC current of the beam. It will be inserted along the beam axis to provide information when the ion beam power does not exceed a few tens of Watt.

### 8.1.5. *Target handling system*

The target handling system is composed by a pick and place structure[95] completed with a storage system. The moving structure is based on the use of a servo wrist unit (WU-M by IAI) connected to a pneumatic gripper (Schunk KGG 60/20) that grips the target holder from the top (Fig. 108). The wrist allows the target holder to turn around his main axis and also a rotation of about 180° around an axis parallel to the beam direction. When the unit is in gripping position and the gripper clamps the target holder, the downwards movement of the cold finger allows the decoupling of the two structures; the wrist now can rotate the holder by 90° around his main axis then again 90° around the other axis in order to allow the outgoing movement.

The internal operations are allowed by the presence of a gate valve that can seal the complete manipulator out of the scattering chamber. The outgoing as well as the in-going movements are allowed by the presence of an external structure which supports a pneumatic cylinder with length of 800 mm (SMC C96 series double effect), the translation is also supported by two cylinders bearing linear guide (Fig. 109).

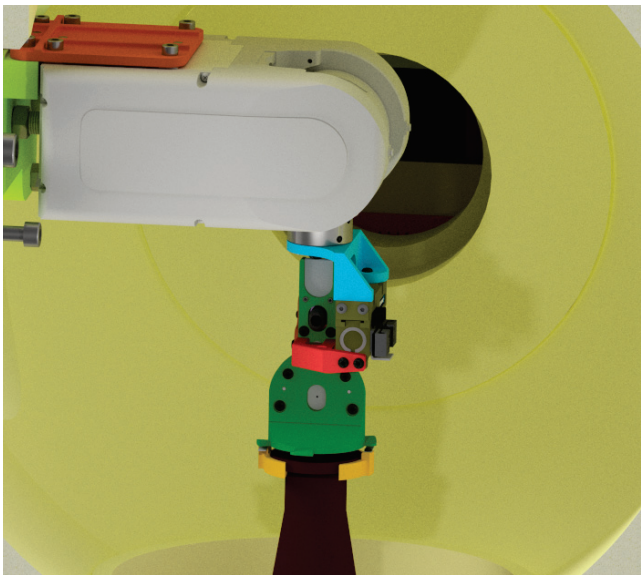

Fig. 108. Renderings of the inner part of the scattering chamber, the manipulator is in the gripping position and the cryo-cooler is disconnected and lowered.

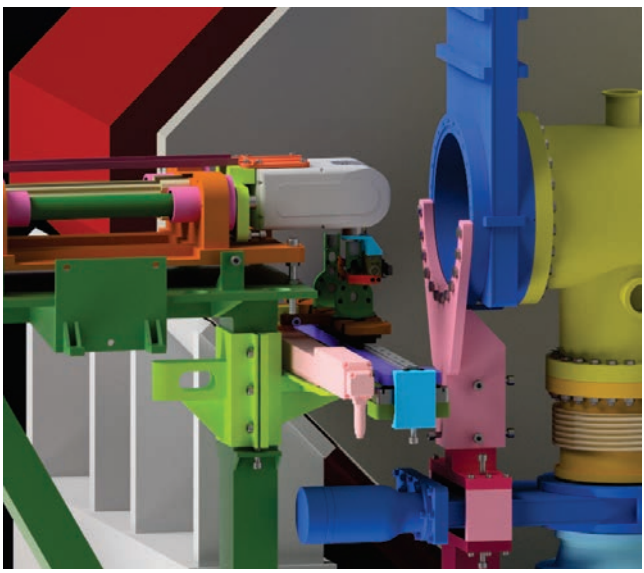

Fig. 109. (Color online) Renderings of the outer part of the scattering chamber with a detail of the storage position. In blue the gate valve.

The target holders are positioned on a rack that can be moved with the help of a linear servo-axis, in order to change the selected position. The lifting movement used to couple the target with the rack is given by two membrane cylinders coupled

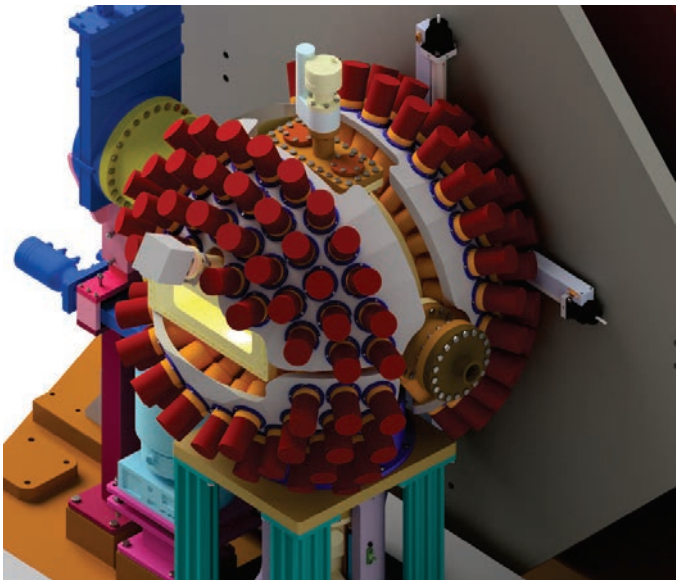

Fig. 110. Sketch of the gamma detector with its $LaBr_3$ cylinders.

by two limiters. This structure constitutes a simple storage system with up to six houses.

The offered solution guarantees already great reliability to the process and positioning precision.

#### 8.1.6. *Gamma detector*

The gamma-ray spectrometer composed of 110 $LaBr_2(Ce)$ scintillator detectors, each with its photomultiplier, will be installed around the scattering chamber, the sensors face at about 240 mm from the target. Since the expected radiation level is high, and this part of apparatus is very crowded with mechanical components and instrumentation, it became very difficult to operate on the gamma-ray detectors. To cope with this problem a solution is under study, is foresees a specific spherical like shape support split in many parts. Automatic systems guide each part towards and away from the chamber.

A sketch of the system is presented in Fig. 110.

### 8.2. *Vacuum chamber*

The FPD vacuum chamber follows the dipole and it is a challenging element of NUMEN.

It has some well-defined, mandatory characteristics and also a very precise functionality. Some of these requests are listed as follows:

- It must resist mechanically to vacuum, at values of $10^{-5} \div 10^{-6}$ mbar.

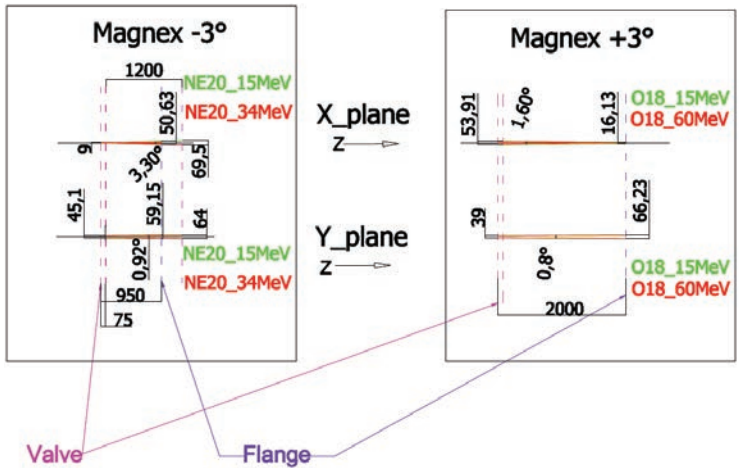


Fig. 111. Simulations of $^{20}$Ne and $^{18}$O beam size on $X$ and $Y$ planes at the gate valve immediately after the dipole and at the vacuum chamber exit.

- It must accommodate the whole Focal Plane Detector (FPD) that works in low gas pressure.
- It must be able to take out of the vacuum volume both the high intensity $^{20}$Ne and $^{18}$O beams.

The development of the vacuum chamber is based on simulations whose results are presented in Fig. 111.

In the $-3°$ MAGNEX configuration, the $15 \div 34$ MeV $^{20}$Ne beam size ranges from 4 mm to 70 mm in $X$ plane and from 45 mm to 64 mm in $Y$ plane on a distance of 1200 mm from the gate valve at the exit of the dipole. Similarly, in the $+3°$ MAGNEX configuration, the $15 \div 60$ MeV $^{18}$O beam size ranges from 54 mm to 16 mm in $X$ plane and from 39 mm to 66 mm in $Y$ plane on a distance of 2000 mm. One can note that the $^{18}$O beam converges in the $X$ plane instead the $^{20}$Ne diverges in the same direction. From these resulting beam spot a reserve of $15 \div 20$ mm was added to the beam envelope for safety considerations. The reason to evaluate the $^{20}$Ne beam over a distance of 1200 mm and the $^{18}$O beam over a distance of 2000 mm is shown in Fig. 112. In addition, both the beam pipes are sketched in the vacuum chamber (Fig. 112).

In the past the FPD was connected with the vacuum chamber and for the fine tuning of its position, a bellows allowed the movement of the whole system in a direction perpendicular to the gate valve, after the dipole. In the new setup the bellows is not foreseen since the two beam lines leaving the vacuum chamber are rigidly fixed to it, the fine focusing of the ejectiles is then obtained with the upgraded dipole surface $\alpha$-coil. A 3D model of the FPD is presented in Fig. 113.

Connections to the two lines for $^{20}$Ne and $^{18}$O beams are represented on the right of the FPD chamber.

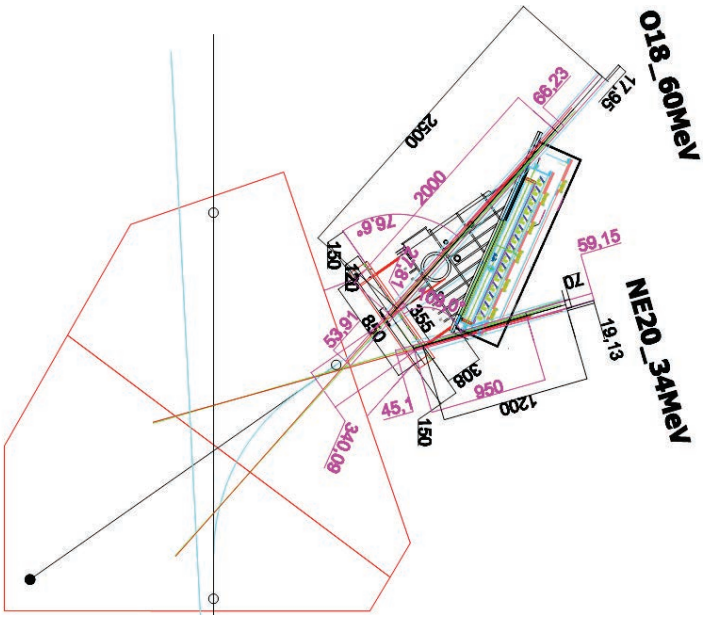


Fig. 112. The beam pipes shapes and sizes through the vacuum chamber, top view.

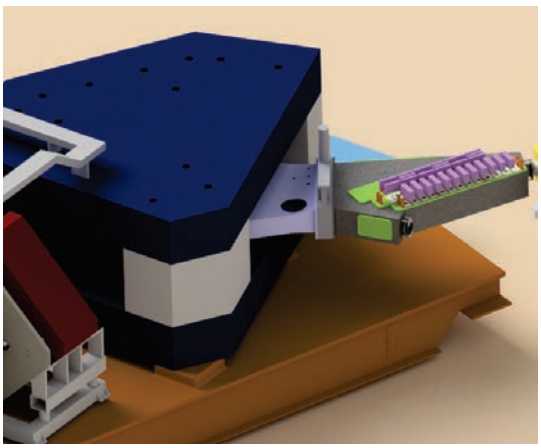

Fig. 113. 3D drawing of the MAGNEX apparatus. The vacuum chamber is on the right of the setup, in gray.

### 8.3. *Beam dump assembly*

The beam dump assembly includes the two beam lines that transport the ions from MAGNEX to the beam dump to stop the beam in a safe mode. Each line includes a bending magnet and a quadruplet composed of two quadrupoles and two steerer magnets. Each line serves different physics cases that allow ion beams

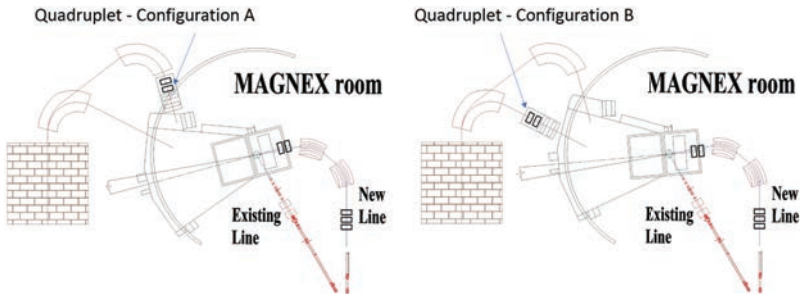


Fig. 114. Scheme of the MAGNEX room. Configuration A of the magnet quadruplet: the platform shows its axis at $-3°$ with the beam direction of the new line from cyclotron. Configuration B of the magnet quadruplet: the platform shows its axis at $+3°$ with the beam direction of the new line from cyclotron.

leaving MAGNEX on the two sides of the FPD. The two configurations for the two beam lines are shown in Fig. 114.

During the measurements, MAGNEX spectrometer can be placed in two different configurations. In configuration A the axis of the spectrometer will be at $-3°$ with respect to the High Intensity line; in configuration B at $+3°$. The beam trajectory to the beam dump will be different in the two cases, thus two different lines have been designed accordingly.

### 8.3.1. *System to displace the magnet quadruplet*

Instead to mount two different sets of magnet quadruplets for the two lines, to save money, it has been proposed a solution of a unique quadruplet set serving both beam dump lines. The total size of the quadruplet is about 100 cm in height, 100 cm in width, 150 cm in length. Each steerer magnet features about 800 kg weight, the first quadrupole about 1000 kg weight and the second one about 3000 kg weight.

Different solutions were considered for the handling of the magnet quadruplet. It is impossible to use a forklift for the limited available maneuvering space.

The use of a crane can be suitable considering not only the movement necessity of the quadruplet of magnets, but also the possible request for assembly and disassembly of the vacuum chamber containing the detectors, positioned after the dipole. However, this solution requires a sufficient height to carry out the movement maneuver that excludes the use of a bridge crane, complicated also by the positioning of the feet of the bridge that would be found along the trajectory of the MAGNEX apparatus going from HI to LI configuration.

Focusing on the movement of magnets quadruplets only, their support could become a suitable cart. In that case a specifically designed rail system has to be integrated in the project. However, the rotation of the magnet quadruplet is mandatory to guarantee the alignment of the system along the beam pipe, even if the positioning with respect the beam line demands for a leveling system that guarantee precise adjustments.

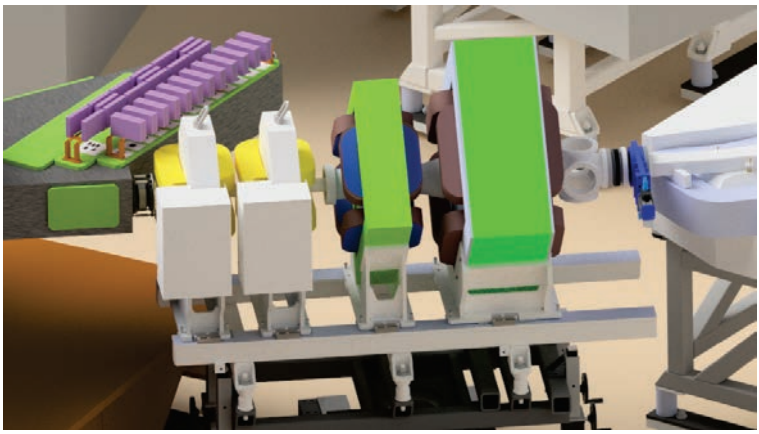

Fig. 115. View of the two steerers and of the two quadrupoles and their leveling system.

However, the route must bypass the MAGNEX rail (4 cm height).

Different solutions were analyzed for the rail system, rectilinear sections are the simplest solution. A piece of rail will be disassembled for the passage of MAGNEX in case this apparatus should connect at 0° with the existing beam line.

The cart includes height leveling mechanisms to align the magnet quadruplet axis to the beam line (Fig. 115) and a slewing gears that guarantee the connection of the magnet quadruplet to one out two ion lines alternatively

## 9. Development of Radiation Tolerant Targets

### 9.1. *Aims and requirements*

The goal of the target development activity is to design and build a number of very thin targets of specific enriched isotopes, to be irradiated with intense ion beams during the NUMEN experiments.

The main issues to deal with arise from the thickness of the target, which affects the energy resolution of the reaction product detection, and the dissipation of the heat produced in the target by the beam energy loss.

The proposed solution is that each target is made by deposition of few 100 $\mu$g/cm$^2$ film of the isotope of interest on a few microns thick support of HOPG, whose tasks are to withstand the target, to fully strip the reaction products, and to quickly transfer the heat to the target cooler.

After a number of trials and tests, the materials characterization procedures have been defined and the deposition parameters have been optimized, in order to minimize the effects of the thickness and rugosity on the energy resolution. Moreover, the cooling technique is under control: for each target, the maximum allowed values of the ion beam intensity can be evaluated, to avoid damages by heat.

The production of about 15 target-cooled systems per each isotope of typical thickness ranging from 150 to 500 $\mu$g/cm$^2$ is planned for the NUMEN Phase 4 experiments. Such targets will be produced at INFN-LNS laboratory.

During the experimental campaigns of the NUMEN project at the LNS Catania upgraded facility (NUMEN Phase 4), heavy-ion induced DCE reactions will be measured on different target isotopes. A list of the main ones is given below: $^{48}$Ca, $^{48}$Ti, $^{76}$Ge, $^{76}$Se, $^{82}$Se, $^{96}$Zr, $^{100}$Mo, $^{106}$Cd, $^{116}$Cd, $^{110}$Pd, $^{110}$Sn, $^{116}$Sn, $^{124}$Sn, $^{128}$Te, $^{130}$Te, $^{130}$Xe, $^{136}$Xe, $^{148}$Nd, $^{150}$Nd, $^{154}$Sm, $^{160}$Gd, $^{198}$Pt.

The main constraints in the design of the NUMEN target system come from:

(1) the heat deposited by the beam in the target;
(2) the resolution on the energy measurement of the DCE reaction products;
(3) the required compactness of the whole target/cooling system.

The first issue is related to the very intense, relatively low-energy heavy-ion beams which will be used in NUMEN Phase 4. It is planned to use $^{18}$O and $^{20}$Ne beams with an intensity up to 13 and 17 $\mu$A, respectively, with energies ranging from 15 MeV/u to 60 MeV/u. The beam spot will have a rectangular shape with standard deviations along the horizontal and vertical directions equal to $\sigma_x = 0.43$ mm and $\sigma_y = 1.06$ mm, respectively. The highest deposited power density in the target will be higher than $10^5$ W/cm$^3$ for the lowest beam energy (0.5 to 1.6 W deposited in targets between 140–550 $\mu$g/cm$^2$ thick, depending on the material and the beam). This amount of power would cause the melting of the target material. To prevent such a damage, a cooling system has been designed. It will be described in the following section.

Concerning the second point, the kinematics of the DCE reactions will be reconstructed from the energy and scattering angle of the reaction products measured with the MAGNEX spectrometer. In order to distinguish from the analysis of the inclusive energy spectra transitions to the ground state and to the first excited state of the residual nucleus, the energy resolution should be lower than the energy difference between these two states, usually on the order of 500 keV. To achieve such a resolution, the targets must be thin (few hundreds of nm) and uniform.

Finally, the system must be as compact as possible, in order to guarantee both sufficient room for the gamma-ray calorimeter placed around the scattering chamber (see Sec. 6) and a large solid angle aperture toward the detectors and instruments inside the scattering chamber.

The first isotopes that have been considered for the design of the target production process are the isotopes used in NUMEN Phase 2, i.e. $^{116}$Sn, $^{116}$Cd, $^{76}$Se, $^{76}$Ge, $^{130}$Te.

The choice of these isotopes was the result of a compromise between scientific interest and technical issues. Among the latter, emphasis was put on the possibility to separate the ground-state to ground-state DCE transition with MAGNEX alone (energy of the first excited state of the residual nucleus larger than 500 keV), and the possibility to build thin targets of isotopically enriched material.

Table 16. Power deposited by a 13 $\mu$A $^{18}$O beam in Sn and Se targets, and by a 17 $\mu$A $^{20}$Ne beam in Te, Ge, and Cd targets at different energies. The target surface densities for each target are indicated.

| Target (Beam) | Surface density [$\mu$g/cm$^2$] | Deposited power [W] | | | |
|---|---|---|---|---|---|
| | | 15 MeV/u | 30 MeV/u | 45 MeV/u | 60 MeV/u |
| $^{116}$Sn ($^{18}$O) | 219 | 0.46 | 0.27 | 0.20 | 0.16 |
| $^{76}$Se ($^{18}$O) | 144 | 0.29 | 0.17 | 0.13 | 0.10 |
| $^{76}$Ge ($^{20}$Ne) | 213 | 0.67 | 0.39 | 0.29 | 0.23 |
| $^{116}$Cd ($^{20}$Ne) | 519 | 1.47 | 0.87 | 0.64 | 0.52 |
| $^{130}$Te ($^{20}$Ne) | 250 | 0.67 | 0.4 | 0.29 | 0.24 |

As the target manufacturing process needs to be adapted to the physical and chemical properties of the isotopes, it can be designed and tested considering natural elements rather than enriched materials.

### 9.2. *Target heating*

A major issue that the design of the targets must face is the large deposition of heat during the passage of the intense swift heavy-ion beams through the target.

The power deposited inside the target depends, not exclusively, on the target thickness. To limit the degradation of the energy resolution and improve the heat dissipation (particularly in poorly conductive targets, such as Se and Te), each target thickness is capped to a certain value. The power released by $^{18}$O and $^{20}$Ne beams at their full intensity (13 and 17 $\mu$A, respectively) at energies ranging from 15 to 60 MeV/u vary from 0.5 to 1.5 W, depending on the target material and physical characteristics (cf. Table 16).

Without a properly designed cooling system, such powers would heat up the targets beyond their melting points; thermal radiation alone would not suffice. Analytical calculations show that even clamping the target in a cold frame cannot guarantee the target integrity.[26]

The heat dissipation can be enhanced by adding a highly thermally conductive substrate, such as HOPG, which is an artificial graphite made by a stack of graphene layers with an orientation parallel within 1°. This material, which can be produced in thin foils down to 2 $\mu$m thick, at room temperature has an in-plane thermal conductivity of 1950 W m$^{-1}$ K$^{-1}$, while the transverse conductivity is about 6 W m$^{-1}$ K$^{-1}$. Thanks to the very high in-plane conductivity, heat can quickly flow from the beam spot to a cold frame clamping the HOPG film leaving the target material exposed.

### 9.3. *Energy resolution*

The resolution in the measured excitation energy spectra must be sufficiently small to separate DCE transitions to the ground state and to the first excited state of

Table 17. Total expected energy resolution for some target considering individual contribution.

| | $^{116}$Sn | $^{116}$Cd | $^{76}$Se | $^{76}$Ge | $^{130}$Te |
|---|---|---|---|---|---|
| Maximum thickness [$\mu$g/cm$^2$] | 219 | 865 | 145 | 213 | 249 |
| Target energy spread [MeV] | 0.24 | 0.56 | 0.13 | 0.15 | 0.15 |
| HOPG energy spread [MeV] | 0.22 | 0.11 | 0.22 | 0.15 | 0.16 |
| MAGNEX resolution [MeV] | 0.26 | 0.29 | 0.26 | 0.29 | 0.29 |
| SC energy spread [MeV] | 0.27 | 0.3 | 0.27 | 0.3 | 0.3 |
| Total resolution [MeV] | 0.49 | 0.71 | 0.45 | 0.47 | 0.47 |

the residual nucleus. For the reactions $^{116}$Sn($^{18}$O, $^{18}$Ne)$^{116}$Cd, $^{76}$Se($^{18}$O, $^{18}$Ne)$^{76}$Ge, $^{76}$Ge($^{20}$Ne, $^{20}$O)$^{76}$Se, $^{130}$Te($^{20}$Ne, $^{20}$O)$^{130}$Xe, the energy gap between the two states is about 500 keV, whereas it is 1.3 MeV for the $^{116}$Cd($^{20}$Ne, $^{20}$O)$^{116}$Sn reaction.

Several factors contribute to the energy resolution: the energy definition $\delta E_{\rm SC}$ of the beam from the LNS Superconducting Cyclotron ($\delta E_{\rm SC}/E \approx 0.1\%$ FWHM), the intrinsic energy resolution of the MAGNEX spectrometer $\delta E_{\rm MAGNEX}$ ($\delta E_{\rm MAGNEX}/E \approx 0.1\%$ FWHM) for a beam spot size $\sigma \sim$ mm, and the spread of energy loss in the target-substrate assembly $\delta E_{\rm Target}$ (energy straggling in the target and in the substrate, dispersion due to the random depth of the reaction point in the target). Straggling and dispersion energy spreads are worsened by thickness nonuniformity.

In principle, an additional contribution comes from the variation of the reaction product energy with the scattering angle over the large acceptance of the MAGNEX spectrometer (the so-called "kinematic effect"). For quasi-elastic reactions at forward angles, including DCE, this contribution is very small and usually negligible. The total energy resolution is thus

$$\delta E^2 \approx \delta E^2_{\rm SC} + \delta E^2_{\rm MAGNEX} + \delta E^2_{\rm Target+HOPG}\,. \tag{8}$$

As an example, Fig. 116 shows the total expected resolution $\delta E$ as a function of the target thickness for the $^{116}$Sn($^{18}$O, $^{18}$Ne)$^{116}$Cd reaction at 15 MeV/u. Here, the thickness nonuniformity is supposed to follow a Gaussian distribution, with a standard deviation equal to 28%. It can be observed that for an average target thickness below $\approx 220$ $\mu$g/cm$^2$ with HOPG substrate 2 $\mu$m thick, the total energy resolution remains within the desired range.

The limit thickness (or equivalently areal density in $\mu$g/cm$^2$) for the other targets have been evaluated similarly; results are listed in Table 17. The listed thicknesses allow to remain below the resolution limit, but they could be further adjusted to meet cooling or other experimental requirements.

### 9.4. *Numerical calculations of the temperature*

To validate the use of an HOPG substrate clamped by a cold frame as a system to cool down the target material, a numerical code was written. This code solves the

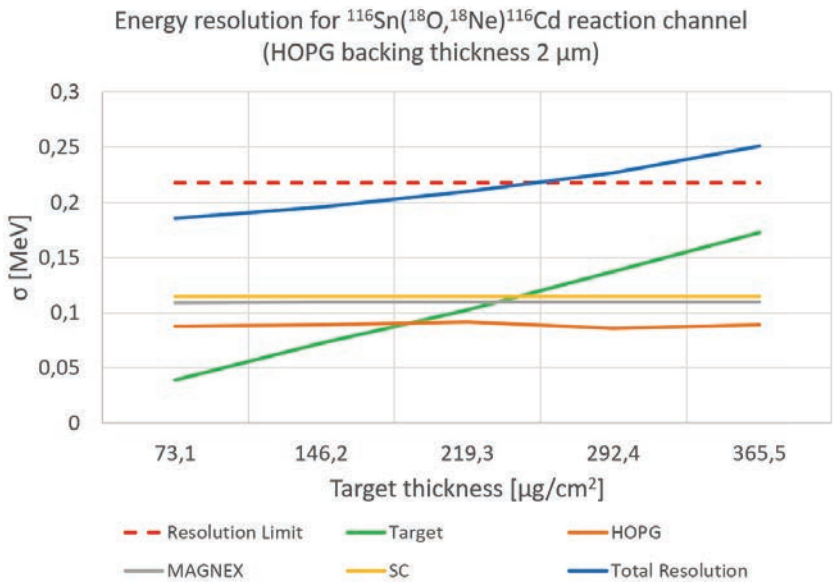


Fig. 116. Total and detailed contributions to the energy resolution reported as functions of the target thickness, for the $^{116}$Sn($^{18}$O, $^{18}$Ne)$^{116}$Cd DCE reaction.

time-dependent temperature equation inside the target + graphite system until the steady state is reached. Calculations were performed assuming target thicknesses suitable for matching the aforementioned resolution requirements listed in Table 16. Like the beam spot, targets are rectangular shaped, measuring 1 cm in the horizontal direction and 1.4 cm in the vertical one. The HOPG substrate thickness was assumed to be 2 $\mu$m. The temperature of the cold frame was set equal to 20 K.

Calculations were performed assuming a 20 $\mu$A beam at 15 MeV/u and a super-Gaussian beam spot with standard deviations $\sigma_x = 0.43$ mm and $\sigma_y = 1.06$ mm. The beam intensity was lowered to 13 $\mu$A for the Se target, since its low melting point and thermal conductivity forbid the use of a more intense beam current. According to the DCE reactions channels of interest, Sn and Se targets are supposed to be irradiated by a $^{18}$O, while Te, Ge and Cd by a $^{20}$Ne beam. The temperature in the graphite along the radial coordinate, i.e. along a direction transverse to the beam, is different from the cold frame temperature only in a annular region of width 10 $\mu$m from the edge of the target. Therefore the exact diameter of the graphite substrate does not influence the steady-state temperature distribution in the target, as long as it is larger than the target diameter. Furthermore, the heat equation needs to be solved explicitly only in the target and in the underlying graphite volume, assuming that the temperature in the graphite at a radial coordinate larger than the target radius is equal to the cold frame temperature.

The steady state is reached within 100 ms for all of the materials, as shown in Fig. 117 and Table 18. In Fig. 117, the targets were assumed to be 400 nm thick

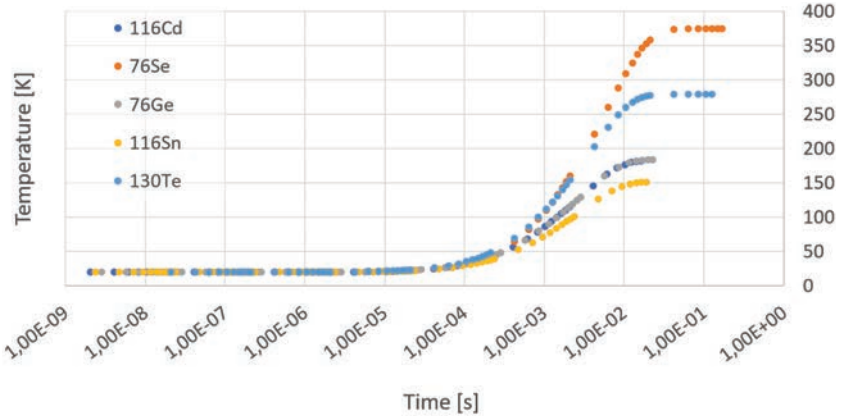


Fig. 117. Evolution of the temperature as a function of time at the center of a 400 nm thick target of various materials irradiated by a 20 $\mu$A beam with an energy of 15 MeV/u. Each target remains safely below the melting point.

Table 18. Melting and steady-state temperatures for different targets backed by a HOPG substrate under a beam with an intensity of 20 $\mu$A ($*$ lowered to 13 $\mu$A for Se) and an energy of 15 MeV/u. The surface densities of the targets are also indicated.

| Target isotope | $^{116}$Sn | $^{76}$Se* | $^{76}$Ge | $^{116}$Cd | $^{130}$Te |
|---|---|---|---|---|---|
| Surface density [$\mu$g/cm$^2$] | 219 | 144 | 213 | 519 | 250 |
| Beam | $^{18}$O | $^{18}$O | $^{20}$Ne | $^{20}$Ne | $^{20}$Ne |
| Melting $T$ [K] | 505 | 494 | 1211 | 594 | 722 |
| Steady $T$ [K] | 213 | 432.4 | 249 | 251 | 381.8 |

to allow a direct comparison among them. The final temperatures differs from the ones reported in Table 18 due to the different beam spot shape: circular in the former and rectangular (and smaller in size) in the latter. However, in both cases the maximum temperatures are lower than the melting point for all of the isotopes.

In practice, the heat can be dissipated from the graphite by a cold sample holder made of copper, shown in Fig. 118, and maintained at low temperature by a cryo-cooler. The detailed numerical calculations presented above are realistic but can be applied only to a simple geometry with a limited size. Evaluating in such a way the thermal behavior of a complete target system would require an unpractical computational power and time. Therefore, the design of the sample holder was performed using the multipurpose physics simulation package COMSOL$^{TM}$. The accuracy of the latter for our application has been checked by comparison to the detailed numerical calculations for the simpler system composed of the target material and the underlying graphite volume. For this validation, the same physical arrangement, with the same conditions, was considered. The time needed to reach thermal equilibrium and final temperatures obtained with COMSOL are consistent with the one obtained with the numerical calculations, within a 7% error.

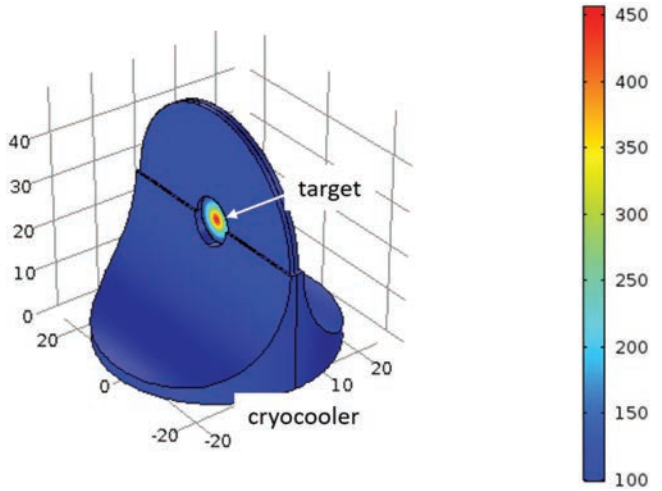


Fig. 118. (Color online) Output of a simulation performed using the software COMSOL; the copper sample holder, kept at ≈100 K, is blue-colored. A Sn film is here used as target.

The shape of the sample holder presented in Fig. 118 has been designed for a circular beam spot. For the current beam shape, a slightly different, rectangular shaped opening for the target will be used, to optimize the dissipation of the heat produced by the rectangular beam. A prototype will be soon produced and tested. However, the working principle remains unchanged and this version will be used in oncoming tests. The shape of the object has been designed to facilitate the heat flow toward the cold finger. In particular, the base is wide to ensure a large contact surface area between the sample holder and the cold finger of the cryo-cooler. On the contrary, the top part is thinner to guarantee a wide solid angle aperture for the possible additional detectors surrounding the target (e.g. $\gamma$-ray calorimeter). The two smaller slots on top of the holder can host additional targets used for example for beam alignment or for measuring the background from reactions on the target graphite backing. The diameter of the copper disks is 5 cm, the HOPG substrate one is 2.5 cm.

### 9.5. *Target production and characterization*

The target system will be composed by a HOPG substrate and a thin film of the target isotope. The substrate diameter will be 2.5 cm, while the target dimensions will be $1 \times 1.4$ cm$^2$. The HOPG thickness will be of 2 $\mu$m; the target will be from 150 to 500 $\mu$g/cm$^2$ thick, depending on the material.

#### 9.5.1. *HOPG substrate characterization*

Since the substrate thickness is not expected to influence the target deposition, the HOPG used for the first trials of deposition is a cheaper one, that is nominally

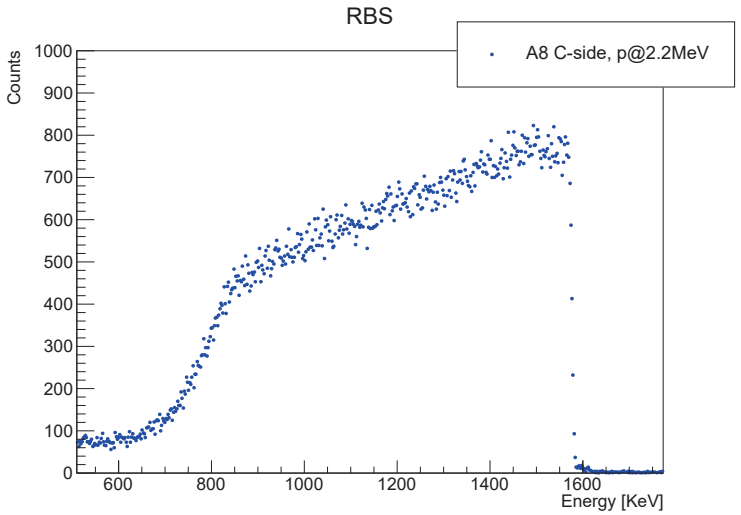


Fig. 119. RBS spectrum of the Sample A8 (HOPG 2200 $\mu$g/cm$^2$).

10 $\mu$m thick. Since the HOPG density is around 2.2 g/cm$^3$, the thickness can be expressed also as 2200 $\mu$g/cm$^2$. This kind of HOPG is largely used for electronic components, therefore it has an acrylic adhesive on one side. Several studies aimed to remove the acrylic have been done, as oxygen plasma etching, thermal treatments and ultrasonic baths. The best results have been obtained with ultrasound baths in acetone. In order to verify the complete removal of the adhesive layer, some samples have been analyzed with Rutherford Backscattering (RBS) at INFN-LNL. RBS tests have been performed with a proton beam at 2174 keV, using a silicon detector placed at 150° with respect to the beam line.

In Fig. 119 a typical RBS spectrum acquired with a 2200 $\mu$g/cm$^2$ thick HOPG foil, treated with ultrasound bath to remove the acrylic adhesive, is shown. The right limit of the plateau (at 1580 keV) corresponds to the energy of a proton which has backscattered on a carbonium atom. There is no other peak that can be referred to other elements contained in the acrylic (as oxygen). This observation confirms that there is no more acrylic on the HOPG sample. The thickness of the sample inferred from this RBS spectrum is consistent with the nominal thickness (10.05 $\mu$m).

To study the topography and surface uniformity of this HOPG, Field Emission Scanning Electron Microscopy (FESEM) analysis has been performed. Figure 120 shows that the surface of the 2200 $\mu$g/cm$^2$ thick HOPG is almost uniform and flat, guaranteeing a good substrate for a uniform deposition. Thinner HOPG films, provided in sheets 1100 $\mu$g/cm$^2$ and 440 $\mu$g/cm$^2$, are flatter, as shown by Fig. 121: on the left the FESEM picture presents the overall topography, while the right image is obtained with Atomic Force Microscopy (AFM) and shows the thickness of the surface structures. Both the images show that this HOPG is flat within tens of nm.

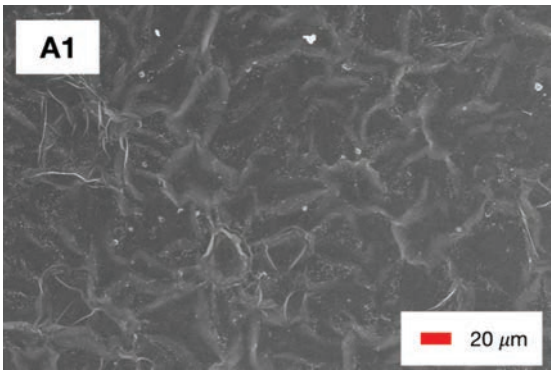


Fig. 120. FESEM image of the Sample A1 (HOPG of 2200 $\mu$g/cm$^2$).

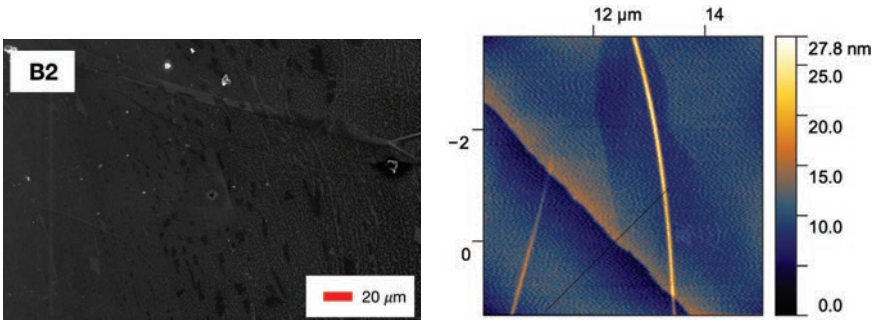


Fig. 121. FESEM (on the left) and AFM (on the right) images of the Sample B2 (HOPG of 1100 $\mu$g/cm$^2$).

The best tool to measure the thickness of thin samples is the alpha particle transmission, which can also give information concerning the thickness uniformity. To measure with accuracy the target deposition thickness, the HOPG thickness has to be measured before the deposition. Data here reported have been acquired using a silicon detector, working in a vacuum chamber. The alpha particles are supplied by an $^{241}$Am source: this isotope emits alpha particles of 5486 keV, that are collimated with an aluminum collimator (diameter of $\simeq 3$ mm) before reaching the sample under study. A $^{152}$Gd source has also been used to perform the energy calibration.

Figure 122 shows the energy spectrum of $^{241}$Am source $\alpha$ particles of 5486 keV that have crossed a sample of 2200 $\mu$g/cm$^2$ of HOPG. The spectrum can be fitted with a crystal ball function, which is typically used for spectra derived from energy loss processes. The peak maximum is around 3580 keV, that corresponds to a crossed thickness of about 2207 $\mu$g/cm$^2$ (10.4 $\mu$m). From the systematic study by alpha transmission of different HOPG samples, the HOPG that is nominally 2200 $\mu$g/cm$^2$ thick has a thickness always varying in the range 2200–2245 $\mu$g/cm$^2$; RBS measurements confirm these values within 1%.

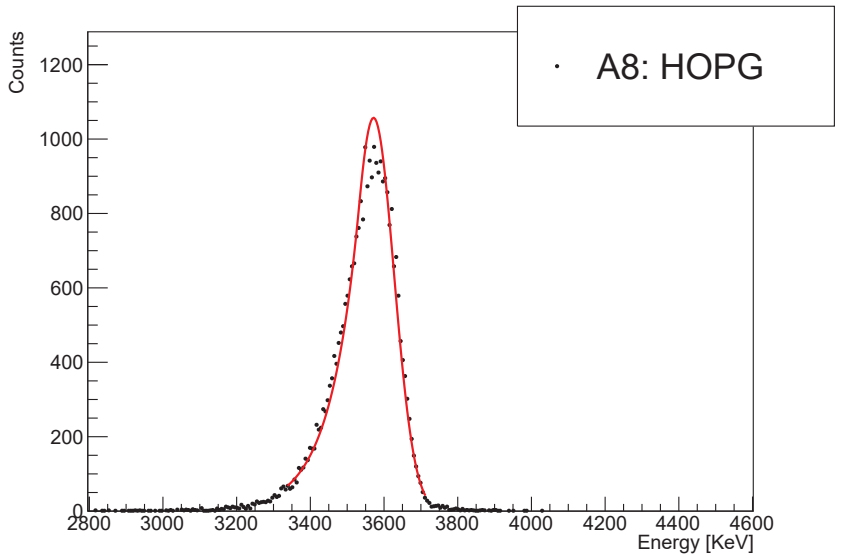


Fig. 122. (Color online) Energy spectrum of alpha particles crossing the Sample A8 (HOPG of 2200 $\mu$g/cm$^2$). The red curve is the result of a fit with crystal ball function.

The FWHM of the spectrum gives information about the thickness uniformity, even if a small contribution is given also by straggling effects and electronics noise, according to

$$\sigma^2_{\text{tot}} = \sigma^2_{\text{nonuniformity}} + \sigma^2_{\text{noise}} + \sigma^2_{\text{straggling}} \,.$$

The straggling effects in a HOPG sample 2200 $\mu$g/cm$^2$ thick contribute to the peak $\sigma$ for around 20 keV. The electronic noise can be studied through by analyzing the $\sigma$ of the alpha peak acquired without any sample between the source and the detector: for the used setup it is 13 keV. The $\sigma$ of the spectrum of Fig. 122 is 55 keV. Thus, for the sample in figure, the $\sigma$ due to the nonuniformity of the sample is around 50 keV, corresponding to 71 $\mu$g/cm$^2$ (that means a thickness irregularity of 3%).

Figure 123 shows the energy spectrum of alpha particles that have crossed a sample of 5 $\mu$m (nominally) HOPG (1100 $\mu$g/cm$^2$). The peak maximum is at 4345 keV, that means a sample thickness of about 1393 $\mu$g/cm$^2$, considerably larger than the nominal thickness. An RBS measurement with a proton beam of 2200 keV has confirmed this value, measuring a thickness of 1404 $\mu$g/cm$^2$ (agreement within 0.1%). Since the $\sigma$ of the alfa transmitted peak is 30 keV and the straggling effects are responsible for $\sigma$ of around 18 keV, the $\sigma$ due to thickness nonuniformity is 20 keV, that corresponds to 22 $\mu$g/cm$^2$. This value means that the thickness irregularity of this thinner HOPG is less than the 2% of the total thickness, lower than the one related to the 2200 $\mu$g/cm$^2$ HOPG.

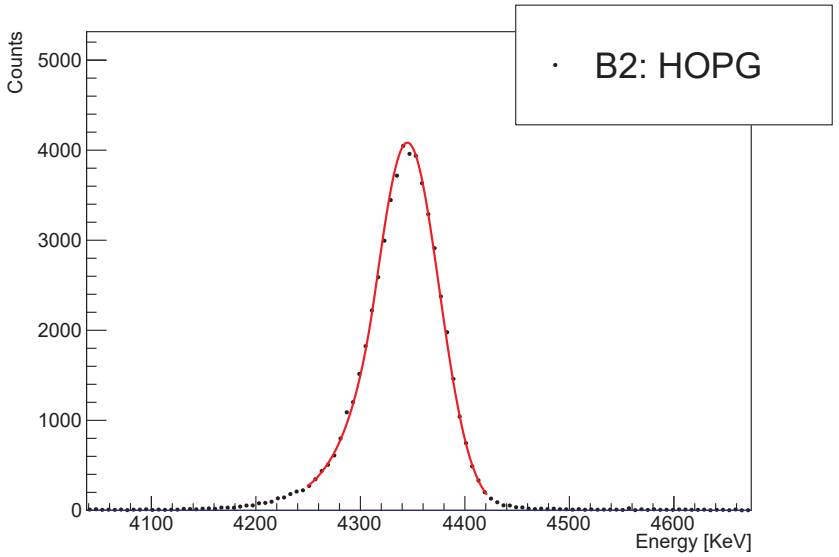


Fig. 123. Energy spectrum of alpha particles crossing the Sample B2 (HOPG of 1100 $\mu$g/cm$^2$)

### 9.5.2. *The target deposition*

The deposition of the target isotope can be done with different Physical Vapor Deposition (PVD) techniques; since some isotopes material of the targets are rare and costly, it is necessary to produce good quality films using small quantity of material and to have a precise control of the deposition parameters. For these reasons the electron beam evaporation and thermal evaporation techniques are considered the best solutions for our purpose, thanks to high control over the deposition and flexibility. In particular, thermal evaporation has been widely used in target production by the Target Production Laboratory of the LNS. A solid know-how of the equipment and the technique itself has been gained along the years. However, thermal evaporation is not well suited when high melting point materials must be evaporated, like Ti or Mo; in such cases, electron beam deposition is preferred.

HOPG is the ideal material for dissipating heat, but its crystal structure makes it a poor substrate for thin layers. The adhesion on its inert surface can be enhanced by using a very thin buffer layer of some specific material. The idea was successfully proved by using Cr and Bi as buffer. Such kind of materials stick easily on most surfaces and are therefore widely used for such purposes. However, due to kinematic reasons, they could interfere with the data of interest; other materials like Al or Mg, more fit for the task, will be studied as alternative buffer.

The temperature of the substrate plays also a key role in obtaining a smooth deposition for some cases. Indeed, for certain materials, providing heat to the graphite substrate during the deposition can promote the formation of bigger grains and facilitate coalescence among grains. Conversely, for other elements a better

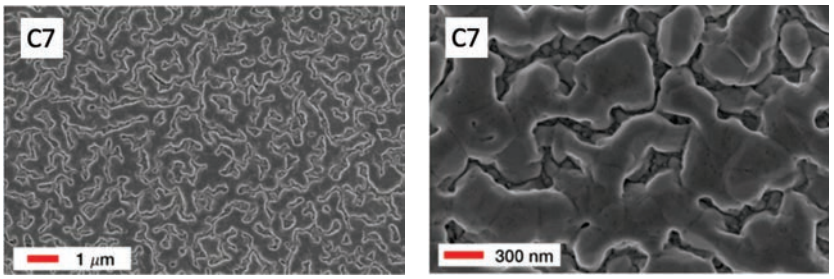


Fig. 124. FESEM image of Sample C7 (Sn deposition on 440 $\mu$g/cm$^2$ HOPG).

uniformity can be achieved by growing an amorphous film, with no heat and a higher deposition rate.

First prototypes have been produced with Te and Sn; examples of FESEM images of these targets deposition are shown here, to evaluate the target topography.

Concerning the Sn targets, different trials varying the HOPG temperatures from 393 K to 448 K have been performed, to investigate how the heat helps the film uniformity. Also the effect of a very thin layer of around 10 nm of Chromium on the substrate has been studied, to find out its role in facilitating the deposition adhesion. The best results have been obtained heating the substrate at 403 K, using a Chromium buffer. The FESEM images of a prototype of this type, named C7, are reported in Fig. 124.

Figure 124 is the FESEM image of the target deposited on the 440 $\mu$g/cm$^2$ thick HOPG. The deposition covers all the substrate, creating an almost uniform layer. The deposition thickness seems to have some irregularities, but not considerably high with respect to the average thickness.

Also for Te different trials of deposition have been done, at room temperature and at 373 K, with and without the Chromium buffer.

From the systematic study of the deposition parameters, it seems that the presence of a Chromium buffer has no influence on this deposition. Regarding the substrate temperature, the substrate heating has been resulted to be not necessary to obtain smooth depositions. For these reasons, the tellurium final targets will be deposited, without Chromium buffer, on HOPG maintained at room temperature (300 K).

FESEM images of Fig. 125 show a typical prototype of Te targets. The deposition of the prototype named C4 has been performed on the 440 $\mu$g/cm$^2$ thick HOPG. The deposition is almost uniform, with small grains on a quite flat underlying layer of deposition.

### 9.5.3. *Target thickness and uniformity measurements*

To evaluate the target thickness and its uniformity, measurements of alpha particles transmitted through the target have been performed.

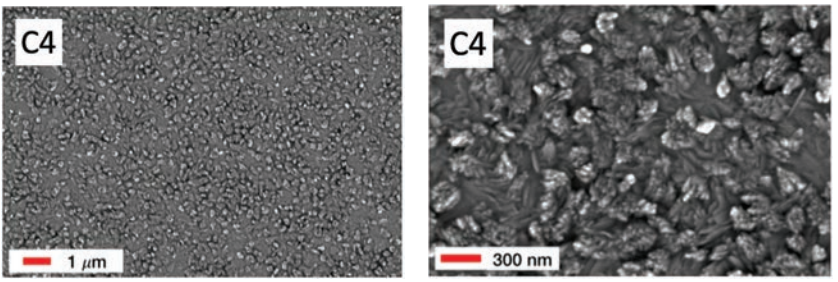


Fig. 125. FESEM image of Sample C4 (Te deposition on 440 $\mu$g/cm$^2$ HOPG).

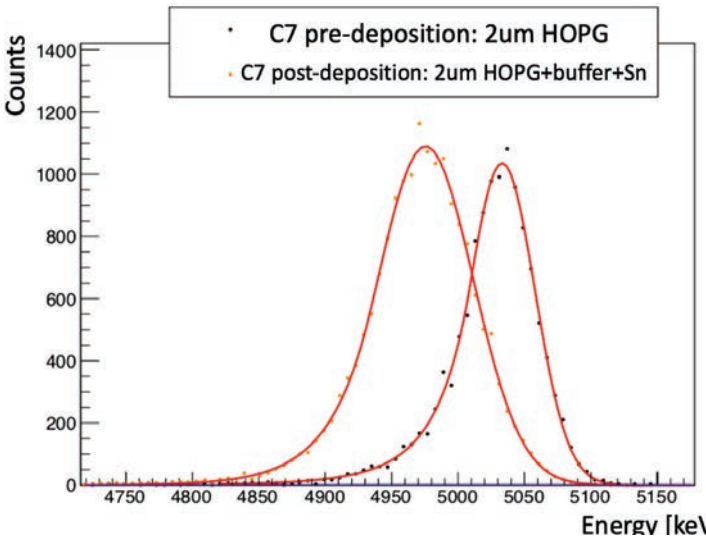


Fig. 126. (Color online) APT spectra acquired with the C7 substrate only (2 $\mu$m HOPG) and after the deposition with the whole target system (Tin deposition and HOPG substrate). Crystal ball function fits of the two peaks are also shown in red.

Figure 126 shows the alpha energy spectra of the prototype of Tin target system named C7, before and after the target deposition. From the spectrum acquired before the target deposition, the HOPG thickness has been deduced as 580 $\mu$g/cm$^2$ with a thickness nonunformity of 4%. Since the Chromium buffer is 40 nm thick (thickness evaluated by RBS measurements, shown below), the comparison between the spectrum acquired before (with a sample of HOPG only) and after the deposition allows the evaluation of the energy loss in the Tin layer; in this way the target thickness can be deduced. For the sample shown, the Tin deposition is 98 $\mu$g/cm$^2$.

The target uniformity can be deduced from the $\sigma$ of the alpha peak after the deposition, as

$$\sigma^2_{\text{after deposition}} = \sigma^2_{\text{before deposition}} + \sigma^2_{\text{target straggling}} + \sigma^2_{\text{target nonuniformity}} \cdot$$

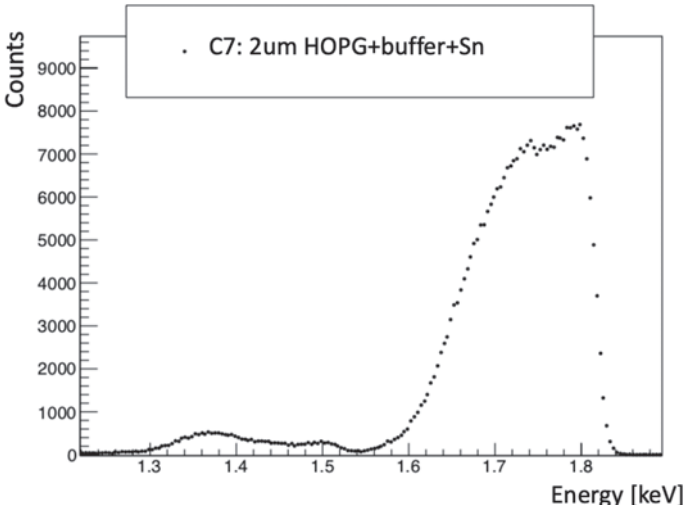


Fig. 127. RBS spectrum of the target system C7, measured with a 2 MeV alpha beam, detected at 160°. The only contributions of target deposition and buffer can be observed, since the beam energy is too low to detect also the HOPG substrate. An additional contribute appears at lower energy, related to impurities in the deposition layer.

The $\sigma^2_{\text{before deposition}}$ is the one measured before with the sample made only of HOPG, and contains the detector resolution, the HOPG nonuniformity contribution and the straggling effects in the HOPG. Evaluating the straggling in the target deposition, the target nonuniformity $\sigma$ can be deduced. For the sample C7, for example, the target nonuniformity is around 61 $\mu$g/cm$^2$, that means deposition thickness irregularities around 62% of the overall deposition thickness.

Figure 127 shows the RBS energy spectrum: the measurements have been performed with an alpha beam of 2 MeV, measuring at an angle of 160°. In the energy spectrum, the contribution at higher energies is related to the Tin target deposition; the peaks at lower energies, instead, are related to the thin Chromium buffer and to some impurities of other elements caused by a bad cleaning of the vacuum chamber of the evaporator. The thickness result obtained with APT for the C7 prototype has been confirmed by RBS, from which the C7 target thickness has been estimated as 92 $\mu$g/cm$^2$ (agreement with alpha measurement within 6%).

For the tellurium prototype C4, the same study has been performed. The deposition of the substrate has been evaluated with APT as 283 $\mu$g/cm$^2$ with a thickness nonuniformity of 10%. The RBS measurements, performed at 160° with an alpha beam of 2 MeV, defined a thickness of 262 $\mu$g/cm$^2$. The agreement between the APT and the RBS thickness results is within 3%.

### 9.6. *In-beam tests of the targets*

In-beam tests were performed at Universidad Nacional Autónoma de México (UNAM) and Instituto Nacional de Investigaciones Nucleares (ININ), Mexico City.

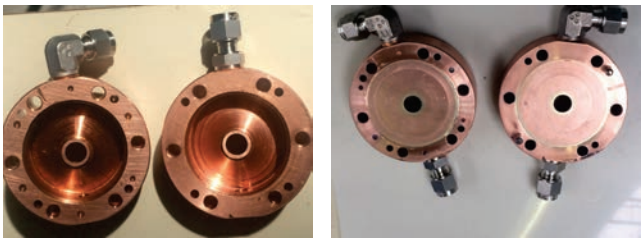

Fig. 128. (Left) Copper sample holder with $LN_2$ flowing chambers open. (Right) Copper sample holder with $LN_2$ flowing chambers closed and soldered.

The tests had a twofold purpose. On one hand, the validation of the code described in Subsec. 9.4; second, a first estimation of the effects of sputtering on thin targets.

A cooling system had been designed to be used in such tests. It is simpler, although similar, to the one that will be installed in NUMEN Phase 4. The working principle remains unchanged, that is clamping a large graphite disk with two cooled copper disks; in this case, the cooling was provided by liquid nitrogen ($LN_2$). The copper disks are larger than the one shown in Fig. 118, since $LN_2$ must flow within them (Fig. 128).

In both the facilities $^{12}C$ ions were accelerated at 3 MeV (UNAM) and 15 MeV (ININ), with intensities of 25 $\mu$A and 1 $\mu$A, respectively. The beam energies were lower with respect to the ones which will be used in NUMEN Phase 4, but the deposited energy was of the same order of magnitude (between 4 and 10 W). This is not a concern for the heat-related part of the test, but it could affect the evaluation of sputtering effects. For light ions such as $^{12}C$, $^{18}O$ or $^{20}Ne$ the maximum sputtering yield is obtained at energies below 100 keV; the yield steadily decreases with increasing the ion energy. However, a significant percentage of the target material could be removed even at much higher energies, especially at high beam intensities.

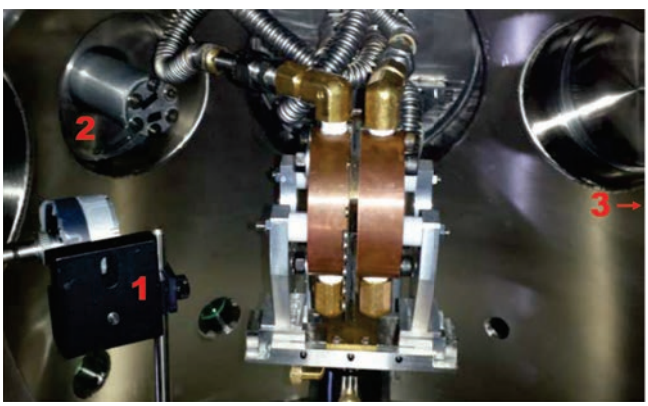


Fig. 129. Side view of the inside of the scattering chamber at UNAM, the detectors numbered as follows: (1) Si detector for real-time RBS analysis, (2) X-ray detector and (3) out of sight, the Faraday cup.

9.6.1. *Numerical code validation*

The temperature on the target was monitored by thermal cameras from outside the scattering chamber; while a thermocouple was used to measure the temperature of the copper sample holder. Two sets of measurements were performed, the first using a HOPG target (mainly for calibration purposes) while the second using a Sn+ HOPG target. Targets were irradiated at different intensities, from 3 to 7 $\mu$A. Collection of reliable data was hampered by the physical limits of the thermal cameras (temperature was too low to be measured for beam currents smaller than 5 $\mu$A and the effect of sputtering. Even with beam currents of few $\mu$A, a Sn target would get consumed in some tens of minutes. Nevertheless, the agreement with measured data and calculated values is remarkable for both of the targets as shown in Figs. 130 and 131.

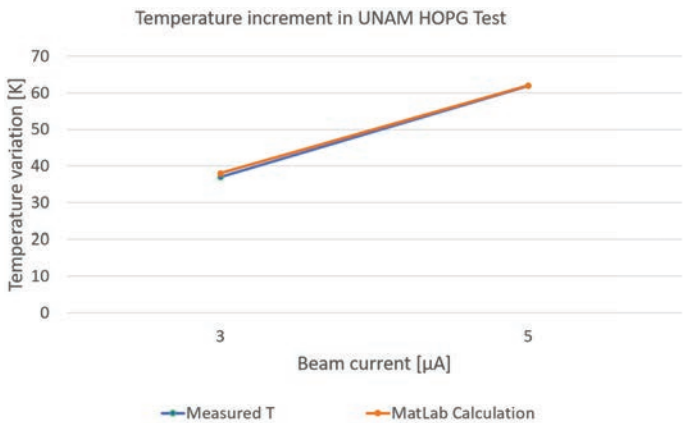


Fig. 130. (Color online) Temperature increase in an HOPG target obtained using a beam current of 3 and 5 $\mu$A (in blue), compared with numerical results (in orange).

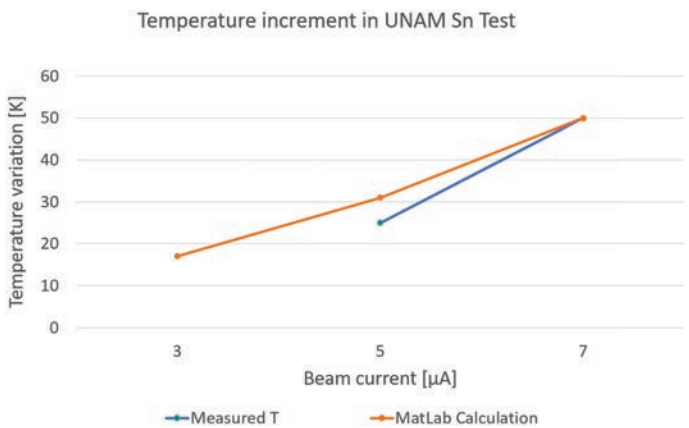


Fig. 131. (Color online) Temperature increase in an Sn target obtained using a beam current of 3, 5 and 7 $\mu$A (in blue), compared with numerical results (in orange).

#### 9.6.2. *Sputtering evaluation*

As already mentioned, the energy used in this test and the one which will be used in NUMEN differ by a factor of about 100. Unfortunately, there is a lack of data and models (mostly empirical) in literature for energies higher than 1 MeV for the projectile-target pairs studied in NUMEN. However, this test can give a first, even if rough, estimation of the life expectancy of a target.

A 250 $\mu$g/cm$^2$ thick Te target was irradiated by a 4 $\mu$A beam of $^{12}C^{3+}$. A Si detector was placed upstream to the target, as shown in Fig. 129, to detect backscattered C ions. After about 30 minutes of irradiation, no further events were collected by the Si detector, signaling that the target had been removed.

Considering the differences between this test and NUMEN (O and Ne ion beam species instead of C, ion energy of 270 MeV instead of 3 MeV, and a beam current of 17 $\mu$A instead of 4 $\mu$A), it is possible to obtain a rough evaluation of the effects of nuclear sputtering alone; serious damages on the target would occur at least after 9 days, which is enough to allow a safe conduction of an experimental run.

Specific tests are foreseen to systematically explore the characteristics of the target involved in the NUMEN experimental runs. In particular radiation tolerance, heat dissipation and life expectancy will be studied.

### 9.7. *Target plus HOPG hardness under NUMEN beams*

The HOPG main function is to dissipate the large amount of heat generated by the ion beam, during nuclear reactions. Because of this, the most important HOPG property to be analyzed is its thermal conductivity. This primarily reflects the integrity of the material crystallographic structure, since the thermal conductivity in allotropic forms of carbon strongly depends on the phonon vibration in the crystal lattice.[96] Although information relating thermal conductivity and defects formation can be found in literature for some carbon compounds — Ref. 97 for instance, suggests that only 0.25% concentration of defects in graphene results in significant reduction of thermal conduction property by around 50% — no data for HOPG was found, thus making it necessary to determine safe operation conditions of HOPG backing under high-intensity heavy-ion irradiation. The result found in Ref. 97 can be important since HOPG is a stack of graphene sheets with a slight disorientation between each other. Due to its particular arrangement of atoms, HOPG has excellent in-plane thermal conductivity (about 2000 W/m $\cdot$ K at room temperature).[96]

The purpose of this study is to estimate of how long time under intense beam flux the HOPG material will maintain its thermal conductivity in order to preserve the target integrity. This information will indicate how frequently the targets must be replaced under the experimental run condition. The HOPG material will be analyzed before and after exposure to particle beams, using techniques that provide information on damage related to defect formation such as atom dislocations, vacancies produced and broken chemical bonds. All this kind of defects decrease the

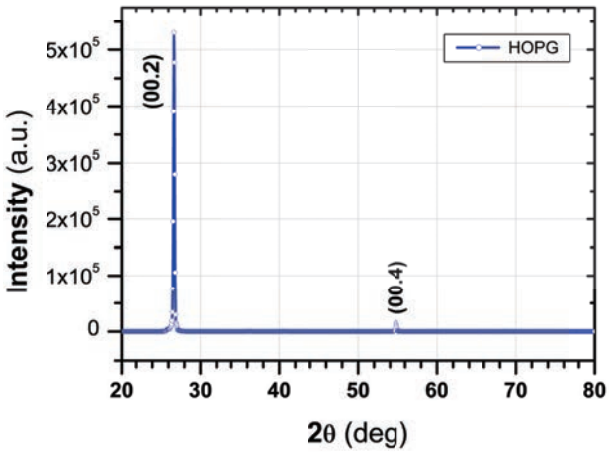


Fig. 132. X-ray diffractogram ($\theta - 2\theta$ scan) showing only reflections of planes parallel to the sample surface. This result indicates a high ordering of the atoms in the HOPG crystal lattice.

periodic and long order arrangement of atoms needed for crystalline structure, also decreasing its thermal conductivity.[96]

Preliminary experimental results for a nonirradiated HOPG foil using X-ray diffraction technique at Centro Universitário FEI, São Paulo, Brazil, proves that HOPG can be treated as a single crystal, indicating the high periodicity of the carbon atoms (see Fig. 132).

Another technique that can be used to study defect formations is the Raman spectroscopy. The Raman spectrum for HOPG is quite similar to one for graphene, as can be seen in Fig. 1 of Ref. 98, where the difference in intensities is due to the number of graphene sheets present in the HOPG structure. In that figure, the Raman spectrum shows a G-band characterized by crystal lattice vibrations only due to $sp^2$ type bonds. The $sp^2$ bonding results in efficient heat transfer by lattice vibrations. It is expected that the irradiation process breaks these bonds, leading to a change in the shape and position of the Raman peaks. In Ref. 96 the relationship of HOPG thermal conductivity ($K$) with material purity, quality and crystallinity is shown. The $K$ value for pyrolytic graphite constitutes the bulk graphite limit of $\sim 2000$ W/mK at room temperature. At low temperature, $K$ is proportional to $T^{\gamma}$ where $\gamma$ varies in a wide range depending on graphite quality. Computer simulations were carried out, using the Transport of Ions in Matter (TRIM) program[99] to verify the energy transfer from the heavy-ion beam to the target and the number of vacancies arising from it, under different conditions, foreseen in the NUMEN project. The results of simulations obtained for different ion beams and target composition are presented below. The first simulations shows that, for the beam energy range of NUMEN interest, the vacancy density is constant throughout the target, allowing the simulation of thinner targets for better efficiency. Simulations were performed until the error on total number of vacancies was better than 5%. To compare the

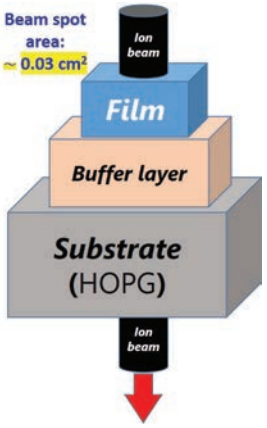


Fig. 133. Schematic of the cylinder with an area equal to the beam spot size of 0.03 cm$^2$ and target plus substrate of the HOPG used in TRIM simulations, considering the system with and without a buffer layer.

Table 19. Beam parameters used for simulations.

| Ion beam | Energy (MeV/nucleon) | Total energy (MeV) |
|---|---|---|
| $^{20}$Ne | 15–30 | 300–600 |
| $^{18}$O | 16–60 | 288–1080 |
| $^{12}$C | 15–30 | 180–360 |

Table 20. Beam fluxes and irradiation time for experimental runs.

| Beam flux (ions/s) | Irradiation time (days) |
|---|---|
| $10^{11}$ | 5 |
| $10^{12}$ | 30 |
| $10^{13}$ | 3 |

integrity of the target post-irradiation, the vacancy density provided by simulations was used to determine the number of vacancies in the target volume under beam interaction, consisting of a cylinder with an area equal to the beam spot size of 0.03 cm$^2$ and target thickness which is about 2.65 microns (see Fig. 133). The vacancy halo and beam spread inside the target is negligible.

In Tables 19–21 some simulated conditions of interest to the NUMEN project are given.

In Fig. 134 the density of displacements found in the TRIM simulation for $^{20}$Ne ions at 300 MeV is shown. In the thin target, the recoils play a major contribution to target damage, but in the HOPG backing the cause of degradation can be assigned almost completely to incoming ions.

Table 21. Target systems simulated.

| Layer | Material | Thickness (nm) |
|---|---|---|
| Target film | Sn ($Z = 50$), Ge ($Z = 32$), Te ($Z = 52$) | ≈300–800 |
| Buffer layer | Cr, Bi, no buffer | ≈10–40 |
| Substrate | HOPG | ≈2000–10,000 |

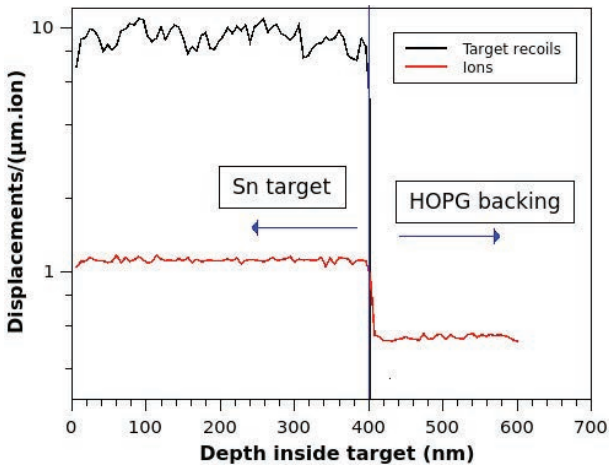


Fig. 134. Density of displacements found for thin target and HOPG backing in the TRIM simulation for $^{20}$Ne ions at 300 MeV.

Figure 135 shows in detail the formation of vacancies as a function of irradiation time, for three different fluxes, considering a $^{20}$Ne beam at 270 MeV incident on Sn plus HOPG.

In Fig. 136, the results indicate that HOPG backing degradation should be accounted for in the NUMEN experimental setup, considering how long the HOPG can stand structure degradation without significant heat conductivity loss. The dashed black line indicates when the material becomes fully amorphous, compromising good thermal conductivity properties. For all ion beams simulated it was used 0.4 $\mu$m Sn plus 2.635 $\mu$m HOPG thickness. The vacancy number is compared to the number of atoms in the same region, obtaining vacancy concentration $C$, as $C =$ vacancies/atoms. $C = 1$ means that, in average, every atom in that region has been displaced from its original position, thus turning HOPG in amorphous carbon in that microvolume, neglecting rare replacement collision events, with serious impact on the material thermal properties. The vacancy number depends on the accumulated beam fluence for any planned experiment, therefore upon particle flux and beam time.

The results obtained through the simulations indicate that, for a flux of $10^{11}$ ions/s, there is a degradation of 0.25% in 240 h, while for $10^{13}$ ions/s, the same percentage of vacancies may occur in about 2.4 h, for $^{20}$Ne beam. Since HOPG

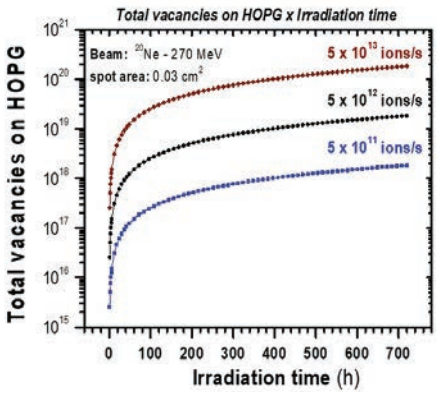


| $^{20}$Ne Beam parameters | |
|---|---|
| Energy (MeV) | 270 |
| Spot area (cm$^2$) | 0.03 |
| Current ($\mu$A) | *variable* |
| Charge state | 10 |
| Flux (ions/s) | *variable* |
| Normal incidence | |

| Target parameters | Sn film | buffer | HOPG substrate |
|---|---|---|---|
| Thickness ($\mu$m) | 0.4 | - | 2.635 |
| Density (g/cm$^3$) | 7.3 | - | 2.22 |
| a.m.u. | 118.7 | - | 12 |
| Surface binding energy (eV) | 3.12 | - | 7.41 |
| Lattice binding energy (eV) | 3.0 | - | 3.0 |
| Irradiated volume (cm$^3$) | $1.2 \cdot 10^{-6}$ | - | $7,905 \cdot 10^{-6}$ |

Fig. 135. Left: Graph of the total vacancies as a function of the irradiation time, for three different fluxes, considering a $^{20}$Ne beam at 270 MeV incident on Sn plus HOPG. Right: The parameters used in the simulations.

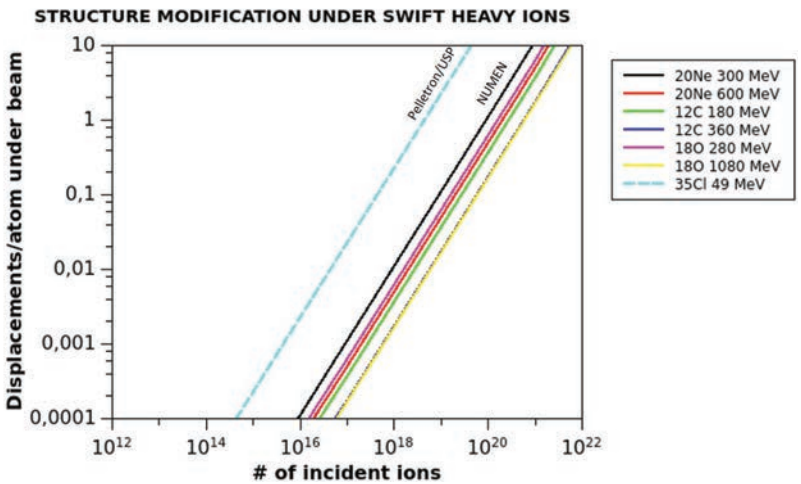


Fig. 136. Displacement concentration $C$ as a function of the ion beam fluence for different heavy-ion beams in 0.4 $\mu$m Sn plus 2.635 $\mu$m HOPG thickness.

presents different thermal conductivity in two orthogonal planes, the degradation may be smaller, in comparison with a graphene foil. In any case, the HOPG is found to be robust enough to allow a realistic performance of the NUMEN experiments, even in the most challenging cases. Experimental evaluation will be carried out at the São Paulo Pelletron accelerator using low-energy heavy ions, such as $^{35}$Cl at $E = 49$ MeV in order to create a high number of atom displacements and emulate the NUMEN target degradation conditions. The simulation results indicate that under these conditions, with a flux of $10^{13}$ ion/s, 0.25% of the HOPG has crystal

defects within 24 h (see Fig. 136). It is important to emphasize that this study may improve the efficiency of NUMEN experiments and the results should generate technological advances related to the development of targets to be used where thermal conductivity is essential.



## 10. Computing Model

### 10.1. *Data transmission and storage*

The electronic modules of NUMEN are designed to provide a data stream which is already formatted according to the standard TPC/IP protocol. Data are routed through a standard Ethernet cable to a dedicated server, which is in charge for the storage on disk. If the entire focal plane detector were read out with a full-intensity beam of $\sim 10^{13}$ pps, the expected data rate would be about 600 MB/s, largely driven by the tracker (see Subsec. 7.6). The throughput expected from the $\gamma$-calorimeter at the lower intensity of $\sim 10^{12}$ pps is also about 600 MB/s, but it can be reduced by a factor of 10 (or more) by an appropriate energy gating (see Subsec. 7.6).

A dual-phase strategy is proposed to moderate such a significant amount of data, so to ease the data handling and to release the requirements on the storage system:

(1) First, to perform an "exploratory" run, with a beam intensity of $\sim 10^{11}$ pps (i.e. far from the maximum allowed by the new CS). Such a run is meant to give a broad overview of the configuration and to select the interesting ground-state to ground-state transition which is relevant for the DCE studies. Since the reactions competing to the DCE typically have much higher cross-sections, they can be studied within a limited beam time (1–2 days) at reduced intensity. When running in the inclusive mode of Subsec. 7.6, namely acquiring only the FPD without the $\gamma$-calorimeter, the anticipated data rate is below 10 MB/s, due to the nonmaximal beam intensity. For the cases in which the $\gamma$-calorimeter is also of interest, the data rate is doubled to about 20 MB/s.

(2) Second, to carry out a run which is tailored to the ground-state to ground-state DCE transitions only. This run would be with full beam intensity ($10^{13}$ pps), but acquiring only a fraction ($< 10\%$) of the FPD channels, i.e. those that are corresponding to the interesting events. For those target nuclei having low-lying excited states, it is necessary to read out also the $\gamma$-calorimeter; the channels of the $\gamma$-calorimeter will be acquired only in coincidence with the FPD. However, the beam current must be limited to $10^{12}$ pps in order to limit the pile-up on the $LaBr_3$ scintillators and to allow for an unambiguous correlation between events in the $\gamma$-calorimeter and delayed events in the FPD. By scaling according to the beam intensity and to the FPD coverage, the anticipated data rates are of the order of 60 MB/s (both for inclusive mode at $\sim 10^{13}$ pps intensity and for the exclusive mode at $\sim 10^{12}$ pps intensity), which is a manageable level.

Such an optimized approach will reduce, in either of the two phases, the expected rate of data to be handled and written on the storage system to a more comfortable level. As discussed above, the expected data rate will range between 10 MB/s (in the FPD only runs at $10^{11}$ pps) and 100 MB/s, depending on the experimental parameters (beam intensity, target) and on the chosen configuration for the trigger logic.

Given the rate and the other operational conditions, offline data handling can be performed entirely using commercially available components. In particular, the core of the system is a one- or two-CPU 32-core main server, equipped with 10 Gbit/s Ethernet cards. The main server receives the data flow, which is routed by means of standard Ethernet cables and a 10 Gbit/s Ethernet switch. There is also the open option to perform data compression in real time, e.g. using gzip or other lossless compression algorithms, such to reduce the total weight of data written on disk and to potentially reduce the costs for storage. The main server is monitored by an additional smaller server (*control server*), which is in charge for run control and for the slow control; this includes the storage of critical detector parameters along the measurement, the start/stop of the data acquisition, the communication with the detectors and the electronic modules, the setup and stability monitoring of detector parameters, as HVs and gains. A backup server, which is ideally a clone of the main server from the hardware and software point of view, is always kept available, such to be a quick replacement in the case of a failure of the main server during a measurement.

During the normal conditions, when the main server is operational, the backup server will be used to perform the event building (i.e. the matching of the data blocks coming from different modules and referring to the same event) and to run reconstruction algorithms and other offline data analysis. It is expected that a relatively quick first-level analysis, to be performed in quasi-real-time, can be very effective in the rejection of noise and background, and for monitoring purposes. The target outcome of the first-level analysis is a skimmed dataset, containing only selected events. Such a dataset is targeted to be a factor of $> 10$ lighter than the full raw data and will be used for the subsequent CPU-intensive levels of the analysis. It is plausible that the bottleneck of the first-level analysis will be given by the disk access and I/O, given the fact that each event has to be built from different DAQ streams written on different files.

The interface to the storage component is a RAID6 Fiber Channel controller: the writing capability is up to 2 GB/s, which is safely above the final data rate expected in NUMEN.

The RAID6 storage system is dimensioned for a total capacity of 500 TB–1 PB, which is readily available on the market. Since NUMEN will be intrinsically divided into many different runs, the option to have a partitioned storage (for instance blocks of $48 \times 4$ TB disks, totaling 160 TB each) looks more convenient and more easily scalable with respect to a single monolithic solution. Additional backup copies of the data taken in each in-beam experiment will be made on tape.

After the end of each in-beam experiment, which will yield O(120 TB) of data, all raw data are backuped on tape in multiple copies. After the backup and the double-checks, raw data are removed from the main storage, leaving only the skimmed files from the first-level analysis, O(10 TB). This strategy is meant to limit the usage of the disk space, by allowing for the long-term storage of raw data on the much cheaper tapes. The first-level analysis could be potentially performed online, thus avoiding to write heavy raw data; however, since this procedure is intrinsically risky for a loss, it will be considered only at later stages in NUMEN.

The computing infrastructure of the NUMEN experiment will be integrated in synergy with the IT service of LNS-INFN.

### 10.2. *Offline analysis software*

The offline analysis, including calibration and event reconstruction, is performed using the existing framework MXSOFT, written in C++. The framework contains a re-engineered and optimized version of the algorithms that were already used and validated in MAGNEX, including those for calibration, selection and ray-tracing. The final high-level analysis output is stored in ROOT format. The main design features of MXSOFT are: (1) modularity and flexibility, such to allow the easy accommodation of extensions, improvements and alternative algorithms; (2) cross-platform compatibility, by means of a dedicated and semi-automatic build procedure based on `configure` scripts; (3) optimization in terms of CPU performance and memory footprint and (4) scalability.

The software to be used for the event building and the first-level analysis, to be performed in real or quasi-real-time, is being designed and will be benchmarked with simulated data streams.

## 11. Theory

Within the NUMEN project, theoretical developments aim at reaching a full description of the DCE reaction cross-section, including also competing channels that may lead to the same final outcome, and at investigating the possible analogies with double beta decay. The main lines of investigation can be identified as follows:

(1) The description of DCE reactions as a two-step mechanism, i.e. a sequence of two charge exchange processes (one-body DCE — 1bDCE). The recent progress made on the modeling of single CE reactions[28] is instrumental to tackle this step. We also aim at working on the analogy between the DCE model and the theory of $2\nu\beta\beta$ decay, which also consists of two uncorrelated steps, though, in principle, a larger variety of intermediate states can be involved in DCE reactions, owing to the non-negligible intermediate momentum transfer. The two-step formalism has been successfully applied to the description of the DCE cross-section in $^{18}O + ^{40}Ca$ reactions at 270 MeV.[100] A thorough comparison with the large set of available experimental data is planned.

(2) The elaboration of the theory of a new DCE mechanism, never considered so far, which assumes a correlation between the two charge changing events, mediated by the exchange of neutral mesons (two-body DCE — 2bDCE) between the pair of nucleons involved in the projectile and/or in the target. The latter can be considered as the closest to the $0\nu\beta\beta$ decay, where the two nucleons undergoing $\beta$ decay are correlated by the $\bar{\nu} - \nu$ pair of Majorana neutrinos.[29]
(3) The evaluation of the cross-section associated with competing processes leading to the same exit channel of the CE reactions, namely multi-nucleon transfer.

An extended description of the points outlined above is presented below.

### 11.1. *DCE reactions as a two-step process and analogies with $2\nu\beta\beta$ decay*

The most conventional description of the DCE mechanism would be to consider it as a two-step process.[101] The latter is given by two uncorrelated single charge exchange events where after the first event the system propagates before a second charge exchange occurs. Each of the single charge exchange processes is induced by the action of one-body operators on the projectile and the target nucleus. Thus, this process can be considered as a two-step one-body double charge exchange reaction. The two-step DCE process is depicted diagrammatically in Fig. 137.

The reaction matrix element, connecting the incident channel $\alpha = a+A$ and the final channel $\beta = b + B$, is written down easily, in Distorted Wave Born Approximation (DWBA), as a quantum mechanical second-order amplitude:

$$\mathcal{M}^{(\mathrm{DCE})}_{\alpha\beta}(\mathbf{k}_\beta, \mathbf{k}_\alpha) = \left\langle \chi^{(-)}_\beta bB \middle| T_{NN} \mathcal{G}^{(+)}(\omega) T_{NN} \middle| aA\chi^{(+)}_\alpha \right\rangle . \tag{9}$$

Initial and final state interactions are taken into account by the distorted waves, $\chi(\mathbf{r})$, obeying incoming and outgoing spherical wave boundary conditions, respectively. The intermediate nuclear propagator may be represented in terms of the

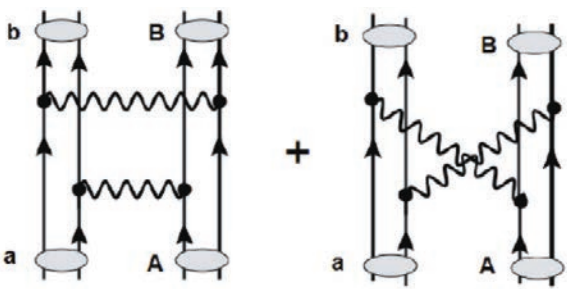


Fig. 137. Graphical representation of the one-body two-step heavy-ion double charge exchange reaction by hadronic interactions. The reaction $a(N_a, Z_a) + A(N_A, Z_A) \rightarrow b(N_a \pm 2, Z_a \mp 2) + B(N_A \mp 2, Z_A \pm 2)$ proceeds by the sequential, but independent, action of two charge-changing strong interaction events, i.e. the exchange of charged mesons. Each of the interaction events acts like a one-body operator on the target and projectile, respectively.

complete system of the nuclear eigenstates $|\gamma\rangle = |cC\,\chi_\gamma^{(+)}\rangle$ which are reached by a SCE reaction

$$\mathcal{G}(\omega) = \sum_{\gamma=c,C} |\gamma\rangle G_\gamma(\omega_\gamma, \omega_\alpha)\langle\tilde{\gamma}|\,, \tag{10}$$

where the reduced Green function $G_\gamma = (\omega_\alpha - \omega_\gamma + i\eta)^{-1}$ describes the propagation of the intermediate scattering states. Above, $\omega_{\alpha,\gamma}$ is the total center-of-mass energy as defined by the rest masses and the kinetic energy in the incident ($\alpha$) or intermediate ($\gamma$) channel, and $\mathbf{k}_{\alpha,\beta}$ defines the relative momentum in the entrance ($\alpha$) or exit ($\beta$) channel. Either of the first and second reaction step is described by the charge-changing part of the nucleon–nucleon $T$-matrix, which in nonrelativistic notation is given by

$$T_{NN} = \big(t_{01} + t_{11}\boldsymbol{\sigma}_a \cdot \boldsymbol{\sigma}_A + t_{T1}S_{12}(\boldsymbol{\sigma}_a, \boldsymbol{\sigma}_A)\big)\Big(\tau_+^{(a)}\tau_-^{(A)} + \tau_-^{(a)}\tau_+^{(A)}\Big) \tag{11}$$

including spin-scalar ($t_{01}$) and spin-vector ($t_{11}$) central interactions and rank-2 tensor interactions given by the usual rank-2 tensor operator $S_{12}$ and with a form factor $t_{T1}$. A suitable representation is obtained by expressing the two-step amplitude in momentum space:

$$\mathcal{M}_{\alpha\beta}^{(\mathrm{DCE})}(\mathbf{k}_\beta, \mathbf{k}_\alpha) = \sum_{\gamma=c,C} \int \frac{d^3k_\gamma}{(2\pi)^3} \mathcal{M}_{\beta\gamma}^{(\mathrm{SCE})}(\mathbf{k}_\beta, \mathbf{k}_\gamma) G_\gamma(\omega_\gamma, \omega_\alpha) \tilde{\mathcal{M}}_{\gamma\alpha}^{(\mathrm{SCE})}(\mathbf{k}_\gamma, \mathbf{k}_\alpha) \tag{12}$$

showing that the DCE amplitude is obtained as a superposition of one-step SCE reaction amplitudes.

The fully quantum mechanical DCE differential cross-section is then given by

$$d\sigma_{\alpha\beta}^{(\mathrm{DCE})} = \frac{m_\alpha m_\beta}{(2\pi\hbar^2)^2} \frac{k_\beta}{k_\alpha} \frac{1}{(2J_A+1)(2J_a+1)} \times \sum_{M_a, M_A \in \alpha, M_b, M_B \in \beta} \big|\mathcal{M}_{\alpha\beta}^{(\mathrm{DCE})}(\mathbf{k}_\beta, \mathbf{k}_\alpha)\big|^2 d\Omega \tag{13}$$

averaged over the initial nuclear spin states and summed over the final nuclear spin states, respectively. Reduced masses in the incident and exit channel are denoted, respectively, by $m_{\alpha,\beta}$.

As it appears from Eq. (12), the description of DCE reactions in terms of the convolution of two uncorrelated SCE processes exhibits close analogies with two neutrino double beta decay.[102] However, owing to the large momentum that can be transferred to the intermediate channel, we expect the virtual intermediate transitions explored in DCE reactions to be actually closer to the ones characterizing $0\nu\beta\beta$.

We finally stress that, as discussed above, a suitable description of the 1bDCE mechanism implies a thorough analysis of SCE processes involving heavy ions. The latter has been the object of a recent dedicated study,[28] where the conditions required to factorize the corresponding cross-section into reaction and structure

parts are discussed in detail. This separation allows one to isolate the nuclear matrix elements relevant to $\beta$-decay processes.[103] Taking advantage of this background, the 1bDCE mechanism is introduced and discussed in detail in Refs. 100 and 104.

Explicit calculations for SCE and DCE reactions, based on the codes HIDEX[27] and FRESCO[105]), have been performed for the reaction $^{18}O + {}^{40}Ca$ at $T_{lab} = 270$ MeV.[28,100,106] The investigation of other NUMEN systems (such as the reaction $^{20}Ne + {}^{116}Cd \rightarrow {}^{20}O + {}^{116}Sn$) is in progress. Among the most important conclusions reached so far, we also emphasize the role played by the imaginary part of the optical potential (i.e. by absorption effects) in determining the amplitude of the full SCE and DCE reaction cross-section. Transition form factors are presently evaluated on the basis of QRPA calculations. We plan to compute the spectroscopic amplitudes and in perspective the radial transition densities also in the scheme of IBFFM2 (IBM for odd–odd nuclei).[107,108] In fact, a code for IBFFM has been developed, in order to have wave functions in the IBM like approach, opening the way to evaluate the spectroscopic amplitudes and the radial transition densities also in that scheme. This will open the possibility to give predictions with IBM models[107,109] in the field of charge exchange reactions, where experimental feedback is available.

### 11.2. *Analogy between DCE reactions and $0\nu\beta\beta$ decay*

In this subsection, we enter into a deeper discussion of the analogies motivating the investigation of heavy-ion DCE reactions as a tool to probe the nuclear structure input to the matrix elements of nuclear double beta decay.

Collisional (or direct) charge exchange by isovector nucleon–nucleon interactions is the most probable cause for transferring charge between colliding ions at energies well above the Coulomb barrier, as discussed e.g. in Refs. 110–113. The SCE process can, of course, occur in higher order. As discussed above, a second-order charge exchange reaction may be given by two independent, sequential SCE reactions, i.e. the ions need to interact twice by two-body interactions between a target and a projectile nucleon. As far as the reaction mechanism is concerned those double-SCE reactions resemble closely nuclear $2\nu\beta\beta$ decay (see Subsec. 11.1).

However, it is possible to envisage a nuclear double-charge changing (DCC) scenario of a close structural similarity to $0\nu\beta\beta$ decay: in the presence of a second nucleus, a correlated double charge exchange transition can be initiated by a particular type of hadronic two-body operator and proceed as a one-step reaction. A correlated pair of nucleons (through the exchange of a neutral meson) changes its total charge by two units under emission of a virtual pair of charged mesons captured by the second ion and there inducing a complementary DCC transition. In an isolated nucleus the two emitted mesons would be reabsorbed immediately thus restoring the nucleonic charge, and no net effect would be observed. The process would be of no particular interest except for contributing to the nuclear short-range correlations, causing nuclear momentum distributions to deviate by 10 to 15% from those expected for independent quasiparticles.[114–117] If, however, the intermediate

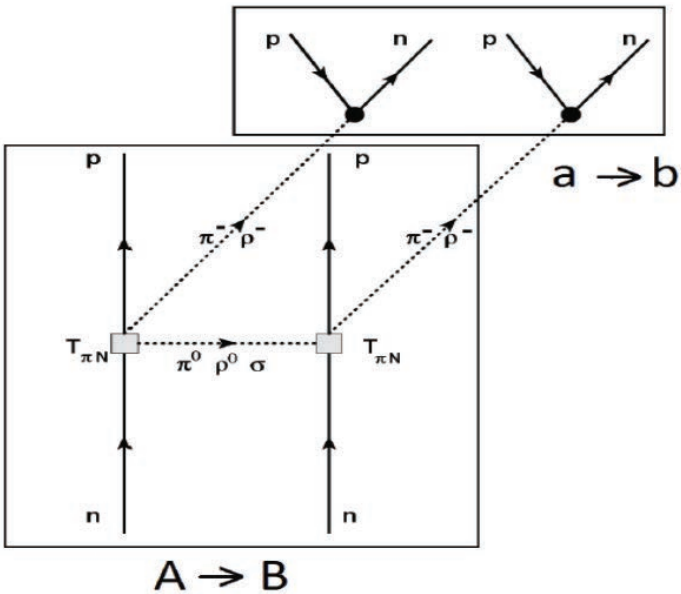


Fig. 138. Generic diagram illustrating the hadronic surrogate process for $0\nu2\beta$ decay. A virtual $nn \to pp\pi^-\pi^-$ scattering process, causing the $\Delta Z = +2$ target transition $A \to B$, is accompanied by $nnp^{-1}p^{-1}$ double-CC excitation in the projectile. As indicated, other isovector mesons as, e.g. the $\rho$-meson isotriplet will contribute too.

charged mesons are absorbed by a second nucleus, both ions will be found to have changed their charge by two units in a complementary manner. Different from a conventional two-step heavy-ion charge exchange reaction the whole reaction proceeds as one-step reaction with respect to counting the ion–ion interaction.

That physical process is depicted in Fig. 138 for an $nn \to pp$ transition. The figure shows the involved nuclear configurations, that are realized by the coherent action of charge-changing meson–nucleon interactions. Overall, the process scrutinized here corresponds on the target side to a $nn \to pp + \pi^-\pi^-$ reaction. In free space, the corresponding charge-conjugated reaction $pp \to nn + \pi^+\pi^+$ reaction and other double-pion production channels were in fact already investigated experimentally at CELSIUS and COSY[118–128] and later also at HADES.[129] Thus these correlations are expected to be present also in more involved nuclear reactions and are the object of our present investigations.[29]

### 11.3. *DCE in eikonal approximation and small momentum transfer*

Using the eikonal approximation and small momentum transfer approximation a simple model for differential cross-section (at very small angles) for double charge exchange has been derived and under those hypotheses, a factorization of the reaction part and the nuclear part holds.[30] Moreover, the explicit form for a double charge exchange effective potential has been derived in the closure approximation

and also the explicit expression for the nuclear matrix elements that are of the form of Double Gamow–Teller and Double Fermi.[30] Those DCE-DGT and DCE-DF have been calculated using microscopic IBM. Finally we have shown a linear relation among DCE-DGT and $0\nu$DGT confirming[130] in shell model.

The DCE matrix elements calculated in microscopic IBM are also at disposal of the HIDEX reaction model code, just as also we plan to complete the calculation with an odd–odd IBFFM program of the single charge exchange matrix elements for the two-step double charge exchange reaction code.[100]

### 11.4. *Competing channels*

To interpret the experimental cross-sections and properly isolate the DCE contribution, the description of competing processes leading to the same exit channel is mandatory. The latter are essentially multi-nucleon transfer reactions. An example is shown in Fig. 139, for the NUMEN reaction $^{20}\mathrm{Ne} + {}^{116}\mathrm{Cd} \rightarrow {}^{20}\mathrm{O} + {}^{116}\mathrm{Sn}$.

The theoretical description of these reactions is generally tackled still within the DWBA approach, although coupled channel calculations (based on the code FRESCO[105]) are also feasible. An important point to consider is the treatment of the spectroscopic information contained in such a theoretical description.

Recently, the formalism for two nucleon transfer reactions[131] has been elaborated also within the microscopic IBM-2.[132–137] This development is particularly appealing; indeed microscopic IBM allows one to calculate in a realistic way the transition matrix elements for heavy, medium nuclei and it has been exploited for the evaluation of neutrinoless double beta decay nuclear matrix elements.[138,139]

Spectroscopic amplitudes of two-proton and two-neutron transfer reactions, which are competing with the two charge exchange, have been computed for the combinations represented in Fig. 139, both with microscopic IBM-2 and with shell model calculations,[140] and inserted as input in the FRESCO code. The

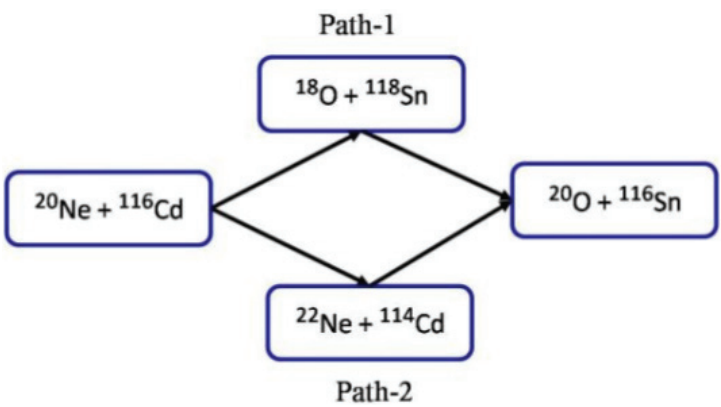


Fig. 139. Schematic illustration of $(2n - 2p)$ or $(2p - 2n)$ transfer paths for the reaction $^{20}\mathrm{Ne} + {}^{116}\mathrm{Cd} \rightarrow {}^{20}\mathrm{O} + {}^{116}\mathrm{Sn}$.

resulting multi-nucleon transfer reaction cross-sections, obtained within the two model schemes, differ by less than a factor of 2.

One observes that these competing processes are far from saturating the total detected experimental cross-section, thus pointing to a dominant role of the double charge exchange contribution. Indeed the calculated transfer cross-section is of the order of $10^{-4} - 10^{-3}$ nb, to be compared with the experimental cross-section of $12 \pm 2$ nb. On the other hand, the calculated two-proton transfer cross-section $^{20}\mathrm{Ne} + {}^{116}\mathrm{Cd} \rightarrow {}^{18}\mathrm{O}_{\mathrm{g.s.}} + {}^{118}\mathrm{Sn}_{\mathrm{g.s.}}$, as obtained employing SM spectroscopic amplitudes, is of the order of 10 nb,[141] which is close to the experimental value ($9 \pm 5$ nb). The latter result can be considered as a further check of the good performances of the full calculation.

In keeping with this analysis, we plan to investigate the role of nucleon transfer with respect to direct charge exchange also for SCE reactions, such as $^{20}\mathrm{Ne} + {}^{116}\mathrm{Cd} \rightarrow {}^{20}\mathrm{F} + {}^{116}\mathrm{In}$. In this case one has to evaluate the cross-section corresponding to a sequential two nucleon transfer, to be compared with the one step process, i.e. with DWBA calculations of the direct SCE process.

We plan to keep on our activity related to the upgrade of the FRESCO code. We intend to insert systematically in the calculations all the channels leading to the same final outcome, namely CE and transfer processes. The final goal would be to treat the corresponding transition amplitudes coherently, so that possible interference effects would be taken into account.

## References


1. J. D. Vergados, H. Ejiri and F. Šimkovic, *Rep. Prog. Phys.* **75**, 106301 (2012).
2. H. Ejiri, J. Suhonen and K. Zuber, *Phys. Rep.* **797**, 1 (2019).
3. J. Barea, J. Kotila and F. Iachello, *Phys. Rev. C* **87**, 014315 (2013).
4. S. Dell'Oro, S. Marcocci, M. Viel and F. Vissani, *Adv. High Energy Phys.* **2016**, 2162659 (2016).
5. J. Engel and J. Menéndez, *Rep. Prog. Phys.* **80**, 046301 (2017).
6. F. Cappuzzello *et al.*, *Eur. Phys. J. A* **54**, 72 (2018).
7. F. Cappuzzello, C. Agodi, M. Bondí, D. Carbone, M. Cavallaro and A. Foti, *J. Phys. Conf. Ser.* **630**, 012018 (2015).
8. C. Agodi, F. Cappuzzello, M. Cavallaro, M. Bondí, D. Carbone, A. Cunsolo and A. Foti, *Nucl. Part. Phys. Proc.* **265-266**, 28 (2015).
9. F. Cappuzzello, C. Agodi, D. Carbone and M. Cavallaro, *Eur. Phys. J. A* **52**, 167 (2016).
10. F. Cappuzzello, M. Cavallaro, C. Agodi, M. Bondì, D. Carbone, A. Cunsolo and A. Foti, *Eur. Phys. J. A* **51**, 145 (2015).
11. D. Carbone *et al.*, *Phys. Rev. C* **95**, 034603 (2017).
12. M. Cavallaro *et al.*, *Phys. Rev. C* **93**, 064323 (2016).
13. M. J. Ermamatov *et al.*, *Phys. Rev. C* **94**, 024610 (2016).
14. D. Carbone *et al.*, *J. Phys.*: *Conf. Ser.* **312**, 082016 (2011).
15. F. Cappuzzello *et al.*, *Nucl. Instrum. Methods Phys. Res. A* **763**, 314 (2014).
16. C. Agodi, G. Giuliani, F. Cappuzzello, A. Bonasera, D. Carbone, M. Cavallaro, A. Foti, R. Linares and G. Santagati, *Phys. Rev. C* **97**, 034616 (2018).

17. F. Cappuzzello, D. Carbone and M. Cavallaro, *Nucl. Instrum. Methods Phys. Res. A* **638**, 74 (2011).
18. S. Calabrese *et al.*, *Acta Phys. Pol. B* **49**, 275 (2018).
19. S. Calabrese *et al.*, *Nucl. Instrum. Methods Phys. Res. A* **980**, 164500 (2020).
20. L. Calabretta, A. Calanna, G. Cuttone, G. D'Agostino, D. Rifuggiato and A. Domenico Russo, *Mod. Phys. Lett. A* **32**, 1740009 (2017).
21. M. Cortesi, S. Rost, W. Mittig, Y. Ayyad-Limonge, D. Bazin, J. Yurkon and A. Stolz, *Rev. Sci. Instrum.* **88**, 013303 (2017).
22. S. Tudisco *et al.*, *Sensors* **18**, 2289 (2018).
23. D. Carbone *et al.*, *Results Phys.* **6**, 863 (2016).
24. A. Lazzaro, F. Cappuzzello, A. Cunsolo, M. Cavallaro, A. Foti, S. Orrigo, M. Rodrigues, J. Winfield and M. Berz, *Nucl. Instrum. Methods Phys. Res. A* **602**, 494 (2009).
25. A. Lazzaro, F. Cappuzzello, A. Cunsolo, M. Cavallaro, A. Foti, S. Orrigo, M. Rodrigues and J. Winfield, *Nucl. Instrum. Methods Phys. Res. A* **585**, 136 (2008).
26. F. Iazzi *et al.*, *WIT Trans. Eng. Sci.* **116**, 61 (2017).
27. F. Cappuzzello *et al.*, *Nucl. Phys. A* **739**, 30 (2004).
28. H. Lenske, J. I. Bellone, M. Colonna and J. A. Lay, *Phys. Rev. C* **98**, 044620 (2018).
29. H. Lenske, F. Cappuzzello, M. Cavallaro and M. Colonna, *Prog. Part. Nucl. Phys.* **109**, 103716 (2019).
30. E. Santopinto, H. Garcia-Tecocoatzi, R. I. Magana Vosevoldovna and J. Ferretti, *Phys. Rev.* **98**, 061601 (2018).
31. J. I. Bellone, M. Colonna, H. Lenske and J. A. Lay, *J. Phys.*: *Conf. Ser.* **1056**, 012004 (2018).
32. J. Blomgren *et al.*, *Phys. Lett. B* **362**, 34 (1995).
33. F. Naulin, C. Détraz, M. Roy-Stéphan, M. Bernas, J. de Boer, D. Guillemaud, M. Langevin, F. Pougheon and P. Roussel, *Phys. Rev. C* **25**, 1074 (1982).
34. D. M. Drake, J. D. Moses, J. C. Peng, N. Stein and J. W. Sunier, *Phys. Rev. Lett.* **45**, 1765 (1980).
35. D. Bes, O. Dragún and E. Maqueda, *Nucl. Phys. A* **405**, 313 (1983).
36. C. H. Dasso and A. Vitturi, *Phys. Rev. C* **34**, 743 (1986).
37. K. Kisamori *et al.*, *Phys. Rev. Lett.* **116**, 052501 (2016).
38. H. Sagawa and T. Uesaka, *Phys. Rev. C* **94**, 064325 (2016).
39. H. Matsubara *et al.*, *Few-Body Syst.* **54**, 1433 (2013).
40. H. Ejiri *et al.*, *J. Phys. Soc. Jpn.* **82**, 044202 (2013).
41. M. Cavallaro, PoS **BORMIO2017**, 015 (2017).
42. M. Cavallaro *et al.*, *Nucl. Instrum. Methods Phys. Res. B* **463**, 334 (2020).
43. A. Spatafora *et al.*, *Phys. Rev. C* **100**, 034620 (2019).
44. M. Cavallaro *et al.*, *Results Phys.* **13**, 102191 (2019).
45. D. Rifuggiato, L. Calabretta, L. Cosentino and G. Cuttone, *Proc. Int. Conf. on Cyclotron and their Applications*, 2013, available at: https://accelconf.web.cern.ch/AccelConf/Cyclotrons2013/papers/moppt011.pdf.
46. L. Calabretta, A. Calanna, G. Cuttone, G. D'Agostino, D. Rifuggiato and A. D. Russo, *Proc. Int. Conf. on Cyclotron and their Applications*, 2016, available at: https://accelconf.web.cern.ch/AccelConf/Cyclotrons2016/papers/moa02.pdf.
47. G. D'Agostino, L. Calabretta, A. Calanna and D. Rifuggiato, *Proc. Int. Conf. on Cyclotron and their Applications*, 2016, available at: https://accelconf.web.cern.ch/AccelConf/Cyclotrons2016/papers/tuc03.pdf.
48. A. Calanna, *Il Nuovo Cimento C* **40**, 101 (2017).
49. K. Shima *et al.*, *Atom. Data Nucl. Data Tables* **51**, 173 (1992).

50. G. Gallo, G. Costa, L. Allegra, G. Messina and E. Zappalá, *Proc. Int. Conf. on Cyclotron and their Applications*, 2016, available at: https://accelconf.web.cern.ch/AccelConf/Cyclotrons2016/papers/thp09.pdf.
51. S. S. Tomic and E. V. Samsonov, *Phys. Rev. E* **65**, 036504 (2002).
52. L. Calabretta, A. Calanna, G. D'Agostino, D. Rifuggiato and A. D. Russo, *IPAC 2017*, available at: https://accelconf.web.cern.ch/AccelConf/IPAC2017/papers/wepva053.pdf.
53. A. D. Russo, L. Calabretta, G. Cardella and P. Russotto, *Nucl. Instrum. Methods Phys. Res. B*, in press (2019).
54. G. D'Agostino, L. Calabretta, W. Kleeven and D. Rifuggiato, *Proc. Int. Conf. on Cyclotron and their Applications*, available at: https://accelconf.web.cern.ch/AccelConf/ipac2019.
55. M. Cavallaro, F. Cappuzzello, D. Carbone, A. Cunsolo, A. Foti, A. Khouaja, M. R. D. Rodrigues, J. S. Winfield and M. Bondì, *Eur. Phys. J. A* **48**, 59 (2012).
56. F. Cappuzzello, M. Cavallaro, A. Cunsolo, A. Foti, D. Carbone, S. Orrigo and M. Rodrigues, *Nucl. Instrum. Methods Phys. Res. A* **621**, 419 (2010).
57. Download Area for Poisson Superfish, https://laacg.lanl.gov/laacg/services/download_sf.phtml.
58. F. Sauli, *Nucl. Instrum. Methods Phys. Res. A* **805**, 2 (2016) [Special Issue in Memory of Glenn F. Knoll].
59. A. Breskin, R. Alon, M. Cortesi, R. Chechik, J. Miyamoto, V. Dangendorf, J. Maia and J. D. Santos, *Nucl. Instrum. Methods Phys. Res. A* **598**, 107 (2009).
60. R. Chechik, A. Breskin, C. Shalem and D. Mörmann, *Nucl. Instrum. Methods Phys. Res. A* **535**, 303 (2004).
61. C. Grupen and B. Shwartz, *Particle Detectors*, Cambridge Monographs on Particle Physics, Nuclear Physics and Cosmology, 2nd edn. (Cambridge University Press, 2008).
62. Y. Ayyad, M. Cortesi, W. Mittig and D. Bazin, *J. Instrum.* **12**, P06003 (2017).
63. C. Shalem, R. Chechik, A. Breskin, K. Michaeli and N. Ben-Haim, *Nucl. Instrum. Methods Phys. Res. A* **558**, 468 (2006).
64. CAEN power supply SY5527, https://www.caen.it/products/sy5527/.
65. F. Cappuzzello, M. Cavallaro, A. Cunsolo, A. Foti, D. Carbone, S. E. A. Orrigo and M. R. D. Rodrigues, *Nucl. Instrum. Methods A* **621**, 419 (2010).
66. M. Cavallaro *et al.*, *Eur. Phys. J. A* **48**, 59 (2012).
67. J. Pouthas *et al.*, *Nucl. Instrum. Methods A* **357**, 418 (1995).
68. S. Aiello *et al.*, *AIP Conf. Proc.* **495**, 353 (1999).
69. R. Bougault *et al.*, *Eur. Phys. J. A* **50**, 47 (2014).
70. G. Knoll, *Radiation Detection and Measurement* (Wiley, 2000).
71. F. La Via *et al.*, *Microelectron. Eng.* **83**, 48 (2006).
72. A. A. Lebedev *et al.*, *Fiz. Tekh. Poluprovodnikov* **38**, 129 (2004).
73. G. Raciti *et al.*, *Nucl. Instrum. Methods A* **834**, 784 (2010).
74. G. Lioliou *et al.*, *Nucl. Instrum. Methods A* **840**, 145 (2016).
75. X. Zhang *et al.*, *IEEE Trans. Nucl. Sci.* **60**, 2352 (2013).
76. S. Tudisco *et al.*, *Il Nuovo Cimento C* **42**, 74 (2019).
77. S. Tudisco *et al.*, in preparation.
78. C. Ciampi *et al.*, *Nucl. Instrum. Methods A* **925**, 60 (2019).
79. G. A. P. Cirrone *et al.*, *Front. Oncol.* **7**, 223 (2017).
80. GEANT manual, http://geant4-userdoc.web.cern.ch/geant4-userdoc/UsersGuides/PhysicsReferenceManual/html/index.html.
81. J. R. B. Oliveira *et al.*, *Eur. Phys. J. A* **56**, 153 (2020).

82. L. Swiderski, R. Marcinkowski, M. Szawłowski, M. Moszyński, W. Czarnacki, A. Syntfeld-Każuch, T. Szczesniak, G. Pausch, C. Plettner and K. Roemer, Non-proportionality of electron response and energy resolution of Compton electrons in scintillators, in *IEEE Nuclear Science Symposium Medical Imaging Conference* (2010), pp. 285–290.
83. M. Cavallaro *et al.*, *Nucl. Instrum. Methods Phys. Res. A* **700**, 65 (2013).
84. CAEN website: https://www.caen.it/products/vx2740/.
85. C. Aalseth *et al.*, *Eur. Phys. J. Plus* **133**, 131 (2018).
86. CAEN website: https://www.caen.it/products/v1782/.
87. CAEN website: https://www.caen.it/products/a1442/.
88. CAEN website: https://www.caen.it/products/dt5730/.
89. CAEN website: https://www.caen.it/products/a5202/.
90. Xilinx device reliability report (2020), www.xilinx.com.
91. K. Huey, Xilinx Virtex-5QV update and space roadmap, *SpacE FPGA Users Workshop*, 3rd edn, 2016, ESA-ESTEC.
92. F. H. Schmidt Jr., Fault tolerant design implementation on radiation hardened by design SRAM-based FPGAs, Master's thesis, Massachusetts Institute of Technology, Dept. of Aeronautics and Astronautics (2013).
93. Radiation-hardened, Space-Grade Virtex-5QV Family, Data Sheet (2018), www.xilinx.com.
94. D. Sartirana, *Il Nuovo Cimento* **44**, 76 (2021).
95. D. Sartirana, D. Calvo, V. Capirossi, C. Ferraresi, F. Iazzi and F. Pinna, *Adv. Serv. Ind. Robot.* **84**, 535 (2020).
96. A. Balandin, *Nat. Mater.* **10**, 569 (2011).
97. B. Mortazavi and S. Ahzi, *Carbon* **63**, 460 (2013).
98. H. Peng, *Surf. Coat. Technol.* **306**, 171 (2016).
99. J. P. Biersack and L. Haggmark, *Nucl. Instrum. Methods* **174**, 257 (1980).
100. J. I. Bellone, S. Burrello, M. Colonna, J.-A. Lay and H. Lenske, *Phys. Lett. B* **807**, 135528 (2020).
101. G. R. Satchler, *Direct Nuclear Reactions*, International Series of Monographs on Physics, Vol. 68 (Oxford University Press, 1983).
102. J. Suhonen and O. Civitarese, *Phys. Rep.* **300**, 123 (1998).
103. T. N. Taddeucci *et al.*, *Nucl. Phys. A* **469**, 125 (1987).
104. H. Lenske and J. Bellone, M. Colonna and D. Gambacurta, *Universe* **7**, 98 (2021).
105. I. J. Thompson, *Comput. Phys. Rep.* **7**, 167 (1988).
106. M. Cavallaro *et al.*, *Front. Astron. Space Sci.* **8**, 61 (2021).
107. F. Iachello and P. Van Isacker, *The Interacting Boson-Fermion Model* (Cambridge University Press, Cambridge, 1991).
108. R. M. Vsevolodovna, E. Santopinto and R. Bijker, Transfer reactions between odd-odd and even-even nuclei by using IBFFM, arXiv:2101.05659.
109. A. Arima and F. Iachello, *Phys. Rev. Lett.* **35**, 1069 (1975).
110. C. Brendel, P. von Neumann-Cosel, A. Richter, G. Schrieder, H. Lenske, H. H. Wolter, J. Carter and D. Schüll, *Nucl. Phys. A* **477**, 162 (1988).
111. H. G. Bohlen *et al.*, *Nucl. Phys. A* **488**, 89 (1988).
112. H. Lenske, H. H. Wolter and H. G. Bohlen, *Phys. Rev. Lett.* **62**, 1457 (1989).
113. H. Lenske and G. Schrieder, *Eur. Phys. J. A* **2**, 41 (1998).
114. F. Froemel, H. Lenske and U. Mosel, *Nucl. Phys. A* **723**, 544 (2003).
115. P. Konrad and H. Lenske, *Eur. Phys. J. A* **33**, 291 (2007).
116. N. Rocco, A. Lovato and O. Benhar, *Phys. Rev. Lett.* **116**, 192501 (2016).
117. O. Benhar, *Nucl. Phys. News* **26**, 15 (2016).

118. J. Johanson *et al.*, *Nucl. Phys. A* **712**, 75 (2002).
119. W. Brodowski *et al.*, *Phys. Rev. Lett.* **88**, 192301 (2002).
120. J. Pätzold *et al.*, *Phys. Rev. C* **67**, 052202(R) (2003).
121. E. Doroshkevich *et al.*, *Eur. Phys. J. A* **18**, 171 (2003).
122. T. Skorodko *et al.*, *Eur. Phys. J. A* **35**, 317 (2008).
123. T. Skorodko *et al.*, *Phys. Lett. B* **679**, 30 (2009).
124. H. Clement *et al.*, *Int. J. Mod. Phys. A* **20**, 1747 (2005).
125. S. Abd El-Bary *et al.*, *Eur. Phys. J. A* **37**, 267 (2008).
126. S. Abd El-Samad *et al.*, *Eur. Phys. J. A* **42**, 159 (2009).
127. T. Tsuboyama, F. Sai, N. Katayama, T. Kishida and S. S. Yamamoto, *Phys. Rev. C* **62**, 034001 (2000).
128. V. V. Sarantsev *et al.*, *Phys. Atom. Nucl.* **70**, 1885 (2007).
129. G. Agakishiev *et al.*, *Phys. Lett. B* **750**, 184 (2015).
130. N. Shimizu, J. Menendez and K. Yako, *Phys. Rev. Lett.* **120**, 142502 (2018).
131. B. Paes *et al.*, *Phys. Rev. C* **96**, 044612 (2017).
132. T. Otskuka, A. Arima, I. Talmi and F. Iachello, *Phys. Lett. B* **76**, 139 (1978).
133. T. Otskuka, A. Arima, I. Talmi and F. Iachello, *Nucl. Phys. A* **309**, 1 (1978).
134. P. D. Duval and B. R. Barrett, *Phys. Rev. Lett.* **46**, 1504 (1981).
135. S. Pittel, D. Duval and B. R. Barrett, *Ann. Phys.* **144**, 168 (1982).
136. A. Frank and P. Van Isacker, *Phys. Rev. C* **26**, 1661 (1982).
137. P. O. Lipas, M. Koskinen, H. Harter, R. Nojarov and A. Faessler, *Nucl. Phys. A* **509**, 509 (1990).
138. J. Barea and F. Iachello, *Phys. Rev. C* **79**, 044301 (2009).
139. J. Barea, J. Kotila and F. Iachello, *Phys. Rev. C* **87**, 014315 (2013).
140. D. Carbone *et al.*, *Phys. Rev. C* **102**, 044606 (2020).
141. J. Ferreira and J. Lubian, private communication.